Réponse acoustique de flammes prémélangées soumises à des ondes sonores harmoniques

Renaud Gaudron

université PARIS-SACLAY

NNT : 2018SACLC073

CentraleSupélec

Acoustic response of premixed flames submitted to harmonic sound waves

Thèse de doctorat de l'Université Paris-Saclay
préparée à CentraleSupélec

École doctorale n°579 Sciences mécaniques et énergétiques, matériaux et géosciences (SMEMAG)
Spécialité de doctorat : Energétique

Thèse présentée et soutenue à Gif-sur-Yvette, le 17/10/2018, par

Renaud GAUDRON

Composition du Jury :

Franck NICOUD Professeur, Université de Montpellier	Président
Françoise BAILLOT Professeur, Université de Rouen	Rapporteur
Thierry POINSOT Directeur de recherche, IMFT/CNRS	Rapporteur
Lutz LESSHAFFT Chargé de recherche, Ecole Polytechnique	Examinateur
Wolfgang POLIFKE Professeur, Technische Universität München	Invité
Thierry SCHULLER Professeur, CentraleSupélec - IMFT/CNRS	Directeur de thèse
Clément MIRAT Ingénieur de recherche, CentraleSupélec	Co-Directeur de thèse

Thèse de doctorat

Remerciements

Ce manuscrit de thèse est la conclusion de plusieurs années de recherche que j'ai eu la chance d'effectuer au sein du laboratoire EM2C. Je tiens en premier lieu à remercier mes deux encadrants, Clément Mirat et Thierry Schuller, pour leurs conseils tout au long de ma thèse. Ils m'ont permis de découvrir une nouvelle discipline scientifique, de nouvelles méthodes de travail, ainsi que la recherche expérimentale de façon générale. Je leur en suis très reconnaissant.

Je souhaite également remercier les membres du jury de ma soutenance de thèse: Thierry Poinsot et Françoise Baillot qui ont accepté d'être les rapporteurs de mon manuscrit de thèse, Franck Nicoud qui a présidé le jury et Lutz Lesshafft qui a accepté d'être examinateur.

Merci également à Olivier Gicquel et Sébastien Ducruix de m'avoir accueilli au sein du laboratoire EM2C. De manière générale, je tiens à remercier tout le personnel du laboratoire et en particulier Yannick et Erika qui ont usiné de nombreuses pièces pour le projet NoiseDyn ainsi que Nathalie, Noï et Brigitte sans qui le laboratoire ne fonctionnerait tout simplement pas.

Je souhaite également remercier Daniel Durox qui m'a donné de précieux conseils en matière de diagnostics expérimentaux et qui m'a permis de découvrir de nouvelles façons de vulgariser la science. Je remercie également les autres chercheurs et professeurs du laboratoire EM2C avec qui j'ai eu de nombreuses discussions fructueuses.

Je tiens à remercier tout particulièrement Marco Gatti avec qui j'ai travaillé en salle d'expérience durant une grande partie de ma thèse, en plus de partager avec lui un même bureau à Châtenay-Malabry puis à Gif-sur-Yvette.

Je remercie également Paul, Benoit, Jorge, Yi, Kevin, Constantin et Junghwa avec qui j'ai eu la chance de partager un bureau que ce soit à Châtenay-Malabry ou à Gif-sur-Yvette. J'en profite pour remercier tous les autres doctorants et post-doctorants du laboratoire EM2C avec qui j'ai passé de bons moments tout au long de ces années.

Je remercie également Malte Merk, Camilo Silva et Wolfgang Polifke avec qui j'ai eu la chance de collaborer dans le cadre du projet NoiseDyn.

J'aimerais également remercier les différents professeurs qui m'ont fait découvrir et aimer les sciences au fil des années, et plus particulièrement Suzel Margaria, Sébastien Candel et Eric Johnsen.

Enfin, je remercie tout spécialement ma famille et mes proches qui m'ont toujours apporté leur soutien et sans qui je n'en serais pas là.

Cette thèse a été rendue possible grâce au financement de l'Agence Nationale de la Recherche par le biais du projet NoiseDyn (ANR-14-CE35-0025-01).

Abstract

Thermoacoustic instabilities, also known as combustion instabilities, are a major concern in the aerospace and energy production industries. They are due to an energy transfer that occurs between a heat source, usually a flame stabilized inside a combustor, and the surrounding acoustic field and may lead to undesirable phenomena such as flame extinction, increased heat fluxes, very large sound emissions at certain frequencies, vibration, structural damage and even catastrophic failure in some cases. Given the potential consequences of such phenomena, a large research effort has been devoted to predicting the onset of combustion instabilities in modern boilers, rocket engines and gas turbines during the past few decades. Unfortunately, the theoretical framework associated with the study of thermoacoustic instabilities is complex and multi-physics and the geometry of practical combustors is an intricate arrangement of 3D cavities. As a consequence, predicting the thermoacoustic stability of a combustor at an early design stage is a challenging task to date.

One way to predict the onset of thermoacoustic instabilities is to couple an acoustic solver with a function that describes the frequency response of the flame when submitted to harmonic sound waves. This function, called a Flame Transfer Function (FTF) or a Flame Describing Function (FDF) when it is nonlinear, is then determined for a large set of forcing frequencies and operating conditions using experiments, numerical simulations or analytical models. However, the impact of many parameters such as the forcing level, the way sound waves are introduced inside the combustor, or a modification of the flame size on the flame frequency response remain poorly understood.

As a consequence, the objective of this thesis is to study the acoustic response of various laminar and turbulent premixed flames submitted to harmonic sound waves in order to improve the thermoacoustic stability predictions of labscale and industrial combustors at an early design stage. This experimental and analytical work is part of the NoiseDyn project which is completed by a numerical and theoretical investigation performed by Malte Merk, Camilo Silva and Wolfgang Polifke at Technische Universität München.

The case of premixed laminar conical flames, which are used in a variety of

domestic and industrial low-power combustors, is first investigated. The concept of FTF is introduced and a few typical FTF models for such flames are presented. These models are compared with measurements and it is concluded that the best FTF model for large premixed laminar conical flames is obtained when the velocity disturbance reaching the flame front is a convective wave with a radial component such that the incompressible mass balance is respected. Moreover, it is observed that an additional model accounting for the flame base motion has no impact on the FTF predictions of large premixed laminar conical flames. On the other hand, no model is able to accurately predict the FTF of small premixed laminar conical flames. It is concluded that an additional modeling effort is needed for such flames.

It is also shown that for large injectors, the FTF of premixed laminar conical flames is controlled by two dimensionless numbers: the reduced frequency and the steady flame tip half angle. For smaller injectors, the dimensionless standoff distance, the dimensionless flame thermal thickness and the Lewis number are further needed in order to fully describe the FTF.

In the second part of this manuscript, the acoustic response of premixed confined turbulent flames submitted to harmonic forcing is investigated using experiments and various modeling strategies. In a first set of experiments, the FDF defined with respect to various reference signal is measured using an optical technique. It is shown that all these describing functions may be related using a nonlinear acoustic network model. Moreover, it is shown that the FDF is different depending on the way acoustic forcing is introduced inside the combustor, except when the reference signal is the acoustic velocity assessed just before the flame. It is thus concluded that this signal should be used as the reference signal when defining a Flame Describing Function.

In a second set of experiments, the Dimensionless Acoustic Transfer Matrix (DATM) of the NoiseDyn burner is measured for cold and reactive operating conditions and with a swirling and non-swirling injector. The acoustic forcing level is controlled at the hot wire location and measurements are performed for various predefined forcing levels. The acoustic response of the NoiseDyn burner is found to be nonlinear for both cold and reactive operating conditions. Moreover, two acoustic network models representing the NoiseDyn burner operated for cold and reactive conditions are assembled. The measured and predicted DATM are then found to be in good agreement for cold and reactive operating conditions and for both injectors. Even though the effect of the forcing level in the predicted DATM is not entirely retrieved, the FDF measured using optical techniques could be reconstructed from the DATM measurements with good agreement.

Finally, the thermoacoustic stability of six distinct configurations of the Noise-

Dyn burner is predicted for reactive operating conditions using two acoustic network models. In the first model, the acoustic response of the flame is accounted for using a measured FDF while in the second model, the flame response is embedded inside a measured DATM. Both models are able to predict the onset of thermoacoustic instabilities and the associated frequency of the instability. However, the model based on the FDF does not predict the correct limit cycle amplitude as opposed to the model based on the DATM measurement. This is attributed to the way acoustic losses occurring inside the combustor are taken into account: in the first model, these losses are modeled whereas in the second model, they are measured, thus leading to better predictions of the limit cycle amplitude.

Résumé

Les instabilités thermoacoustiques, également appelées instabilités de combustion, sont un problème majeur pour la production d'électricité ainsi que dans l'industrie aérospatiale. Ces instabilités sont dues à un transfert d'énergie entre une source chaude, le plus souvent une flamme stabilisée dans un brûleur, et le champ acoustique environnant. Les instabilités de combustion peuvent avoir de nombreuses conséquences délétères telles que l'extinction de la flamme, l'augmentation des flux de chaleur pariétaux, l'émission d'ondes sonores de grande amplitude à certaines fréquences, des vibrations importantes, des dégâts structurels et même l'explosion du moteur dans certains cas. Étant donné les conséquences potentielles de tels phénomènes, d'importants moyens de recherche ont été consacrés à la prédiction de l'apparition d'instabilités de combustion dans les chaudières, les moteurs de fusée et les turbines à gaz ces dernières décennies. Néanmoins, le cadre théorique associé à l'étude de ces instabilités est complexe et nécessite l'emploi de nombreuses disciplines de la physique. De plus, les brûleurs industriels sont constitués de nombreuses cavités tridimensionnelles interagissant entre elles d'un point de vue acoustique. Pour toutes ces raisons, la prédiction de la stabilité thermoacoustique d'un brûleur demeure une tâche ardue à ce jour.

Une technique pour prédire l'apparition d'instabilités de combustion est de coupler un solveur acoustique avec une fonction décrivant la réponse de la flamme lorsque celle-ci est soumise à des ondes acoustiques harmoniques. Cette fonction, appelée Fonction de Transfert de Flamme (FTF) ou Fonction Descriptive de Flamme (FDF) lorsqu'elle est non-linéaire, est ensuite déterminée pour une large gamme de fréquences et de conditions opératoires en utilisant des expériences, des simulations numériques ou des modèles analytiques. Cependant, l'impact de divers paramètres tels que le niveau de forçage acoustique, la façon dont le forçage est introduit dans le système ou encore la modification de la taille de la zone réactive sur la réponse acoustique de la flamme est encore mal compris.

En conséquence, l'objectif de cette thèse est d'étudier la réponse acoustique de flammes prémélangées laminaires et turbulentes soumises à des ondes acoustiques harmoniques dans le but d'améliorer la prédiction de la stabilité ther-

moacoustique des brûleurs, qu'ils soient industriels ou de taille plus réduite, lors de leurs phases de conception. Ce travail expérimental et analytique fait partie du projet NoiseDyn qui est également constitué des simulations aux grandes échelles effectuées par Malte Merk, Camilo Silva et Wolfgang Polifke à la Technische Universität München.

Le cas des flammes prémélangées laminaires coniques, qui sont rencontrées dans de nombreux brûleurs industriels et domestiques de faible puissance, est examiné dans la première partie de ce manuscrit. Le concept de FTF est décrit et quelques modèles classiques de FTF de flammes prémélangées laminaires coniques sont présentés. Les prédictions liées à ces modèles sont ensuite comparées à des mesures expérimentales. Les meilleures prédictions pour des flammes prémélangées laminaires coniques de grande taille sont obtenues avec une perturbation de vitesse dans les gaz frais de type convective avec une composante radiale de telle sorte que l'équation de conservation de la masse soit respectée. De plus, l'inclusion d'un modèle supplémentaire prenant en compte le mouvement du pied de flamme n'a aucun impact sur les prédictions de FTF de flammes prémélangées laminaires coniques de grande taille. D'autre part, aucun modèle n'est capable de prédire la FTF de flammes prémélangées laminaires coniques de petite taille. Des recherches supplémentaires sont ainsi nécessaires afin de prédire correctement la réponse de ces flammes à des ondes acoustiques.

Il est également démontré que la FTF des flammes prémélangées laminaires coniques de grande taille est contrôlée par deux nombres sans dimension: la fréquence réduite et le demi angle au sommet de la flamme stationnaire. Pour les petites flammes, la distance de stabilisation adimensionnée, l'épaisseur thermique de flamme adimensionnée ainsi que le nombre de Lewis sont également nécessaires afin de décrire entièrement l'évolution de la FTF.

Dans un second temps, la réponse acoustique de flammes prémélangées confinées turbulentes soumises à des ondes acoustiques harmoniques est étudiée d'une part expérimentalement et d'autre part en employant plusieurs approches analytiques. Une première série d'expériences est consacrée à l'étude des FDF définies par rapport à différents signaux de référence. Il est démontré que toutes ces FDF peuvent être reliées entre elles analytiquement en utilisant un réseau non-linéaire d'éléments acoustiques. De plus, il est observé que la FDF est différente en fonction de la façon dont le forçage acoustique est introduit dans le brûleur, excepté lorsque le signal de référence est la vitesse acoustique juste avant la flamme. Il est ainsi conclu que ce signal doit être utilisé comme signal de référence lors de la définition de la FDF.

Dans une seconde série d'expériences, la matrice de transfert acoustique représentant le brûleur NoiseDyn est mesurée à froid et à chaud (c'est-à-dire en présence

d'une flamme) et pour un injecteur tourbillonnant et non-tourbillonnant. Le niveau de forçage acoustique est contrôlé au niveau du fil chaud et des mesures sont effectuées pour plusieurs niveaux de forçage prédéfinis. Il est ainsi démontré que la réponse acoustique du brûleur NoiseDyn est non-linéaire aussi bien à froid qu'à chaud. De plus, deux réseaux d'éléments acoustiques représentant le brûleur NoiseDyn à froid et à chaud sont conçus. Les mesures et prédictions de la matrice de transfert acoustique sont en accord aussi bien à froid qu'à chaud. Même si l'effet du niveau de forçage n'est pas parfaitement prédit par le réseau acoustique, la FDF mesurée en utilisant une technique optique est reconstruite avec succès à partir des mesures de la matrice de transfert acoustique.

Enfin, la stabilité thermoacoustique de six configurations différentes du brûleur NoiseDyn est prédite en utilisant deux réseaux d'éléments acoustiques. Dans le premier réseau, la réponse acoustique de la flamme est prise en compte en utilisant une FDF préalablement mesurée tandis que dans le second réseau, la réponse de la flamme est incluse dans la mesure de la matrice de transfert acoustique correspondant à la majeure partie du brûleur. Ces deux modèles sont capables de prédire l'apparition d'instabilités thermoacoustiques ainsi que la fréquence de ces instabilités le cas échéant. Néanmoins, le modèle basé sur la FDF ne prédit pas l'amplitude du cycle limite de façon satisfaisante contrairement au modèle basé sur la mesure de la matrice de transfert acoustique. Cette observation s'explique par la façon dont les pertes acoustiques à l'intérieur du brûleur sont prises en compte: dans le premier modèle, ces pertes sont entièrement modélisées alors que dans le second modèle, elles sont directement mesurées.

Contents

Nomenclature

Acronyms :

ATM	Acoustic Transfer Matrix
CCD	Charge-Coupled Device
CTA	Constant Temperature Anemometry
DATM	Dimensionless ATM
DF	Describing Function
ICCD	Intensified CCD
FDF	Flame Describing Function
FFT	Fast Fourier Transform
FTF	Flame Transfer Function
HW	Hot Wire
LDA	Laser Doppler Anemometry
LDV	Laser Doppler Velocimetry
MMM	Multiple Microphone Method
PMT	Photomultiplier
RMS	Root Mean Square
SPL	Sound Pressure Level
TF	Transfer Function
TMM	Three Microphone Method
TTL	Transistor Transistor Logic
UV	Ultraviolet

Latin Characters :

a	Hole radius
a_k	Thermal diffusivity of species k
A	Cross section area
A_ω	Harmonic wave amplitude
B_ω	Harmonic wave amplitude
c	Sound speed
c_p	Specific heat capacity at constant pressure
c_v	Specific heat capacity at constant volume
C	Coherence factor
C_b	Confinement ratio
C_{xy}	Coherence function between x and y
d	Inter-hole spacing
D	Diameter
$D_{m,k}$	Mass diffusivity of species k
D_0	Binary diffusion coefficient
$\hat{\mathbf{e}}$	Unit vector
E	Volumetric expansion ratio
f	Frequency
f_i	Imaginary part of the characteristic equation root
f_r	Real part of the characteristic equation root
f_s	Sampling frequency
f_*^0	Frequency at which the FTF gain is maximum
F	FTF or FDF

F_A	FTF model due to the velocity perturbations
F_B	FTF model due to the anchoring point dynamics
F_C	TF between the flame base motion and the flame surface area fluctuations
F_{HW}	DF defined with respect to the hot wire probe
F_{HWC}	DF defined with respect to the acoustic velocity just before the flame
F_{MC}	DF defined with respect to the microphone MC
F_{MHW}	DF defined with respect to the microphone MHW
G	Gain
$\mathcal{G}$	Scalar function describing the flame front position
h	Flame height
He	Helmholtz number
H_{xy}	TF between x and y
$\mathcal{H}$	Enthalpy
i	local pixel intensity
I	OH* chemiluminescence intensity
I_x	Modified Bessel function of the first kind and of order x
J_x	Bessel function of the first kind and of order x
k	Wave number
$k_\bullet$	Modified wave number
k_*	Dimensionless parameter
K_r	Rayleigh conductivity
K_x	Modified Bessel function of the second kind and of order x
l	Distance
L	Length
Le	Lewis number
M	Mach number
M	Acoustic transfer matrix
$\widetilde{M}$	Dimensionless acoustic transfer matrix
$\hat{\mathbf{n}}$	Normal unit vector
N	Number of holes
p	Pressure
P	Flame thermal power
P_{xx}	Auto power spectral density of x
P_{xy}	Cross power spectral density between x and y
q	Volumetric heat released
Q	Total heat released
Q_c	Convective heat transfer
r	Specific gas constant
R	Radius
Re	Reynolds number
R_e	Acoustic resistance
$\mathcal{R}$	Acoustic reflection coefficient
$\mathcal{R}_l$	Acoustic reflection coefficient at l
s	Entropy
S	Swirl number
S	Surface
St	Strouhal number
S_L	Laminar flame speed
S_L^b	Non-adiabatic flame speed at the flame base
$\mathcal{S}$	Source term
t	Time variable
T	Temperature
T_a	Activation temperature
T_{ad}	Adiabatic temperature
T_b	Burnt gases temperature
T_s	Burner outlet temperature
T_u	Unburnt gases temperature
T_*	Dimensionless adiabatic temperature
u	Axial flow velocity
$\mathbf{u}$	Eulerian velocity vector
u_b	Bulk flow velocity

u_c	Velocity at which vortices are convected
v	Radial flow velocity
V	Volume
V_f	Flame volume
$\mathcal{V}$	Control volume
$\mathbf{x}$	Position vector
X	Acoustic reactance
X_u	Species concentration in the fresh gases
Y_x	Bessel function of the second kind and of order x
z	Characteristic acoustic impedance
Z	Acoustic impedance
Z_s	Specific acoustic impedance
Ze	Zeldovich number

Greek Characters :

α	Flame tip half angle
α_b	Angle at the flame base
β	Gradient of the square of the sound speed
γ	Adiabatic index
δ	Flame thermal thickness
δ_*	Dimensionless flame thermal thickness
δ_0	Unflanged Levine-Schwinger end correction
δ_∞	Flanged Levine-Schwinger end correction
ϵ	Surface emissivity
ζ	Rayleigh conductivity model
ζ_a	Volumetric acoustic losses
θ_*	Ratio between burnt gases and adiabatic temperatures
Θ_*	Dimensionless temperature
ι	Dimensionless frequency
κ	Thermal conductivity
λ	Wavelength
μ	Dynamic viscosity
ν	Kinematic viscosity
Ξ	TF between the velocity perturbations and the flame base motion
ρ	Density
Σ	Lateral surface
τ	Time lag
τ_c	Thermalization time
τ_ω	Oscillation period
φ	Phase lag
ϕ	Equivalence ratio
ψ	Flame stand-off distance
ψ_*	Dimensionless flame stand-off distance
ω	Angular frequency
$\hat{\omega}$	Dimensionless frequency
ω_i	Acoustic damping rate
ω_*	Reduced frequency
ω_*^0	Reduced frequency at which the FTF gain is maximum

Subscripts :

$*$	Dimensionless
x	Axial coordinate (cartesian system)
r	Radial coordinate (cylindrical system)
θ	Orthoradial coordinate (cylindrical system)

z	Axial coordinate (cylindrical system)
ω	Harmonic
xp	Experimental
th	Theoretical
max	Maximum
min	Minimum
open	Open acoustic boundary
closed	Closed acoustic boundary
ref	Reference
u	Upstream
d	Downstream
$\oplus$	Positive harmonic convention
$\ominus$	Negative harmonic convention
i	At section (i)
ij	Between sections (i) and (j)

Superscripts :

o	Original configuration
s	Switched configuration
f	Final
con	Convective model
inc	Incompressible convective model
uni	Uniform model

Diacritics :

$\bar{x}$	Steady-state value of x
x'	Fluctuating value of x
$\dot{x}$	Time derivative of x

Mathematical Symbols :

$\|x\|$	Modulus of x
$\angle x$	Angle of x
$\langle x \rangle$	x averaged over the flame volume
∂x	Partial derivative with respect to x
dx	Total derivative with respect to x
Δx	Variation of x
∇x	Gradient of x
$\nabla \cdot x$	Divergence of x
$\nabla^2 x$	Laplacian of x
$x \cdot y$	Dot product of x and y
$\sim x$	Same magnitude as x
$\propto x$	Proportional to x
$\mathrm{Re}(x)$	Real part of x
$\mathrm{Im}(x)$	Imaginary part of x
$(x)^*$	Complex conjugate of x

Blueprint Symbols :

$\varnothing$	Diameter
$\square$	Length of the square side

Introduction

Context

Combustion is a reduction-oxidation chemical reaction between a fuel and an oxidant releasing a large amount of heat. While the oxidant is usually the oxygen contained in the atmosphere (or sometimes pure oxygen), a variety of solid, liquid or gaseous fuels may be used, such as wood, coal, crude oil, methane, hydrogen and many others. Combustion reactions require large activation energies which is why they are not so easily initiated, but they are usually self-sustained as long as the fuel and oxidant are still available. The required activation energies may be found in nature, through a lightning strike for instance.

Since all the ingredients (fuel, oxidant and activation energy) can be found in nature, combustion was the first source of energy controlled by humans around one million years ago (Bowman et al. 2009). As of 2015, 91.1% of the world's primary energy is still produced by combustion reactions as depicted in Fig. 1 (International Energy Agency 2017), completed by 4.9% of nuclear energy and 4.0% of renewable energy that do not originate from combustion-based technologies (such as the energy extracted from water or wind for instance). These primary energy sources are then used to generate electricity (coal-fired power plants, gas turbines, nuclear power plants, hydropower plants, etc.), manufacture goods through industrial processes, heat residential and commercial buildings and fuel individual and public transports among others.

Figure 1 also shows that the world's primary energy production (and consumption) is increasing steeply: the global primary energy produced by humanity was multiplied by a factor of 2.2 between 1973 and 2015. If fossil fuels and renewable energies based on combustion technologies are considered alone, the energy production still increased by a factor of 2.1 between 1973 and 2015.

Even though the share of the world's primary energy obtained from burning various types of fuels dropped from 97.2% to 91.1% between 1973 and 2015, it is widely accepted that combustion is going to remain the first source of energy for mankind in the foreseable future for economical and technical reasons. In fact, combustion technologies are usually cheap compared to competing tech-

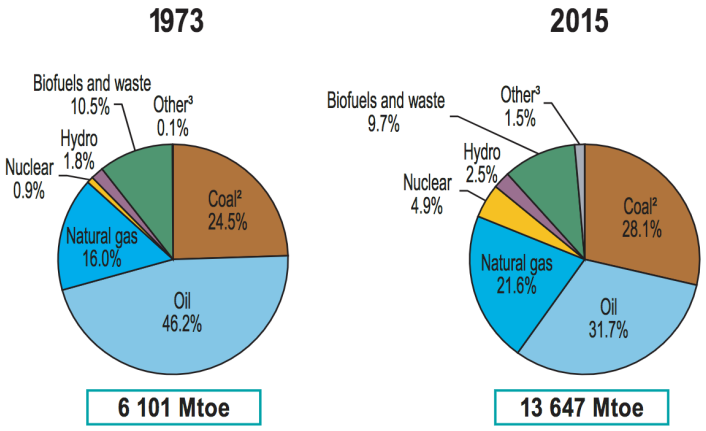

Figure 1: *World primary energy sources in 1973 (Left) and 2015 (Right). Reproduced from Key World Energy Statistics 2017.*

nologies. In some sectors such as commercial air transport or rocket launchers, there are no competitors at all because of the very high energy densities required (Shepherd 2003). Traditional combustion technologies are among the most well-established techniques for electricity production and air transport. However, it should be noted that new combustion technologies also constitute the largest source of renewable energy: in 2015, 9.7% of the world's primary energy is extracted from biofuels and waste incineration which are renewable and combustion-based technologies.

Combustion reactions are essentially used because they generate a lot of heat per unit mass of fuel, but they also generate undesirable by-products depending on the type of fuel and oxidant employed. These pollutants may include:

- **CO_2** (Carbon dioxide): a long-lived greenhouse gas responsible for climate change.
- **CO** (Carbon monoxide): a highly toxic colorless, odorless, and tasteless gas.
- **NO_x** (Nitrogen oxides): gases that cause or worsen respiratory diseases and have several detrimental effects on the environment.
- **SO_x** (Sulfur oxides): gases that are air pollutants and toxic for humans.
- **CH_x** or **UHCs** (Unburned hydrocarbons): chemical compounds that disrupt the atmosphere chemistry.

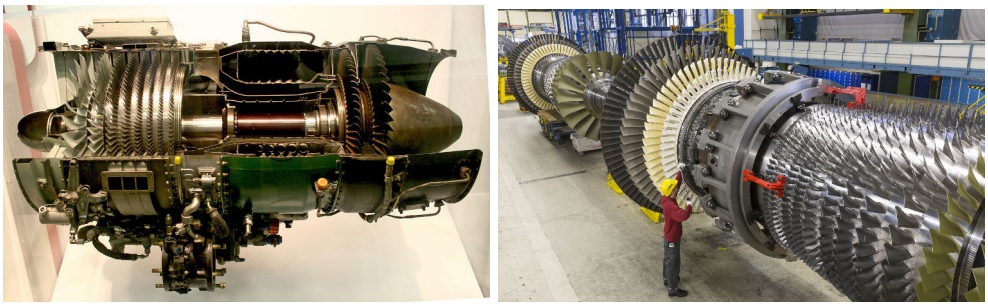

Figure 2: *Examples of gas turbines. (Left): General Electric J85, a single-shaft turbojet engine. (Right): Siemens SGT-8000H, an industrial gas turbine for power generation.*

- **Soot**: nanoscale and microscale particles that are responsible for climate change and cause various lung diseases as well as cancer.

Combustion is going to remain a major source of primary energy in the upcoming decades but due to the rising environmental and health concerns, a huge research effort is needed in order to reduce the pollutants emissions while concomitantly increasing the overall energy efficiency of combustion technologies. Various strategies have been adopted accordingly depending on the type of combustor and specific pollutants targeted.

Gas turbines are an important class of combustors used in the aerospace and power production industries. Two gas turbines used for propulsion and power generation are presented in Fig. 2-(Left) and (Right) respectively. The General Electric J85 gas turbine depicted in Fig. 2-(Left) is a single-shaft turbojet engine comprising an air inlet on the left followed by a multi-stage compressor and a combustion chamber, where kerozene is injected. A two-stage turbine is then used to drive the rotating shaft, followed by a propelling nozzle which generates thrust. On the other hand, the Siemens SGT-8000H depicted in Fig. 2-(Right) is an industrial gas turbine with a peak thermal power production of 1000 MW.

One way to reduce the NO_x and soot emissions of gas turbines is to operate them for lean premixed conditions as opposed to rich or partially premixed conditions which were traditionally employed (Correa 1993). This change of operating conditions also increases the overall efficiency of gas turbines. However, a lean premixed flame stabilized inside a gas turbine is less stable as thermoacoustic instabilities are promoted for such operating conditions (Sattelmayer et al. 1992; Keller 1995).

Thermoacoustic instabilities

A thermoacoustic instability is characterized by a large positive energy transfer from a heat source to the surrounding acoustic field that cannot be counterbalanced by the linear acoustic losses generated at the boundaries or inside the system. As a consequence, the amplitude of the acoustic oscillations grow until saturation is reached due to nonlinear processes. This limit cycle regime is rarely desirable as it has many detrimental consequences: very large sound emissions at certain frequencies (Schuller 2003; Poinsot 2017), flame extinction (Candel 1992; McManus et al. 1993; Ducruix et al. 2003), structural damage (Candel 1992; McManus et al. 1993; Ducruix et al. 2003; Dowling and Morgans 2005) and increased heat fluxes (McManus et al. 1993; Ducruix et al. 2003; Dowling and Morgans 2005) among others.

Thermoacoustic instabilities were known long before they became a major industrial concern. There is evidence that these phenomena have been observed since the Middle Ages at least, when glassblowers noticed that they could generate sound by blowing into a cold pipe connected to a hot glass bulb (Sondhauss 1850).

The first scientific investigation of thermoacoustic instabilities was performed by Byron Higgins in 1777 using a single hydrogen/air flame stabilized inside a tube (Higgins 1802). The tone emitted was modified by changing the tube length. This experiment was then reproduced in Italy by Brugnatelli and Volta who popularized it (Higgins 1802).

A few decades later, Auguste Pinaud reproduced the glassblowers' observations in a controlled experiment, where he used a tube with an open end and a closed heated end (Pinaud 1837). These experiments were further investigated by Marx (Marx 1841) and Sondhauss (Sondhauss 1850), who gave his name to this tube with an heated closed end. Rijke proposed a variation of the Sondhauss tube, called Rijke tube, featuring a cylindrical tube open at both ends with a disc of wire gauze placed inside the tube at a distance equal to one quarter of the total tube length (Rijke 1859). These experimental investigations pioneered the field of thermoacoustics but until the second half of the 19^{th} century, the physical phenomena at stake were still obscure.

A first attempt at describing thermoacoustic instabilities using a mathematical formalism was performed a few years after Rijke's discovery (Kirchhoff 1868). However, the real breakthrough in the field of combustion instabilities is due to Rayleigh, who published an article providing the correct explanation of the physical mechanisms occuring in Rijke's tubes (Rayleigh 1878). This article also contains the first description of the famous Rayleigh's criterion that is still used today to predict the onset of thermoacoustic instabilities (Rayleigh 1878).

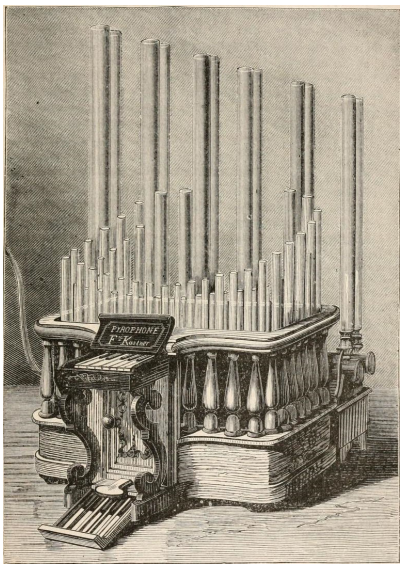

Figure 3: *Sketch depicting the pyrophone, invented by Kastner. Image reproduced from The popular science monthly, August 1875, p. 449*

Until the 1940s, thermoacoustic instabilities were either employed as a source of entertainment, using various devices such as the pyrophone depicted in Fig. 3 (Kastner 1876) or seen as an exotic physical phenomenon. The development of rocket and aircraft engines with extremely large energy densities completely changed this perspective in the 1950s and 1960s as a significant proportion of these early engine designs were thermoacoustically unstable which could sometimes lead to dramatic outcomes (Candel 2002). As a consequence, a large theoretical and experimental research effort was initiated in order to design thermoacoustically stable engines (Gunder and Friant 1950; Crocco 1951; Blackshear 1953; Merk 1957). This research effort was further amplified during the late 1980s and the 1990s, when a new generation of gas turbines operated with lean premixed flames and especially prone to thermoacoustic instabilities began to be massively employed (Sattelmayer et al. 1992; Correa 1993; Keller 1995).

Thermoacoustic stability prediction

Modern predictive approaches

Despite the fact that combustion instabilities have been studied for more than two centuries, the onset of these instabilities is still not perfectly understood because of the large number of physical phenomena involved, the nonlinearity of the flame acoustic response, and the complexity of the combustors geome-

tries (Candel 2002; Poinsot 2017). In practice, various approaches based on purely analytical models (Keller 1995; Dowling and Stow 2003) or used along with measurements (Paschereit and Polifke 1998; Schuermans et al. 2000; Polifke et al. 2003; Noiray et al. 2008) or numerical simulations (Nicoud et al. 2007; Han et al. 2015) may be used to predict the thermoacoustic stability of a combustor. One of these approaches is quickly introduced below.

A gas turbine operated for reactive conditions can be represented by a network of cavities which possesses a set of discrete frequencies at which it acoustically resonates (Munjal 1987; Candel and Poinsot 1988). The flame frequency response to the incoming sound wave may be described using a Flame Transfer Function (FTF) or its nonlinear extension, a Flame Describing Function (FDF). The FTF/FDF may be determined using experiments (Becker and Günther 1971; Noiray et al. 2008; Gatti et al. 2018), numerical simulations (Kornilov et al. 2009; Tay Wo Chong et al. 2010; Han and Morgans 2015) or analytical models (Crocco 1951; Merk 1957; Ducruix et al. 2000; Schuller et al. 2003a; Palies et al. 2011).

Used along with suitable upstream and downstream acoustic boundary conditions, the acoustic network model combined with the FDF leads to a characteristic equation that predicts the thermoacoustic stability of the combustor (Noiray et al. 2008). If an unstable thermoacoustic mode is triggered, the characteristic equation also provides the frequency and amplitude of the limit cycle oscillations (Noiray et al. 2008; Boudy et al. 2011).

The frequency and damping rate of each thermoacoustic mode depends on many parameters, including the burner geometry (Paschereit and Polifke 1998; Schuermans et al. 2000), the acoustic boundary conditions (Munjal 1987; Paschereit and Polifke 1998), the Mach number of the mean flow (Paschereit and Polifke 1998; Hirschberg and Rienstra 2004), the presence of a flame (Keller 1995; Paschereit and Polifke 1998) and the acoustic damping rate inside the setup (Paschereit and Polifke 1998; Fischer et al. 2006). Until recently, the flame frequency response was considered to be independent of the forcing level (Merk 1957; Becker and Günther 1971; Schuermans et al. 1999; Polifke et al. 2001; Candel 2002) but during the past two decades, analytical developments (Dowling 1997; Noiray et al. 2008), experiments (Noiray et al. 2008; Boudy et al. 2011; Gaudron et al. 2017c) and simulations (Krediet et al. 2012; Han and Morgans 2015) showed that this response depends on the amplitude of the sound waves impinging on the flame.

Current challenges

Despite these recent advances, the impact of the amplitude of the incoming acoustic waves on the flame frequency response and on the damping of the

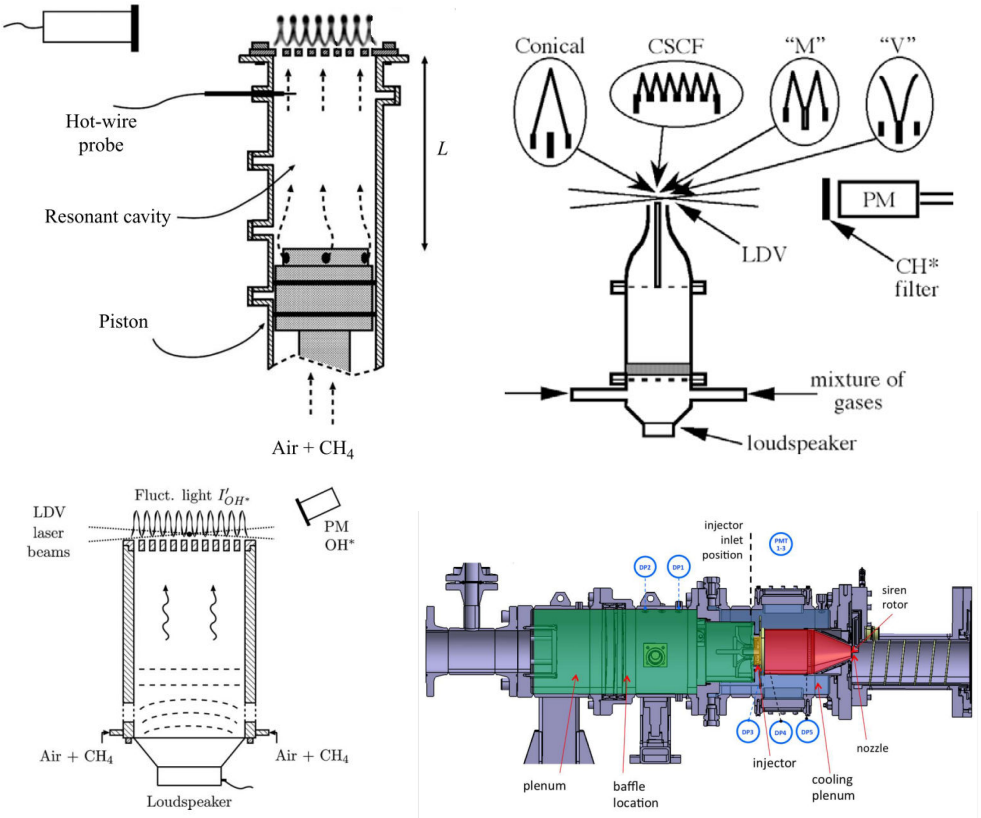

Figure 4: *Original sketches depicting the experimental setups used in previous studies investigating the FTF of premixed flames. Reproduced from Noiray et al. (2008) (Top left), Durox et al. (2009) (Top right), Boudy et al. (2011) (Bottom left) and Hochgreb et al. (2013) (Bottom right).*

acoustic waves inside the system is still poorly understood. Experimental and numerical works that explicitly consider the effects of the forcing level on these physical phenomena still remain scarce and the source of nonlinearity is not always clearly identified.

Another challenge associated with the experimental or numerical investigation of the frequency response of a flame is related to the way the FTF/FDF is determined. In fact, two distincts reference signals may be used when defining a FTF/FDF: the acoustic pressure or the acoustic velocity. Moreover, these acoustic variables may be assessed at the flame location or at some distance inside the injector.

For instance, the FTF/FDF defined with respect to different reference signals and obtained using four distinct experimental setups employed in previous investigations (Noiray et al. 2008; Durox et al. 2009; Boudy et al. 2011; Hochgreb

et al. 2013) are represented in Fig. 4. The reference signal may be defined as the signal recorded by a hot-wire probe located inside the plenum (Noiray et al. 2008), as shown in Fig. 4-(Top left) or reconstructed using the two-microphone method (Hochgreb et al. 2013), as shown in Fig. 4-(Bottom right). Alternatively, the reference signal may be defined as the acoustic velocity at the flame base location, obtained using Laser Doppler Velocimetry (Durox et al. 2009; Boudy et al. 2011), as shown in Fig. 4-(Top right) and (Bottom left). Many other reference signals based on the acoustic pressure inside the injector or at the flame location may be defined as well. However, a detailed comparison between FTF/FDF defined with respect to several reference signals but determined using the same experimental setup has yet to be performed. Moreover, the analytical links between all these FTF/FDF has yet to be established and it is not clear whether all these FTF/FDF can be used equivalently when performing a thermoacoustic stability analysis.

Another important issue when determining a FTF/FDF is related to the way acoustic forcing is introduced inside the experimental setup or the numerical domain. For instance, an upstream loudspeaker may be used to generate acoustic waves (Durox et al. 2009; Boudy et al. 2011), as shown in Fig. 4-(Top right) and (Bottom left). Alternatively, acoustic waves may be generated from the downstream side of the combustor using loudspeakers (Krebs and Flohr 2002) or a siren (Hochgreb et al. 2013), as shown in Fig. 4-(Bottom right). However, it is unclear whether the experimental or simulated FTF/FDF determined with upstream and downstream acoustic forcing are equivalent.

Moreover, the flame acoustic response may be measured experimentally using an optical technique (Noiray et al. 2008; Boudy et al. 2011) or using acoustic measurements only (Paschereit and Polifke 1998; Schuermans et al. 2000; Paschereit et al. 2002). The first method is based on the FTF/FDF formalism and requires an optical access inside the combustion chamber. This method can be used to determine the acoustic response of perfectly premixed lean hydrocarbon flames and is relatively easy to implement. The second method is based on the Acoustic Transfer Matrix (ATM) formalism and does not require an optical access into the combustion chamber. Moreover, this purely acoustic method can be used to determine the acoustic response of a large array of flames but it requires large sets of experimental data and complex post-processing routines. A detailed comparison between these two methods for controlled acoustic forcing levels has yet to be performed.

Finally, the impact of a number of other physical parameters such as the flame size, the Lewis number of the premixed gases or the temperature of the burnt gases have not been systematically examined using experiments. Additional research efforts based on experiments and analytical approaches are thus needed in order to investigate these poorly understood yet crucial aspects.

Thesis objectives and contents

The objective of this thesis is to study the acoustic response of various laminar and turbulent premixed flames submitted to harmonic sound waves in order to improve the thermoacoustic stability predictions of labscale and industrial combustors at an early design stage. First, the fundamental case of premixed laminar conical flames is investigated, followed by a study of swirling and non-swirling premixed confined turbulent flames.

Premixed laminar conical flames

In the first part of this manucript, the elementary class of premixed laminar conical flames is investigated. **Chapter 1** contains a literature review summarizing the main results regarding the Flame Transfer Functions (FTF) of premixed laminar conical flames. Then, three typical analytical models aiming at predicting these FTF are described along with an additional model accounting for the impact of the flame base motion. **Chapter 2** includes a thorough description of the experimental setup and associated diagnostics used to study the acoustic response of premixed laminar conical flames submitted to harmonic sound waves. The associated operating conditions are also described in this chapter.

The subsequent measurements are compared with analytical models in **Chapter 3** for injectors of various sizes in order to find which analytical model yields the best predictions. A parametric study of the response of premixed laminar conical flames submitted to acoustic forcing is then performed in **Chapter 4** for flames of varying temperatures, sizes and Lewis number. A physical analysis of the flame dynamics undergoing acoustic forcing is also performed. Finally, a new physical mechanism explaining the presence of a gain overshoot in the Flame Transfer Function of small premixed laminar conical flames is introduced.

Premixed confined turbulent flames

In the second part of this manuscript, premixed confined turbulent flames are investigated. Most of the results presented in the following chapters were obtained for swirling and non-swirling flames in order to cover a wide range of flames used in practical applications. **Chapter 5** contains a detailed description of the NoiseDyn burner which was designed during this thesis. The operating conditions for all premixed turbulent flames studied in this work are also defined. **Chapter 6** includes a comprehensive description of the diagnostics employed to characterize the acoustic response of premixed turbulent flames.

Chapter 7 is an introduction to the theory of linear acoustics applied to low-Mach non-reactive flows. The notion of acoustic impedance, acoustic reflection coefficient and acoustic transfer matrix is also presented in this chapter. **Chap-**

ter 8 is an extension of the previous chapter to low-Mach reactive flows. The acoustic transfer matrices corresponding to a variety of elements such as 1D ducts, compact and non-compact area changes and lean premixed flames are also derived in these two chapters.

The Flame Describing Function (FDF) of swirling and non-swirling premixed turbulent flames is analyzed in **Chapter 9**. Analytical links between the FDF defined with respect to various reference signals are established using linear and nonlinear models and the FDF obtained with upstream and downstream acoustic forcing are compared. Finally, it is demonstrated that the FDF based on the acoustic velocity just before the flame depends on the frequency and on the amplitude of the acoustic velocity only. If another reference signal is used, such as the acoustic velocity inside the injector or the acoustic pressure at the flame location, the FDF also depends on the amplitude of the acoustic pressure.

Measurements of the acoustic transfer matrices representing the NoiseDyn burner are carried out in **Chapter 10** for cold and reactive operating conditions and for swirling and non-swirling injectors. The acoustic forcing level is controlled at the hot wire location and measurements are performed for various predetermined forcing levels. Acoustic network models are also constructed for both operating conditions and analytical predictions are compared with measurements. The acoustic losses generated at the swirling vane are accounted for and the flame frequency response is represented using a FDF for reactive operating conditions.

Finally, the thermoacoustic stability of the NoiseDyn burner is investigated in **Chapter 11**, where measurements are compared with analytical predictions based on two distinct network models. In the first model, the flame response is represented with a FDF measured using an optical technique. In the second model, the flame response is embedded in a measured acoustic transfer matrix. It is shown that the thermoacoustic stability predictions according to both models are equivalent but that the predicted amplitude of the limit cycle oscillations differ because the acoustic damping inside the combustor is analytically modeled in the first model whereas it is directly measured in the second one.

Appendices

A few additional topics are analyzed at the end of this manuscript. First, a discussion regarding the impact of the harmonic convention and acoustic boundary orientation is proposed in **Appendix A**. Then, a few fundamental limitations affecting the usual procedure used to predict the thermoacoustic stability of combustors is presented in **Appendix B**.

Part I

Premixed Laminar Conical Flames

Chapter 1

Flame Transfer Functions Modeling

Thermoacoustic instabilities coupled to self-sustained mixture flowrate oscillations are observed in many domestic boilers and industrial burners operated with premixed laminar conical flames. The stability margin of these systems may be predicted by using the acoustic response of the system along with the Flame Transfer Function (FTF), i.e the flame frequency response when submitted to harmonic flowrate modulations. As a conseqence, the FTF of such flames was studied and modeled extensively during the past decades. A review of the current state of knowledge on the physics controlling the FTF shape of premixed laminar conical flames is first presented. Various analytical models describing the FTF of such flames are then introduced and discussed in the second part of this chapter.

1.1 Introduction

Flame Transfer Functions (FTF) are often used in combination with an acoustic model of the system in order to predict the thermoacoustic stability of combustors. This algebraic relation linking heat release rate perturbations to incoming flow disturbances is a black-box that conceals the physical complexity associated with the interactions between flow dynamics, acoustics and unsteady combustion processes. This formalism is used to perform stability analysis of the combustor at reduced computational costs (Dowling 1995; Sattelmayer and Polifke 2003). Due to the major problems caused by combustion instabilities in practical systems, there is a large theoretical, experimental and numerical research effort oriented towards the development of tools easing the determination of Flame Transfer Functions (Candel 2002; Lieuwen 2005; Poinsot 2017).

Premixed laminar conical flames submitted to harmonic flowrate modulations

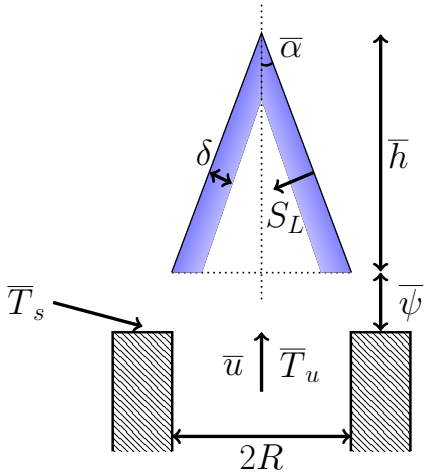

Figure 1.1: *Simplified structure of a premixed laminar conical flame stabilized above a burner.*

constitute an elementary case that can be used to validate theoretical models and numerical simulations (Duchaine et al. 2011; Kedia et al. 2011; Schlimpert et al. 2015). It also brings to light some of the main physical mechanisms controlling the response of premixed flames to incoming flow perturbations (Ducruix et al. 2000; Preetham et al. 2008). Finally, there are many domestic and industrial low-power burners operated with premixed laminar conical flames which exhibit regimes with self-sustained combustion oscillations accompanied by large noise emission (Zähringer et al. 2003; Durox et al. 2009; de Goey et al. 2011). The dynamic response of these combustors may be modeled and predicted using the FTF formalism.

It is thus worth developing physics-based models describing accurately the FTF of premixed laminar conical flames. Much progress was achieved in this field of research and the main findings are summarized in Sec. 1.2. It is emphasized that this analysis is limited to the case of fully premixed flames submitted to flowrate oscillations in the absence of mixture composition disturbances (Lieuwen 2005).

1.2 Flame Transfer Functions of premixed laminar conical flames

Let us consider a steady laminar conical flame with a heat release rate $\overline{\dot{Q}}$ stabilized above a burner and fed by fully premixed gases with an injection velocity $\bar{u}$ as represented in Fig 1.1. Throughout this work, the overline ($^{-}$) and prime ($'$) stand for mean and fluctuating variables respectively. The transfer function of this flame submitted to harmonic flowrate modulations is a linear operator defined in the frequency domain as (Fleifil et al. 1996; Ducruix et al. 2000):

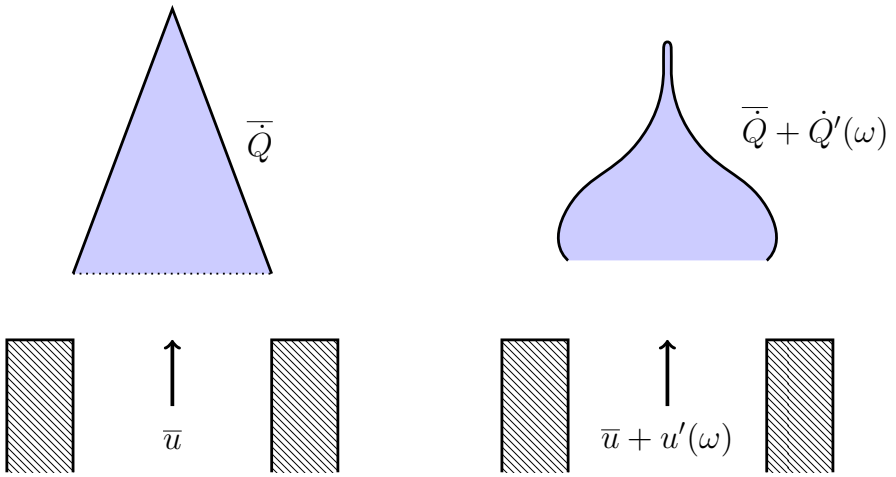

Figure 1.2: *Illustration of a premixed laminar conical flame for steady injection conditions (Left) and submitted to a harmonic flowrate modulation at a forcing angular frequency ω (Right).*

$$F(\omega) = \frac{\dot{Q}'/\overline{\dot{Q}}}{u'/\overline{u}} = G(\omega)\exp\left(i\varphi(\omega)\right) \tag{1.1}$$

where $\dot{Q}'$ denotes the heat release rate fluctuation around the steady-state value $\overline{\dot{Q}}$ examined at the same angular frequency ω as the incoming harmonic velocity disturbance u' around the steady-state injection velocity $\overline{u}$ as shown in Fig. 1.2.

Equation (1.1) sets a clear framework for theoretical modeling, but already raises difficulties for experiments and simulations. In practice, the quantities $\overline{\dot{Q}}$ and $\overline{u}$ are often taken as the mean values of the unsteady signals averaged over many oscillation cycles (Ducruix et al. 2000; Karimi 2014; Mejia et al. 2015; Gaudron et al. 2017b). Moreover, the injection velocity is frequently replaced in Eq. (1.1) by a reference velocity measured at some distance from the burner outlet in a region where the flow is as uniform as possible (Karimi et al. 2009; Gaudron et al. 2017b). However, the distance between the reference point and flame base needs to be compact with respect to the acoustic (Truffin and Poinsot 2005) and hydrodynamic (Schuller et al. 2002) characteristic length scales.

Finally, the forcing level $|u'|/\overline{u}$ needs to be taken as low as possible in order to avoid nonlinear effects (Schuller et al. 2003a; Lieuwen 2005; Durox et al. 2009; Karimi et al. 2009; Mejia et al. 2015), but cannot be set to zero in experiments and simulations. FTF are often obtained at a fixed perturbation level resulting from a trade-off between maximizing the signal-to-noise ratio

and not triggering nonlinear effects. Linearity of the response can be checked by verifying that the measured FTF is independent of perturbation amplitude (Schuller et al. 2003b; Durox et al. 2009; Karimi et al. 2009). When this is not feasible, it is better to consider only the components of the heat release rate and velocity signals at the forcing angular frequency ω obtained using the cross and auto power spectral densities of these signals in order to reduce artefacts due to the finite duration of the signals and the finite sampling rate of data. In this case, linearity is well approximated if the amplitude of the first harmonic component is at least one order of magnitude lower than the amplitude of the fundamental component at ω. If all these conditions are met, the simulated or measured FTF converges to the definition in Eq. (1.1) and corresponds to a complex-valued function that can be expressed as a gain $G(\omega)$ corresponding to the FTF modulus and a phase lag $\varphi(\omega)$ between the response $\dot{Q}'$ and the input u'. One of the main advantages of this representation is to explicitly state the gain G and phase lag φ dependence on the angular frequency ω.

An example of a Flame Transfer Function of a large premixed laminar conical flame of equivalence ratio $\phi = 1.08$ stabilized above a burner of radius $R = 11$ mm with a fresh reactant stream of bulk velocity $\bar{u}_b = 1.96$ m/s and for four different forcing levels is presented in Fig. 1.3 (Durox et al. 2009). The top and bottom plots represent the FTF gain and phase lag respectively as a function of the reduced frequency, a dimensionless parameter that will be introduced in Sec. 1.2.1.

An extensive research effort has been devoted to finding the main dimensionless numbers controlling the FTF of premixed laminar conical flames (Fleifil et al. 1996; Ducruix et al. 2000; Schuller et al. 2003a). The sketch in Fig. 1.1 introduces the main physical and geometrical parameters used in this study, where R is the burner exit radius, u is a reference velocity that does not necessarily correspond to the bulk velocity u_b within the injector, T_u is the fresh gas temperature, T_s is the burner outlet temperature, ψ is the stand-off distance of the flame base with respect to the burner outlet, h is the flame height, α is the flame tip half angle, S_L is the laminar burning velocity and δ is the flame thermal thickness. It is reminded that the overline stands for steady conditions. Additional parameters will be introduced later.

First, the main findings regarding the FTF of large premixed laminar conical flames are summarized in Sec. 1.2.1. An example of such a flame of equivalence ratio $\phi = 0.95$ stabilized above an injector of radius $R = 11$ mm with a fresh reactant stream of bulk velocity $\bar{u}_b = 2.5$ m/s is represented in Fig. 1.4-(Left) (Durox et al. 2004). The same review is performed for the FTF of collections of small premixed laminar conical flames, presented in Sec. 1.2.2. An example of a collection of 21 small premixed laminar conical flames at stoichiometry fed by fresh gases of bulk velocity $\bar{u}_b = 1.48$ m/s stabilized on a plate featuring 21

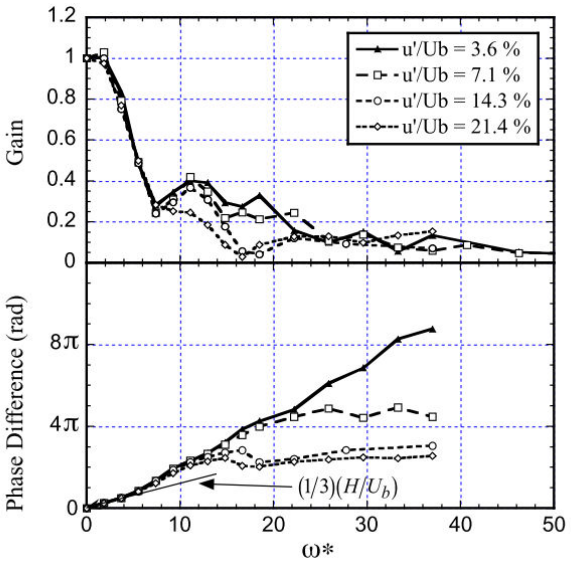

Figure 1.3: *Flame Transfer Function of a large premixed laminar conical methane/air flame of equivalence ratio $\phi = 1.08$ stabilized above a burner of radius $R = 11$ mm traversed by a fresh reactant stream of bulk velocity $\bar{u}_b = 1.96$ m/s and for four different forcing levels. Reproduced from Durox et al. (2009).*

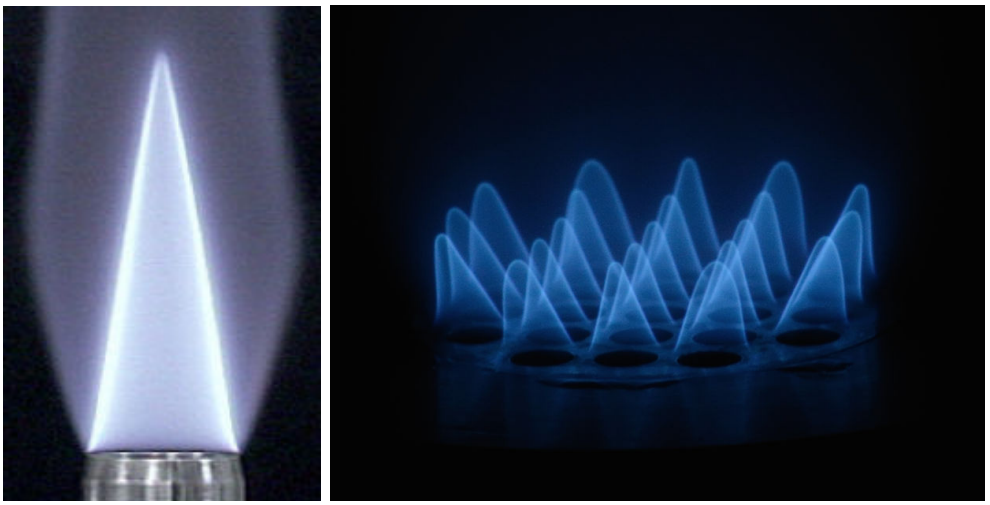

Figure 1.4: *(Left): Example of a large premixed laminar conical CH_4/Air flame of equivalence ratio $\phi = 0.95$ obtained with an injector of radius $R = 11$ mm traversed by a fresh reactant stream of bulk velocity $\bar{u}_b = 2.5$ m/s, reproduced from Durox et al. (2004). (Right): Example of a collection of small premixed laminar conical CH_4/Air flames at stoichiometry stabilized on a plate featuring 21 holes of radius $R = 1.5$ mm traversed by a fresh reactant stream of bulk velocity $\bar{u}_b = 1.48$ m/s.*

holes of radius $R = 1.5$ mm is represented in Fig. 1.4-(Right).

1.2.1 FTF of large premixed laminar conical flames

Early investigations

Due to the relative simplicity of the experimental setup, the response of a single premixed laminar conical flame submitted to acoustic forcing has been the topic of many early investigations. These experiments revealed that flame front wrinkling is the main mechanism leading to heat release rate disturbances (Blackshear 1953). Early theoretical analysis aimed at describing the dynamics of these wrinkles and led to simple expressions by analogy with the $n-\tau$ time-lag model (Crocco 1951) developed for rocket engines stability analysis. One of the first expressions for the FTF of a premixed laminar conical flame was developed in the 1950s (Merk 1957). In this model, the FTF phase lag increases with the angular frequency ω and the steady flame height $\bar{h}$ and is proportional to the inverse of the injection bulk velocity $\varphi \sim \omega\bar{h}/\bar{u}_b$ (Merk 1957). However, this model could not capture the low-pass filter behavior of the FTF gain.

Another important step was taken with the introduction of kinematic models based on a G-equation used to analyze the dynamics of flame wrinkles (Boyer and Quinard 1990). These models were found to well reproduce the flame front motion observed in experiments provided that the correct flow disturbances structure is prescribed (Boyer and Quinard 1990; Baillot et al. 1992; Baillot et al. 1996).

Effects of the velocity perturbation model

A linear analysis based on a perturbed G-equation led to the first derivation of an analytical expression for the FTF of elongated conical flames ($\bar{\alpha} \to 0$) in a uniform flow submitted to bulk flow oscillations (Fleifil et al. 1996). Based on this model, the FTF was only controlled by a Strouhal number defined as St$= \omega R/S_L$. This model was later generalized to any steady flame tip half angle $\bar{\alpha}$ by introducing the reduced frequency ω_* (Ducruix et al. 2000):

$$\omega_* = \frac{\omega R}{S_L \cos\bar{\alpha}} \tag{1.2}$$

It was found that the uniform velocity model well reproduces the low-frequency behavior of the FTF of large premixed laminar conical methane/air and propane/air flames stabilized on $R = 11$ and $R = 15$ mm injectors (Ducruix et al. 2000). Overall, experiments revealed a good match for the FTF gain over the frequency range of interest (Ducruix et al. 2000; Karimi et al. 2009), but the model was unable to predict the correct evolution of the phase lag at high frequencies, when $\omega_* \geq 6$. The origin was found to be in the coarse description of

the incoming flow perturbations that cannot be assumed uniform in the fresh reactants, even though the flame can be considered to be acoustically compact (Baillot et al. 1992; Schuller et al. 2002).

Low-frequency perturbations at the burner outlet are convected by the mean flow (Baillot et al. 1992; Baillot et al. 1996; Birbaud et al. 2006). By taking this aspect into account, new expressions were derived for the FTF of single premixed laminar conical flames submitted to convected perturbations (Schuller et al. 2003a). Based on this approach, the FTF was found to be a function of two independent parameters, the first being the reduced frequency ω_* given by Eq. (1.2) and the second the steady flame tip half angle $\bar{\alpha}$ or equivalently the steady flame aspect ratio $\bar{h}/R$ (Schuller et al. 2003a; Preetham et al. 2008). This convective model barely changes the FTF gain predictions, but yields the correct evolution of the phase lag of elongated flames ($\bar{\alpha} \to 0$) that regularly increases with frequency and also that of nearly planar flames ($\bar{\alpha} \to \pi/2$) that saturates at $\pi/2$ at high frequencies. Karimi *et al.* found that this model suitably reproduces the FTF of premixed laminar conical flames stabilized in a setup with a $R = 12.5$ mm injector enclosed in a $D = 50$ mm flame tube (Karimi et al. 2009; Karimi 2014). However, this convective model violates mass balance.

As a consequence, analytical expressions for the FTF with a 2D axisymmetric velocity perturbation convected by the mean flow which satisfies the incompressible mass balance were proposed (Baillot et al. 1992; Baillot et al. 1996; Schuller et al. 2002; Preetham et al. 2008; Cuquel 2013; Orchini and Juniper 2016). Simulations with a bulk flow oscillation, a purely axial velocity wave convected by the mean flow and a 2D velocity wave convected by the mean flow and respecting the incompressible mass balance showed that the uniform velocity modulation rapidly fails in predicting the correct shape of the perturbed flames, which is better reproduced by considering incompressible velocity disturbances that are convected by the mean flow (Schuller et al. 2002).

A comparison between three experimental FTF obtained for large premixed laminar conical flames featuring various bulk velocities and two analytical models is presented in Fig. 1.5, reproduced from Schuller *et al.* (2002). Model A is based on convective velocity disturbances whereas model B is based on incompressible convective velocity disturbances (i.e. the mass balance is respected). Overall, the incompressible model yields better results than the convective model, especially for the phase lag plot.

An extensive modeling effort mainly conducted by Prof. Lieuwen's research group at Georgia Tech led to analytical expressions for the FTF including the effects of the mean flow velocity profile, celerity of the convected perturbations, anchoring point dynamics, flame stretch, flame curvature and of finite ampli-

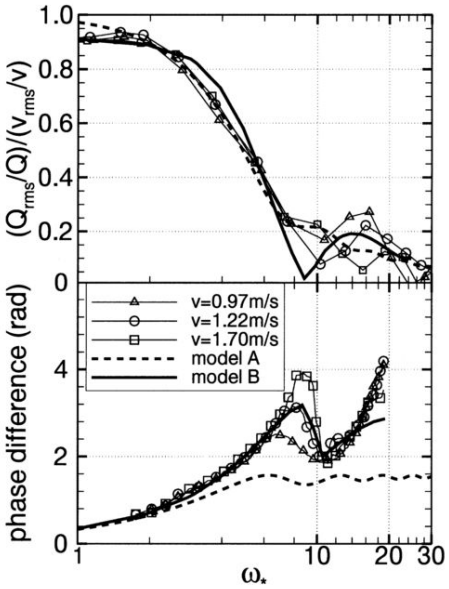

Figure 1.5: *Comparisons between predicted and experimental Flame Transfer Functions obtained for a single large premixed laminar conical methane/air flame. Symbols: measurements for mean flow velocities $\bar{u}_b = 0.97$ m/s, $\bar{u}_b = 1.22$ m/s and $\bar{u}_b = 1.70$ m/s at a prescribed equivalence ratio $\phi = 0.85$. Dashed line: convective velocity disturbances model. Solid line: incompressible convective velocity disturbances model. Reproduced from Schuller et al. (2002).*

tude perturbations (Lieuwen 2005; Preetham et al. 2008). However, it should be noted that these studies rarely provide comparisons with experiments or simulations on a quantitative basis.

Effects of the flame base motion

In a system with an injector of radius $R = 5$ mm, conical flames submitted to harmonic flowrate disturbances and flames stabilized over an oscillating ring in a uniform flow feature very similar FTF gains, but their FTF phase lags differ and reach two different asymptotic limits, as displayed in Fig. 1.6 (Kornilov et al. 2007). Flames submitted to flowrate modulations feature a FTF phase lag increasing with the forcing frequency, while flames submitted to modulations of their anchoring position feature a phase lag saturation at $\pi/2$, as shown in Fig. 1.6. This reveals that the anchoring point dynamics needs to be considered in order to reproduce the correct FTF phase lag evolution (Kornilov et al. 2007).

It was shown recently that the contribution of the anchoring point dynamics to flame wrinkling is the leading mechanism at high frequency and large forcing amplitudes (Karimi et al. 2009), a feature that has been shown to be responsible

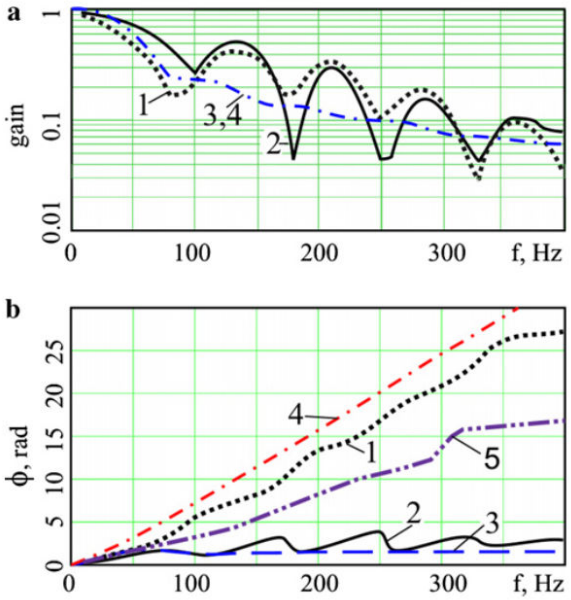

Figure 1.6: *The transfer function gain (a) and phase delay (b) of a large premixed laminar conical methane/air flame when submitted to an acoustic wave (curve 1) and when the flame holder oscillates in the jet direction (curve 2) and in the transversal direction (curve 5). Analytical transfer function based on the uniform velocity perturbation model (curve 3) and on the convective velocity perturbation model (curve 4). Experiments were performed for a bulk velocity* $\bar{u}_b = 1.65$ *m/s and an equivalence ratio* $\phi = 0.85$. *Reproduced from Kornilov et al. (2007).*

for the saturation of the FTF phase lag at high frequencies (Cuquel et al. 2013a). The effects of heat transfer from the flame base to the injector outlet on the anchoring point dynamics was then investigated. It was established that changing the burner cooling alters the flame anchoring point dynamics and as a consequence the FTF (Mejia et al. 2015). As the burner exit plate temperature is increased, a slight decrease of the low-frequency FTF gain is observed, but no change in the FTF phase lag could be detected (Mejia et al. 2015).

Effects of exothermicity

Analytical expressions of FTF derived from kinematic models usually neglect the impact of exothermicity (Mehta et al. 2005). Exothermicity was shown to alter the fresh reactants stream dynamics by two separate mechanisms. First, the steady-state velocity field is modified due to the slight overpressure generated by the burnt gases and acting on the upstream flow. This phenomenon causes an acceleration of the flow along the burner axis leading to elongated flames, but it is only perceptible for oxy-flames (Higuera 2009) or confined conical flames when the burnt gases cannot fully expand (Cuquel et al. 2013b).

The main effect is indirect and deeply alters the unsteady flow field upstream of the flame front. Due to exothermicity, flame wrinkles convected along the reaction layer act as a perturbed vorticity sheet, which in turn modifies the dynamics of the acoustically perturbed flow field through the Biot-Savart law (Blanchard et al. 2015). The strength of this mechanism increases with the volumetric expansion ratio $E = \bar{\rho}_u/\bar{\rho}_b$ between burnt and unburnt gases and with flame wrinkle curvature. This phenomenon was shown to be responsible for the convected waves observed at low frequencies in the fresh reactants of acoustically perturbed laminar flames. Its penetration depth through the perturbed flow field is inversely proportional to the forcing frequency (Birbaud et al. 2006) and a progressive transition to a purely acoustic field takes place as the forcing frequency increases (Birbaud et al. 2006). Direct numerical simulations of acoustically perturbed conical flames were able to reproduce this phenomenon (Schlimpert et al. 2015). This mechanism is reminiscent to Darrieus-Landau instabilities (Clanet and Searby 1998), but for perturbed flames (Blanchard et al. 2015).

Effects of the forcing level

The impact of the forcing level on the FTF gain of large premixed laminar conical flames is limited, as observed in the experiments presented in Fig. 1.3 (Durox et al. 2009) and in numerical simulations (Schuller et al. 2003a). On the other hand, the FTF phase lag plot was shown to saturate when the forcing amplitude was increased (Durox et al. 2009). This saturation occurs for lower frequencies when the forcing level is increased, as shown in Fig. 1.3.

In this work, the flame frequency response is investigated for reduced frequencies $\omega_* < 15$. As a consequence, the forcing level is always prescribed at $|u'|/\bar{u} = 0.10$ RMS, unless it is specifically mentioned otherwise. This ensures that the flame frequency response remains in the linear regime for all forcing frequencies of interest.

1.2.2 FTF of collections of small premixed laminar conical flames

Many industrial and domestic burners operate with a collection of small premixed laminar conical flames stabilized above matrix injectors featuring different patterns of circular and/or rectangular holes, as exemplified in Fig. 1.7. The FTF of these flames have been the topic of many investigations due to their technological applications (Matsui 1981; Sugimoto and Matsui 1982; Noiray et al. 2006b; Durox et al. 2009).

An example of a Flame Transfer Function of a collection of small premixed laminar conical flames of equivalence ratio $\phi = 1.08$ stabilized on a 3 mm thick

Figure 1.7: *(Left) Baxi Solo 2PF domestic boiler. Reproduced from www.lovekin.co.uk (Right) ERB Special high capacity, triple slot burner, used for industrial baking. Reproduced from www.selas.com.*

plate comprising 49 holes of radius $R = 1$ mm traversed by a fresh reactant stream of bulk velocity $\bar{u}_b = 2.12$ m/s and for seven different forcing levels is presented in Fig. 1.8 (Durox et al. 2009).

The early analysis (Matsui 1981; Sugimoto and Matsui 1982) have shown that small flames may feature FTF gain values largely exceeding unity, corresponding to an amplification of the incoming flow perturbations by the unsteady combustion processes. Noiray *et al.* found that despite the small radii of their injectors ($R = 1.0$ mm and $R = 1.5$ mm) that are of the same order of magnitude as the flame thickness, the response of a collection of small curved conical flames submitted to low-frequency acoustic waves still feature convected velocity waves in the fresh stream of reactants (Noiray et al. 2006a). This observation is consistent with the regularly increasing phase lag of the measured FTF (Noiray et al. 2006b; Durox et al. 2009), as shown in Fig. 1.8. However, the FTF gain of these flames exceeds unity over a broad range of frequencies, a feature that is not predicted by the kinematic models presented in the previous section (Fleifil et al. 1996; Ducruix et al. 2000; Schuller et al. 2003a; Preetham et al. 2008) and represented in Fig. 1.5 for instance.

The frequency response of premixed laminar planar flames stabilized above porous burners and matrix burners with small injection holes was investigated at Eindhoven University in a series of articles (Schreel et al. 2002; Rook et al. 2002; Rook and De Goey 2003; Schreel et al. 2005; de Goey et al. 2011). Experiments and simulations led to the conclusion that the FTF is mainly controlled

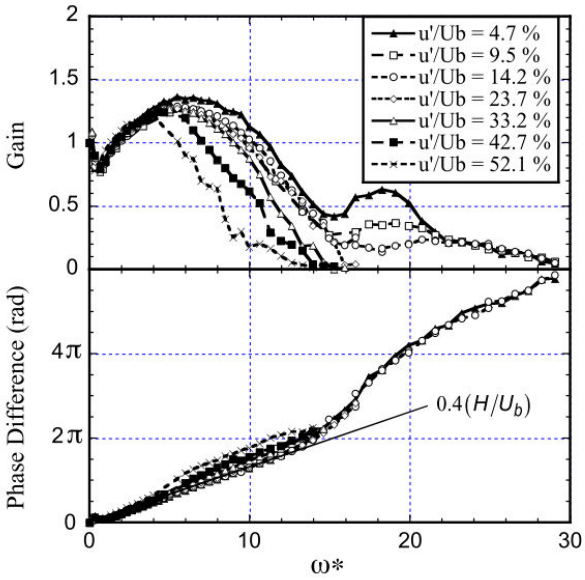

Figure 1.8: *FTF of a collection of small premixed laminar conical methane/air flames of equivalence ratio $\phi = 1.08$ stabilized on a 3 mm thick plate comprising 49 holes of radius $R = 1$ mm traversed by a fresh reactant stream of bulk velocity $\bar{u}_b = 2.12$ m/s and for seven different forcing levels. Reproduced from Durox et al. (2009).*

by the combined effects of acoustic forcing and unsteady heat transfer between the flame base and the burner exit plate. As a consequence, the dynamics of the flame leading edge stabilized close to the injector is an essential feature of the frequency response of small flames stabilized over perforated burners that are submitted to acoustic forcing. By considering the flame as a uniform planar unsteady and non-adiabatic reaction layer impinged by acoustic waves, they were able to reproduce the general trend of the gain featuring a large gain overshoot $G > 1$ in a narrow frequency range and the correct phase lag behavior observed in experiments and simulations (de Goey et al. 2011). In the analytical model developed by Rook *et al.*, constructive interferences between 1) heat and mass transfer between the flame and the burner and 2) the flame anchoring point motion lead to a resonance-like behavior for the FTF gain with values largely exceeding unity (Schreel et al. 2002; Rook et al. 2002). An example of an analytical FTF featuring a large gain overshoot predicted by this mechanism is presented in Fig. 1.9.

This mechanism is controlled by a dimensionless parameter $\hat{\omega}$ defined as (Rook et al. 2002; de Goey et al. 2011):

$$\hat{\omega} = \frac{\omega\delta}{\bar{u}_b} \tag{1.3}$$

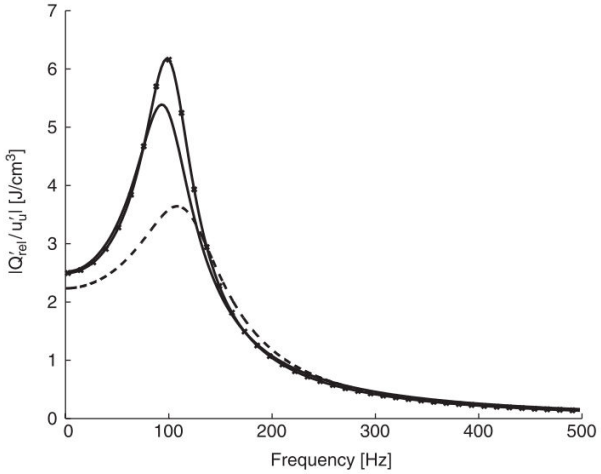

Figure 1.9: *Predictions of the FTF gain of a premixed laminar planar methane/air flame stabilized above a burner according to the analytical model developed at Eindhoven University (dashed line), according to a numerical model with one-step chemistry (solid line) and according to a numerical model with skeletal chemistry (solid line with symbols). Reproduced from Rook et al. (2002).*

where δ is the thermal thickness of the freely propagating adiabatic flame and $\bar{u}_b$ is the injection bulk velocity.

This planar model was later generalized by Prof. Ghoniem's research group to analyze the FTF of a collection of small conical flames stabilized above injection holes interconnected by planar reaction layers (Altay et al. 2009; Kedia and Ghoniem 2013). The authors found that the resonant peaks are dominated by the flame burning velocity oscillations arising as a result of the unsteady heat losses to the burner. Flame area oscillations become significant above the resonant frequency, generating heat release rate oscillations and reducing the time lag between the heat release rate and the inlet velocity.

In a recent study, two regions were defined in order to take into account the flame speed variation along the flame front and subsequently to describe the flame base dynamics along with flame-burner heat interactions (Kedia and Ghoniem 2013). The authors found that the "two-dimensionality" of the flame contributes to the heat release rate fluctuations and the gain overshoot. The FTF predictions (Kedia and Ghoniem 2013) match fairly well the results of direct numerical simulations (Kedia et al. 2011) provided that the flame base stand-off distance and the plate surface temperature are well adjusted, as shown in Fig. 1.10.

Comparisons are also reported with experiments (Manohar 2011) where larger

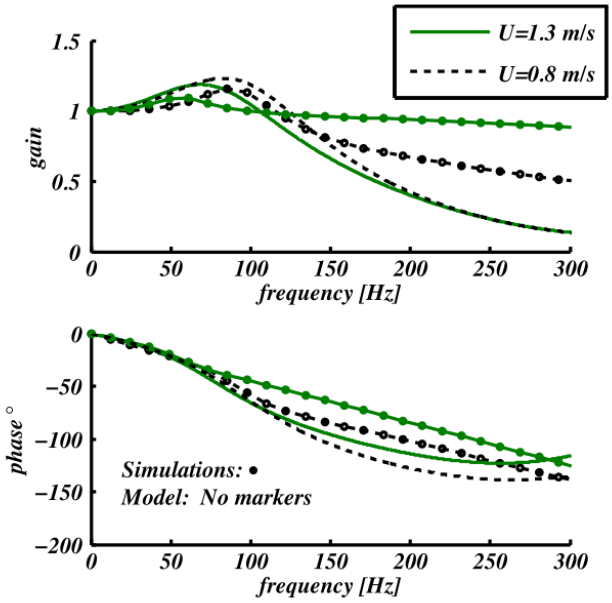

Figure 1.10: *Comparison of the FTF of a collection of small premixed laminar conical methane/air flames obtained from simulations (Kedia et al. 2011) and from an analytical model (Kedia and Ghoniem 2013) for a bulk velocity $\bar{u}_b = 1.3$ m/s, an equivalence ratio $\phi = 0.75$, a perforation ratio $\kappa = 2$ and with a burner outlet of thermal conductivity $\lambda = 1.5$ W/mK. Reproduced from Kedia and Ghoniem (2013).*

differences are observed, but the authors conclude that results are very sensitive to the coupling parameters between the flame stand-off distance and the burner surface temperature and to external heat losses. In these developments, unsteady heat transfer between the flame base and the injector generates the flame base motion (Rook et al. 2002), which constitutes an additional source of flame wrinkles that are convected along the flame front (Cuquel et al. 2013a).

Detailed comparisons between experiments and direct numerical simulations of the FTF of premixed laminar conical flames stabilized over a series of small 2D slits were also explored (Kornilov et al. 2009). In this article, a parametric study was carried out, where the injection bulk velocity $\bar{u}_b$, the equivalence ratio ϕ of methane/air mixtures, the slit width and the distance between slits were varied. It was shown that the measured and computed FTF are qualitatively the same for simulations carried out at a fixed burner outlet temperature $\overline{T}_s = 100°\text{C}$.

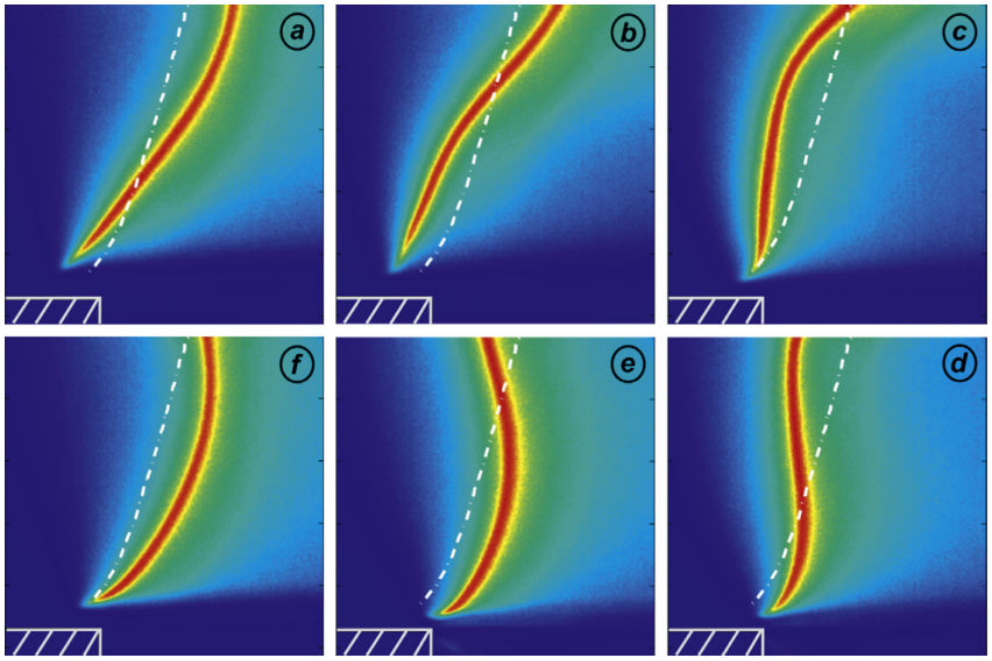

Figure 1.11: *Phase average pictures of the flame base motion and associated convected wrinkles of a premixed laminar methane/air V-flame of equivalence ratio* $\phi = 1.03$ *fed by fresh gases of bulk velocity* $\bar{u}_b = 1.56$ *m/s stabilized above a burner of radius* $R = 11$ *mm and submitted to harmonic forcing at a frequency* $f = 100$ *Hz for a forcing level* $|u'|/\bar{u} = 0.10$. *Reproduced from Cuquel et al. (2013a).*

1.3 Analytical modeling of the FTF of premixed laminar conical flames

In this work, a kinematic description of the perturbed flame dynamics is used (Kerstein et al. 1988; Lieuwen 2005). The main contribution to heat release rate fluctuations is assumed to come from flame surface area variations due to flame wrinkles. Fluctuations of the local burning rate are neglected except near the flame base (Preetham et al. 2008).

Flame wrinkles partly originate from the response of the flame reaction layer to the perturbed velocity field (Fleifil et al. 1996; Dowling 1999). This contribution is designated here as $F_A(\omega)$. Coincidently, flame wrinkles are also generated by the displacement of the flame base (Pertersen and Emmons 1961; Quinard 1996; Kornilov et al. 2007) and are then convected along the flame front, as shown in Fig. 1.11 for a premixed laminar V-flame (Cuquel et al. 2013a). This contribution is designated here as $F_B(\omega)$. The Flame Transfer Function is then the sum of these two contributions (Lee and Lieuwen 2003; Cuquel et al. 2013a; Mejia et al. 2015):

$$F(\omega) = F_A(\omega) + F_B(\omega) \tag{1.4}$$

where $F_A(\omega)$ depends on the velocity perturbation model used to describe the flow upstream of the flame front and $F_B(\omega)$ depends on the model used to describe the anchoring point dynamics.

This analysis is used as a starting point in this work. Three different velocity models are considered for $F_A(\omega)$ in order to revisit this problem for large and small premixed laminar conical flames: 1) a uniform velocity perturbation (UNI), 2) an axial velocity perturbation convected by the mean flow (CON) and 3) an axial plus radial velocity disturbance convected by the mean flow and verifying the incompressible mass balance (INC). These three models are detailed in Sec. 1.3.1. Furthermore, an anchoring point dynamics model is also used to describe $F_B(\omega)$ in this work (Cuquel et al. 2013a). This model is detailed in Sec. 1.3.2.

1.3.1 Analytical models for $\mathbf{F_A}$

Since the description of the perturbed flame dynamics is purely kinematic, the expression of F_A is entirely determined by the expression of the axial and radial velocity perturbations in the fresh gases, respectively denoted by u' and v' in Fig. 1.12. In the remainder of this work, u' and v' are assumed to be harmonic and thus are proportional to $e^{\pm i\omega t}$ depending on the harmonic convention (See Appendix A). For the sake of consistency with previous works, the harmonic convention retained here is $e^{-i\omega t}$ (Schuller et al. 2003a; Preetham et al. 2008).

In this kinematic framework, the flame front is an infinitely thin layer described by a scalar function $\mathcal{G}(\mathbf{x}, t)$, where $\mathbf{x}$ is the position vector and t is the time variable, such that at the interface separating the fresh gases from the burnt gases:

$$\mathcal{G}(\mathbf{x}, t) = 0 \tag{1.5}$$

In this work, the fresh gases region corresponds to $\mathcal{G}(\mathbf{x}, t) < 0$ while the burnt gases region corresponds to $\mathcal{G}(\mathbf{x}, t) > 0$. Assuming that the steady-state flow is purely axial and uniform, the flame front dynamics is then described by a $\mathcal{G}$-equation (Markstein 1964):

$$\frac{\partial \mathcal{G}}{\partial t} + \mathbf{u} \cdot \nabla \mathcal{G} = S_L |\nabla \mathcal{G}| \tag{1.6}$$

where $\mathbf{u}$ is the Eulerian velocity vector and S_L is the laminar burning velocity. The expression of the flame front position is then obtained with the following procedure. First, a velocity perturbation model is chosen. The Eulerian

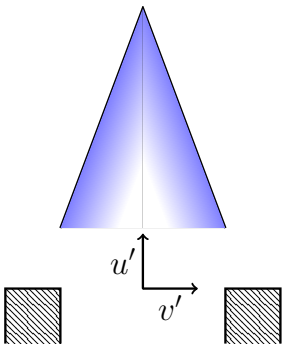

Name	Velocity perturbation model	
Uniform (UNI)	$\begin{cases} u' = ue^{-i\omega t} \\ v' = 0 \end{cases}$	(1.8) (1.9)
Convective (CON)	$\begin{cases} u' = ue^{ikx-i\omega t} \\ v' = 0 \end{cases}$	(1.10) (1.11)
Incompressible (INC)	$\begin{cases} u' = ue^{ikx-i\omega t} \\ v' = ik(R-y)ue^{ikx-i\omega t}/2 \end{cases}$	(1.12) (1.13)

Figure 1.12: *Velocity perturbation models for the $e^{-i\omega t}$ harmonic convention.*

velocity **u** is subsequently decomposed into its steady-state and fluctuating components in Eq. (1.6). Then, the reference frame is changed and a telegraph integral is performed (Boyer and Quinard 1990; Schuller et al. 2003a; Cuquel et al. 2013a). The analytical expression for $F_A(\omega)$ is then obtained by integrating the flame front position over the complete flame surface. Since the flame surface area S is assumed to be proportional to the flame heat release rate $\dot{Q}$ (Hurle et al. 1968), the relative heat release rate fluctuations $\dot{Q}'/\bar{\dot{Q}}$ are shown to be proportional to the relative velocity fluctuations $u'/\bar{u}$ by a factor F_A corresponding to a Flame Transfer Function:

$$\frac{\dot{Q}'}{\bar{\dot{Q}}} = \frac{S'}{\bar{S}} = F_A \frac{u'}{\bar{u}} \tag{1.7}$$

The three velocity perturbation models assessed in this work are reproduced in Fig. 1.12 for the $e^{-i\omega t}$ harmonic convention. The wave number k is the ratio

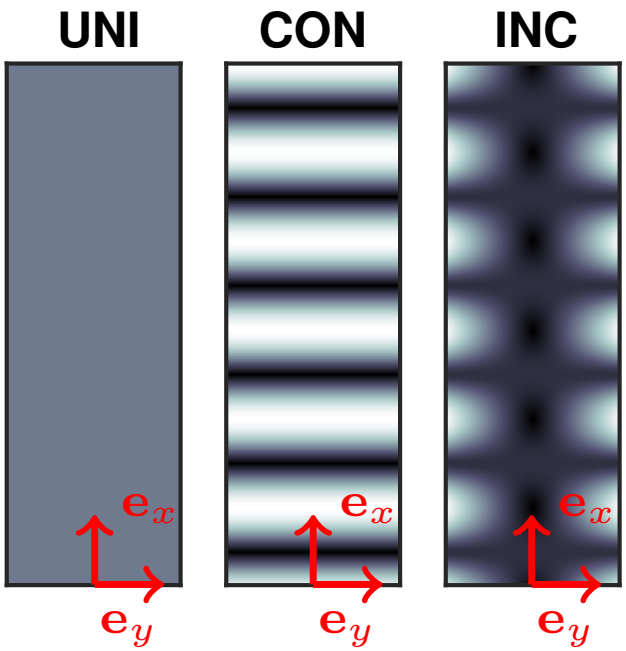

Figure 1.13: *Modulus of the velocity perturbations* $\mathbf{u}' = u'\mathbf{e}_x + v'\mathbf{e}_y$ *for the uniform velocity perturbation model (Left), the convective velocity perturbation model (Center), and the incompressible convective velocity perturbation model (Right). The axial propagation direction is vertical and the radial direction is horizontal. Maximum and minimum velocity disturbances magnitudes are represented respectively in white and black. All physical parameters were chosen arbitrarily.*

between the angular frequency ω and the convection speed u_c and R is the radius of the cylindrical injector.

The uniform velocity perturbation model (UNI) is a purely axial and uniform velocity disturbance (Fleifil et al. 1996; Ducruix et al. 2000). The convective velocity perturbation model (CON) corresponds to a wave propagating in the axial direction, with no radial component (Schuller et al. 2003a). The incompressible convective velocity perturbation model (INC) corresponds to a wave propagating in the axial direction with a radial component such that the incompressible mass balance is respected (Schuller et al. 2002; Preetham et al. 2008). The spatial distribution of these velocity disturbances is represented in Fig. 1.13. The specificities of each of these three models are now presented in details.

The uniform velocity perturbation model (UNI):

First proposed for premixed laminar conical elongated flames (Fleifil et al. 1996) and later generalized to any steady flame tip half angle $\overline{\alpha}$ (Ducruix et al.

2000), the uniform velocity perturbation model (UNI) is the simplest kinematic model based on the integration of the $\mathcal{G}$-equation. The associated velocity perturbation field is uniform in the axial direction and zero in all other directions, as expressed in Eqs. (1.8) and (1.9). This description was proposed because the flame is usually considered to be compact with respect to acoustic and hydrodynamic perturbations (Schuller et al. 2002; Truffin and Poinsot 2005). The associated FTF, denoted F_A^{uni}, was shown to be a function of the reduced frequency ω_* only (Ducruix et al. 2000):

$$F_A^{uni}(\omega_*) = \frac{2}{\omega_*^2}\left(1 - \exp(i\omega_*) + i\omega_*\right) \tag{1.14}$$

The gain and phase lag of F_A^{uni} are represented in blue in Fig. 1.14 as functions of the reduced frequency ω_*. These curves corresponding to the uniform velocity perturbation model are the same for all premixed laminar conical flames. The gain $G(\omega_*)$ tends towards 1 as $\omega_* \to 0$, as predicted by theory (Polifke and Lawn 2007). When the reduced frequency is increased, the gain quickly drops and tends towards 0 as $\omega_* \to +\infty$. The modeled flame response behaves like a low-pass filter. On the other hand, the phase lag plot increases linearly with the reduced frequency until it reaches $\omega_* \sim 5$, where the phase lag is approximately $\varphi \sim \pi/2$. The phase lag then oscillates around $\pi/2$ until the oscillations are completely damped.

The convective velocity perturbation model (CON):

The saturation of the FTF phase lag at $\pi/2$ as predicted by the uniform velocity perturbation model (UNI) is not observed experimentally for elongated flames (Ducruix et al. 2000; Schuller et al. 2002; Kornilov et al. 2007; Durox et al. 2009; Karimi 2014). As a consequence, a new model, called the convective velocity perturbation model (CON) was proposed. In this second kinematic model, the axial velocity perturbation is a wave propagating in the flow direction whereas the radial velocity perturbation is set to zero, as expressed in Eqs. (1.10) and (1.11). The associated Flame Transfer Function F_A^{con} is then a function of two parameters: the steady flame tip half angle $\bar{\alpha}$ and the reduced frequency ω_* (Schuller et al. 2003a):

$$F_A^{con}(\omega_*, \bar{\alpha}) = \frac{2}{\omega_*^2(1 - \cos^2\bar{\alpha})}\left[1 - \exp(i\omega_*) + \frac{\exp(i\omega_*\cos^2\bar{\alpha}) - 1}{\cos^2\bar{\alpha}}\right] \tag{1.15}$$

The gain $G(\omega_*, \bar{\alpha})$ and phase lag $\varphi(\omega_*, \bar{\alpha})$ associated with the convective velocity perturbation model are represented in Fig. 1.15 as functions of the reduced frequency ω_* (x-axis) and steady flame tip half angle $\bar{\alpha}$ (y-axis). The values of the FTF gain G and phase lag φ are then represented using a colorbar. Figure 1.15 clearly shows that once again, the flame frequency response is a

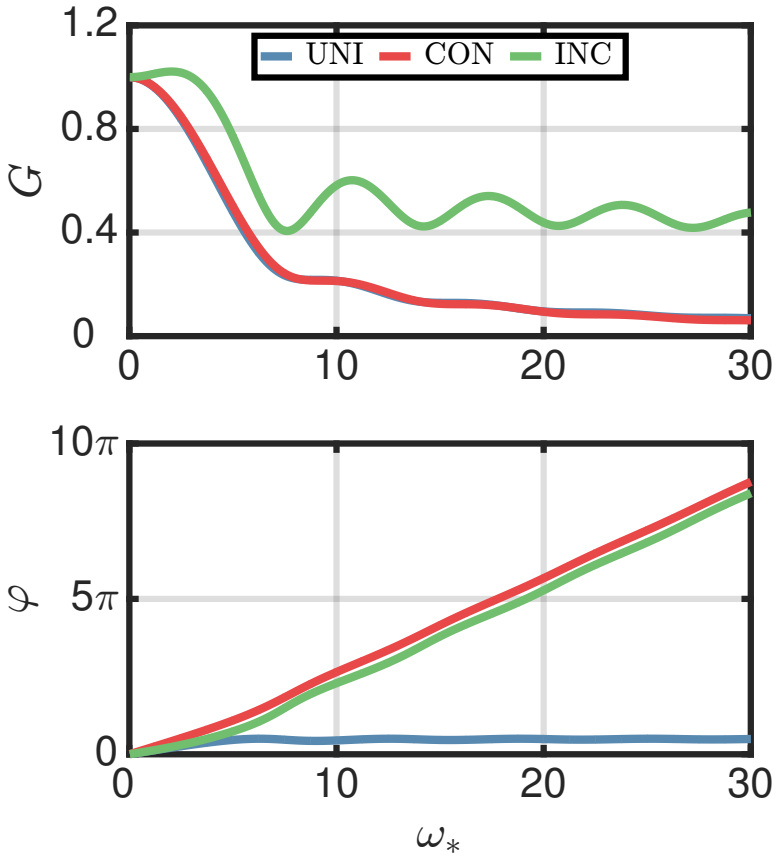

Figure 1.14: *Gain (Top plot) and phase lag (Bottom plot) of a Flame Transfer Function according to the uniform (blue), convective (red) and incompressible convective (green) velocity perturbation models. The steady flame tip half angle is set to* $\bar{\alpha} = 14.5°$ *for the last two models.*

low-pass filter.

In order to compare the uniform (UNI) and convective (CON) velocity perturbation models, the steady flame tip half angle is set to $\bar{\alpha} = 14.5°$, corresponding to all flames explored in the present work, and the FTF predictions associated with the convective model are plotted in red in Fig. 1.14. Once again, the gain plot indicates that the flame response is a low-pass filter. The gain predictions according to the uniform and convective perturbation models are almost the same. On the other hand, the phase lag increases indefinitely with the reduced frequency in the case of the convective perturbation model, as opposed to the uniform perturbation model where the phase lag quickly saturates. It should be noted that when $\bar{\alpha} \to 0$, the convective model described by Eq. (1.15) collapses to the uniform model described by Eq. (1.14).

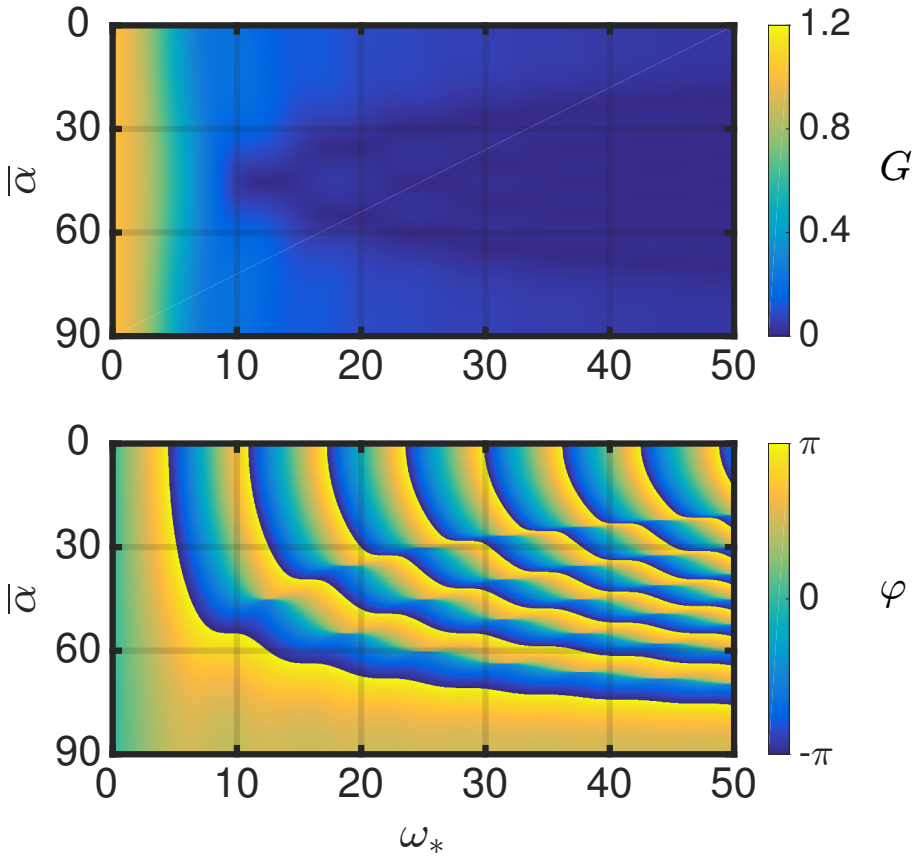

Figure 1.15: *Gain (Top plot) and phase lag (Bottom plot) of the Flame Transfer Function predicted by the convective velocity perturbation model (CON) as functions of the reduced frequency ω_* (x-axis) and steady flame tip half angle $\bar{\alpha}$ (y-axis).*

The incompressible convective velocity perturbation model (INC):

The convective velocity perturbation model (CON) has a major drawback: mass balance is violated. This issue is solved by considering a radial velocity perturbation in addition to the axial convective wave such that the incompressible mass balance is ensured (Preetham et al. 2008; Cuquel 2013; Orchini and Juniper 2016). These velocity disturbances are expressed in Eqs. (1.12) and (1.13). The corresponding Flame Transfer Function F_A^{inc} is a function of the steady flame tip half angle $\bar{\alpha}$ and the reduced frequency ω_*. For the sake of simplicity, an additional parameter is introduced: $k_* = \omega_* \cos^2 \bar{\alpha}$. This parameter is redundant as it is expressed solely in terms of $\bar{\alpha}$ and ω_*. The Flame Transfer Function F_A^{inc} is then given by (Cuquel 2013):

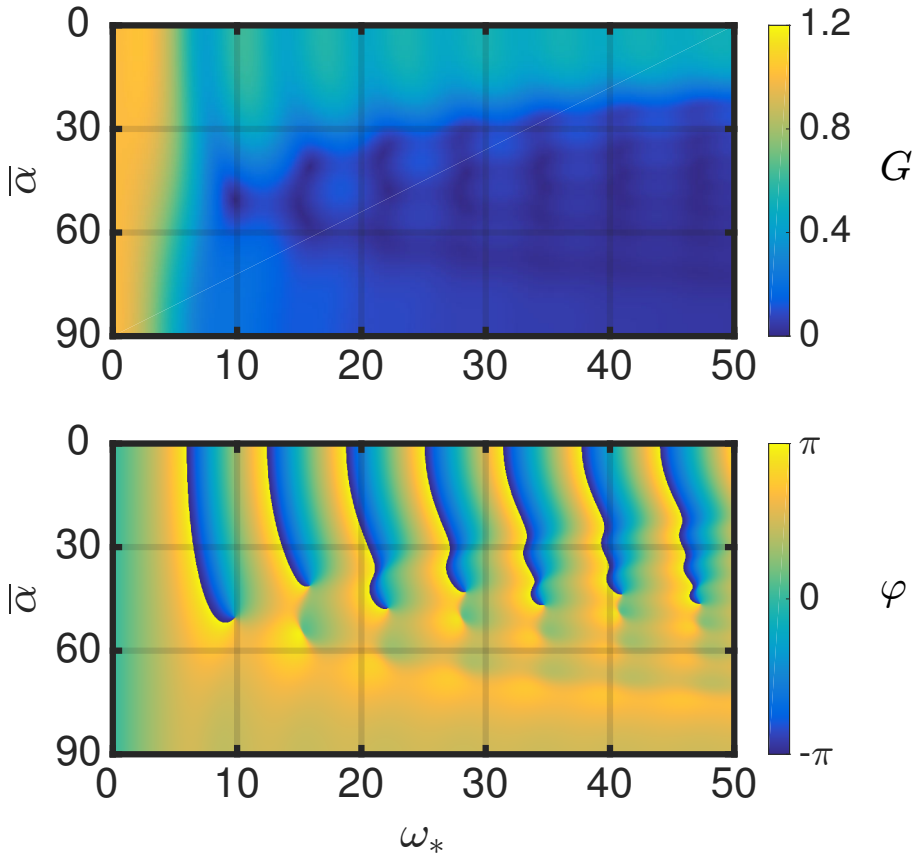

Figure 1.16: *Gain (Top plot) and phase lag (Bottom plot) of the Flame Transfer Function predicted by the incompressible convective velocity perturbation model (INC) as functions of the reduced frequency ω_* (x-axis) and steady flame tip half angle $\overline{\alpha}$ (y-axis).*

$$F_A^{inc}(\omega_*, \alpha) = \frac{1}{i(k_* - \omega_*)} \left[\left(2 - ik_* - \frac{k_*}{k_* - \omega_*} \right) \times \left(\frac{\exp(ik_*) - 1}{ik_*} - \frac{\exp(i\omega_*) - 1}{i\omega_*} \right) + \left(\exp(ik_*) - \frac{\exp(ik_*) - 1}{ik_*} \right) \right] \quad (1.16)$$

The gain $G(\omega_*, \overline{\alpha})$ and the phase lag $\varphi(\omega_*, \overline{\alpha})$ associated with the incompressible convective velocity perturbation model (INC) are represented in Fig. 1.16 as functions of the reduced frequency ω_* (x-axis) and steady flame tip half angle $\overline{\alpha}$ (y-axis). The values of the gain G and phase lag φ are then represented using a colorbar. Once again, it is clear from Fig. 1.16 that the modeled flame response is a low-pass filter.

In order to compare the incompressible convective (INC) perturbation model to the uniform (UNI) and convective (CON) perturbation models, the steady

flame tip half angle is again set to $\bar{\alpha} = 14.5°$, corresponding to all flames explored in the present work, and the FTF associated with the incompressible model is plotted in green in Fig. 1.14. The FTF phase lag plots as predicted by the incompressible (INC) and convective (CON) models increase indefinitely with the reduced frequency ω_* and are almost superimposed. On the other hand, the FTF gain plot as predicted by the incompressible model is larger compared to the predictions according to the uniform and convective models. The low-frequency limit of G is still 1 but as the reduced frequency increases, a small gain overshoot can be observed. Moreover, the flame is still a low-pass filter but the gain slowly decreases with the reduced frequency. At $\omega_* = 30$, the gain of the FTF as predicted by the incompressible model is $G \sim 0.5$ as opposed to $G < 0.1$ for the two previous models.

One way to solve this issue is to consider a new velocity perturbation model based on an acoustic wave with an exponentially decaying amplitude in the axial direction (Cuquel 2013). The radial component of the velocity disturbance is then obtained by solving the incompressible mass balance. However, there is no physical justification for such a velocity perturbation model and as a consequence, this model will not be considered in this work.

1.3.2 Analytical models for $\mathbf{F_B}$

In addition to the flame response to velocity disturbances, wrinkles are also induced by the motion of the flame base. This contribution, denoted F_B in this work, is the product of two transfer functions (Cuquel et al. 2013a):

$$F_B = F_C \times \Xi \tag{1.17}$$

The first transfer function F_C relates flame surface area fluctuations to the unsteady motion of the flame base which generates flame wrinkles (Boyer and Quinard 1990; Lee and Lieuwen 2003). The second transfer function Ξ describes the motion of the flame base as a function of the incoming velocity perturbations. This contribution has been investigated in a series of articles for planar flames stabilized above perforated plates (Rook et al. 2002; de Goey et al. 2011).

The transfer function F_C can be deduced solely from kinematic considerations and behaves like a low-pass filter. It is a function of the reduced frequency ω_* and of the steady flame tip half angle $\bar{\alpha}$ and it is expressed as (Cuquel et al. 2013a):

$$F_C(\omega_*, \bar{\alpha}) = 2\cos\bar{\alpha}\frac{e^{i\omega_*} - 1}{i\omega_*} \tag{1.18}$$

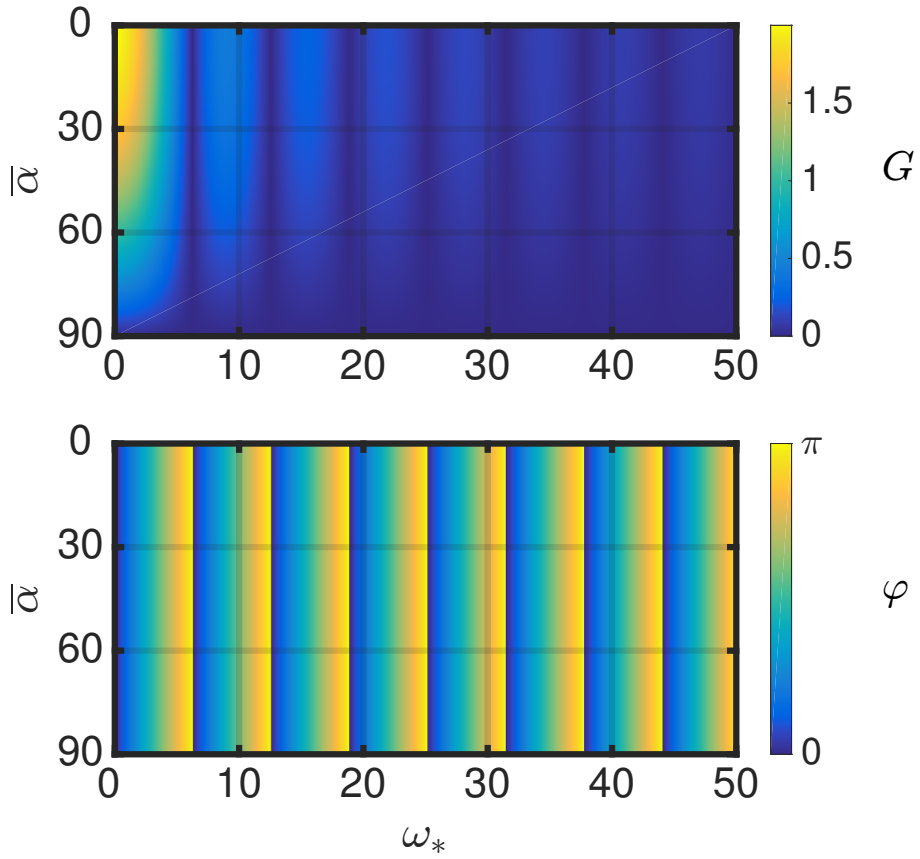

Figure 1.17: *Gain (Top plot) and phase lag (Bottom plot) of the transfer function $F_C(\omega_*, \bar{\alpha})$ as functions of the reduced frequency ω_* (x-axis) and steady flame tip half angle $\bar{\alpha}$ (y-axis).*

The gain $G(\omega_*, \bar{\alpha})$ and phase lag $\varphi(\omega_*, \bar{\alpha})$ of $F_C(\omega_*, \bar{\alpha})$ are represented in Fig. 1.17 as functions of the reduced frequency ω_* (x-axis) and steady flame tip half angle $\bar{\alpha}$ (y-axis). Once again, the values of the gain and phase lag are represented using a colorbar. This transfer function behaves like a low-pass filter, especially when $\bar{\alpha} \to 0$, as shown in Fig. 1.17. The incoming acoustic wave is amplified when the gain of the transfer function is larger than one, which happens for low forcing frequencies and for a steady flame tip half angle smaller than 60°.

The second transfer function Ξ is much more complex than F_C because it is deduced from a dynamic analysis involving unsteady heat and mass transfer between the flame and the burner (de Goey et al. 2011; Cuquel et al. 2013a). In addition to the reduced frequency ω_* introduced in Eq. (1.2) and the steady flame tip half angle $\bar{\alpha}$, the retained expression for Ξ (Cuquel 2013; Cuquel et al.

2013a) depends on the Zeldovich number Ze, the dimensionless flame thermal thickness δ_*, and an additional dimensionless parameter Θ_*:

$$\begin{cases} \delta_* = \dfrac{\delta \cos\bar{\alpha}}{R} & (1.19) \\ \mathrm{Ze} = \dfrac{T_a}{T_b}\dfrac{T_b - T_u}{T_b} & (1.20) \\ \Theta_* = \dfrac{1}{2}\log_{10}\left(\dfrac{T_{ad} - T_u}{T_{ad} - T_b}\right) & (1.21) \end{cases}$$

where $T_a = 15\ 000$ K is an activation temperature, T_b and T_u are the burnt and unburnt gas temperatures respectively and T_{ad} is the adiabatic flame temperature (Cuquel et al. 2013a). The expression for $\Xi(\omega_*, \bar{\alpha}, \mathrm{Ze}, \delta_*, \Theta_*)$ is then given by:

$$\Xi(\omega_*, \bar{\alpha}, \mathrm{Ze}, \delta_*, \Theta_*) = (\mathcal{A} - 1)\exp(i\omega_*\delta_*\Theta_* \sin 2\bar{\alpha}) \times \left[(i\omega_* \cos\bar{\alpha})^{-1} - \frac{\cos\bar{\alpha}}{2} + \delta_*\Theta_* \sin\bar{\alpha}\right] \quad (1.22)$$

where $\mathcal{A}$ is given by:

$$\mathcal{A}(\omega_*, \mathrm{Ze}, \delta_*, \Theta_*) = \left[1 - \frac{4i\delta_*\omega_*}{\mathrm{Ze}} \sinh(\Theta_*) \exp\left(\Theta_* \sqrt{1 - 4i\omega_*\delta_*}\right)\right]^{-1} \quad (1.23)$$

It should be noted that Ξ is flame dependent and that it is not derived from purely kinematic considerations. As a consequence, F_B is different for every flame and experiments or simulations are needed in order to provide the adequate input variables. Moreover, it depends on five distinct variables which makes an experimental or numerical parametric study tedious.

Several expressions for Ξ have been proposed (Rook et al. 2002; Kedia et al. 2011; Cuquel et al. 2013a) but the expression for $\Xi(\omega_*, \bar{\alpha}, \mathrm{Ze}, \delta_*, \Theta_*)$ given in Eq. (1.22) was validated by pictures of the flame base motion, shown in Fig. 1.11, and was shown to adequately reproduce the high frequency behavior of the FTF gain and phase lag for a premixed laminar conical methane/air flame stabilized over an injector of radius $R = 11$ mm, as shown in Fig. 1.18 (Cuquel et al. 2013a). A similar model was derived (Kedia et al. 2011), but the authors do not provide detailed comparisons of the FTF with experiments.

The total transfer function F_B describing the motion of the flame base is represented in Fig. 1.19 as a function of the reduced frequency ω_* and steady

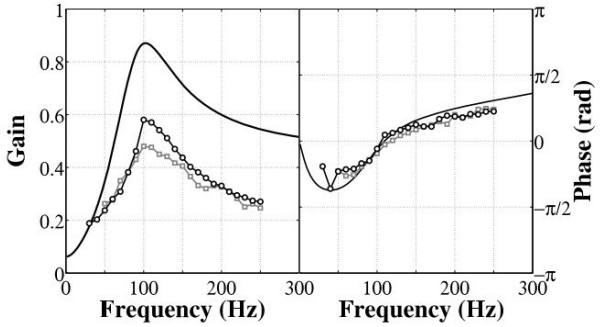

Figure 1.18: *Gain (left) and phase lag (right) of the transfer function* Ξ *for a premixed laminar conical methane/air flame of equivalence ratio* $\phi = 1.03$ *and bulk flow velocity* $\bar{u}_b = 1.56$ *m/s as a function of the frequency. The theoretical prediction (black) is compared to measurements for two forcing levels* $|u'|/\bar{u} = 0.05$ *(grey squares) and* $|u'|/\bar{u} = 0.10$ *(black circles). Reproduced from Cuquel et al. (2013).*

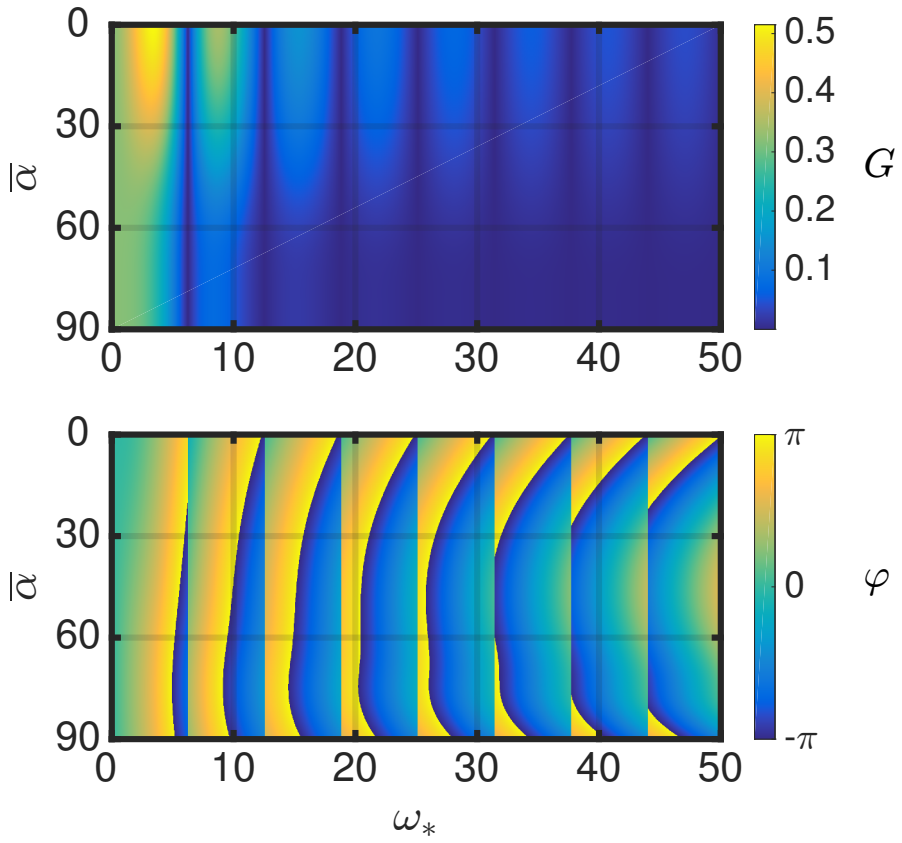

Figure 1.19: *Gain (Top plot) and phase lag (Bottom plot) of the transfer function* F_B *describing the anchoring point dynamics as functions of the reduced frequency* ω_* *(x-axis) and steady flame tip half angle* $\bar{\alpha}$ *(y-axis) for* $\delta_* = 0.1$*,* $Ze = 8$ *and* $\Theta_* = 1$*.*

flame tip half angle $\bar{\alpha}$. The three remaining parameters are set in this work to $\delta_* = 0.1$, $\mathrm{Ze} = 8$ and $\Theta_* = 1$, which are typical values for the premixed laminar conical methane/air and propane/air flames stabilized over a burner outlet of radius $R = 11$ mm that were investigated in this study. This transfer function behaves like a low-pass filter, especially when the steady flame tip half angle is limited, as shown in Fig. 1.19.

1.4 Conclusion

A comprehensive literature review about the acoustic response of premixed laminar conical flames submitted to harmonic forcing was performed in this chapter. It was shown that this response may be characterized by a Flame Transfer Function (FTF) that relates the relative oscillations of the flame heat release rate to the relative oscillations of the flow velocity. This FTF may be decomposed into two distincts contributions: 1) a transfer function F_A that depends on the velocity perturbation impinging on the flame and 2) a transfer function F_B related to the flame base motion.

Three models for F_A based on uniform, convective and incompressible convective velocity perturbations were then presented based on previous investigations. An additional model for the transfer function F_B was also reproduced.

Based on previous experimental and numerical investigations, it seems that the frequency response of collections of small premixed laminar conical flames differ from the response of large premixed laminar conical flames. It is then worth investigating the FTF of both types of flames using experiments and analytical approaches.

Chapter 2

Experimental Setup and Diagnostics

The experimental setup used to determine the Flame Transfer Functions of premixed laminar conical flames is presented in this chapter. The various diagnostics employed, including velocity and chemiluminescence measurements, are also described. Finally, the physical parameters of all flames explored in the present study are introduced along with the corresponding steady-state flame pictures.

2.1 The laminar burner

The burner used to analyze the frequency response of premixed laminar conical flames in this study is presented in Fig. 2.1. It is a new version of the so-called Durox burner (Ducruix et al. 2000; Schuller et al. 2002; Birbaud et al. 2006; Durox et al. 2009; Cuquel et al. 2013a). The various geometrical and physical parameters used in this chapter are introduced in Fig. 1.1.

The different mass flowrates injected are controlled with Bronkhorst EL-FLOW devices. Pure methane (CH_4) or propane (C_3H_8) is mixed with air at a large distance from burner (not represented in Fig. 2.1). The resulting perfectly premixed gases are injected at the bottom of the burner in a tranquilization box, above a loudspeaker used to generate harmonic flowrate perturbations. The flow is then pushed through a perforated plate and a honeycomb structure to break the large turbulence scales thus generating a laminar flow in the plenum. At the top of the plenum, a finely-meshed grid impedes downward flame propagation in the event of a flashback.

A convergent nozzle (contraction ratio: 8.73) placed after the plenum accelerates the fresh gases and creates an almost planar velocity profile at the burner outlet (Schuller 2003; Cuquel 2013). A water-cooled support is added at the

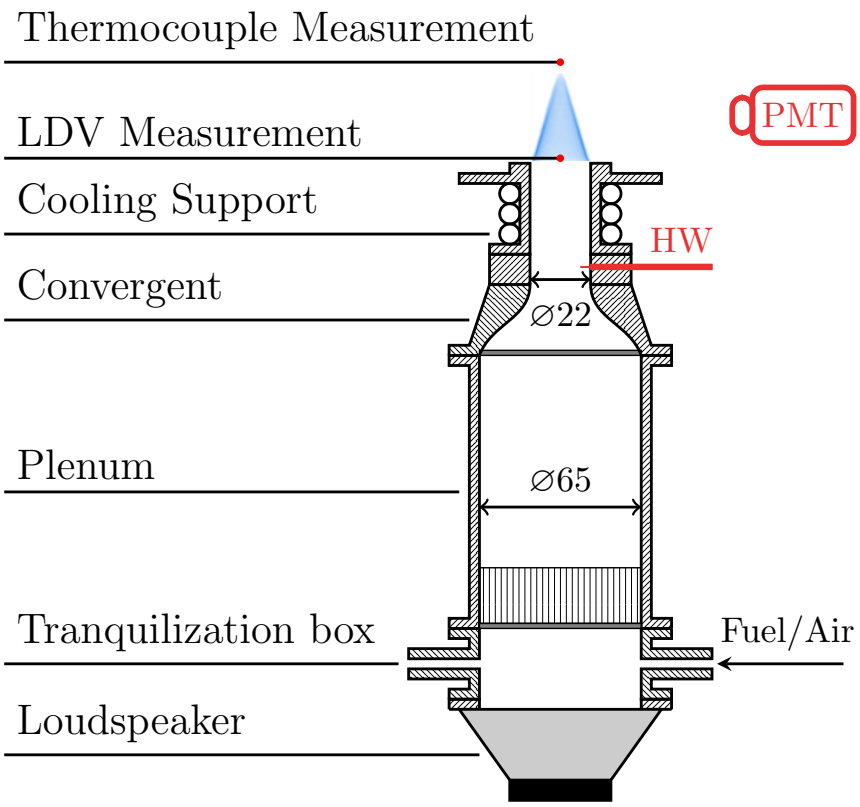

Figure 2.1: *Laminar burner (black & gray) and its associated diagnostics (red). The premixed gases are injected in a tranquilization box just after the loudspeaker and the flame is stabilized above the cooling support at the top of the burner. Diagnostics include a hot-wire probe (HW), a photomultiplier with an OH* filter (PMT), Laser Doppler Velocimetry (LDV) and thermocouple measurements. Dimensions are given in mm.*

top of the burner to control the steady-state burner outlet temperature, kept constant and equal to $\overline{T}_s = 300$ K for all experiments. By default, the burner exit radius is equal to $R = 11$ mm, corresponding to Fig. 2.2-(a), but adaptation elements shown in Fig. 2.2 may be used to modify the flame size. The first element is a sleeve used to reduce the radius of the burner outlet to $R = 7$ mm, corresponding to Fig. 2.2-(b). Two perforated plates with circular holes regularly distributed over a square pattern of size d can also be mounted at the top of the burner. The first plate features 21 holes of radius $R = 1.5$ mm with an inter-hole space $d = 4$ mm, corresponding to Fig. 2.2-(c). The second plate features 25 holes of radius $R = 1.0$ mm separated by $d = 3$ mm, corresponding to Fig. 2.2-(d). The burnt gases are then exhausted to the atmostphere.

It should be noted that the velocity profiles at the burner outlet slightly differ depending on the burner outlet radius. For the burner outlets with $R = 11$ mm

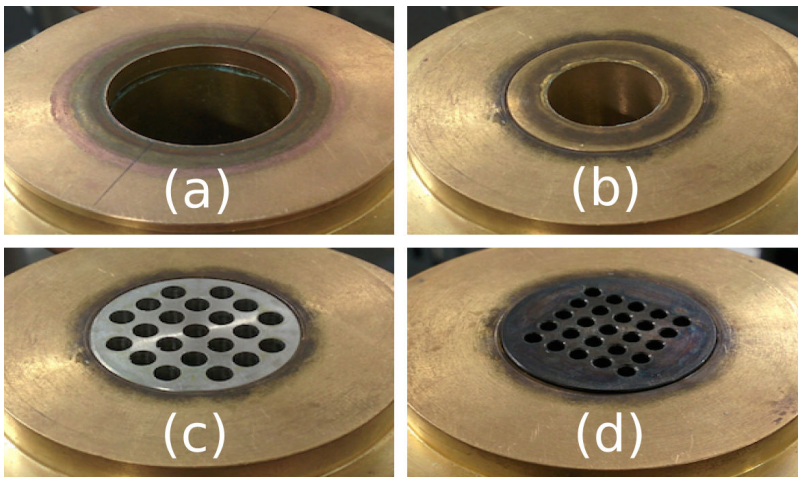

Figure 2.2: *Burner outlet elements with various perforation radii and patterns. (a) 1 hole, $R = 11$ mm. (b) 1 hole, $R = 7$ mm. (c) 21 holes, $R = 1.5$ mm. (d) 25 holes, $R = 1.0$ mm.*

and $R = 7$ mm, the velocity profile is flat (Durox et al. 2004). For the perforated plates with injection holes of radii $R = 1.5$ mm and $R = 1.0$ mm, the velocity profile is parabolic (Noiray 2007). However, a parabolic mean velocity profile (Fleifil et al. 1996) and a flat mean velocity profile (Ducruix et al. 2000) lead to very similar results for the FTF gain and phase lag plots with a uniform velocity perturbation model. As a consequence, the impact of the mean velocity profile at the burner outlet will not be considered in this study.

2.2 Diagnostics

The various diagnostics employed in this study are now quickly described.

2.2.1 Temperature measurements

R-type and K-type thermocouples are used to measure the temperature in the burnt gases one millimeter above the steady-state flame tip, as represented in Fig. 2.1. All temperature measurements presented in this part of the manuscript and performed in the burnt gases region are corrected for radiative heat losses (Guiberti 2015). More details about temperature measurements are given in Chapter 6.

2.2.2 Velocity measurements

The frequency response of premixed laminar conical flames is explored using two different types of velocity measurements. In all cases, harmonic acoustic

forcing is generated by the loudspeaker located at the bottom of the burner. In a first set of experiments, corresponding to the data presented in Sec. 4.2, a hot-wire probe (Dantec Dynamics - Probe 55P16 with a mini-CTA 54T30), denoted HW in Fig. 2.1, records the velocity signal 35 mm below the burner outlet, in the uniform region of the steady-state flow. The hot-wire signal is used to determine the reference velocity $\bar{u}$ corresponding to the steady-state velocity in the absence of acoustic forcing and the forcing level $|u'|/\bar{u}$, kept constant and in the linear regime for all operating conditions.

In a second set of experiments, corresponding to the data presented in Chapter 3 and Sec. 4.3, the axial velocity is measured using Laser Doppler Velocimetry (LDV) at the burner outlet. The measurement volume is in this case located 1 mm above the burner outlet and on the symmetry axis. A continuous 3-Watts Argon Laser is used to generate two beams of wavelength $\lambda = 514$ nm separated by a distance $l = 40$ mm before they reach a converging lens of focal distance $f = 250$ mm used to create the interference pattern. The flow is seeded with small oil droplets of diameter 3 μm with a nebulizer (Durox et al. 1999). The data collection rate is always greater than $10,000$ s^{-1} and the LDV bench is calibrated before all measurements. The LDV velocity signal is then used to determine the reference velocity $\bar{u}$ corresponding to the steady-state velocity at the flame base and in the absence of acoustic forcing, the velocity disturbance u' at the forcing angular frequency ω and the forcing level $|u'|/\bar{u}$, kept constant and in the linear regime for all operating conditions. Hot-wire anemometry and Laser Doppler Velocimetry are presented in more details in Chapter 6.

2.2.3 Chemiluminescence measurements

It is assumed in this study that the mean $\bar{\dot{Q}}$ and fluctuating $\dot{Q}'$ heat release rate signals are linearly related to the mean $\bar{I}$ and fluctuating I' OH* chemiluminescence intensities originating from the entire flame region (Hurle et al. 1968). This relation was checked for lean premixed hydrocarbon flames (Higgins et al. 2001; Schuller et al. 2002; Candel et al. 2004; Li et al. 2015). The OH* chemiluminescence signal is recorded with a photomultiplier (Hamamatsu H5784-04) equipped with a narrow band-pass filter (Asahi Spectra ZBPA310 - $\lambda = 310$ nm and 10 nm width). Another interferometric filter with the same characteristics may be used in front of the ICCD camera, presented thereafter.

2.2.4 Experimental Flame Transfer Functions

Measurements at low frequencies require a large acquisition time in order to reach statistical convergence. As a consequence, all signals including the hot-wire, LDV and photomultiplier signals were recorded for a minimum duration of $t = 10$ s and at a sampling rate $f_s = 8196$ Hz. All measured signals are recorded for a duration corresponding to at least 50 periods of the forcing cycle. The

FTF is then deduced from the cross power spectral density between the photomultiplier signal and the LDV signal divided by the auto power spectral density of the LDV signal. The Welch periodogram method examined at the forcing frequency is utilized. More details about the experimental determination of Flame Transfer Functions is presented in Sec. 9.2.

2.2.5 Flame pictures with the ICCD camera

A signal generator (Hameg Instruments HM8030-3) is used to generate both a sinusoidal wave and the corresponding TTL signal. The sinusoidal signal is amplified and sent to a loudspeaker (Monacor SPH-115, 50 Watts RMS) mounted at the bottom of the burner to force the flow, as depicted in Fig. 2.1. On the other hand, the TTL signal triggers an ICCD camera (Princeton Instruments PI-MAX4 1024x1024 pixels) mounted with an UV objective (Nikon U.V. Nikkor 105 mm f/4.5) with and without an interferometric filter ($\lambda = 310$ nm and 10 nm width). This technique is employed to get phase average pictures of the flame at various forcing frequencies and forcing levels. Pictures of the flames at steady flow injection conditions are also taken with the ICCD camera without interferometric filter, as shown in Figs. 2.3, 2.4, 2.5 and 2.6. All flame pictures taken with the ICCD camera are averaged over 100 frames. More details about flame imaging techniques are presented in Chapter 6.

2.3 Operating conditions

All flames investigated in this work are fully premixed laminar conical flames with a steady flame tip half angle $\bar{\alpha} = 14.5°$ corresponding to a steady flame aspect ratio $\bar{h}/R = 4$ for large flames, as shown in Figs. 2.3 and 2.4. Small flames stabilized on perforated plates experience strong curvature effects at their flame tip, as shown in Figs. 2.5 and 2.6. The curvature at the flame tip is controlled by preferential diffusion (Lewis and von Elbe 1987). Consequently, the aspect ratio of small flames is slightly smaller than $\bar{h}/R = 4$ and depends on the Lewis number Le of the fuel/air mixture, but the flame angle away from the flame base and flame tip is still equal to $\bar{\alpha} = 14.5°$ as for the large conical flames.

Two types of fuels are used in this study: methane (CH_4) and propane (C_3H_8). As a first approximation, the Lewis number of the premixed gases is assumed to be independent of the equivalence ratio (Gaudron et al. 2017b). Fresh gases have a Lewis number Le=0.93 and Le=1.80 for the CH_4/air and C_3H_8/air mixtures respectively.

The main physical parameters of the flames investigated in this study are summarized in Table 2.1, where P is the thermal power of a single conical flame. For small flames stabilized above perforated plates, P corresponds to the total thermal power divided by the number of perforations. The other parameters

Table 2.1: *Main physical parameters for all premixed laminar conical flames explored in this study. Laminar burning velocities S_L are taken from Vagelopoulos and Egolfopoulos (1998). Flame thicknesses δ are taken from Yamaoka and Tsuji (1985).*

Name	Fuel	P (W)	R (mm)	ϕ	T_{ad} (K)	$\overline{T}_b$ (K)	S_L (m/s)	$\overline{\psi}$ (mm)	δ (mm)
FS1	CH_4	1855	11	1.00	2225	1522	0.38	0.70	1.00
FS2	C_3H_8	1807	11	0.91	2190	1530	0.38	0.65	0.84
FS4	CH_4	34.3	1.5	1.00	2225	1627	0.38	0.68	1.00
FS5	C_3H_8	33.6	1.5	0.91	2190	1543	0.38	0.71	0.84
FS6	C_3H_8	1094	11	0.75	1964	1395	0.28	1.12	1.18
FS7	CH_4	985	11	0.80	1997	1388	0.27	0.89	1.33
FS11	C_3H_8	1513	11	0.84	2100	1470	0.34	0.75	0.94
FS12	CH_4	1164	11	0.84	2055	1419	0.31	0.93	1.23
FS13	C_3H_8	28.1	1.5	0.84	2100	1466	0.34	1.16	0.94
FS14	CH_4	21.6	1.5	0.84	2055	1466	0.31	0.85	1.23
FS15	CH_4	748	7	1.00	2225	1492	0.38	1.21	1.00
FS16	C_3H_8	729	7	0.91	2190	1481	0.38	1.12	0.84
FS17	C_3H_8	613	7	0.84	2100	1413	0.34	1.58	0.94
FS18	CH_4	472	7	0.84	2055	1403	0.31	1.35	1.23
FS19	CH_4	32.4	1.5	0.98	2207	1571	0.36	0.75	1.02
FS20	C_3H_8	34.7	1.5	0.93	2206	1573	0.38	0.53	0.84
FS21	CH_4	25.2	1.5	0.88	2108	1503	0.31	0.85	1.12
FS23	CH_4	14.3	1	0.98	2207	1543	0.36	0.75	1.02
FS24	C_3H_8	15.2	1	0.93	2206	1481	0.38	1.00	0.84
FS25	CH_4	15.1	1	1.00	2225	1565	0.38	0.88	1.00
FS26	C_3H_8	14.9	1	0.91	2190	1447	0.38	1.12	0.84
FS27	CH_4	9.6	1	0.84	2055	1441	0.31	0.71	1.23

are: R the burner outlet radius, ϕ the equivalence ratio and T_{ad} and $\overline{T}_b$ the adiabatic flame temperature (computed with a GRI-MECH 3.0 mechanism) and burnt gases temperature (measured with a thermocouple) respectively. The laminar burning velocities S_L are taken from a previous experimental investigation (Vagelopoulos and Egolfopoulos 1998). Flame stand-off distances $\overline{\psi}$ are assessed from steady-state flame pictures. Flame thicknesses δ are also taken from a previous study (Yamaoka and Tsuji 1985).

One way to obtain the frequency response of a flame is to force it with a loudspeaker that generates harmonic sound waves over a wide range of forcing frequencies. However, if the laminar burning velocity is too low or too high, the flame may be blown off or may flash back inside the injector respectively. Ethylene/air flames were initially considered in this study but they were too sensitive to flashback when submitted to harmonic forcing and were thus not retained. These flames are not included in Table 2.1.

Steady-state pictures of all flames described in Table 2.1 are presented in Figs. 2.3, 2.4, 2.5 and 2.6 for decreasing burner outlet radii $R = 11$ mm, $R = 7$ mm, $R = 1.5$ mm and $R = 1$ mm. For each flame, the ICCD picture obtained without interferometric filter is depicted on the left and the associated Abel deconvolution (Abel 1826) is depicted on the right.

2.4 Conclusion

The experimental setup and the associated diagnostics used to investigate the frequency response of large and small premixed laminar conical flames was first introduced. Then, the operating conditions corresponding to twenty-two methane/air and propane/air flames stabilized above four different burner outlets of decreasing radii $R = 11$ mm, $R = 7$ mm, $R = 1.5$ mm and $R = 1$ mm and featuring different equivalence ratios ranging from $\phi = 0.75$ to $\phi = 1.00$ were defined. Steady-state pictures of all these flames were taken using an ICCD camera with and without an interferometric filter corresponding to the OH* chemiluminescence wavelength.

Since the flame tip half angle $\overline{\alpha}$ was already identified as an important dimensionless parameter controlling the flame frequency response in previous studies, its impact was not considered in this work. As a consequence, the flame tip half angle away from the flame base and flame tip was always fixed to $\overline{\alpha} = 14.5°$ corresponding to a steady flame aspect ratio $\overline{h}/R = 4$ for large flames.

It is now worth examining whether the frequency response of large and small premixed laminar conical flames assessed using the experimental setup presented in this chapter are consistent with the models introduced in Chapter 1.

Figure 2.3: *Premixed laminar conical flames stabilized above the burner outlet of radius R = 11 mm. For each flame, the ICCD picture without interferometric filter (Left) and the corresponding Abel deconvolution (Right) are represented.* ***FS1****: CH_4/air flame with $\phi = 1.00$.* ***FS2****: C_3H_8/air flame with $\phi = 0.91$.* ***FS6****: C_3H_8/air flame with $\phi = 0.75$.* ***FS7****: CH_4/air flame with $\phi = 0.80$.* ***FS11****: C_3H_8/air flame with $\phi = 0.84$.* ***FS12****: CH_4/air flame with $\phi = 0.84$.*

Figure 2.4: *Premixed laminar conical flames stabilized above the burner outlet of radius $R = 7$ mm. For each flame, the ICCD picture without interferometric filter (Left) and the corresponding Abel deconvolution (Right) are represented.* ***FS15****: CH_4/air flame with $\phi = 1.00$.* ***FS16****: C_3H_8/air flame with $\phi = 0.91$.* ***FS17****: C_3H_8/air flame with $\phi = 0.84$.* ***FS18****: CH_4/air flame with $\phi = 0.84$.*

Figure 2.5: *Premixed laminar conical flames stabilized above the perforated plate with 21 holes of radius R = 1.5 mm. For each flame, the ICCD picture without interferometric filter (Left) and the corresponding Abel deconvolution (Right) are represented.* ***FS4****: CH_4/air flame with $\phi = 1.00$.* ***FS5****: C_3H_8/air flame with $\phi = 0.91$.* ***FS13****: C_3H_8/air flame with $\phi = 0.84$.* ***FS14****: CH_4/air flame with $\phi = 0.84$.* ***FS19****: CH_4/air flame with $\phi = 0.98$.* ***FS20****: C_3H_8/air flame with $\phi = 0.93$.* ***FS21****: CH_4/air flame with $\phi = 0.88$.*

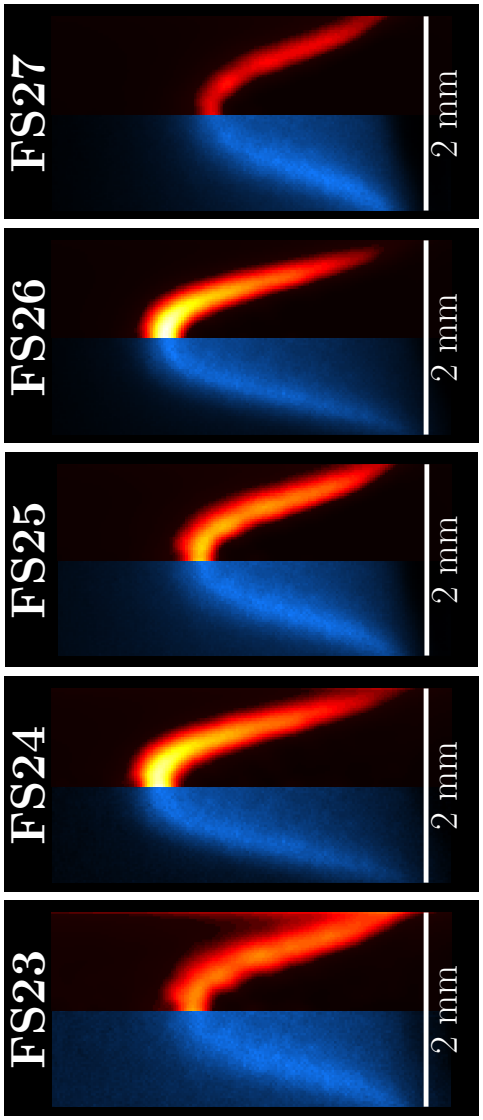

Figure 2.6: *Premixed laminar conical flames stabilized above the perforated plate with 25 holes of radius $R = 1$ mm. For each flame, the ICCD picture without interferometric filter (Left) and the corresponding Abel deconvolution (Right) are represented.* ***FS23****: CH_4/air flame with $\phi = 0.98$.* ***FS24****: C_3H_8/air flame with $\phi = 0.93$.* ***FS25****: CH_4/air flame with $\phi = 1.00$.* ***FS26****: C_3H_8/air flame with $\phi = 0.91$.* ***FS27****: CH_4/air flame with $\phi = 0.84$.*

Chapter 3

Comparison Between Predicted and Measured Flame Transfer Functions

The experimental FTF of premixed laminar conical flames are compared with analytical expressions when the burner outlet radius is reduced. The steady flame aspect ratio is kept constant corresponding to a steady flame tip half angle $\bar{\alpha} = 14.5°$ and the radius of the injector is reduced from $R = 11$ mm to $R = 1.5$ mm. The three different velocity perturbation models introduced in Chapter 1 are tested, with and without the additional model accounting for the flame anchoring point dynamics. For the largest flames with $R = 11$ mm and 7 mm, the best agreement is found for a FTF model with an incompressible convective velocity disturbance in the fresh reactants stream. The anchoring point dynamics has only a weak influence on the FTF gain and phase lag plots of these flames. For the smallest flames with $R = 1.5$ mm, a FTF model based on a uniform flow perturbation yields the best match with experiments for the phase lag plot, but none of the three velocity perturbation models reproduce the FTF gain evolution as measured in experiments. Including the contribution of the anchoring point dynamics to the FTF models for the small flames significantly changes the FTF gain predictions, but it does not allow to reproduce the main features observed in the measured gain curves and the phase lag predictions worsen.

3.1 Introduction

From the literature review presented in Chapter 1, the following parameters are known to be relevant when analyzing the frequency response of premixed laminar conical flames to flowrate disturbances:

- The reduced frequency $\omega_* = \omega R/(S_L \cos\bar{\alpha})$ (Fleifil et al. 1996; Ducruix

et al. 2000).

- The steady flame tip half angle $\bar{\alpha}$ or equivalently, the steady flame height relative to the burner exit radius $\bar{h}/R$ (Schuller et al. 2003a; Preetham et al. 2008).

- The acoustic forcing level $|u'|/\bar{u}$ (Preetham et al. 2008; Durox et al. 2009; Karimi et al. 2009).

The impact of these parameters has been studied extensively and will not be considered in the present work. Hence, all flames studied here have the same relative height $\bar{h}/R = 4$ or equivalently the same flame tip half angle $\bar{\alpha} = 14.5°$ for steady-state conditions. The acoustic modulation level is always chosen in the linear regime. Except if mentioned otherwise, the root-mean-square (RMS) value of the acoustic forcing level is equal to $|u'|/\bar{u} = 0.10$. The measured FTF gains and phase lags are generally plotted as functions of the reduced frequency ω_*.

On the other hand, it was shown in Chapter 1 that experimental investigations exploring the effects of more complex physical parameters on the FTF of premixed laminar conical flames still remain scarce. As a consequence, the impact of the following physical phenomena is worth investigating:

- Preferential diffusion, that controls heat and molecular transport in the vicinity of the reaction layer, is analyzed by modifying the fuel. Methane is used to investigate flames with a Lewis number Le ~ 1. Propane is used to investigate flames with Le > 1.

- Flame size effects, that modify heat losses to the burner and change the proportion of fresh gases affected by heat and mass transport near the flame reaction layer, are analyzed by modifying the injector hole size. Results are compared when the ratio δ/R progressively increases, where δ is the thermal flame thickness and R is the injector radius.

- Thermal dilatation of the burnt gases, that acts as a feedback on the hydrodynamic velocity field upstream of the flame front, is analyzed by modifying the equivalence ratio ϕ of the injected reactants. Results are examined as a function of the ratio $T_* = T_{ad}/\overline{T}_u - 1$, where T_{ad} is the adiabatic flame temperature and $\overline{T}_u$ is the unburnt gas temperature.

In Chapter 1, the main findings regarding the frequency response of premixed laminar conical flames were presented along with a detailed description of various analytical FTF models. Nonetheless, a systematic attempt to validate these models with experiments when the injector size is varied and for different

Table 3.1: *Summary of all flames investigated in this chapter.*

Name	Fuel	R (mm)	ϕ	Name	Fuel	R (mm)	ϕ
FS4	CH_4	1.5	1.00	**FS14**	CH_4	1.5	0.84
FS5	C_3H_8	1.5	0.91	**FS15**	CH_4	7	1.00
FS6	C_3H_8	11	0.75	**FS16**	C_3H_8	7	0.91
FS7	CH_4	11	0.80	**FS17**	C_3H_8	7	0.84
FS13	C_3H_8	1.5	0.84	**FS18**	CH_4	7	0.84

fuels and equivalence ratios has yet to be performed. This constitutes the main objective of the present chapter.

The scope of this chapter is restricted to fully premixed laminar conical CH_4/Air or C_3H_8/Air flames stabilized above the cylindrical injectors described in Chapter 2. All flames share the same steady flame tip half angle $\bar{\alpha} = 14.5°$ and the equivalence ratio remains unaltered since the flames are submitted to flowrate disturbances only. The frequency response of ten different flames, described in Table 3.1, is explored in this chapter.

More information about these flames may be found in Table 2.1. The FTF gain and phase lag of all premixed laminar conical flames retained here are first plotted as functions of the forcing frequency in Fig. 3.1-(Top). Both the gain and phase lag curves depicted in this figure highly depend on the burner outlet radius R, equivalence ratio ϕ and type of fuel (CH_4 or C_3H_8). As a consequence, the analytical models describing the FTF gain and phase lag have to depend on these physical quantities.

It is reminded that the FTF of a premixed laminar conical flame can be expressed as the sum of two contributions, as seen in Chapter 1: $F = F_A + F_B$ where F_A depends on the type of the velocity perturbation model used to describe the flow upstream of the flame front and F_B depends on the type of model used to describe the flame anchoring point dynamics. In this chapter, the analytical predictions for F_A according to the uniform (UNI), convective (CON) and incompressible convective (INC) velocity perturbation models introduced in Chapter 1 are compared with FTF measurements of premixed laminar conical flames obtained with the experimental setup presented in Chapter 2 when the injector size is reduced.

The contribution of the flame anchoring point dynamics through the expression of F_B presented in Sec. 1.3.2 is either accounted for (plots denoted by $F_A + F_B$)

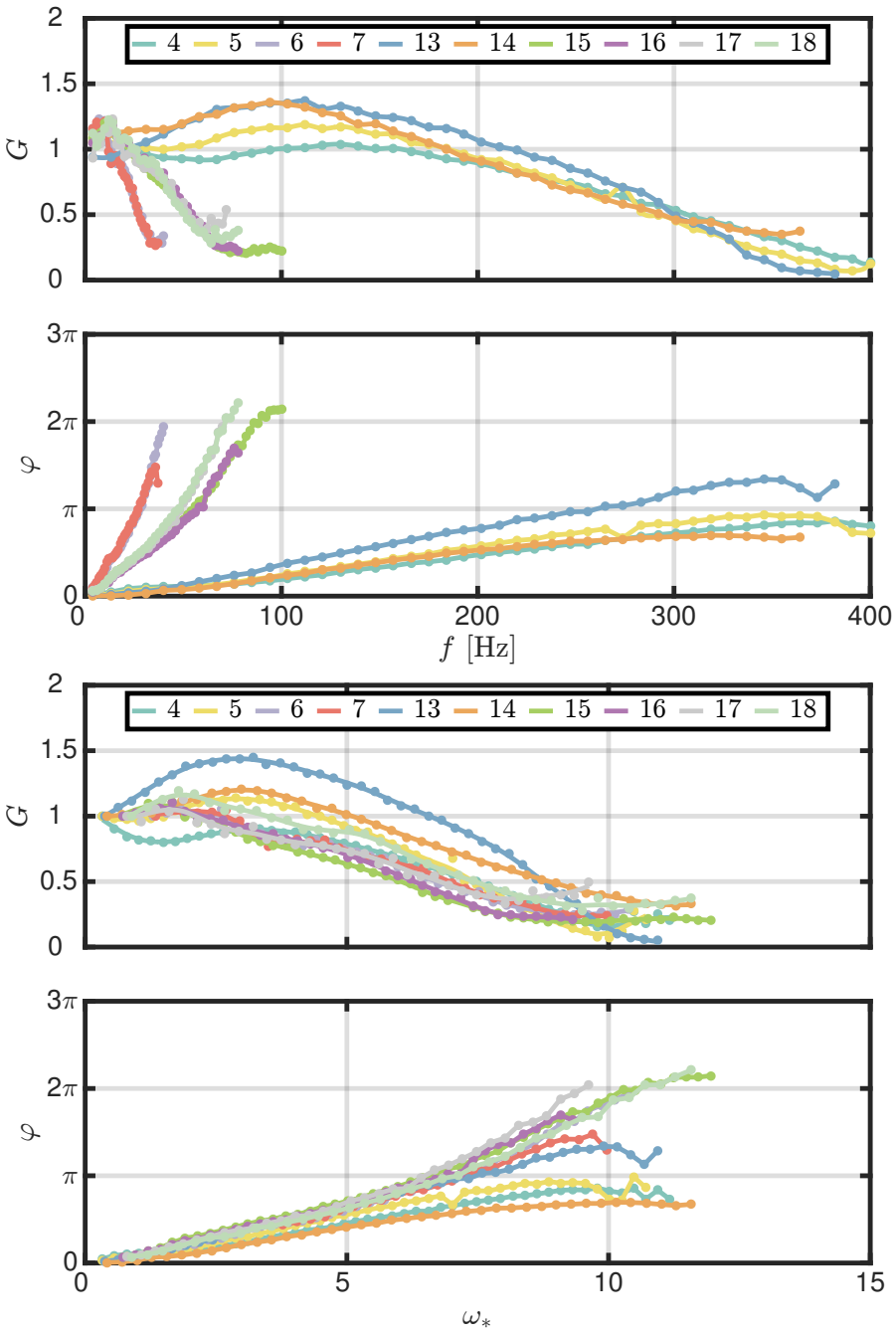

Figure 3.1: *FTF gain (Top subplot) and phase lag (Bottom subplot) as functions of the forcing frequency f (Top plots) and reduced frequency ω_* (Bottom plots).* ***FS4****: Turquoise -* ***FS5****: Yellow -* ***FS6****: Gray-blue -* ***FS7****: Red -* ***FS13****: Blue -* ***FS14****: Orange -* ***FS15****: Green -* ***FS16****: Violet -* ***FS17****: Gray -* ***FS18****: Light green.*

or neglected (plots denoted by F_A). Results are plotted as functions of the dimensionless parameter ω_* and for a prescribed steady flame tip half angle $\overline{\alpha}$. These parameters were identified as relevant parameters in the three velocity perturbation models presented in Chapter 1 (Fleifil et al. 1996; Ducruix et al. 2000; Schuller et al. 2003a; Preetham et al. 2008; Cuquel 2013; Orchini and Juniper 2016). All the physical parameters needed to determine ω_*, $F_A(\omega_*, \overline{\alpha})$ and F_B are summarized in Table 2.1. The corresponding steady-state pictures of all ten flames explored here are presented in Chapter 2.

It is worth recalling that the theoretical low frequency limit of the FTF gain of a premixed flame submitted to flowrate disturbances at a constant equivalence ratio is $G = 1$ (Polifke and Lawn 2007). However, since the flame stand-off distance varies from 0.7 to 1.3 mm depending on the operating conditions, while the LDV measurement volume is always located 1 mm away from the burner outlet, the FTF gain at zero frequency ranges from 0.9 to 1.1, as shown in Fig. 3.1-(Top). This is due to the fact that the amplitude of the acoustic velocity decreases progressively in the axial direction in the fresh gases region of a conical flame (Birbaud et al. 2006). This issue is tackled by dividing the gain by its low-frequency value. The corresponding gain variation is always lower than 10%. The phase plot are left unchanged since the involved distances are small compared to the convective wavelengths. This observation raises the question of the impact of the exact velocity measurement location on the FTF. This issue is scrutinized in the second part of this manuscript for premixed confined turbulent flames.

Based on this analysis, the FTF gain and phase lag of all ten flames presented earlier are now plotted as functions of the reduced frequency ω_* in Fig. 3.1-(Bottom). By comparing this figure with Fig. 3.1-(Top), it is clear that the reduced frequency ω_* is a relevant dimensionless parameter when studying the FTF of premixed laminar conical flames. However, the FTF gain and phase lag plots are not superimposed for all flames. For instance, some flames feature FTF gains larger than 1 for certain frequencies while this feature is not observed for the majority of the flames. The FTF phase lags plotted as functions of the reduced frequency also differ depending on the flame. Since all three analytical models for F_A depend on the reduced frequency ω_* only when the steady flame tip half angle $\overline{\alpha}$ is prescribed, this observation advocates for the use of an anchoring point dynamics model.

Results are first presented for the injector featuring an outlet radius $R = 11$ mm in Sec. 3.2, followed by the injector with $R = 7$ mm in Sec. 3.3. Finally, results obtained for small conical flames stabilized over the perforated plate with 21 holes of radius $R = 1.5$ mm are presented in Sec. 3.4.

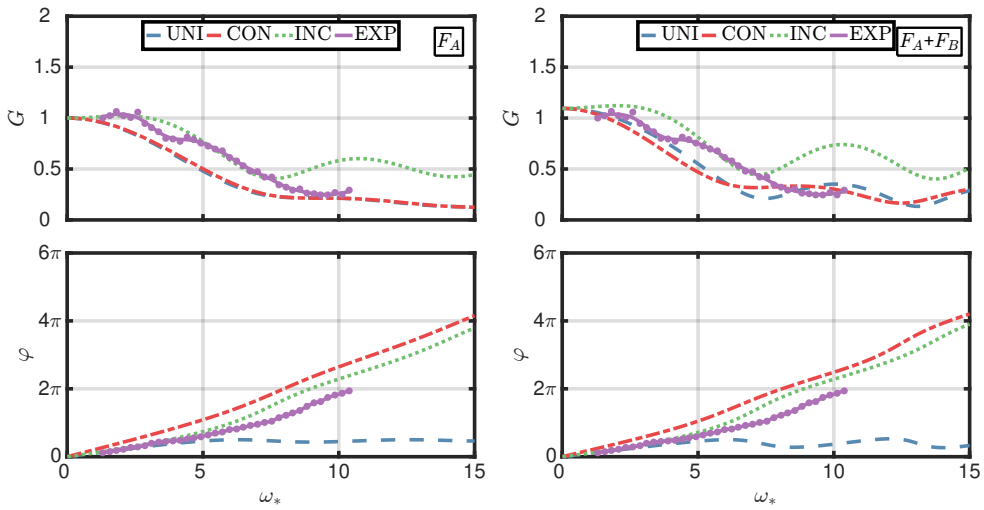

Figure 3.2: ***FS6****: C_3H_8/air flame with an equivalence ratio $\phi = 0.75$ stabilized over an injector of radius $R = 11$ mm. Velocity perturbation models : UNI (blue), CON (red) and INC (green). Experiments : EXP (purple). Left : F_A. Right : $F_A + F_B$.*

3.2 Results for a burner outlet of radius R=11 mm

The frequency responses of propane/air (**FS6**) and methane/air (**FS7**) premixed laminar conical flames stabilized above the injector of radius $R = 11$ mm are investigated first. The contribution F_A from the three analytical models are plotted in Fig. 3.2-(Left) and Fig. 3.3-(Left) along with FTF measurements.

The incompressible convective (INC) velocity perturbation model yields the best match for both the gain and the phase lag plots in Fig. 3.2-(Left) and Fig. 3.3-(Left). For $3 < \omega_* < 5$, small differences are observed between the FTF gain predictions and measurements, where the gain slightly decreases and subsequently increases. The incompressible convective (INC) model also predicts a minimum gain $G \sim 0.4$ followed by an increase up to $G \sim 0.6$ for $\omega_* = 11$ while the measured FTF continues to drop until the gain reaches $G = 0.2$ at $\omega_* = 10$ for both flames **FS6** and **FS7**. This problem at high frequencies was already identified in the past and can be solved by prescribing a spatial decay of the flow perturbations in the flow direction (Schuller et al. 2002). Except for these minor deviations, the agreement between analytical and experimental FTF gain plots is very satisfactory when the incompressible convective (INC) velocity perturbation model is considered.

Regarding the phase lag plots, the agreement between calculations with the incompressible convective model and the measured FTF phase lag is almost perfect for $\omega_* < 5$, followed by an increasing gap between theory and measurements. Nevertheless, the incompressible convective velocity perturbation model

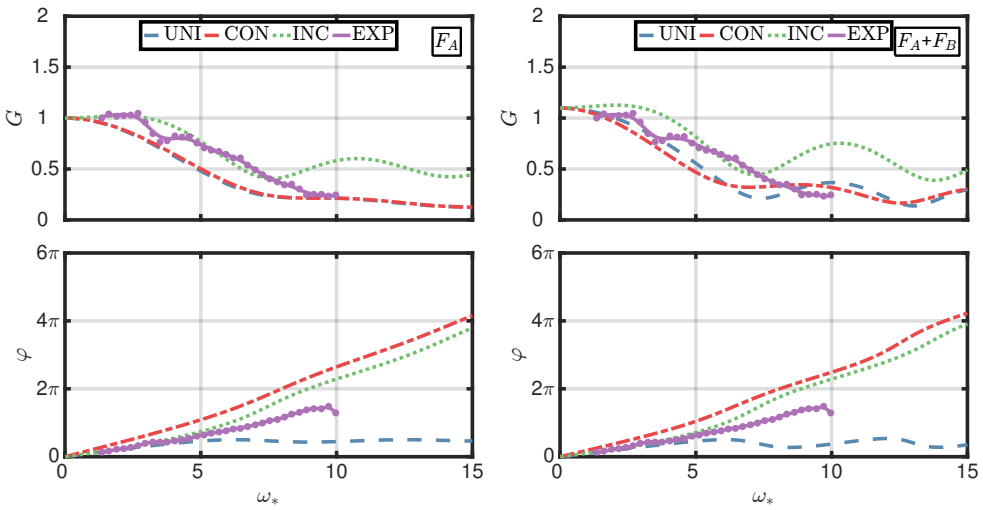

Figure 3.3: ***FS7****: CH_4/air flame with an equivalence ratio $\phi = 0.80$ stabilized over an injector of radius $R = 11$ mm. Velocity perturbation models : UNI (blue), CON (red) and INC (green). Experiments : EXP (purple). Left : F_A. Right : $F_A + F_B$.*

remains the most accurate model in terms of FTF phase lag prediction for both the propane/air and methane/air premixed laminar conical flames stabilized on the largest injector.

Analytical FTF predictions including the effects of the anchoring point dynamics $F_A + F_B$ as shown in Fig. 3.2-(Right) and Fig. 3.3-(Right) are now examined. Several changes are observed. First, the quasi-steady limit of the analytical FTF gain differs from unity for both flames **FS6** and **FS7**. The deviation is small but this is in contradiction with theory (Polifke and Lawn 2007). At this point, it is worth noting that all velocity models studied here, namely the uniform, convective and incompressible convective models, reach the theoretical quasi-steady limit when the anchoring point dynamics is not considered. This is shown in all FTF gain plots corresponding to contribution F_A alone. But since F_B does not tend toward 0 at low frequencies, the sum $F_A + F_B$ cannot tend toward 1 in the low-frequency limit and the theoretical quasi-steady limit is not respected.

Additionally, the gain predictions according to $F_A + F_B$ at high frequencies in Fig. 3.2-(Right) and Fig. 3.3-(Right) are larger than those according to F_A in Figs. 3.2-(Left) and 3.3-(Left) that were already too large compared to measurements (though it is possible that the measured FTF does not capture the gain rebound because of the lack of data in the high frequency range). Finally, the experimental gain curves plotted in Figs. 3.2-(Right) and 3.3-(Right) do not match with any analytical model curve at low reduced frequencies $\omega_* < 10$.

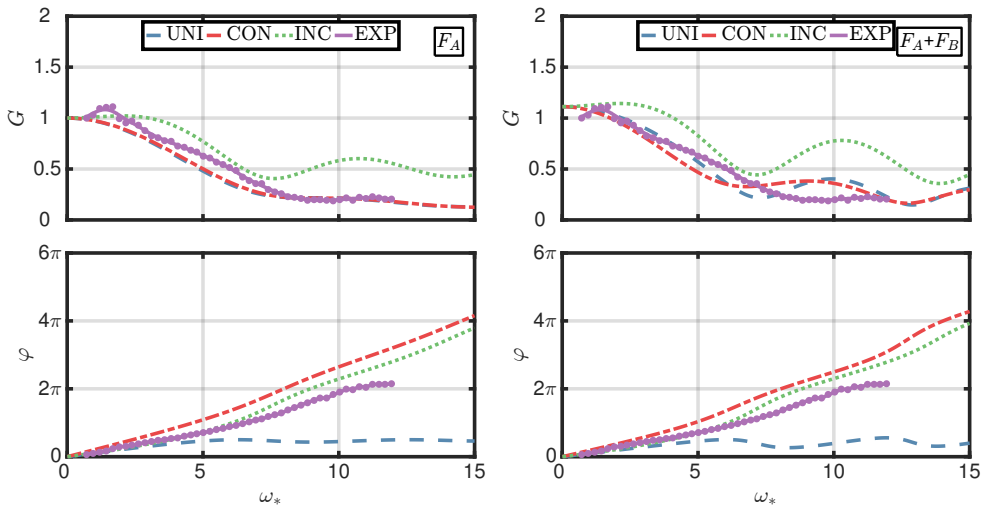

Figure 3.4: ***FS15****: CH_4/air flame with an equivalence ratio $\phi = 1.00$ stabilized over a burner outlet of radius $R = 7$ mm. Velocity perturbation models : UNI (blue), CON (red) and INC (green). Experiments : EXP (purple). Left : F_A. Right : $F_A + F_B$.*

As a conclusion, the anchoring point dynamics model used in addition to the velocity perturbation model is unnecessary and even detrimental when predicting the frequency response of large premixed laminar conical flames. This type of anchoring point dynamics model was shown to be more adapted for the study of the frequency response of small premixed laminar conical flames (Kedia et al. 2011) and large premixed laminar conical flames at high frequencies (Cuquel et al. 2013a). At the relatively low reduced frequencies and forcing levels investigated in this study, the contribution of the anchoring point dynamics to the FTF of propane/air and methane/air large premixed laminar conical flames does not improve the FTF predictions.

3.3 Results for a burner outlet of radius R=7 mm

The next step is to analyze the frequency response of premixed laminar conical flames stabilized over a smaller injector of radius $R = 7$ mm. Results for the transfer functions of **FS15**, **FS16**, **FS17** and **FS18** are plotted in Figs. 3.4, 3.5, 3.6 and 3.7 respectively. Overall, predictions associated with the incompressible convective velocity perturbation model without the flame anchoring point dynamics model yield the best match with the measured FTF gain and phase lag plots. Predictions associated with this model for the FTF phase lag perfectly match measurements for $\omega_* \leq 5$ for both propane/air and methane/air flames. The measured phase lag of **FS17** represented in Fig. 3.6-(Left) is even reproduced by this model for all reduced frequencies investigated.

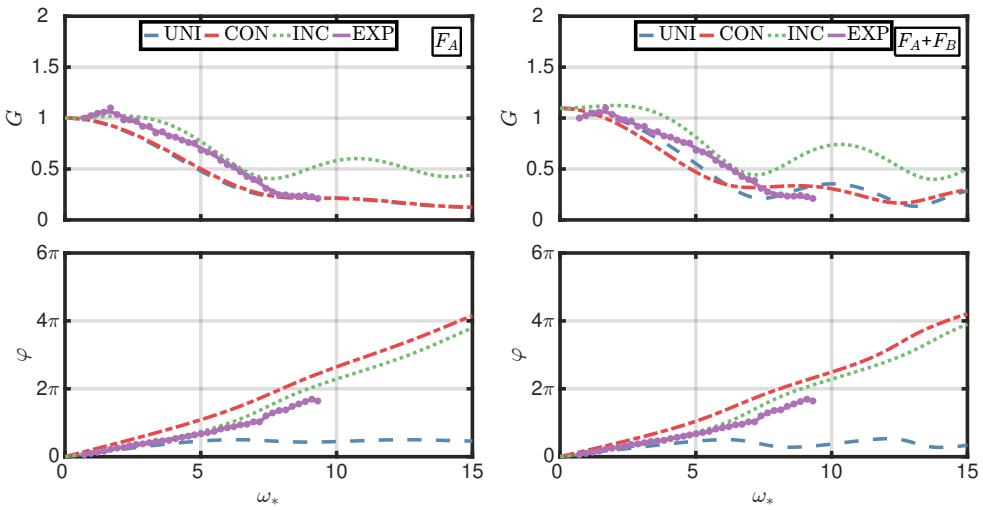

Figure 3.5: ***FS16****: C_3H_8/air flame with an equivalence ratio $\phi = 0.91$ stabilized over a burner outlet of radius $R = 7$ mm. Velocity perturbation models : UNI (blue), CON (red) and INC (green). Experiments : EXP (purple). Left : F_A. Right : $F_A + F_B$.*

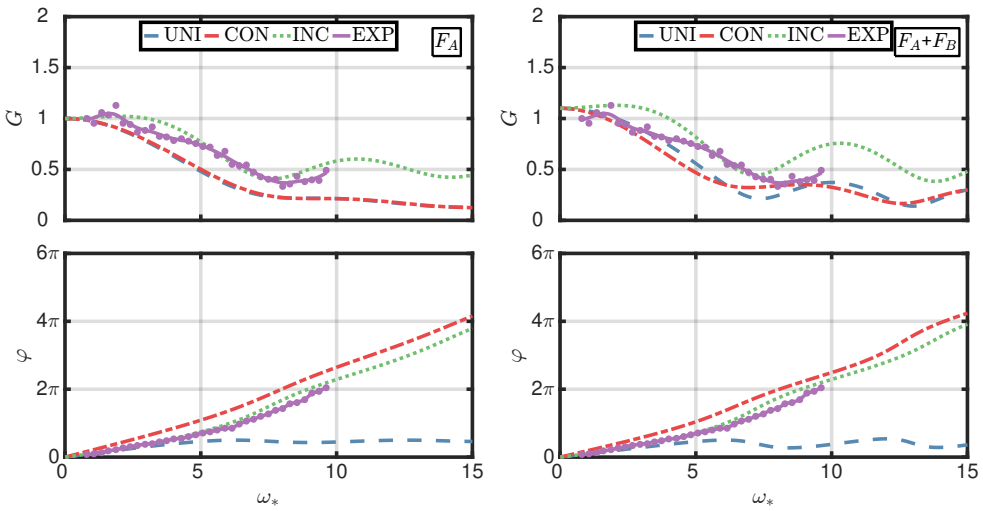

Figure 3.6: ***FS17****: C_3H_8/air flame with an equivalence ratio $\phi = 0.84$ stabilized over a burner outlet of radius $R = 7$ mm. Velocity perturbation models : UNI (blue), CON (red) and INC (green). Experiments : EXP (purple). Left : F_A. Right : $F_A + F_B$.*

The FTF gain plots obtained for propane/air flames (**FS16** and **FS17**) represented in Fig. 3.5-(Left) and Fig. 3.6-(Left) are in very good agreement with the incompressible convective model when the anchoring point dynamics is neglected except in the high frequency range in Fig. 3.5-(Left) where the uniform and convective models yield better results.

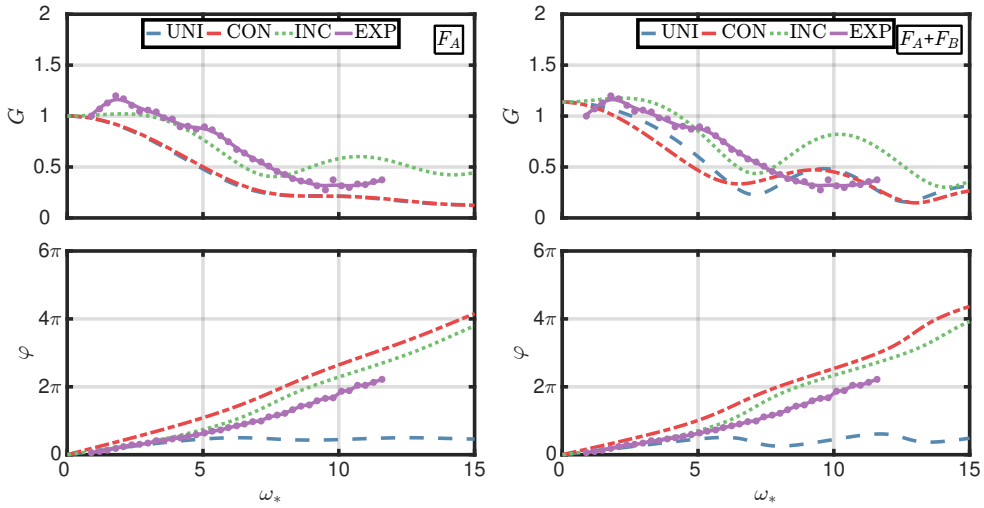

Figure 3.7: ***FS18****: CH_4/air flame with an equivalence ratio $\phi = 0.84$ stabilized over a burner outlet of radius $R = 7$ mm. Velocity perturbation models : UNI (blue), CON (red) and INC (green). Experiments : EXP (purple). Left : F_A. Right : $F_A + F_B$.*

On the other hand, the FTF gain plots obtained for methane/air flames (**FS15** and **FS18**) represented in Fig. 3.4-(Left) and Fig. 3.7-(Left) are not fully reproduced by any velocity perturbation model. For $\omega_* \leq 7$, the uniform and convective models underestimate the FTF gain. The measured FTF gain behavior is better reproduced in Fig. 3.7-(Left) in this frequency range by considering the incompressible convective model. Slight differences are found at very low reduced frequencies $\omega_* \simeq 2$ in Fig. 3.4-(Left) and Fig. 3.7-(Left) where small amplitude overshoots are observed in the measured FTF gain but not predicted by any model. Predictions associated with the incompressible convective model also slightly overestimate the gain in the intermediate frequency range for the stoichiometric methane/air flame in Fig. 3.4-(Left). The agreement is better for the lean methane/air mixture in Fig. 3.7-(Left). At higher frequencies, the incompressible convective model again largely overestimates the FTF gain. Once again, in this frequency range, the uniform and convective models yield better results.

Once more, adding the contribution of the flame anchoring point dynamics F_B to the flame transfer function does not improve the predictions as shown in Fig. 3.4-(Right), Fig. 3.5-(Right), Fig. 3.6-(Right) and Fig. 3.7-(Right). The phase lag plots of the different models for $F_A + F_B$ remain essentially unaltered compared to Fig. 3.4-(Left), Fig. 3.5-(Left), Fig. 3.6-(Left) and Fig. 3.7-(Left). The same issues that were already identified in the FTF gain plots for the injector of radius $R = 11$ mm still apply: the theoretical quasi-steady limit is not reached by any model when the anchoring point dynamics is considered. However, the agreement between the modeled and measured FTF gains is much

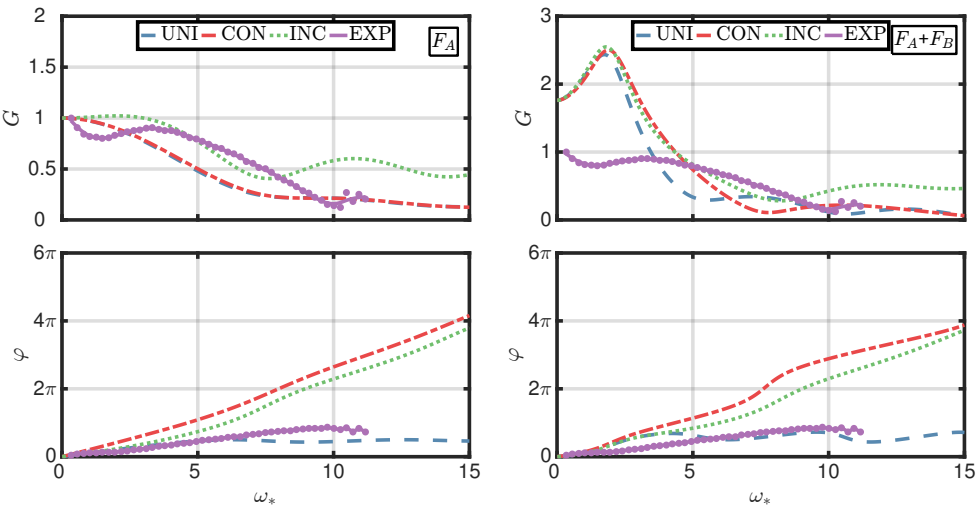

Figure 3.8: ***FS4****: CH_4/air flame with an equivalence ratio $\phi = 1.00$ stabilized over a perforated plate with 21 holes of radius $R = 1.5$ mm. Velocity perturbation models : UNI (blue), CON (red) and INC (green). Experiments : EXP (purple). Left : F_A. Right : $F_A + F_B$.*

better for the uniform and convective models in Fig. 3.4-(Right) and Fig. 3.5-(Right) when $\omega_* \leq 7$. The FTF gain behavior for $\omega_* > 7$ is less well captured by the three models tested when the anchoring point dynamics is considered. The worst model at high frequencies is again the incompressible convective model used along with the anchoring point dynamics model that largely overestimates the measured FTF gain for **FS15**, **FS16**, **FS17** and **FS18**.

3.4 Results for a perforated plate with 21 holes of radius R=1.5 mm

The last step is to analyze the frequency response of small flames corresponding to **FS4**, **FS5**, **FS13** and **FS14**. Results are plotted in Figs. 3.8, 3.9, 3.10 and 3.11 respectively. These flames are stabilized on a perforated plate with 21 holes of radius $R = 1.5$ mm distributed over a square pattern of size $d = 4$ mm, as shown in Fig. 2.2-(c). It is known that the dynamics of premixed laminar conical flames may be altered by neighboring flames if they are too close (Cuquel et al. 2013b). It was demonstrated that this effect can be neglected as long as the burnt gases can fully expand (Cuquel et al. 2013a) which can be assessed by using the following dimensionless parameter:

$$C_b = \frac{R}{R_1}\left(1 - \frac{E-1}{E}\cos\bar{\alpha}\right)^{-1/2} \tag{3.1}$$

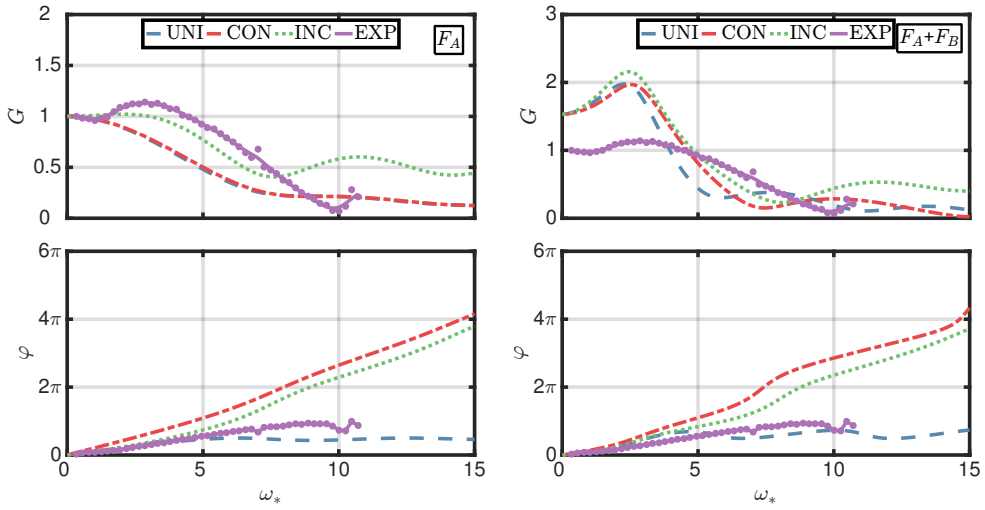

Figure 3.9: ***FS5****: C_3H_8/air flame with an equivalence ratio $\phi = 0.91$ stabilized over a perforated plate with 21 holes of radius $R = 1.5$ mm. Velocity perturbation models : UNI (blue), CON (red) and INC (green). Experiments : EXP (purple). Left : F_A. Right : $F_A + F_B$.*

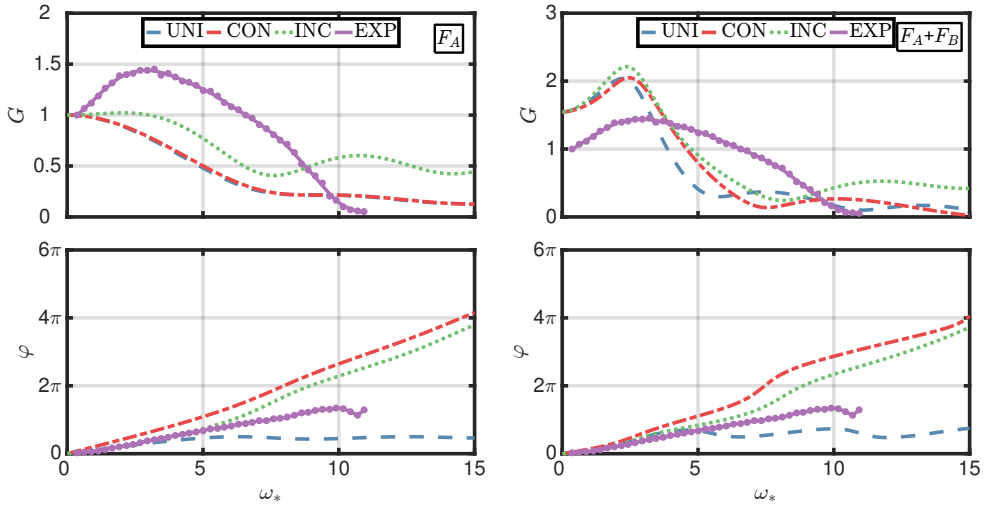

Figure 3.10: ***FS13****: C_3H_8/air flame with an equivalence ratio $\phi = 0.84$ stabilized over a perforated plate with 21 holes of radius $R = 1.5$ mm. Velocity perturbation models : UNI (blue), CON (red) and INC (green). Experiments : EXP (purple). Left : F_A. Right : $F_A + F_B$.*

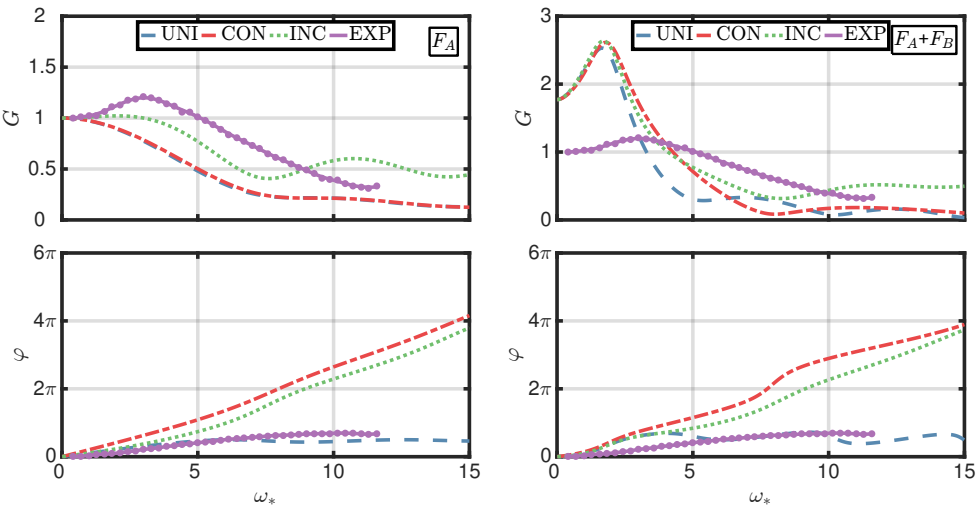

Figure 3.11: ***FS14****: CH_4/air flame with an equivalence ratio $\phi = 0.84$ stabilized over a perforated plate with 21 holes of radius $R = 1.5$ mm. Velocity perturbation models : UNI (blue), CON (red) and INC (green). Experiments : EXP (purple). Left : F_A. Right : $F_A + F_B$.*

where R is the burner outlet radius and R_1 is an equivalent radius such that $\pi R_1^2 = d^2$. Moreover, $E = \bar{\rho}_u/\bar{\rho}_b = \overline{T}_b/\overline{T}_u$ is the volumetric expansion ratio and $\bar{\alpha}$ denotes the steady flame tip half angle.

When $C_b \geq 1$, the fresh reactant stream is accelerated in the axial direction because the burnt gases cannot fully expand due to the limited available space. This in turn leads to elongated flames with altered Flame Transfer Functions (Cuquel et al. 2013a). **FS4**, **FS5**, **FS13** and **FS14** yields values in the range $C_b = 1.3 - 1.4$, a value slightly higher than unity. Nevertheless, the flame angle away from the flame tip and flame leading edge are kept constant and equal to $\bar{\alpha} = 14.5°$ in these experiments so that this effect can be neglected. This is confirmed by the steady-state flame pictures obtained using the ICCD camera and presented in Chapter 2.

Moreover, the thin flame assumption is necessary in order to use the kinematic models presented in Chapter 1. Even though this assumption can be debated in the case of small flames stabilized above perforated plates, it is worth examining whether kinematic models can reproduce some of the features of the frequency response of these flames.

Measurements and predictions according to the FTF models are represented in Fig. 3.8-(Left), Fig. 3.9-(Left), Fig. 3.10-(Left) and Fig. 3.11-(Left) when the anchoring point dynamics is not considered. The frequency response of these small premixed laminar conical flames stabilized over a perforated plate largely

differs from those measured in Figs. 3.2-3.7 that were obtained for larger injectors. It is also interesting to note that the FTF gain and phase lag of these small flames are significantly affected when the fuel or equivalence ratio are modified, as opposed to the FTF gain and phase lag of larger flames that remained roughly identical when these parameters were varied.

Predictions according to the incompressible convective (INC) model without the anchoring point dynamics model do not yield the best match with experiments anymore. This model rapidly leads to an over-prediction of the FTF phase lag for $\omega_* > 2$ for both propane/air and methane/air flames. This observation is also valid for the convective (CON) model. On the other hand, measurements of the FTF phase lag of **FS4** and **FS14** are accurately reproduced by the theoretical expression corresponding to the uniform (UNI) model for all reduced frequencies investigated. The FTF phase lag of **FS5** and **FS13** are also correctly reproduced by the uniform model up to $\omega_* = 5$.

Regarding the FTF gain plots, predictions according to the incompressible convective model without the anchoring point dynamics model are the closest to the experimental values. Nevertheless, the differences between theory and experiments are much larger than for the flames stabilized above the larger injectors of radius $R = 11$ mm or $R = 7$ mm, especially for **FS13**. Moreover, the local extrema of the gain curves and their associated reduced frequencies do not match those observed in experiments. It is clear that an additional mechanism needs to be accounted for in order to reproduce the evolution of the FTF of small premixed laminar conical flames.

In an attempt to reduce the gap between experiments and theoretical predictions, results for the analytical transfer functions including the contribution of the anchoring point dynamics are investigated in Fig. 3.8-(Right), Fig. 3.9-(Right), Fig. 3.10-(Right) and Fig. 3.11-(Right). It has been shown that the motion of the flame leading edge largely contributes to heat release rate fluctuations in the case of small flames (Rook et al. 2002; Kedia et al. 2011). It has also been shown that the transfer function of planar flames stabilized over porous materials or perforated plates features an amplification behavior with gain values largely exceeding unity at relatively low forcing frequencies (Schreel et al. 2002; de Goey et al. 2011), as shown in Fig. 1.9.

It is obvious from Fig. 3.8-(Right), Fig. 3.9-(Right), Fig. 3.10-(Right) and Fig. 3.11-(Right) that the model accounting for the flame anchoring point dynamics significantly alters the analytical FTF gain predictions. The amplification behavior expected in the low-frequency range is reproduced by the analytical models. However, the reduced frequencies associated with the local gain maxima are not well captured by the different models. The values for these gain overshoots are also largely overestimated. Finally, the theoretical

quasi-steady limit for the FTF gain is once again not respected. Overall, the analytical FTF gain plots do not yield the correct trend identified in the FTF gain measurements depicted in Figs. 3.8-3.11. On the other hand, the analytical phase lag predictions barely change when the contribution of the anchoring point dynamics is considered. In the end, none of the analytical models including the effects of the anchoring point dynamics is able to reproduce the evolution of the measured FTF.

3.5 Conclusion

The transfer functions of methane/air and propane/air premixed laminar conical flames stabilized over three different injectors with holes of radii $R = 11$ mm, $R = 7$ mm and $R = 1.5$ mm were investigated. FTF measurements were compared to analytical expressions obtained for three different velocity perturbation models with and without an additional model accounting for the flame anchoring point dynamics, as described in Chapter 1.

The three velocity perturbation models retained in this study were the uniform (UNI), convective (CON) and incompressible convective (INC) velocity perturbation models. Overall, the best match between the FTF gain and phase lag measurements was achieved with the INC model. However, when the size of the injector hole is reduced, predictions with this model became less accurate.

For the smallest flames stabilized over the perforated plate with holes of radius $R = 1.5$ mm, the phase lag plots were better reproduced by considering a uniform flow perturbation in the stream of reactants, corresponding to the UNI model. However, none of the explored analytical models yielded the correct trend in terms of gain for the injector with $R = 1.5$ mm. The analytical predictions did not improve when an additional contribution to the flame transfer function corresponding to the flame anchoring point dynamics was considered.

It was also shown that the theoretical model used here to describe the flame anchoring point dynamics (Cuquel et al. 2013a) led to a theoretical difficulty. The expected quasi-steady limit for the FTF gain was not achieved as the frequency went to zero. For all cases investigated, the gain at zero frequency was greater than unity. On the other hand, this additional contribution did allow to qualitatively reproduce some of the features of the FTF gain of small premixed laminar conical flames stabilized over matrix injectors. These flames feature an amplification behavior with FTF gain values exceeding unity at low frequencies. However, the analytical models explored here largely overestimated the values of these FTF gain maxima and did not accurately predict the resonant frequencies at which they occur.

It is finally concluded that wrinkles generated by the flame leading edge motion and then convected along the flame front are of minor importance when considering large flames stabilized above injectors of radii $R = 11$ mm and $R = 7$ mm, i.e. when the burner outlet radius is large with respect to the flame thickness. For smaller matrix injectors with holes of radius $R = 1.5$ mm, i.e. of the same order of magnitude of the flame thickness, the motion of the flame base needs to be considered, but the way it contributes to the Flame Transfer Function needs to be revisited.

Chapter 4

Impact of the Injector Size on the Flame Frequency Response

Flame Transfer Functions (FTF) of premixed laminar conical CH_4/air and C_3H_8/air flames submitted to flow rate modulations are investigated for a large set of injection conditions and burner outlet radii R. The steady flames investigated all feature the same flame tip half angle $\bar{\alpha} = 14.5°$. When R is large compared to the flame thickness δ, FTF measurements collapse to the same curve when they are plotted as a function of the reduced frequency $\omega_* = \omega R/(S_L \cos\bar{\alpha})$, where ω is the forcing angular frequency and S_L the laminar burning velocity. When the injector size is reduced and δ/R becomes sizable, additional parameters are needed to fully describe the FTF. The Lewis number Le and burnt gases temperature are shown to alter the low frequency evolution of the FTF of small flames stabilized above matrix injectors. These flames feature FTF gain values exceeding unity, called gain overshoots, at low reduced frequencies. Larger FTF gain overshoots are found as the injector size is reduced or as the flame temperature is reduced. A model accounting for the flame mutual interactions and unsteady heat and mass transfer at the flame base predicts the value of the reduced frequency ω_*^0 at which the FTF gain is maximum. This expression is shown to better match measurements than previous models that only consider unsteady heat and mass transfer between the flame base and the burner. Flame mutual interactions due to interpenetrating diffusion layers and unsteady heat transfer at the flame base both lead to FTF gain values exceeding unity but the former mechanism is largely dominant for the configurations investigated here. It is finally suggested that the FTF of flames stabilized over small injectors may be fully described by five dimensionless parameters: the reduced frequency ω_*, the flame tip half angle $\bar{\alpha}$, the Lewis number Le, the dimensioness stand-off distance $\bar{\psi}/R$ and the dimensionless flame thickness $\delta\cos\bar{\alpha}/R$.

4.1 Introduction

The objective of this chapter is to elucidate the differences between the frequency responses of large and small premixed laminar conical flames when submitted to flow rate perturbations in the linear regime, as observed in Chapter 3.

Once again, the effects of mixture composition inhomogeneities (Cho and Lieuwen 2005) are not considered. All flames have the same flame tip half angle $\bar{\alpha} = 14.5°$ in steady-state conditions, corresponding to a relative height $\bar{h}/R = 4$ for the large flames. The acoustic modulation level is always chosen in the linear regime. Except if mentioned otherwise, the root-mean-square (RMS) value of the acoustic forcing level is taken equal to $|u'|/\bar{u} = 0.10$. The measured FTF gains and phase lags are always plotted as functions of the reduced frequency ω_*.

The present chapter is organized as follows. First, the structure of the perturbed flames is investigated in Sec. 4.2. Their FTF is then analyzed in Sec. 4.3. Finally, Sec. 4.4 contains a discussion about the experimental results and a new physical interpretation explaining these results is introduced.

4.2 Analysis of flame pictures

The response of three premixed laminar conical flames, denoted **FS15**, **FS19** and **FS21** in Table 2.1, to harmonic flow rate modulations is first investigated by examining unsteady flame pictures.

Phase average pictures (over 100 frames) of the flame motion are recorded with the ICCD camera for a reduced forcing frequency set to $\omega_* = 2$. This forcing frequency is low enough to generate large flame surface area fluctuations (Ducruix et al. 2000) and highlights the differences between the various configurations explored. The camera gate width is small enough compared to the forcing period to freeze the motion and obtain unblurred pictures.

Figure 4.1 shows results for a stoichiometric CH_4/air flame stabilized above the $R = 7$ mm radius injector. This flame is submitted to an harmonic flow rate modulation at a forcing frequency $f = 16.7$ Hz, corresponding to a reduced frequency $\omega_* = 2$ and at a forcing level $|u'|/\bar{u} = 0.30$ RMS. This relatively high forcing level generates a large flame motion. For each of the six phases presented in Fig. 4.1, the original ICCD picture is represented on the left and the corresponding Abel deconvoluted image is represented on the right. The origin of the cycle $\varphi = 0°$ is arbitrarily defined as the phase at which the flame reaches its maximum height. Colors were changed in Fig. 4.1 to improve contrast. The same images were also recorded with the interferometric filter in front of the ICCD camera to isolate the OH^* chemiluminescence signal and infer the heat release rate.

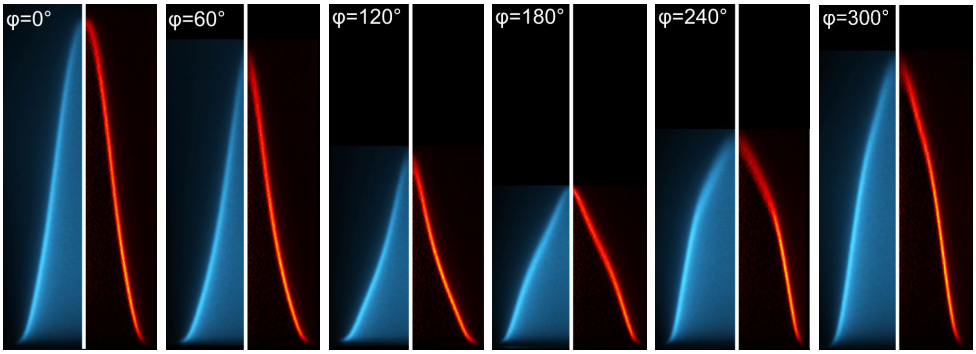

Figure 4.1: *Phase average images of a CH_4/air flame at $\phi = 1.00$, $\bar{h}/R = 4$, $R =$ 7 mm (**FS15**) forced at a reduced frequency $\omega_* = 2$ and forcing level $|u'|/\bar{u} = 0.30$ RMS. ICCD pictures without interferometric filter (Left) and their associated Abel deconvolution (Right). Colors were changed to improve contrast.*

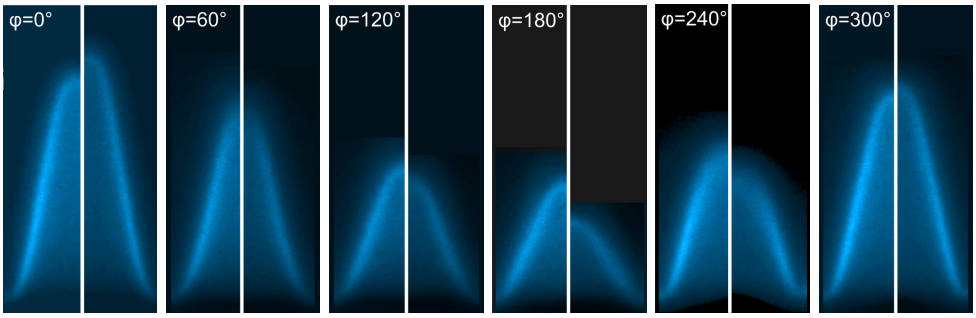

Figure 4.2: *Phase average pictures of two CH_4/air flames with $\bar{h}/R = 4$ and R=1.5 mm forced at a reduced frequency $\omega_* = 2$ and forcing level $|u'|/\bar{u} = 0.30$ RMS. Left: $\phi = 0.98$ (**FS19**). Right: $\phi = 0.88$ (**FS21**). Colors were changed to improve contrast.*

Figure 4.2 represents phase average pictures of flames stabilized above the burner with injection holes of radius $R = 1.5$ mm corresponding to **FS19** and **FS21** and sharing the same flame angle $\bar{\alpha} = 14.5°$ as those investigated in Fig. 4.1. They are also submitted to the same harmonic flow disturbances at $\omega_* = 2$ and $|u'|/\bar{u} = 0.30$ RMS corresponding to a forcing frequency $f = 74.0$ Hz for the flame on the left and $f = 63.7$ Hz for the flame on the right.

The oscillation cycles in Figs. 4.1 and 4.2 are qualitatively similar despite the large differences in terms of forcing frequencies f and burner exit radii R. These introductory results confirm that the reduced frequency ω_* and the steady flame tip half angle $\bar{\alpha}$ are well suited to analyze the response of large and small premixed laminar conical flames to harmonic flow rate modulations. However, the flame on the right in Fig. 4.2 experiences larger height excursions as well as larger luminosity oscillations over the cycle than the flame shown on the left.

This observation is further examined by determining the heat release rate fluctuations using these perturbed flame pictures. In many investigations, the heat release rate fluctuations of premixed laminar flames are directly related to flame surface area fluctuations (Schuller et al. 2002). Another approach is proposed in this work. For axisymmetric flames, the heat release rate $\dot{Q}$ can be expressed as:

$$\dot{Q} = \int_V \dot{q}(r,z)dV = \int_z \int_r \dot{q}(r,z)2\pi r dr dz \tag{4.1}$$

where $\dot{q}$ denotes the volumetric heat release rate and V the flame volume. Equation (4.1) may be rewritten as:

$$\dot{Q} = \langle \dot{q}(r,z) \rangle V \tag{4.2}$$

where $\langle \dot{q} \rangle$ is volumetric heat release rate averaged over the flame volume V.

For perturbed flames, these variables may be decomposed into their average (denoted with an overline) and fluctuating (denoted with a prime) components thus leading to the following expression for each phase in the oscillation cycle:

$$\frac{\dot{Q}'}{\overline{\dot{Q}}} = \frac{\langle \dot{q} \rangle'}{\overline{\langle \dot{q} \rangle}} + \frac{V'}{\overline{V}} \tag{4.3}$$

where $\overline{\langle \dot{q} \rangle} = \overline{\dot{Q}}/\overline{V}$ is the steady-state value of the spatial average of $\dot{q}$ over the steady flame volume $\overline{V}$ and $\langle \dot{q} \rangle'$ is the perturbed volumetric heat release rate averaged over the flame volume. The first term in the right hand side of Eq. (4.3) represents the contribution to heat release rate disturbances resulting from fluctuations of the spatially-averaged volumetric rate of heat released during the forcing cycle. The second term in Eq. (4.3) stands for heat release rate disturbances due to flame wrinkling, *i.e.* changes associated with geometrical modifications of the flame shape and perturbations of the flame thickness.

These two contributions are extracted from OH* Abel deconvoluted images and compared to values recorded by the photomultiplier equipped with the same OH* filter. For lean premixed hydrocarbon flames, the OH* signal is a good indicator of the heat release rate (Hurle et al. 1968; Li et al. 2015). The photomultiplier thus yields a signal of intensity $I \propto \dot{Q}$. Assuming that the local pixel intensity is proportional to the volumetric heat release rate $i(r,z) \propto \dot{q}(r,z)$, the total heat release rate $\dot{Q}$ and flame volume V may also be deduced from flame pictures:

$$\dot{Q} \propto \sum_z \sum_r i(r,z)2\pi r \quad \text{and} \quad V \propto \sum_z \sum_r 2\pi r \tag{4.4}$$

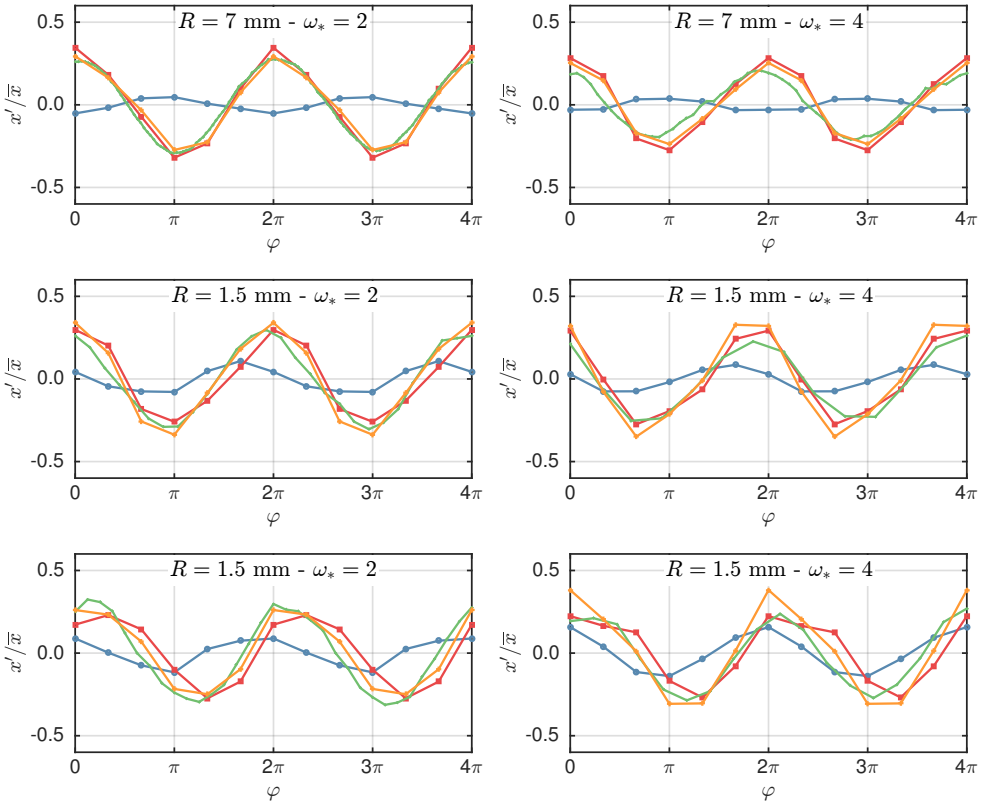

Figure 4.3: *Evolution of the spatially-averaged volumetric heat release rate (blue curve - $\langle\dot{q}\rangle'/\overline{\langle\dot{q}\rangle}$), flame volume (red curve - $V'/\overline{V}$), heat release rate (green curve - $\dot{Q}'/\overline{\dot{Q}}$) and sum of the volumetric heat release rate and flame volume (orange curve - $\langle\dot{q}\rangle'/\overline{\langle\dot{q}\rangle} + V'/\overline{V}$) over an oscillation cycle for $\omega_* = 2$ (Left) and $\omega_* = 4$ (Right) and for a forcing level $|u'|/\bar{u} = 0.30$ RMS. Top: CH_4/air, $\phi = 1.00$, $\bar{h}/R = 4$ and $R = 7.0$ mm (**FS15**). Middle: CH_4/air, $\phi = 0.98$, $\bar{h}/R = 4$ and $R = 1.5$ mm (**FS19**). Bottom: CH_4/air, $\phi = 0.88$, $\bar{h}/R = 4$ and $R = 1.5$ mm (**FS21**).*

where only pixels above a threshold intensity level are considered for the summations in Eq. (4.4). The spatially-averaged volumetric heat release rate is deduced from $\langle\dot{q}(r,z)\rangle \propto \dot{Q}/V$.

This analysis is used to determine the different contributions $\dot{Q}'/\overline{\dot{Q}}$, $\langle\dot{q}\rangle'/\overline{\langle\dot{q}\rangle}$ and $V'/\overline{V}$ which are plotted in Fig. 4.3 for **FS15**, **FS19** and **FS21**. Measurements for $\dot{Q}'/\overline{\dot{Q}}$ (interconnected orange symbols) deduced from flame images are also compared with photomultiplier measurements obtained with the same OH* filter (green curve). In all cases, the results are very close confirming that the local pixel value of the OH* chemiluminescence distribution is a good tracer of the volumetric heat release rate for the lean premixed flames investigated (Li et al. 2015). The signals plotted in orange in Fig. 4.3 correspond to

the summation $\dot{Q}'/\overline{\dot{Q}} = \langle \dot{q} \rangle' / \overline{\langle \dot{q} \rangle} + V'/\overline{V}$ of the two contributions in blue and red respectively.

The main contribution to $\dot{Q}'/\overline{\dot{Q}}$ is associated with the term $V'/\overline{V}$ (interconnected red symbols) for flames stabilized over the burner of radius $R = 7$ mm in Fig. 4.3-(Top). The flame thickness is in this case $\delta = 1.00$ mm (Yamaoka and Tsuji 1985). The contribution of $\langle \dot{q} \rangle' / \overline{\langle \dot{q} \rangle}$ (interconnected blue symbols) to $\dot{Q}'/\overline{\dot{Q}}$ remains weak at $\omega_* = 2$ and $\omega_* = 4$ for this burner outlet, but its relative proportion with respect to $V'/\overline{V}$ increases with the forcing frequency mainly because the oscillation level of $V'/\overline{V}$ slightly drops. The contributions $\langle \dot{q} \rangle' / \overline{\langle \dot{q} \rangle}$ and $V'/\overline{V}$ are out of phase by about π in Fig. 4.3-(Top). As the burner size is reduced, the contribution of $\langle \dot{q} \rangle' / \overline{\langle \dot{q} \rangle}$ to $\dot{Q}'/\overline{\dot{Q}}$ increases and becomes sizeable in the middle and bottom plots in Fig. 4.3 obtained for flames stabilized above the perforated plate with injection holes of radius $R = 1.5$ mm. The flame thickness is $\delta = 1.02$ mm for an equivalence ratio $\phi = 0.98$ and $\delta = 1.12$ mm for $\phi = 0.88$ (Yamaoka and Tsuji 1985). In these plots, the phase shift between $\langle \dot{q} \rangle' / \overline{\langle \dot{q} \rangle}$ and $V'/\overline{V}$ has changed and is closer to $\pi/2$.

The same procedure was repeated with various threshold values above which the OH^* chemiluminescence is considered, and results were found to be independent of this value in a certain range. These observations confirm that changes of the spatially-averaged volumetric rate of heat released during the forcing cycle can be ignored for flames stabilized above large injectors $\dot{Q}'/\overline{\dot{Q}} \simeq V'/\overline{V}$ when $\delta/R \ll 1$. Assuming a fixed flame thickness, the classical expression $\dot{Q}'/\overline{\dot{Q}} \simeq A'/\overline{A}$ is retrieved, where A denotes the flame surface area. This relation was verified for premixed laminar conical flames stabilized above $R = 11$ and $R = 15$ mm injector radii (Schuller et al. 2002; Li et al. 2015). However, this expression needs to be reconsidered to analyze the response of small flames when δ/R increases, as shown in Fig. 4.3.

The last aspect investigated in this section is the flame anchoring point dynamics. The evolution of the forced flame stand-off distance ψ examined at the reduced forcing frequency $\omega_* = 2$ corresponding to the flames **FS15**, **FS19** and **FS21** is represented in Fig. 4.4. The stand-off distance ψ is defined as the distance between the burner outlet and the flame leading edge, for an OH^* pixel intensity in the Abel deconvoluted image higher than a threshold value. The threshold level is kept constant for all flames and equal to the value used for the previous analysis of heat release rate fluctuations.

Results for $\psi'/\overline{\psi}$ plotted in Fig. 4.4 at $\omega_* = 2$ demonstrate that despite the large differences in terms of injector sizes R and forcing frequencies f, the flame stand-off distance ψ oscillates for all cases explored with about the same amplitude, roughly equal to $\psi'/\overline{\psi} \simeq 0.15$ RMS. This value is about half the

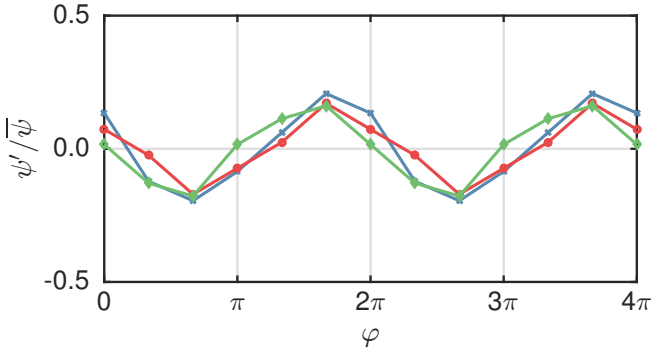

Figure 4.4: *Evolution of the flame stand-off distance as a function of the phase in the oscillation cycle at the reduced frequency $\omega_* = 2$ with an acoustic forcing level $|u'|/\bar{u} = 0.30$ RMS . Blue Crosses : CH_4/air, $\phi = 1.00$, $\bar{h}/R = 4$ and $R = 7$ mm (**FS15**). Red Circles : CH_4/Air, $\phi = 0.98$, $\bar{h}/R = 4$ and $R = 1.5$ mm (**FS19**). Green Diamonds : CH_4/Air, $\phi = 0.88$, $\bar{h}/R = 4$ and $R = 1.5$ mm (**FS21**).*

velocity oscillation level $|u'|/\bar{u} = 0.30$ RMS measured with the hot wire probe inside the injector. It is thus concluded that ω_* is a relevant dimensionless parameter to analyze the anchoring point dynamics. It is also worth noting that the flame stand-off distance oscillation amplitude does not seem to be correlated to changes in the volumetric heat release rate oscillation amplitudes $\langle\dot{q}\rangle'/\overline{\langle\dot{q}\rangle}$ observed in Fig. 4.3.

4.3 Analysis of Flame Transfer Functions

The FTF of premixed laminar conical flames are now examined as functions of the reduced frequency ω_*. Velocity measurements are obtained using LDV with a measurement volume located 1 mm above the burner outlet exit plate and on the burner symmetry axis. The reference velocity $\bar{u}$ denotes the mean value of this velocity signal in this section. Heat release rate measurements are deduced from a photomultiplier with an OH* filter. For each forcing frequency f, the voltage triggering the loudspeaker is determined by a binary search algorithm in order to keep the forcing level constant and equal to $|u'|/\bar{u} = 0.10$ RMS within 5%. The photomultiplier and LDV signals are sampled at $f_s = 8192$ Hz during at least $t = 10$ s. Both signals are measured for at least 50 forcing periods. The FTF is then deduced from the cross and auto power spectral densities of the signals assessed at the forcing frequency, as described in Chapter 2.

Figure 4.5 shows the FTF gain (Top) and phase (Bottom) plots for a premixed laminar conical CH_4/air flame with $\phi = 1.00$, $\bar{h}/R = 4$ and $R = 7$ mm (**FS15**). The two other dimensionless parameters, Le $= 0.93$ and $T_* = 6.42$, are introduced later.

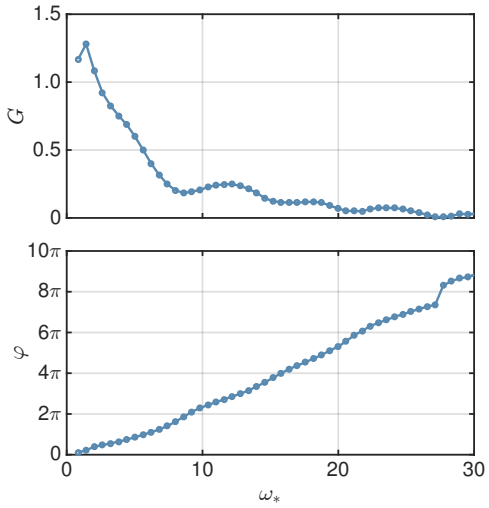

Figure 4.5: *Gain (Top) and phase (Bottom) of the FTF of a premixed laminar conical CH_4/air flame with $\phi = 1.00$, $\bar{h}/R = 4$, $R = 7$ mm, $Le = 0.93$ and $T_* = 6.42$ (**FS15**).*

The reduced frequency ω_* spans from 0 to 30. The phase lag φ increases linearly with ω_*. A gain greater than 1, *i.e.* a gain overshoot, is observed for $0 < \omega_* < 2$ with a maximum peak at around $\omega_* = 1.4$. The gain curve then rapidly drops as ω_* increases. A first rebound is observed for $\omega_* \sim 12$ and a second one for $\omega_* \sim 18$. At low gain values, it is more difficult to determine the phase lag due to the low signal-to-noise ratio. The FTF gain drops below $G < 0.25$ for $\omega_* > 10$. As a consequence, the analysis of the FTF in the remainder of this work focuses on the low frequency behavior, $\omega_* < 10$, which corresponds to the frequency range where the flame strongly responds to acoustic forcing.

Impact of the Lewis number

For a given flame tip half angle $\bar{\alpha}$, steady-state images shown in Chapter 2 indicate that curvature effects increase at the flame tip as the injector size is reduced. The impact of the Lewis number Le is first analyzed to examine whether the acoustic response of the investigated flames is related to preferential diffusion effects as the injector size is reduced. The Lewis number of a species k is defined as Le$= a_k/D_{m,k}$, where a_k is the thermal diffusivity of k and $D_{m,k}$ is the mass diffusivity of k. These quantities are determined in the reactants for mixtures of methane or propane with air at different equivalence ratios. Since the fresh reactants are a mixture of multiple gases, the expression of the Lewis number Le of the mixture is not trivial and the definition adopted here is (Bouvet et al. 2013):

$$\mathrm{Le} = \frac{\kappa}{\rho c_p D_0} \tag{4.5}$$

where κ, ρ and c_p are the mixture equivalent thermal conductivity, density and specific heat capacity at constant pressure and D_0 is the binary diffusion coefficient between CH_4 or C_3H_8 and air (Wakeham and Slater 1973).

The equivalence ratio ϕ barely changes the effective Lewis number. Equation (4.5) indicates that the binary diffusion coefficient remains constant as long as the fuel remains the same, and the combustible mixture thermo-physical properties are almost equal to the air properties since fuel represents only a small fraction of the total mass of the premixed gases. Hence, the CH_4/air flames investigated have a Lewis number in the range $\text{Le} = [0.933 - 0.935]$ and the C_3H_8/air flames have a Lewis number in the range $\text{Le} = [1.784 - 1.822]$, a variation smaller than 2% in both cases. For the remainder of this study, all CH_4/air flames are considered to have a Lewis number Le = 0.93 and all C_3H_8/air flames are considered to have a Lewis number Le = 1.80.

The FTF of lean premixed laminar conical CH_4/air and C_3H_8/air flames are compared in Fig. 4.6 when the injector exit radius is reduced from R = 11, 7, 1.5 to 1.0 mm. These flames share the same steady aspect ratio $\bar{h}/R = 4$ and dimensionless parameter $T_* = 6.4$ that is introduced below. In all cases, the FTF phase lag φ regularly increases with ω_*. The FTF phase and gain plots corresponding to Le = 0.93 (methane/air) and Le = 1.80 (propane/air) collapse to a single curve for experiments conducted with the largest injectors of radius $R = 11$ mm and $R = 7$ mm. The FTF gain and phase lag for the flames stabilized above the perforated plate with injection holes of radius $R = 1.5$ mm slightly differ for a Lewis number Le = 0.93 and Le = 1.80. Differences are more notable between the FTF of propane/air and methane/air flames with the burner featuring the smallest injection holes of radius $R = 1.0$ mm.

When the injector radius is small enough, the FTF gain and phase plots of the lean premixed conical flames featuring Lewis numbers $\text{Le} \sim 1$ and $\text{Le} > 1$ do not collapse to a single curve. The Lewis number is thus a discriminating dimensionless parameter when investigating the frequency response of small premixed laminar conical flames. However, the emergence of a gain overshoot for flames characterized by two distinct Lewis numbers when the burner outlet radius is reduced seems to indicate that additional dimensionless parameters are needed to describe the dynamics of these flames. Further investigations of the flame frequency response for combustible mixtures featuring Lewis numbers smaller than unity are required in order to generalize these results.

Effects of the flame size are further investigated in Fig. 4.7 for premixed laminar conical flames featuring the same steady aspect ratio $\bar{h}/R = 4$. Results for methane/air mixtures at Le = 0.93 are presented on the left and results for propane/air mixtures at Le = 1.80 are presented on the right. For the injectors of radius $R = 11$ mm and $R = 7$ mm, the FTF gain and phase lag collapse to

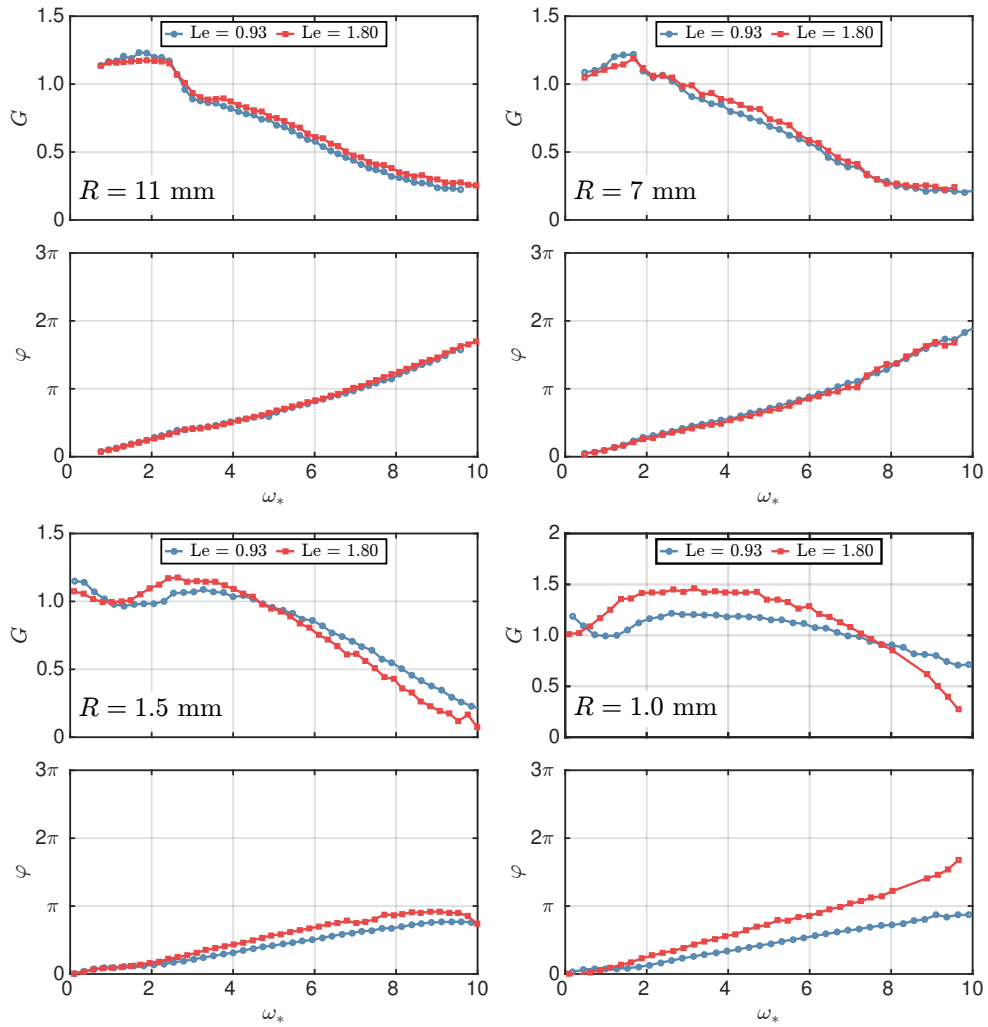

Figure 4.6: *FTF gain and phase of CH_4/air flames (**FS1**, **FS15**, **FS19** and **FS23**) with Le = 0.93, $\bar{h}/R = 4$ and $T_* = 6.4$ (blue) and of C_3H_8/air flames (**FS2**, **FS16**, **FS20** and **FS24**) with Le = 1.80, $\bar{h}/R = 4$ and $T_* = 6.4$ (red) stabilized above injectors of different radii $R = 11$ mm (Top Left), $R = 7$ mm (Top Right), $R = 1.5$ mm (Bottom Left) and $R = 1.0$ mm (Bottom Right).*

the same curve except at high reduced frequencies. Moreover, Fig. 4.7 demonstrates that for a given mixture Lewis number, the burner radius R needs to be considered to analyze the FTF of small flames. Deviations for the FTF gain and phase lag as the burner radius R is reduced are found to differ for methane/air flames (Le = 0.93) and propane/air flames (Le = 1.80). These observations again confirm that preferential diffusion effects need to be considered, but cannot fully explain the experimental observations. Finally, the FTF gain overshoot clearly increases as the injector radius R decreases for both

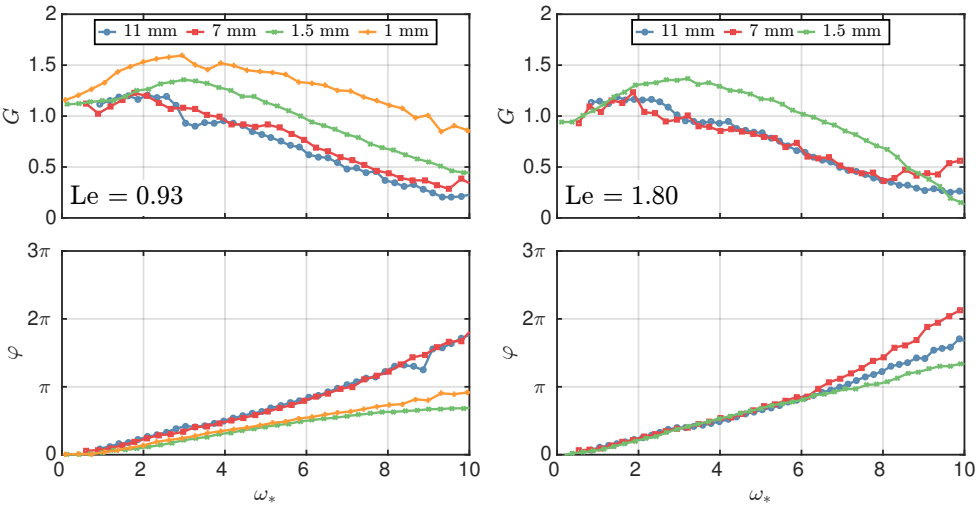

Figure 4.7: *FTF gain and phase of CH_4/air flames (**FS12**, **FS14**, **FS18** and **FS27**) with $\bar{h}/R = 4$, $T_* = 5.85$, $Le = 0.93$ (Left) and of C_3H_8/air flames (**FS11**, **FS13** and **FS17**) with $\bar{h}/R = 4$, $T_* = 6.00$, $Le = 1.80$ (Right) stabilized above injectors of different burner radius $R = 11$ mm (blue), $R = 7$ mm (red), $R = 1.5$ mm (green) and $R = 1.0$ mm (orange).*

methane/air flames (Le = 0.93) and propane/air flames (Le = 1.80).

Impact of heat losses

The effects of heat losses and thermal flow expansion are now examined as the burner size is reduced. The burnt gases temperature $\overline{T}_b$ is measured one millimeter above the tip of all steady-state flames and corrected for radiative heat losses, as explained in Chapter 2. The adiabatic flame temperature T_{ad} is also determined with the GRI-MECH 3.0 mechanism. Analysis of heat losses is carried out by examining the ratio $\theta_* = \overline{T}_b/T_{ad}$ that is found to vary from 0.68 to 0.73 with an average value $\theta_* = 0.71$ for all conditions explored. The deviation from this average value never exceeds 4% and thus, θ_* can be considered to be constant in these experiments. One important consequence is that the adiabatic flame temperature T_{ad} and the burnt gases temperature $\overline{T}_b$ are equivalent parameters in the present study, and the former quantity is retained for further analysis.

A new dimensionless parameter $T_* = T_{ad}/\overline{T}_u - 1$ is now introduced, quantifying the excess of volume occupied by the burnt gases at T_{ad} with respect to unburnt gases at $\overline{T}_u$. The quantity $T_* = E - 1$, where E is the volumetric expansion ratio, is useful to describe the effects of exothermicity. This quantity has been shown to alter the response of conical flames and M-flames (Cuquel et al. 2013b; Blanchard et al. 2015).

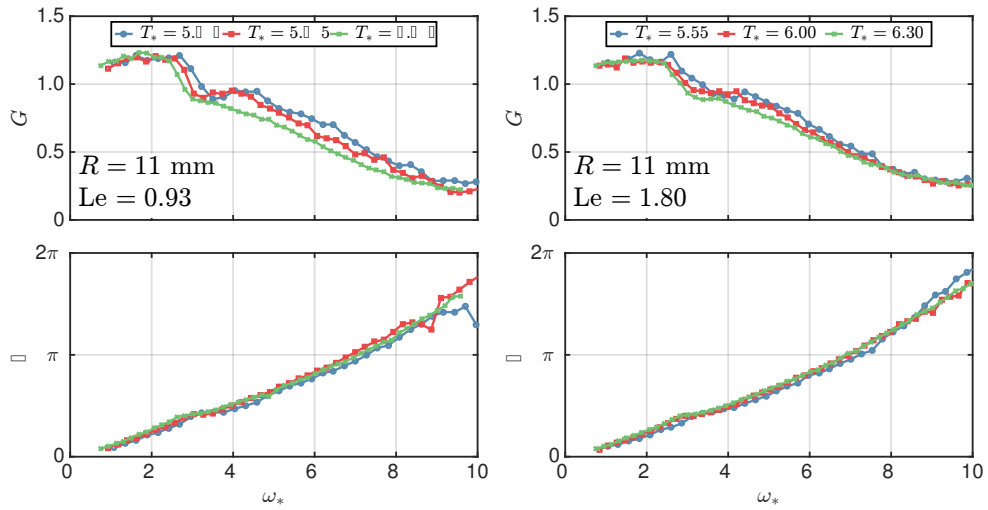

Figure 4.8: *FTF gain and phase of CH_4/air flames (**FS1**, **FS7** and **FS12**) and C_3H_8/air flames (**FS2**, **FS6** and **FS11**) stabilized above the $R = 11$ mm radius injector and sharing the same relative height $\bar{h}/R = 4$. Left: CH_4/air with Le $= 0.93$ and $T_* = 5.66$ (blue), $T_* = 5.85$ (red) and $T_* = 6.42$ (green). Right: C_3H_8/air with Le $= 1.80$ and $T_* = 5.55$ (blue), $T_* = 6.00$ (red) and $T_* = 6.30$ (green).*

The impact of T_* is examined by varying the equivalence ratio and bulk injection velocity of methane/air and propane/air mixtures sharing the same steady flame aspect ratio $\bar{h}/R = 4$. Flame Transfer Functions measured for propane/air (Le $= 1.80$) and methane/air (Le $= 0.93$) flames stabilized above the $R = 11$ mm injector are found to be independent of T_* in Fig. 4.8. In these experiments, T_* varies between 5.55 and 6.42 with relative variations of about 16% that are larger than the changes of θ_* ($< 4\%$), thus justifying the approximation of a constant $\theta_* = 0.71$ throughout this chapter. Flame Transfer Functions of propane/air and methane/air flames stabilized above the $R = 7$ mm radius injector and plotted in Fig. 4.9 also barely change with T_*. A small difference for the gain curves of methane/air flames at $T_* = 5.85$ and $T_* = 6.42$ can however be noticed.

Large deviations are found in Fig. 4.10 between the FTF of premixed laminar conical flames stabilized above the perforated plate with holes of radius $R = 1.5$ mm. The FTF gain drops as T_* increases for both methane/air flames (Le $= 0.93$) and propane/air flames (Le $= 1.80$), while the phase lag is less affected. However, the phase plots feature an inflection point at a relatively low reduced frequency. It is worth recalling that the reference velocity $\bar{u}$ used when determining the FTF is not the bulk flow velocity at the injector outlet, but corresponds to the time-averaged value measured with Laser Doppler Velocimetry 1 mm above the injector outlet. This is the reason why the gain does

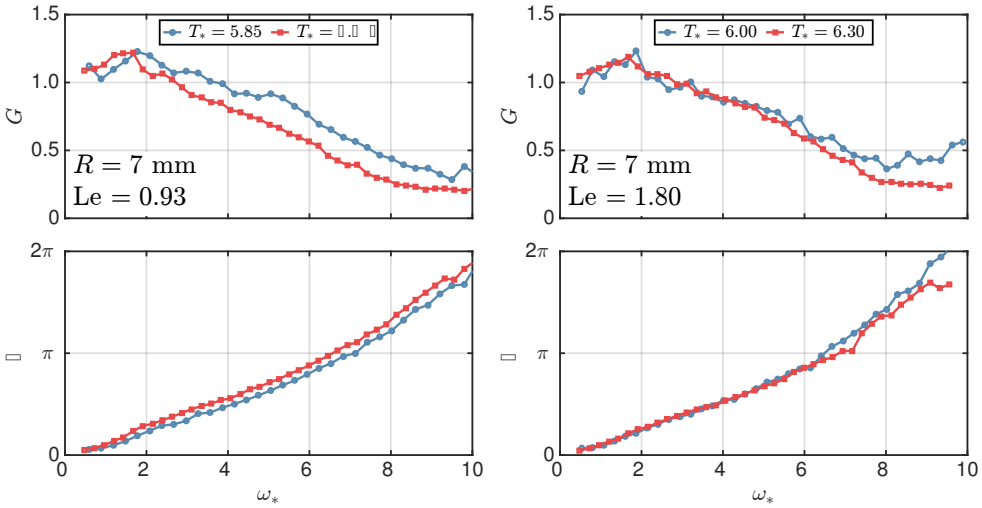

Figure 4.9: *FTF gain and phase of CH_4/air flames (**FS15** and **FS18**) and C_3H_8/air flames (**FS16** and **FS17**) stabilized above the $R = 7$ mm radius injector and sharing the same relative height $\bar{h}/R = 4$. Left: CH_4/air with Le $= 0.93$ and $T_* = 5.85$ (blue) and $T_* = 6.42$ (red). Right: C_3H_8/air with Le $= 1.80$ and $T_* = 6.00$ (blue), $T_* = 6.30$ (red).*

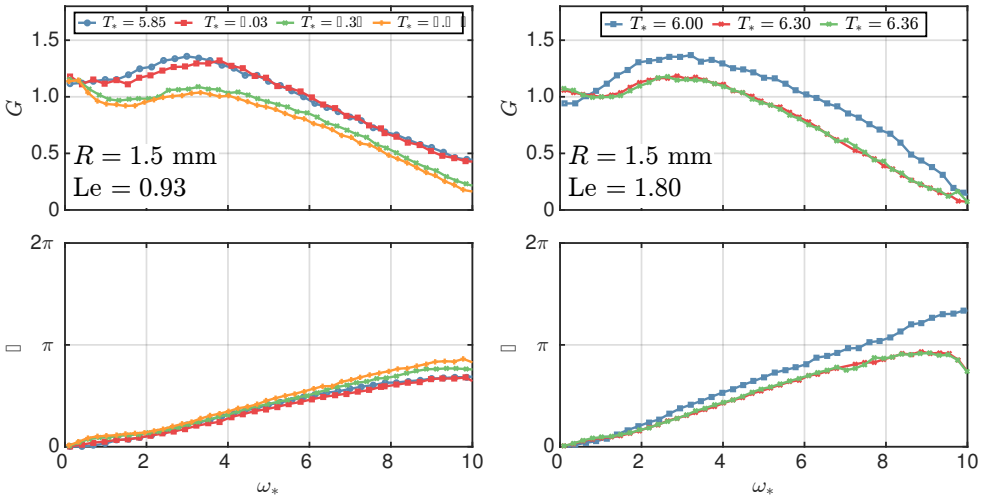

Figure 4.10: *FTF gain and phase of CH_4/air flames (**FS4**, **FS14**, **FS19** and **FS21**) and C_3H_8/air flames (**FS5**, **FS13** and **FS20**) stabilized above the $R = 1.5$ mm radius injector and sharing the same relative height $\bar{h}/R = 4$. Left: CH_4/air with Le $= 0.93$ and $T_* = 5.85$ (blue), $T_* = 6.03$ (red), $T_* = 6.36$ (green), $T_* = 6.42$ (orange). Right: C_3H_8/air with Le $= 1.80$ and $T_* = 6.00$ (blue), $T_* = 6.30$ (red), $T_* = 6.36$ (green).*

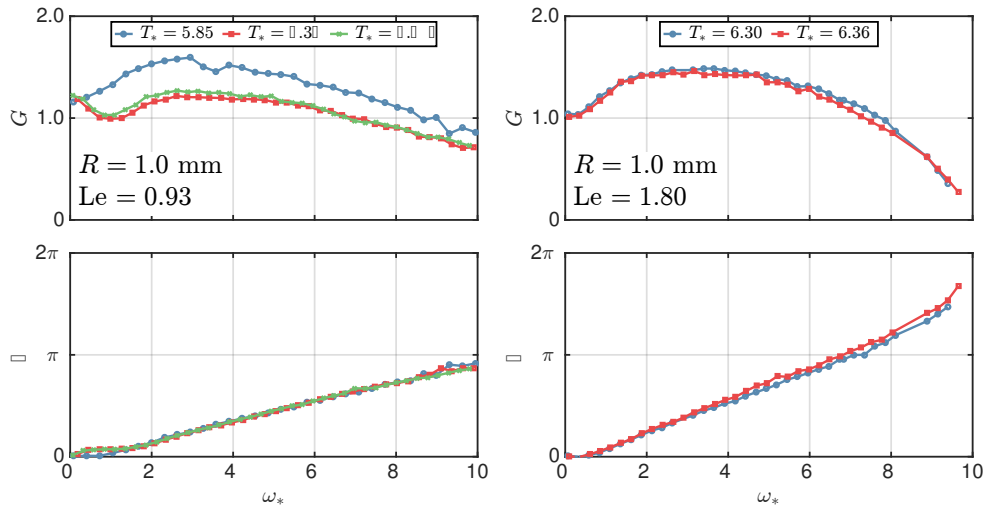

Figure 4.11: *FTF gain and phase of CH_4/air flames (**FS23**, **FS25** and **FS27**) and C_3H_8/air flames (**FS24** and **FS26**) stabilized above the $R = 1.0$ mm radius injector and sharing the same relative height $\bar{h}/R = 4$. Left: CH_4/air with Le $= 0.93$ and $T_* = 5.85$ (blue), $T_* = 6.36$ (red), $T_* = 6.42$ (green). Right: C_3H_8/air with Le $= 1.80$ and $T_* = 6.30$ (blue curve), $T_* = 6.36$ (red curve).*

not converge to unity when $\omega_* \to 0$, but reaches values slightly larger than unity.

The low frequency behavior of the FTF gain also changes depending on T_*. For the methane/air FTF shown in Fig. 4.10-(Left), the blue and red gain curves obtained for $T_* = 5.85$ and $T_* = 6.03$ both feature a gain overshoot larger than the quasi steady-state value when $\omega_* = 0$. The green and orange gain curves corresponding to $T_* = 6.36$ and $T_* = 6.42$ feature a rebound of the gain with a peak value lower than the quasi steady-state value. This behavior may also be observed for the propane/air FTF in Fig. 4.10-(Right), even though differences between the peak and quasi steady-state values of the gain are reduced for the green and red curves.

The impact of T_* is even more striking in Fig. 4.11 obtained for flames stabilized above the perforated plate with holes of radius $R = 1.0$ mm. In Fig. 4.11-(Right), both the FTF gain and phase plots collapse to a single curve for C_3H_8/air flames featuring almost the same T_*. In the left figure, the FTF gain plots differ when T_* changes, while the phase lag plots all collapse to a single curve. The FTF gain overshoot is observed in a large range of reduced frequencies for $T_* = 5.85$. The maximum gain also increases as T_* decreases.

Figures 4.8-4.11 reveal that T_* is also a discriminating dimensionless parameter that needs to be considered when analyzing the FTF of small premixed laminar conical flames. In the following section, a physical analysis is performed in order

to determine the origin of these experimental observations.

4.4 Physical analysis

Large gain overshoots for the FTF of small premixed laminar conical flames is a well documented feature (Noiray et al. 2006b; Noiray et al. 2007) that is often attributed to the unsteady heat transfer between the flame and the burner (Rook et al. 2002; Altay et al. 2009). The dimensions of the small conical flames stabilized above the matrix injectors of radii $R = 1.5$ mm and $R = 1.0$ mm are close to those investigated in these studies. It is therefore worth analyzing the results presented in the previous sections with the associated theoretical developments (Rook et al. 2002; Altay et al. 2009).

The impact of unsteady heat and mass transfer between the flame leading edge and the burner outlet on flame dynamics has been described in past investigations (Rook et al. 2002; Altay et al. 2009; de Goey et al. 2011). A quick description of this mechanism is now presented. When a non-adiabatic planar flame stabilized above a burner oscillates around its mean position, the heat loss from the reacting layer to the burner oscillates as well, because of the resulting changes in the temperature gradient at the burner exit plate. An enthalpy wave is then convected by the mean velocity $\bar{u}$ from the burner outlet to the reaction layer. When this wave reaches the flame front standing at ψ with a time lag $\tau = \psi/\bar{u}$, the flame speed S_L and flame position ψ are modified because of the changes in flame temperature due to the enthalpy fluctuations. In such a system, the dynamics of the anchoring point is formally governed by:

$$\frac{\partial \psi}{\partial t} = u - S_L\left(\psi, \mathcal{H}'(t-\tau)\right) \tag{4.6}$$

where the flame speed S_L is a function of both the flame leading edge position ψ and the enthalpy wave $\mathcal{H}'$ generated at the burner exit plate at $t - \tau$. For small harmonic disturbances, the burning rate instantaneously adapts to changes of the enthalpy at the flame front (Rook et al. 2002; de Goey et al. 2011), meaning that these two quantities are in phase.

This mechanism has been shown to lead to an amplification behavior with values of the FTF gain greater than unity $G > 1$ (Kedia et al. 2011) when the phase lag associated with the average convective time lag $\bar{\tau}$ is equal to $\pi/2$:

$$\overline{\Delta\varphi} = \bar{\tau}\omega = \frac{\overline{\psi}\omega}{\bar{u}} = \frac{\pi}{2} \tag{4.7}$$

It is reminded that the overline and prime stand for mean and fluctuating quantities respectively. Figure 4.12 illustrates this mechanism, designated in

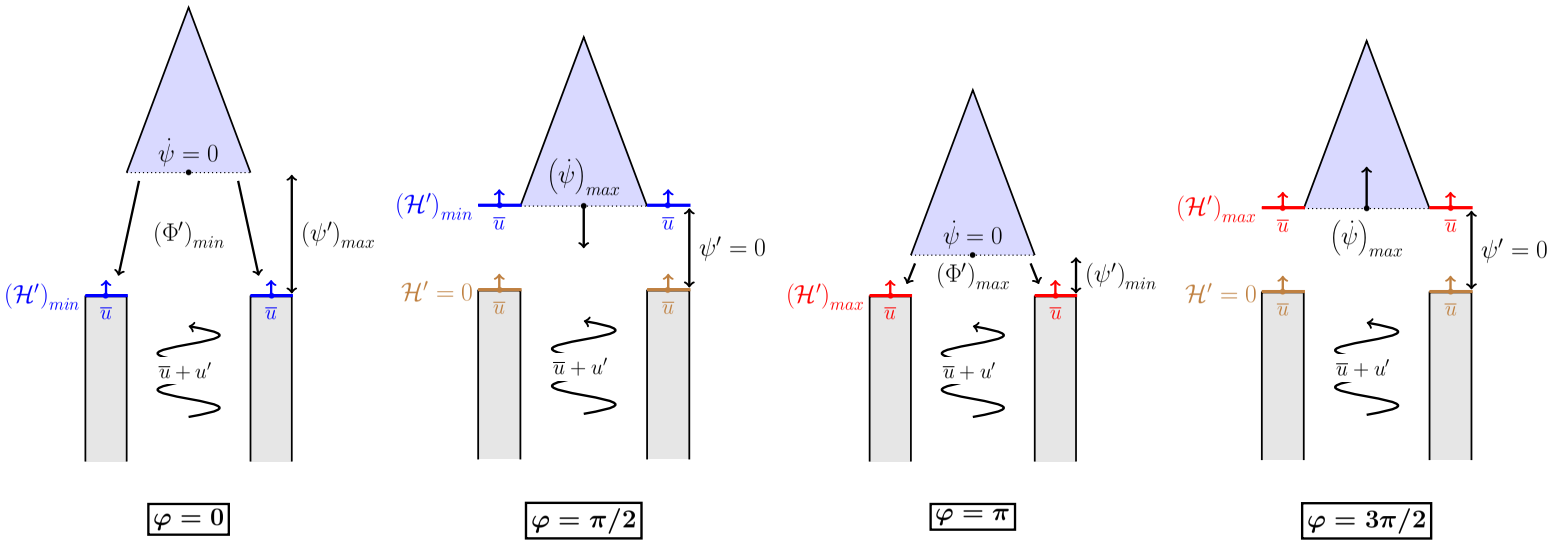

Figure 4.12: *Illustration of the vertical heat loss mechanism when* $\overline{\Delta\varphi} = \pi/2$ *at different phases during the forcing cycle. From left to right:* $\varphi = 0$, $\varphi = \pi/2$, $\varphi = \pi$, $\varphi = 3\pi/2$.

this work as the vertical heat and mass transfer mechanism, for a premixed laminar conical flame when the phase lag between the enthalpy fluctuations at the burner outlet and at the average flame leading edge position is equal to $\overline{\Delta\varphi} = \pi/2$.

Harmonic disturbances are prescribed and the reference phase in Fig. 4.12 is arbitrarily set to $\varphi = 0$ when the flame leading edge stand-off distance is the largest $(\psi')_{max}$, and the flame base displacement velocity $\dot{\psi} = \partial\psi/\partial t$ is zero. This instant also corresponds to the smallest enthalpy fluctuation $(\mathcal{H}')_{min}$ generated at the injector outlet. This enthalpy wave is then convected at an average speed of $\bar{u}$ and hits the flame leading edge at $\varphi = \pi/2$, when the flame base displacement velocity $\partial\psi/\partial t$ is the greatest and oriented towards the burner, i.e. with negative values. The enthalpy fluctuation $(\mathcal{H}')_{min}$ being the smallest, the flame speed S_L is the largest at $\varphi = \pi/2$ leading to an amplification of the flame base displacement speed towards the burner $\dot{\psi} = \partial\psi/\partial t < 0$. The same kind of reasoning can be made when the largest enthalpy fluctuation $(\mathcal{H}')_{max}$ generated at $\varphi = \pi$ at the burner outlet reaches the flame leading edge at $\varphi = 3\pi/2$. In this case, the flame speed is drastically reduced, leading to a larger flame displacement velocity $\dot{\psi} > 0$.

Results shown in the previous sections are analyzed in light of this mechanism in which the theoretical resonant frequency f^0 associated with the peak value of the FTF gain is (Rook et al. 2002; Altay et al. 2009):

$$f^0 \sim \frac{1}{4\ \bar{\tau}} \sim \frac{S_L^b}{4\ \sin\bar{\alpha}_b\ \overline{\psi}} \tag{4.8}$$

where S_L^b denotes the non-adiabatic flame speed at the flame base (Rook et al. 2002). The additional factor $\sin\bar{\alpha}_b = \bar{u}/S_L^b$ was added in Eq. (4.8) to account for the steady flame angle at its base $\bar{\alpha}_b$ with respect to the main flow direction and corresponds to a generalization of the planar flame model. In the general case, the non-adiabatic burning velocity S_L^b differs from the adiabatic burning velocity of a freely propagating flame S_L.

Since $\theta_* = \overline{T}_b/T_{ad}$ was shown to be constant for all flames in the present study, one may assume that the ratio S_L^b/S_L, despite being lower than unity, remains roughly constant. As a first approximation, S_L^b is here taken equal to $S_L^b \approx S_L$. This rough approximation is justified because the main interest of the present section lies in the modification of the reduced resonant frequency ω_*^0 when the injectors radius R is reduced. Since the steady flame stand-off distances, summarized in Table 2.1, are almost the same for all the injectors sizes, and since it was shown that stand-off distances oscillate with the same amplitude for all flames in Fig. 4.4, the flame leading edge displacement speed is expected to be about the same for all cases explored. It is thus reasonable to assume that

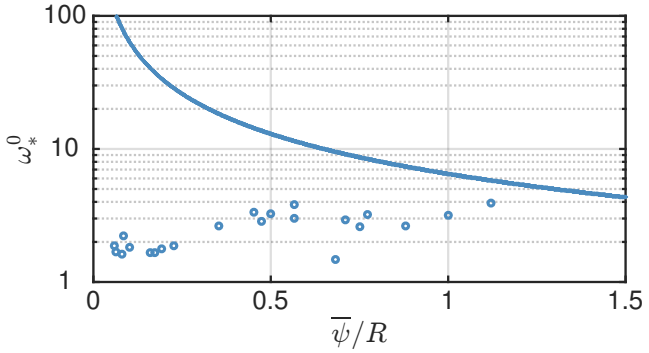

Figure 4.13: *Resonant reduced frequency ω_*^0 as a function of $\overline{\psi}/R$. Blue curve: theoretical prediction from Eq. (4.9). Filled symbols : Experimental values corresponding to all flames described in Table 2.1.*

S_L^b/S_L remains also constant for all flames of the present study. Equivalently, the flame angle is assumed to remain constant along the flame front $\bar{\alpha} = \bar{\alpha}_b$. With this additional assumption, Eq. (4.8) is expressed in terms of the reduced frequency:

$$\omega_*^0 \simeq \frac{\pi}{\sin 2\bar{\alpha}} \left(\frac{R}{\overline{\psi}}\right) \tag{4.9}$$

Steady-state stand-off distances $\overline{\psi}$ are determined with the macro-photographies of the steady flames shown in Figs. 2.3, 2.4, 2.5 and 2.6. Values for $\overline{\psi}$ are found to decrease as T_* increases. The resonant reduced frequencies ω_*^0 associated with the FTF gain peak values are also deduced from FTF measurements. These frequencies are compared with predictions of ω_*^0 according to Eq. (4.9) as a function of $\overline{\psi}/R$ in Fig. 4.13. For $\overline{\psi}/R \sim 1$, the order of magnitude of the resonant reduced frequency ω_*^0 is correctly predicted by Eq. (4.9), but results largely differ at lower $\overline{\psi}/R$ values. In the experiments, ω_*^0 first increases with $\overline{\psi}/R$ and then reaches an asymptotic limit at large $\overline{\psi}/R$ values. Equation (4.9) shows that ω_*^0 linearly scales with $R/\overline{\psi}$. Additionally, results plotted in Fig. 4.4 revealed that for a fixed reduced frequency, flames stabilized above small $R = 1.5$ mm and large $R = 7$ mm injectors feature the same flame base oscillation amplitude $\psi'/\overline{\psi}$ while they feature large differences for ω_*^0 in the FTF plotted in Figs. 4.9 and 4.10.

These comparisons in Fig. 4.13 indicate that an additional mechanism needs to be considered in order to accurately predict the resonant reduced frequency at which the FTF gain is maximum. An improved version of this mechanism, called the bidimensional mechanism in the remainder of this work, is now proposed. Rather than considering the flame as a rigidly oscillating body that

instantly responds to enthalpy waves hitting the flame leading edge by adjusting its fuel burning rate (Rook et al. 2002; Altay et al. 2009; Altay et al. 2010; de Goey et al. 2011), the flame is now considered to be deformable. Moreover, the largest burning rate fluctuations are no longer considered to take place at the flame base, but at the axial location $z_A(t) = \bar{z}_A + z'_A(t)$ where the preheating diffusion layers between adjacent flame fronts merge as described in Fig. 4.14. The physical justification is developed below.

At the flame leading edge, the flame elements facing each other are separated by a layer of fresh reactants at the center of the burner where the temperature and species concentrations remain uniform and equal to $\overline{T}_u$ and X_u respectively. Opposite flame elements lying in this region are unaffected by each other from a thermal and chemical viewpoint. At a certain height $z_A(t)$ downstream of the burner outlet, the diffusion layers of flame elements facing each other merge and for all axial positions greater than $z_A(t)$, there is no fresh gas layer between the two opposite flame elements. In this region, lateral heat and mass transfers are modified and the fuel burning rate is greatly reduced (Echekki et al. 1996; Wichman and Vance 1997). For steady operating conditions, this is the well known mechanism leading to flame tip bending controlled by preferential diffusion (Lewis and von Elbe 1987). It has already been shown that the FTF of large flames featuring mutual interactions of flame elements lead to large FTF gains exceeding unity over a broad frequency range (Schuller et al. 2003a; Durox et al. 2005) due to flame tip pinch-off and are also accompanied by large noise emissions at these forcing frequencies (Schuller et al. 2003a; Talei et al. 2011).

When acoustic forcing is applied, the axial position $z_A(t)$ oscillates for two reasons: (1) the flame stand-off distance oscillates and (2) the flame height oscillates. These two additive contributions lead to large oscillation amplitudes $z'_A/\bar{z}_A$ with a large fraction of fresh gases successively entering and leaving the preheating diffusion layer of the flame during the forcing cycle. These oscillations are expected to be comparatively larger than the oscillation $\psi'/\overline{\psi}$ at the flame base.

Figure 4.14 illustrates this mechanism for a flame with a sizeable diffusion layer thickness δ with respect to the burner exit radius R. The flame diffusion layer thickness is represented in blue in this figure and corresponds to the region where the temperature rises from the fresh gases temperature $\overline{T}_u$ to the burnt gases temperature $\overline{T}_b$. Alternatively, a species diffusion layer could be chosen as well. Reasoning is made here for a unity Lewis number. Adjacent flame elements located at $z \sim z_A(t)$ experience large burning rate oscillations due to both the vertical oscillation of z_A and lateral heat and mass transfers in the interpenetrating diffusion layers. These burning rate oscillations may be much larger than the ones felt by flame elements at the bottom of the flame that only

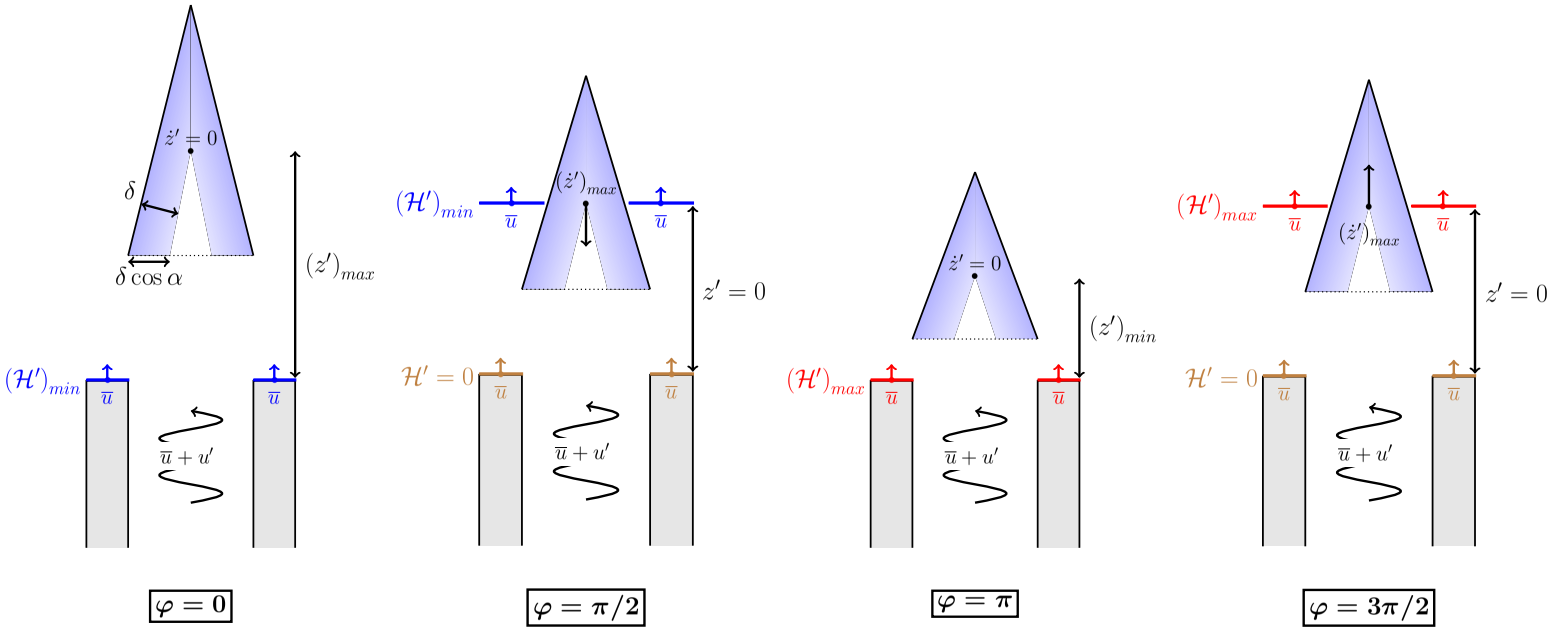

Figure 4.14: *Illustration of the bidimensional heat and mass transfer mechanism when* $\overline{\Delta\varphi} = \pi/2$ *at different phases during the forcing cycle. From left to right:* $\varphi = 0$, $\varphi = \pi/2$, $\varphi = \pi$, $\varphi = 3\pi/2$.

experience fluctuations of the burning rate through the vertical mechanism described before. Enthalpy waves convected by the mean flow generate larger flame speed oscillations S'_L at $z \sim z_A(t)$ and accordingly a larger displacement velocity $\dot{z}'$ compared to the flame leading edge displacement velocity $\dot{\psi}$ close to the flame base. In other words, enthalpy waves hitting the location where the diffusion layers merge increase the burning rate oscillation amplitude and at the same time, increase the flame surface area oscillation amplitude.

Flame Transfer Function gain overshoots are expected to be important when the phase lag between the enthalpy wave generated at the burner exit $\mathcal{H}'(0)$ and the enthalpy wave hitting the axial location where the diffusion layers merge $\mathcal{H}'(z_A)$ is equal to $\overline{\Delta\varphi} = \pi/2$. This reasoning constitutes the basis of the bidimensional heat and mass transfer mechanism. The ratio of the radial projection of the flame thickness δ to the burner radius R is introduced to further investigate this mechanism:

$$\delta_* = \frac{\delta \cos \bar{\alpha}}{R} \tag{4.10}$$

This quantity was already introduced to analyze the impact of the flame base dynamics on the FTF of large premixed laminar conical flames (Cuquel et al. 2013a). It characterizes the strength of the interactions of adjacent flame diffusion layers facing each other. When $\delta_* \ll 1$, mutual interactions remain weak and the FTF is barely influenced as shown by the results obtained for the R =11 and 7 mm radii injectors presented in Sec. 4.3. The FTF is in this case mainly controlled by flame surface wrinkling. When $\delta_* \sim 1$, the bidimensional heat and mass transfer mechanism needs to be considered. The flame experiences in this case both vertical and lateral heat and mass transfer oscillations, thus generating large fuel burning rate oscillations that will in turn generate large flame surface area oscillations. The values for the flame thermal diffusion layer thicknesses used in the following analysis are summarized in Table 2.1 (Yamaoka and Tsuji 1985).

Predictions of the resonant reduced frequencies ω_*^0 associated with the bidimensional heat and mass transfer mechanism are now examined. The derivation is the same as for the vertical heat and mass transfer mechanism, but the governing time lag $\bar{\tau}$ is now associated with the convection of enthalpy waves between the burner outlet and the average axial location $\bar{z}_A$ where the flame diffusion layers merge. From geometrical considerations, it is found that $\bar{z}_A = \bar{h}\,(1 - \delta_*) + \overline{\psi}$. Assuming again that the ratio S_L^b/S_L remains constant and close to unity, the resonant reduced frequency is given by:

$$\omega_*^0 \simeq \frac{\pi}{\sin 2\bar{\alpha}} \left[\frac{1}{\bar{h}/R\,(1 - \delta_*) + \overline{\psi}/R} \right] \tag{4.11}$$

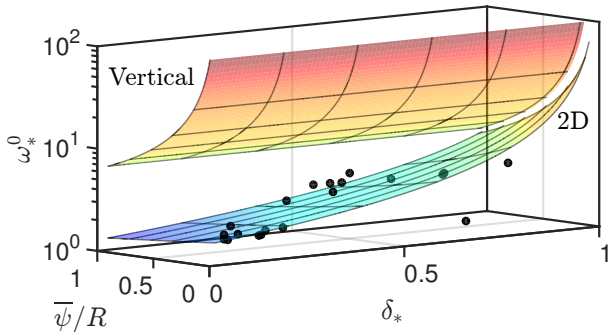

Figure 4.15: *Resonant reduced frequency ω_*^0 as a function of the dimensionless stand-off distance $\overline{\psi}/R$ and the dimensionless diffusion layer thickness δ_* according to the vertical mechanism from Eq. (4.9) (upper surface) and the bidimensional mechanism from Eq. (4.11) (lower surface). Experimental values corresponding to all flames described in Table 2.1 are represented as black spheres.*

The steady flame aspect ratio $\overline{h}/R$ or equivalently the steady flame tip half angle $\overline{\alpha}$ and the dimensionless steady stand-off distance $\overline{\psi}/R$ appear explicitly in this expression. The ratio δ_* takes into account the bidimensional heat and mass transfer mechanism. It is clear that this expression is only valid for $\delta_* < 1$. When the flame aspect ratio is small $\overline{h}/R \ll 1$ or when $\delta_* \sim 1$, the resonant frequency is only controlled by $\overline{\psi}/R$ as for the purely vertical heat and mass transfer mechanism and Eq. (4.9) is retrieved. When the flame aspect ratio is large $\overline{h}/R \gg \overline{\psi}/R$ and $\delta_* \ll 1$, the resonant frequency is only controlled by $\overline{h}/R$ and δ_* and associated to purely lateral heat and mass transfer within interpenetrating adjacent flame diffusion layers. In the general case, heat and mass transfers are bidimensional.

Theoretical predictions from Eq. (4.11) are found in the range $1.5 \leq \omega_*^0 \leq 8.0$, which is in good agreement with experiments presented in the previous section. Moreover, the slight variation of ω_*^0 with the injector radius R is also well captured. Figure 4.15 shows the resonant reduced frequency ω_*^0 in a log scale as a function of $\overline{\psi}/R$ and δ_* according to Eq. (4.9) associated with the vertical mechanism and Eq. (4.11) associated with the bidimensional mechanism. It is reminded that the steady flame aspect ratio is kept constant and equal to $\overline{h}/R = 4$ in this study. Experimental values are displayed as black spheres. The resonant reduced frequencies predicted by the bidimensional mechanism are in much better agreement with experiments than the resonant reduced frequencies predicted by the vertical mechanism. It is also worth noting that when $\delta_* \to 1$, both mechanisms predict the same resonant reduced frequency. In this case, the diffusion layers of adjacent flame elements merge at the flame leading edge position, and both models are equivalent.

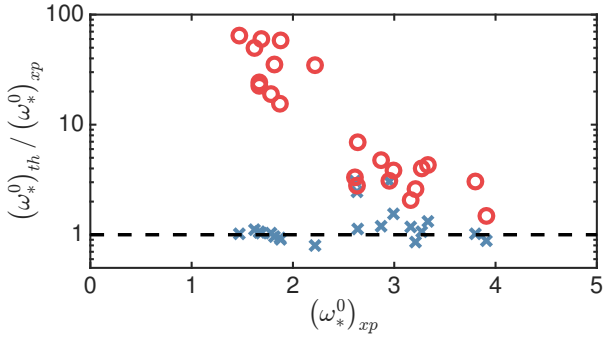

Figure 4.16: *Ratio between theoretical* $(\omega_*^0)_{th}$ *and experimental* $(\omega_*^0)_{xp}$ *resonant reduced frequencies for all flames described in Table 2.1 as a function of* $(\omega_*^0)_{xp}$*. Predictions are assessed by considering the vertical (red circles) or bidimensional (blue crosses) heat and mass transfer mechanisms.*

This three-dimensional representation is completed by Fig. 4.16 showing the ratio between the theoretical $(\omega_*^0)_{th}$ and measured $(\omega_*^0)_{xp}$ resonant reduced frequencies as a function of $(\omega_*^0)_{xp}$ for the vertical mechanism given by Eq. (4.9) (Red circles) and the bidimensional mechanism given by Eq. (4.11) (Blue crosses). The y-axis is represented with a log scale. The proximity to unity in Fig. 4.16 indicates how well analytical predictions match measurements.

For large experimental values $(\omega_*^0)_{xp}$, both the vertical and bidimensional mechanisms yield the correct resonant reduced frequency. But as $(\omega_*^0)_{xp}$ decreases, predictions associated with the vertical transfer mechanism become less accurate, leading to a two orders of magnitude difference between theory and experiments. Predictions of $(\omega_*^0)_{th}$ associated with the bidimensional mechanism are always close to the measured values, hence advocating for the validity of this mechanism over a much wider range of operating conditions corresponding to a wide variety of premixed laminar conical flames. An overall good agreement is found between experiments and predictions by considering the bidimensional heat and mass transfer mechanism.

4.5 Conclusion

The frequency response of methane/air and propane/air premixed laminar conical flames with the same aspect ratio $\bar{h}/R = 4$ submitted to harmonic flow rate modulations were investigated for decreasing injector radii. The analysis was carried out with four injector radii and for different equivalence ratios and injection velocities. Heat release rate oscillations were shown to be driven by oscillations of the spatially-averaged volumetric heat release rate and by flame

volume oscillations. The first contribution, associated with changes of the burning rate, can be neglected for large injectors, i.e. when the injector radius is large compared to the flame thickness. However, this contribution increases as the burner size is reduced. The second contribution is mainly associated with flame surface wrinkling. It was also found that the flame leading edge stand-off distance oscillates around its steady position for all the perturbed flames investigated. For a given reduced frequency $\omega_* = \omega R/(S_L \cos\bar{\alpha})$, the amplitude of this motion was found to be independent of the burner radius and operating conditions.

It was then shown that the reduced frequency ω_* is an adequate dimensionless number to investigate the Flame Transfer Function (FTF) of premixed laminar conical flames stabilized over injectors with different sizes for steady flames of constant aspect ratio $\bar{h}/R$ or flame tip half angle $\bar{\alpha}$. The FTF was also found to be independent of the Lewis number for mixtures with Le ~ 1 and Le > 1 as long as the injector radius is large enough. For flames stabilized over small injectors, the flame diffusion layer thickness becomes sizeable with respect to the injector radius and large differences between FTF were found for mixtures with Le ~ 1 and Le > 1. Large modifications of the FTF shapes were also highlighted while decreasing the burner outlet radius and modifying the flame temperature. The main observations are the following. The FTF of small premixed laminar conical flames feature FTF gain values largely exceeding unity at low reduced frequencies, reaching a peak value at a resonant reduced frequency ω_*^0. This peak FTF gain value increases when the flame temperature or the injector radius are reduced.

A model predicting ω_*^0 was then derived. This quantity was shown to be a function of the steady flame aspect ratio $\bar{h}/R$, the dimensionless steady flame base stand-off distance $\overline{\psi}/R$, and $\delta_* = \delta\cos\bar{\alpha}/R$, the ratio between the flame diffusion layer thickness projected along the radial direction and the injector radius. This framework generalizes previous one-dimensional approaches where FTF gain values exceeding unity, i.e. flames amplifying flow perturbations, were solely attributed to unsteady heat losses between the flame base and the burner outlet.

Bidimensional effects associated with 1) unsteady vertical heat losses between the flame base and the burner and 2) lateral heat and mass transfers between adjacent flame elements through the interpenetration of their diffusion layers were shown to lead to a more accurate description of the physical processes involved. Moreover, predictions of ω_*^0 with this new model were shown to better reproduce measurements over the wide variety of injector sizes and operating conditions explored.

The main results may be synthesized as follows. For large injectors, i.e. when

$\delta_* \ll 1$, the transfer function of premixed laminar conical flames is controlled by two dimensionless numbers, the reduced frequency ω_* and the steady flame tip half angle $\bar{\alpha}$ or equivalently the steady flame aspect ratio $\bar{h}/R$. For smaller injectors, i.e. when $\delta_* \sim 1$, the additional dimensionless parameters $\bar{\psi}/R$ and δ_*, accounting for the motion of the flame base and the motion of the interpenetrating diffusion layers, are necessary to describe the FTF. The Lewis number Le should also be considered when describing the FTF of small premixed laminar conical flames.

Part II

Premixed Confined Turbulent Flames

Chapter 5

The NoiseDyn burner

The NoiseDyn burner is presented in this chapter. A base configuration is used to introduce the core elements of the NoiseDyn burner. The upstream and downstream elements are then discussed. One of the specificities of this setup is that acoustic forcing may be generated using loudspeakers located on the upstream or downstream sides of the combustor. Moreover, many elements such as the swirler or the exhaust tubes can be easily modified if needed. The main geometrical configurations explored in this work are also listed along with the retained operating conditions.

The NoiseDyn burner was designed using Computer-Aided Design softwares, namely Autodesk Inventor 2015 and Catia v5, and built at the EM2C laboratory. Its design is an evolution of previous confined turbulent burners (Palies et al. 2011a; Guiberti 2015). It is represented in Fig. 5.1. Its design is highly modular and can be divided into three main parts:

- The upstream elements, located below the region where the fresh gases are injected.
- The downstream elements, located after the combustion chamber exhaust nozzle, in the hot gases region.
- The core elements, located in-between and comprising the swirler and the combustion chamber among others.

The upstream and downstream elements are changed depending on the type of forcing and/or acoustic boundary condition desired. Moreover, the burner design allows many of the core elements to be changed as well (Gatti et al. 2017). However, all the core elements other than the swirling vane are prescribed for the experiments presented in this work.

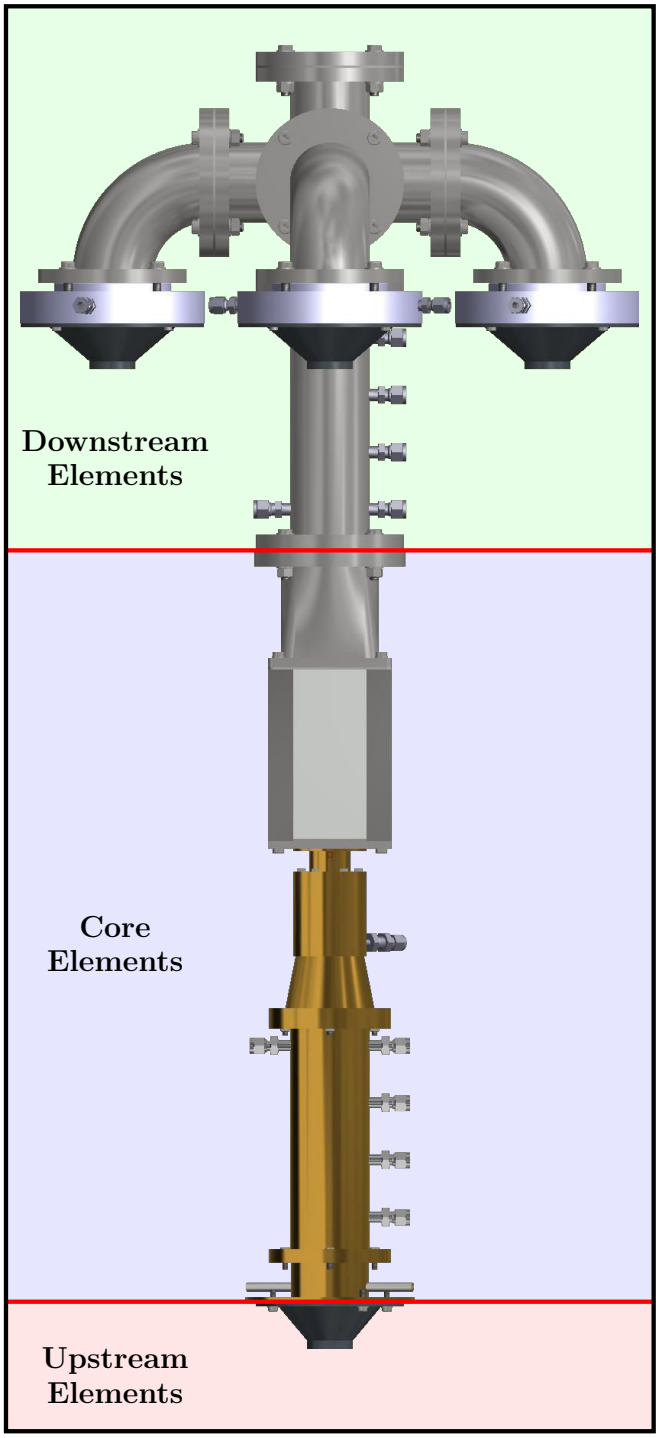

Figure 5.1: *Upstream, core and downstream elements of the NoiseDyn burner. The premixed gases are injected near the bottom of the experimental setup, flow through the core and downstream elements, and are then exhausted.*

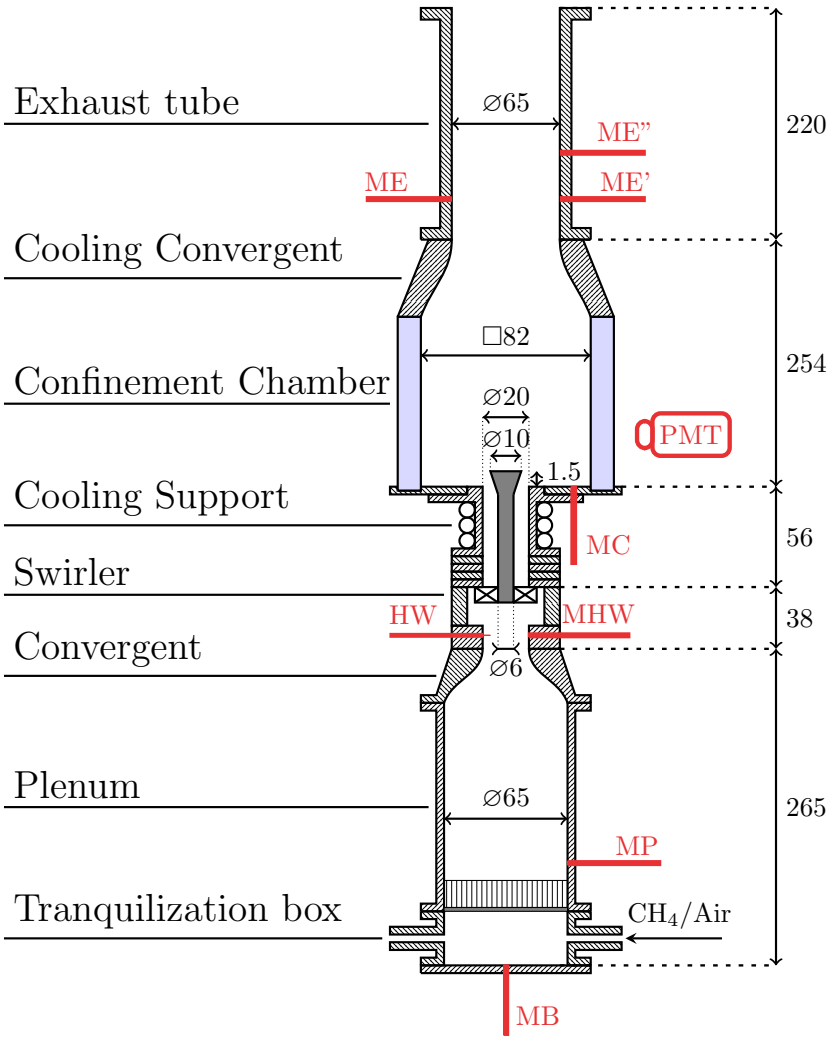

Figure 5.2: *The base configuration, used to describe the core elements of the NoiseDyn burner. Various diagnostics are represented in red. All dimensions are in mm.*

First, the core elements are examined in Sec. 5.1, followed by a brief description of the upstream and downstream elements in Sec. 5.2. The main geometrical configurations of the NoiseDyn burner are then listed in Sec. 5.3. Finally, the operating conditions explored in this work are detailed in Sec. 5.4.

5.1 The core elements

The core elements of the NoiseDyn burner are now presented through the so-called base configuration, depicted in Fig. 5.2.

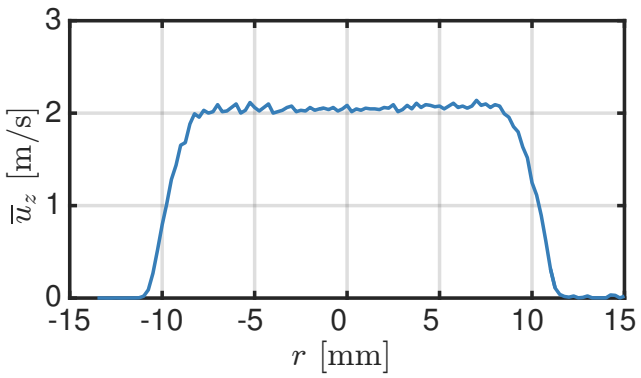

Figure 5.3: *Steady-state axial velocity profile $\bar{u}_z$ as a funtion of the distance r from the burner axis of symmetry measured at the convergent nozzle outlet with a hot wire probe.*

5.1.1 Tranquilization box, plenum and convergent

The mass flow rates of methane and air are controlled independently with Bronkhorst EL-FLOW mass flow meters and premixed far upstream of the burner. These elements are fully described in previous studies (Guiberti 2015) and therefore will not be detailed here. The perfectly premixed gases are then injected in the tranquilization box by two opposed apertures at the bottom of burner, as shown in Fig. 5.2. The flow is then pushed through a grid and a honeycomb structure that reduce the turbulence intensity in the plenum. Several apertures separated by a distance of 50 mm (except the last two apertures, located at the same axial position) can be used to flush-mount up to 5 microphones in the plenum, as shown in Fig. 5.1. A convergent nozzle (contraction ratio: 8.73) generates a laminar flow with a top-hat velocity profile just after the convergent. A velocity scan performed with a hot wire probe (Dantec Dynamics Mini-CTA 54T30 with a 55P16 probe) at the convergent exit, shown in Fig. 5.3, confirms that the flow has a top-hat velocity profile in this region.

Downstream the convergent nozzle, the same hot wire probe, called HW in Fig. 5.2, is used to determine the average $\bar{u}$ and fluctuating u' velocity signals at the nozzle outlet in the top-hat region of the velocity profile. An additional aperture, located in front of the hot wire probe at the same axial location, is used for further measurements. In Fig. 5.2, this aperture is used to set up a microphone denoted by MHW.

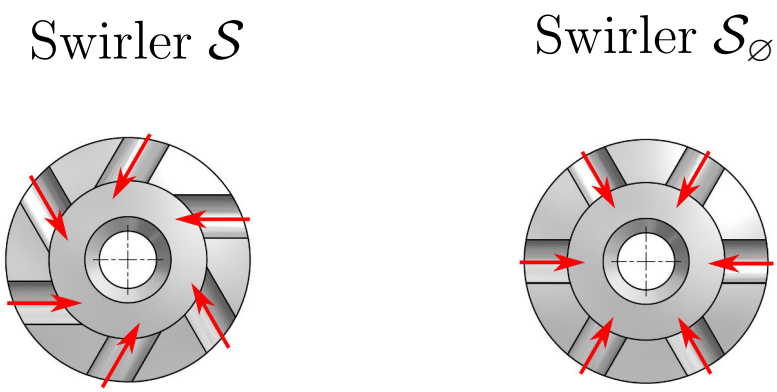

Figure 5.4: *Cross-sectional top view of the swirlers used in the NoiseDyn burner. A cylindrical bluff body fills the central aperture. The premixed gases flow from the outer to the inner regions of the swirler channels. (Left): Swirler $\mathcal{S}$ that generates a swirling flow characterized by a Swirl number $S = 0.8$. (Right): Swirler $\mathcal{S}_\varnothing$ that generates a non-swirling flow.*

5.1.2 Swirler

A swirler support is placed above the hot wire probe support. Two distinct radial swirlers, both featuring six holes of radius $R = 3$ mm (contraction ratio: 7.41), may be mounted on the swirler support depending on the type of flow desired. The first swirler, represented in Fig. 5.4-(Left) and denoted by $\mathcal{S}$, is used to create a swirling flow characterized by a Swirl number $S = 0.8$ measured at the burner outlet. The second swirler, represented in Fig. 5.4-(Right) and denoted by $\mathcal{S}_\varnothing$, is used to generate a non-swirling flow. This difference between the flows generated by swirlers $\mathcal{S}$ and $\mathcal{S}_\varnothing$ originates from the direction of the swirler channels. When they are directed towards the burner axis of symmetry, a non-swirling flow is generated. If the holes are off-centered, the flow rotates around the axis of symmetry, thus generating a swirling motion. In the remainder of this work, the various configurations of the NoiseDyn burner including swirler $\mathcal{S}$ (respectively swirler $\mathcal{S}_\varnothing$) will be denoted without a subscript (respectively with a subscript $\varnothing$).

The Swirl number of the flow generated by swirler $\mathcal{S}$ was determined using Laser Doppler Velocimetry with a measurement volume 2 mm away from the cylindrical bluff body of radius $R = 3$ mm topped by a cone of radius $R = 5$ mm that is used to stabilize the flame (see Fig. 5.2). The axial u_z, orthoradial u_θ, and radial u_r velocity components are determined for cold conditions without the combustion chamber for a bulk velocity $\bar{u}_b = 5.4$ m/s at the hot wire probe location. More details are presented in Chapter 6. The average and RMS profiles presented in Fig. 5.5 for the axial u_z, orthoradial u_θ, and radial u_r velocities are obtained with a spatial resolution of 0.5 mm. The Swirl number was then assessed using the formula (Chigier and Chervinsky 1967):

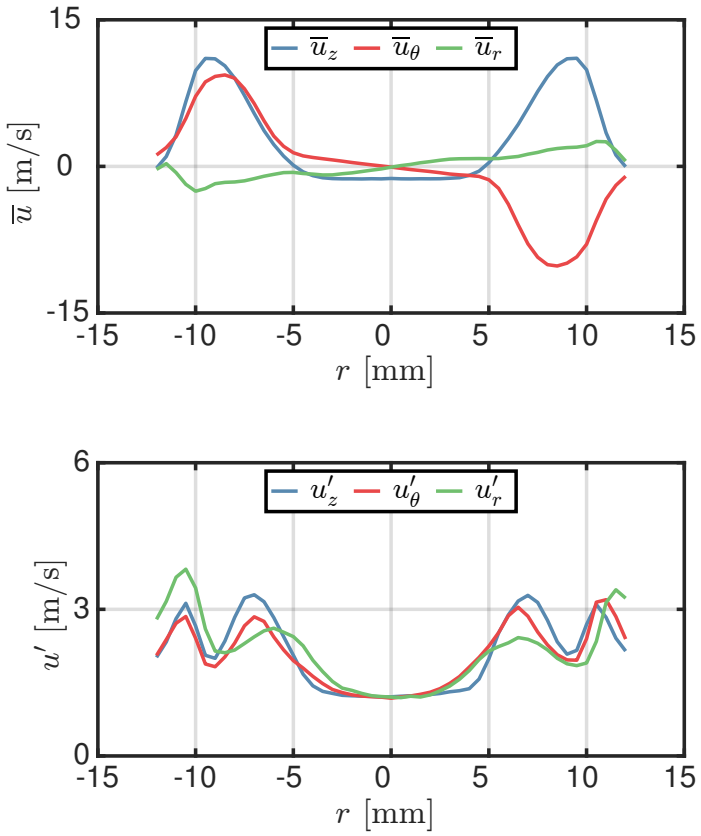

Figure 5.5: *Axial u_z (blue), orthoradial u_θ (red) and radial u_r (green) velocity profiles generated by swirler $\mathcal{S}$ for cold unconfined conditions with a bulk velocity $\bar{u}_b = 5.4$ m/s assessed at the hot wire location. (Top) Mean velocity profiles - (Bottom) RMS velocity profiles.*

$$S = \frac{1}{R} \frac{\int u_\theta u_z r^2 dr}{\int u_z^2 r dr} \tag{5.1}$$

where $R = 10$ mm is the injector inner radius. In addition to computing the Swirl number of the flow, these velocity scans were used to validate Large Eddy Simulations of the NoiseDyn burner in stable and unstable conditions (Merk et al. 2017).

The three velocity profiles presented in Fig. 5.5 are symmetric. The mean axial velocity profile features a central recirculation zone with negative velocities in the wake of the central bluff body which is also altered by vortex breakdown. This phenomenon promotes flame stabilization. The mean orthoradial velocity features a Rankine-like profile in the center part of the flow. The mean radial

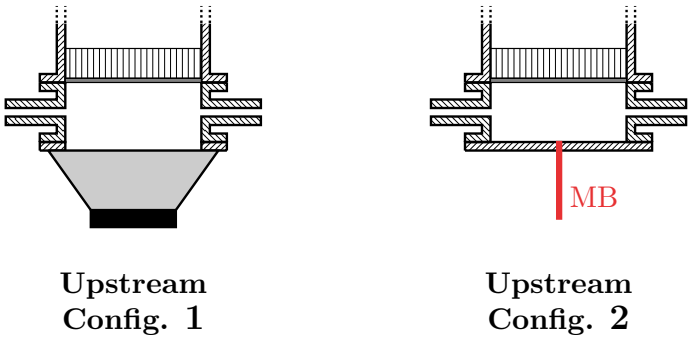

Figure 5.6: *Upstream configurations of the NoiseDyn burner. (Left): Configuration **1** - (Right): Configuration **2**.*

velocity is close to zero for all radial positions.

The Swirl number of the flow generated by swirler $\mathcal{S}_{\varnothing}$ was measured at the burner outlet in a different study using Particle Image Velocimetry (PIV) (Gatti et al. 2018). The three velocity profiles were also shown to be symmetric.

Downstream the swirler, the bluff body of conical shape extends into the combustion chamber over a distance of 1.5 mm, as shown in Fig. 5.2. The impact of the injector geometry on the Swirl number and shape of the Flame Transfer Function (FTF) was assessed in a separate study (Gatti et al. 2017).

5.1.3 Combustion chamber

A water-cooled support is placed above the swirler support to prescribe the combustion chamber backplate temperature. The backplate features an aperture through which a microphone or a thermocouple can be inserted, as shown in Fig. 5.2. Optical access into the combustion chamber is granted by four quartz windows that are transparent for both the visible and near ultraviolet wavelengths, corresponding to the OH* ($\lambda = 307$ nm) and CH* ($\lambda = 431$ nm) chemiluminescence wavelengths. Four metal rods are used to hold the four quartz windows. This assemby is made airtight by using ceramic fibers. A second convergent (contraction ratio: 2.03) with a water-cooled top flange is added at the top of the combustion chamber, followed by various exhaust components through which the burnt gases are exhausted to the atmosphere.

5.2 The upstream and downstream elements

The upstream and downstream elements of the NoiseDyn burner were designed to be easily interchanged depending on the experimental needs.

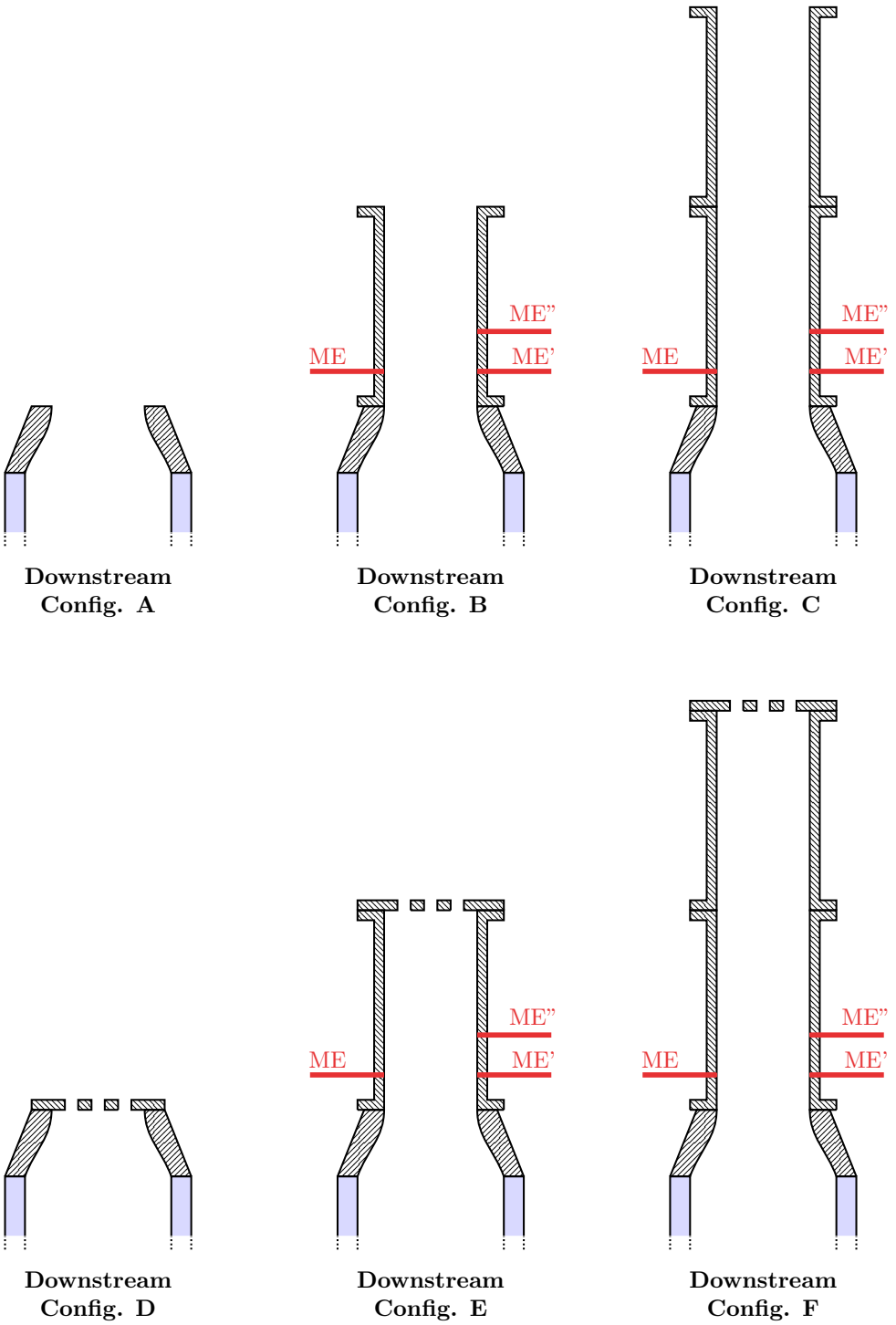

Figure 5.7: *Passive downstream configurations of the NoiseDyn burner. (Top Left) : Configuration **A** - (Top Center) : Configuration **B** - (Top Right) : Configuration **C** - (Bottom Left) : Configuration **D** - (Bottom Center) : Configuration **E** - (Bottom Right) : Configuration **F**.*

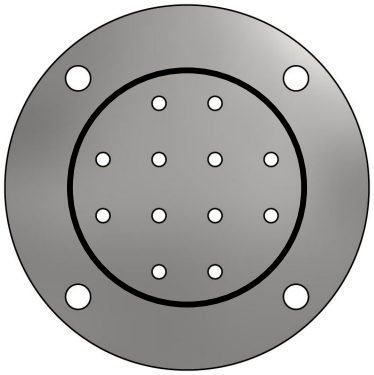

Figure 5.8: *Perforated plate featuring a square pattern of 12 holes of radius $R = 2.5$ mm with an inter-hole spacing $d = 20$ mm. This perforated plate is mounted at the top of the burner in Configurations **D**, **E** and **F**. The black circle represents the inner diameter of the exhaust element located just before the perforated plate.*

5.2.1 Upstream configurations

Two upstream configurations, represented in Fig. 5.6, are retained in the present work. The first upstream configuration, called Configuration **1** and depicted in Fig. 5.6-(Left), consists of a large loudspeaker (Monacor SP6/108PRO, 100 Watts RMS) and its adaptation support. This configuration is used to acoustically force the flow from the fresh gases region.

The second upstream configuration, called Configuration **2** and depicted in Fig. 5.6-(Right), is made of a rigid plate tightly attached to the bottom of the tranquilization box. This upstream configuration is used when natural thermoacoustic instabilities are studied for instance. It features an aperture through which a microphone or a thermocouple can be inserted.

In the remainder of this work, the superscripts **1** and **2** are used to designate the NoiseDyn burner mounted with the upstream elements corresponding to Configurations **1** and **2** respectively.

5.2.2 Passive downstream configurations

Seven downstream configurations are explored in this study. The first six configurations, called Configurations **A** to **F** and depicted in Fig. 5.7, are passive. They correspond to various acoustic boundary conditions obtained using between zero and two exhaust tubes of length 220 mm with and without a perforated plate placed at the top. Figure 5.8 is a representation of this perforated plate which features a square pattern of 12 holes of radius $R = 2.5$ mm with an inter-hole spacing $d = 20$ mm. For Configurations **B**, **C**, **E** and **F**, several apertures located on the first exhaust tube can be used to mount microphones,

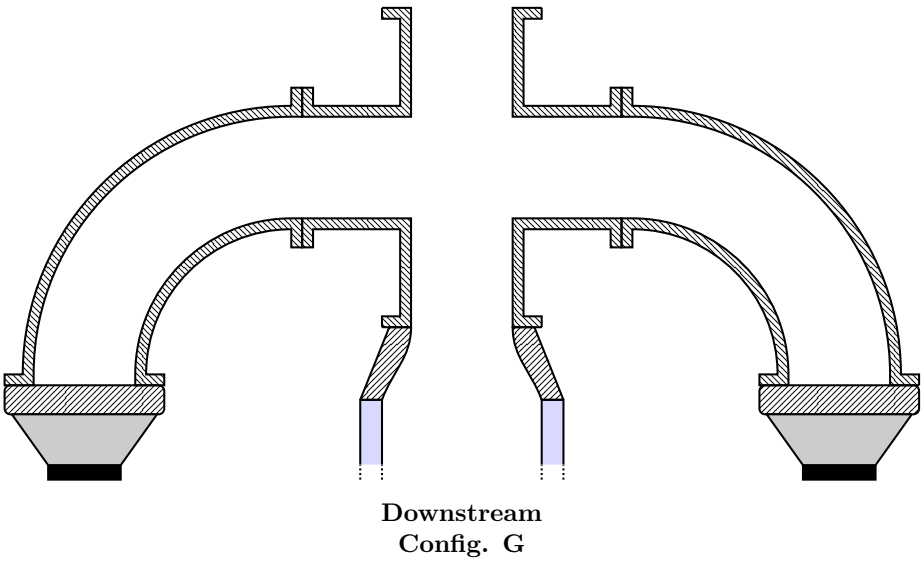

Figure 5.9: *Active downstream configuration of the NoiseDyn burner : Configuration **G**. The elements placed above the louspeakers are water-cooled in order to protect the loudspeakers' membranes.*

as shown in Fig. 5.1.

5.2.3 Active downstream configuration

An additional downstream configuration, called Configuration **G**, is used to generate downstream acoustic forcing, as represented in Fig. 5.9. Since acoustic forcing is applied in the high-temperature burnt gases region, the loudspeakers cannot be direcly mounted on the exhaust pipe. Moreover, thermal dilation due to the presence of the flame increases the bulk flow velocity and decreases the gas density in the hot gases region. More acoustic power is thus required in order to reach the same forcing level $|u'|/\bar{u}$ assessed at the hot wire location, in the fresh gases region. Due to these two reasons, the following design is adopted: first, an exhaust tube junction consisting of six branches is connected to the top of the convergent by its lower branch, as depicted in Figs. 5.1 and 5.2. The upper branch is used to exhaust the hot gases to the atmosphere. The first lateral branch is used to fix the setup to a rigid structure while the three remaining branches are connected to curved pipes, themselves connected to two or three loudspeakers (Monacor SP-6/108PRO - 100 W RMS). The elements holding the loudspeakers are water-cooled in order to protect the loudspeakers' membranes against high temperatures, as shown in Fig. 5.1. Since the loudspeakers are sealed to the setup, there is no flow inside the curved tubes.

Table 5.1: *Main geometrical configurations of the NoiseDyn burner.*

Config.	Up. forcing	Swirler	Exhaust tube	Perforate	Down. forcing
$\mathbf{A}^1$	✓	$\mathcal{S}$	0 mm	✗	✗
$\mathbf{B}^1$	✓	$\mathcal{S}$	220 mm	✗	✗
$\mathbf{C}^1$	✓	$\mathcal{S}$	440 mm	✗	✗
$\mathbf{E}^1$	✓	$\mathcal{S}$	220 mm	✓	✗
$\mathbf{F}^1$	✓	$\mathcal{S}$	440 mm	✓	✗
$\mathbf{G}^1$	✓	$\mathcal{S}$	0 mm	✗	✓
$\mathbf{A}^2$	✗	$\mathcal{S}$	0 mm	✗	✗
$\mathbf{B}^2$	✗	$\mathcal{S}$	220 mm	✗	✗
$\mathbf{C}^2$	✗	$\mathcal{S}$	440 mm	✗	✗
$\mathbf{D}^2$	✗	$\mathcal{S}$	0 mm	✓	✗
$\mathbf{E}^2$	✗	$\mathcal{S}$	220 mm	✓	✗
$\mathbf{F}^2$	✗	$\mathcal{S}$	440 mm	✓	✗
$\mathbf{G}^2$	✗	$\mathcal{S}$	0 mm	✗	✓
$\mathbf{B}^1_\varnothing$	✓	$\mathcal{S}_\varnothing$	220 mm	✗	✗
$\mathbf{C}^1_\varnothing$	✓	$\mathcal{S}_\varnothing$	440 mm	✗	✗
$\mathbf{G}^1_\varnothing$	✓	$\mathcal{S}_\varnothing$	0 mm	✗	✓

5.3 List of the main geometrical configurations

The NoiseDyn burner is a highly modular burner with two possible upstream configurations, seven possible downstream configurations and two different swirlers. Twenty-eight different configurations may be built from these elements. However, not all possible combinations of these configurations have been explored. Table 5.1 summarizes the main geometrical configurations explored in this work.

5.4 Operating conditions

The operating conditions are the same for all the geometrical configurations explored in this study. A perfectly premixed methane/air flame with an equivalence ratio $\phi = 0.82$ and a thermal power of 5.5 kW is stabilized inside the combustion chamber. The corresponding adiabatic flame temperature is $T_{ad} = 2022$ K assessed using a GRI-MECH 3.0 detailed chemistry mechanism. The bulk velocity associated with these operating conditions in a tube of diameter $D = 22$ mm corresponding to the hot wire probe support is $\overline{u}_b = 5.4$ m/s,

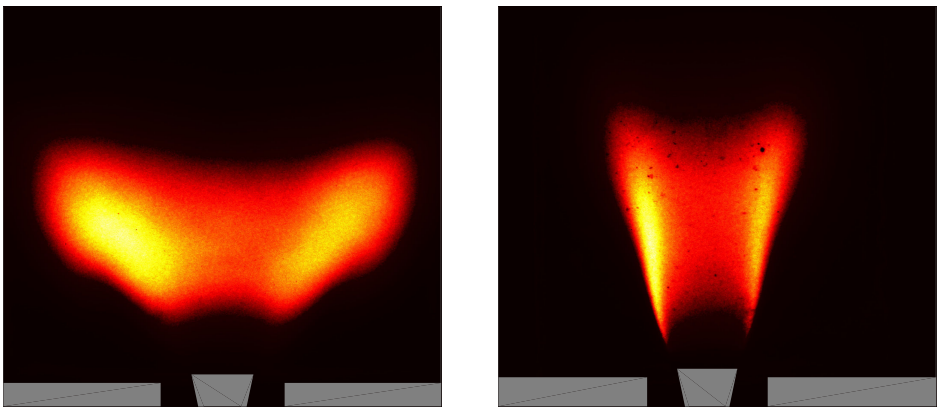

Figure 5.10: *Steady-state OH* chemiluminescence distributions integrated over the line of sight obtained with an ICCD camera equipped with an OH* filter for two different swirlers. (Left): Swirler $\mathcal{S}$ with $S = 0.8$ - (Right): Swirler $\mathcal{S}_{\varnothing}$ with $S \sim 0$.*

yielding a Reynolds number of approximately $Re = \bar{u}_b D/\nu = 7000$ where ν is the kinematic viscosity of the fresh gases assessed at $\overline{T}_u = 293$ K. For cold flow conditions, methane is not injected and the air mass flow rate is increased in order to reach the same bulk velocity $\bar{u}_b$ as for reactive conditions. In all cases, the forcing level $|u'|/\bar{u}$ is measured with the hot wire probe located before the swirler and denoted by HW in Fig. 5.2.

For cold and reactive conditions, the highest velocity $\bar{u}_{max} = 12$ m/s is reached by the flow inside the swirler injection holes. It corresponds to a Mach number $M_{max} = 0.035$ meaning that the flow regime remains incompressible everywhere inside the NoiseDyn burner.

The steady-state OH* chemiluminescence distributions corresponding to the flames stabilized above the cylindrical bluff body are displayed in Fig. 5.10-(Left) for swirler $\mathcal{S}$ and Fig. 5.10-(Right) for swirler $\mathcal{S}_{\varnothing}$. These pictures were averaged over a hundred snapshots obtained with an ICCD camera, as described in Chapter 6.

5.5 Conclusion

A highly modular burner, called the NoiseDyn burner, was designed to study the acoustic response of premixed confined turbulent flames. Various upstream and downstream configurations were introduced and the burner core elements, including the swirler and the combustion chamber, were also described. Finally, the main geometrical configurations used in this study were listed as well as the retained operating conditions.

Chapter 6

Diagnostics

The diagnostics employed with the NoiseDyn burner presented in Chapter 5 are described in this chapter. Temperature measurements followed by pressure drop and velocity measurements are first introduced. Then, a description of acoustic pressure measurements is performed. Chemiluminescence and flame imaging techniques are then presented. Finally, two distinct methods used to determine the acoustic impedance are described in details.

6.1 Temperature measurements

6.1.1 Thermocouples and infrared pyrometer

Gas and wall temperature measurements are performed using standard K-type thermocouples for temperatures lower than 1200 K and R-type thermocouples for temperatures larger than 1200 K. When measuring the temperature of a hot gas, a correction accounting for the radiative heat losses at the thermocouple surface should be applied (Hindasageri et al. 2013). However, these corrections are of the order of the measurement accuracy $\Delta T \sim 10 - 20$ K and always smaller than 2% of the absolute temperature value. As a consequence, the radiative heat losses correction is neglected for all premixed turbulent flame experiments presented in this work.

An additional temperature measurement technique, called infrared pyrometry, is employed to measure wall temperatures inside the burner during reactive operation. These measurements are performed with a Fluke 572-2 pyrometer, which infers the wall temperature from thermal radiation (called blackbody radiation and following Planck's law) emitted by the surface of interest. If the surface emissivity ϵ is exactly known, the measurement accuracy is around 1 %.

Table 6.1: *Exhaust gases temperature for Configurations **A**, **B** and **C** of the NoiseDyn burner.*

Configuration	Exhaust tube	Perforated plate	Exhaust temperature
A	0 mm	✗	1129 K ± 31 K
B	220 mm	✗	996 K ± 27 K
C	440 mm	✗	843 K ± 23 K

6.1.2 Gas and wall temperature measurements

For cold flow conditions, the gas temperature is equal to $\overline{T}_u = 293$ K everywhere inside the burner. For reactive conditions, the gas temperature is equal to $\overline{T}_u = 293$ K upstream the confinement chamber and increases drastically at the flame location to a value approaching the adiabatic flame temperature. The parietal and radiative heat losses are responsible for a drop in temperature after the flame. These heat losses are geometry-dependent and the length of the elements placed downstream the confinement chamber will strongly affect them. As a consequence, the average hot gases temperature measured at the exhaust tube exit and along the burner axis of symmetry differs depending on the downstream configuration, as exemplified in Table 6.1.

Numerical simulations of thermoacoustically stable and unstable configurations of the NoiseDyn burner with parietal heat losses are investigated by Prof. Polifke's research group (Merk et al. 2017), thus requiring additional wall temperature measurements. First, the average temperature of the outer surface of the quartz windows is measured with a thermocouple for stable reactive conditions. For each of the four windows, five measurements at different locations are performed. The average temperature of the outer surface of the quartz windows is found to be 622 K ± 17 K, with values ranging from 580 K ± 16 K at the bottom of the confinement chamber up to 651 K ± 18 K at the center and down to 579 K ± 16 K at the top of the window, near the combustion chamber exhaust nozzle.

Another temperature measurement needed for numerical simulations is the conical bluff body surface temperature during stable reactive operation. It is measured using the infrared pyrometer (Fluke 572-2) for a surface emissivity $\epsilon = 0.85$ valid for stainless steel oxydized at high temperatures (Gubareff et al. 1960). The average temperature is found to be equal to 608 K ± 79 K. However, this measurement should be considered with caution since it was performed without the confinement chamber. Besides, the surface emissivity of the conical bluff body is poorly known, thus generating large measurement uncertainties.

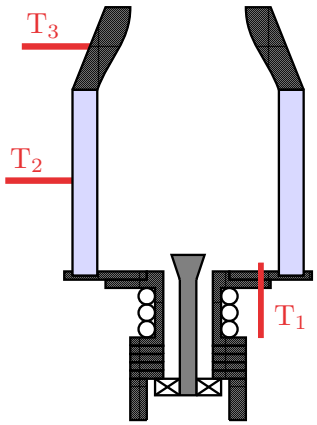

Figure 6.1: *Experimental setup used to assess the thermalization time τ_c of the NoiseDyn burner. Three K-type thermocouples are used: T_1, T_2 and T_3.*

Three additional thermocouples, denoted by T_1, T_2 and T_3 in Fig. 6.1, are used to measure the transient temperature at the bottom of the combustion chamber, inside one of the metal rods and on the outer surface of the combustion chamber exhaust nozzle respectively, as detailed in the next section.

6.1.3 Thermalization time

Just after the flame ignition, the temperature of the elements downstream the flame suddenly increase and reach their steady-state value after a certain period of time called thermalization time and denoted by τ_c. During this transient regime, heat losses as well as sound speed in the hot gases evolve with time thus impacting flow stabilization (Guiberti et al. 2015) and the thermoacoustic behavior of the combustor. In order to eliminate this variability, all measurements presented in this work are performed for $t > \tau_c$, when the wall and gas temperatures are stabilized everywhere.

In order to estimate the thermalization time τ_c, three K-type thermocouples are placed at various locations on the NoiseDyn burner, as depicted in Fig. 6.1. The first thermocouple T_1 is inserted inside the combustion chamber through the aperture in the chamber backplate. The tip of thermocouple T_1 protrudes inside the hot gases recirculation zone over a distance $l \sim 2$ mm. The second thermocouple T_2 is flush-mounted inside one of the metal rods maintaining the combustion chamber structure. It is located 84 mm downstream the combustion chamber backplate. Finally, the last thermocouple T_3 is in contact with the outer surface of the combustion chamber exhaust nozzle. The time evolution of these temperatures is represented in Fig. 6.2 for Configuration A^2 (See Table 5.1 in Chapter 5). Measurements are also performed for other configurations, leading to similar results.

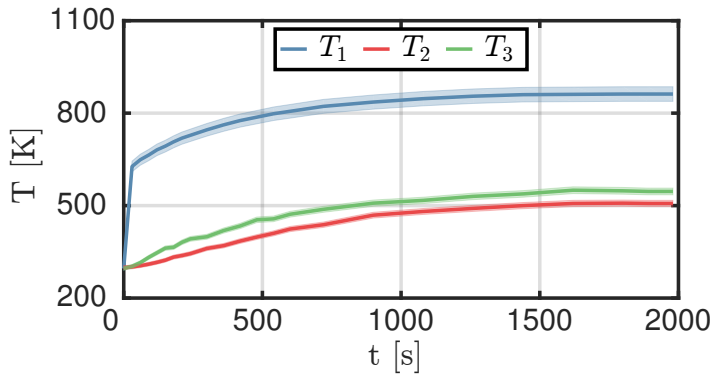

Figure 6.2: *Temperature as a function of time for three different K-type thermocouples. (Blue): T_1 located in the hot gases region, just after the combustion chamber backplate - (Red): T_2 flush-mounted in one of the metal rods of the combustion chamber - (Green): T_3 placed in contact with the outer surface of the combustion chamber exhaust nozzle. The shaded area around each curve accounts for the measurement uncertainties.*

At all times, the highest temperature is reached in the hot gases recirculation zone, measured by thermocouple T_1, followed by the temperature of the outer surface of the combustion chamber exhaust nozzle, measured by thermocouple T_3. The temperature inside the combustion chamber metal rod, measured by thermocouple T_2, is the lowest. Their respective steady-state values are 862 K $\pm$ 24 K, 546 K $\pm$ 11 K and 507 K $\pm$ 10 K. After 21 minutes, the temperatures have reached 97% to 99% of their steady-state values. After 30 minutes, the difference between the measured temperatures and associated steady-state values is of the order of a few degrees. As a consequence, the thermalization time τ_c of the NoiseDyn burner is comprised between 20 and 30 minutes depending on the desired accuracy. The value $\tau_c = 20$ minutes is retained here.

6.2 Pressure drop measurements

The NoiseDyn burner is operated at ambient pressure. The pressure drop across the NoiseDyn burner is defined as the difference between the pressure in the tranquilization box and the ambient pressure (See Fig. 5.2 in Chapter 5). The swirler and the perforated plate placed at the top of the burner in Configurations **D**, **E** and **F**, shown in Fig. 5.7, are responsible for most of the total pressure drop across the setup.

Pressure drops have to be considered for two main reasons. First, a large pressure drop implies that the absolute pressure inside the burner will vary

Table 6.2: *Pressure drops across the NoiseDyn burner for cold and reactive conditions for all configurations explored in this study. The burner is operated at atmospheric pressure.*

Configuration	Cold pressure drop	Reactive pressure drop
A B C	250 Pa	315 Pa
D E F	300 Pa	410 Pa
G	250 Pa	417 Pa
$\mathbf{A}_{\varnothing}$ $\mathbf{B}_{\varnothing}$ $\mathbf{C}_{\varnothing}$	125 Pa	128 Pa

considerably, thus impacting the mean flow variables such as gas density. Furthermore, pressure drops may have an impact on the thermoacoustic behavior of the combustor, especially when the Mach number of the flow becomes significant (Paschereit and Polifke 1998; Polifke et al. 2001).

Pressure drops across the NoiseDyn burner are measured for all downstream configurations and all swirlers. The upstream elements have no impact on the pressure drop. These measurements are performed for both thermoacoustically stable reactive conditions and cold conditions using an electronic differential manometer (KIMO MP111) and a U-shaped tube differential manometer connected to the bottom of the tranquilization box. The U-shaped tube leads to more precise measurements since it filters high-frequency oscillations of the pressure without any further operation. The results are averaged and summarized in Table 6.2.

For all configurations investigated, the pressure drop across the NoiseDyn burner is always lower than 0.5% of the ambient pressure. As a consequence, the mean pressure inside the NoiseDyn burner is considered to be constant in the remainder of this work. Moreover, the maximum Mach number in the NoiseDyn burner for the retained operating conditions is very low as discussed in Sec. 5.4. Therefore, the impact of the pressure drop on the fluctuating physical variables is also neglected except if mentioned otherwise.

6.3 Velocity measurements

Two velocity measurement techniques are used in this work: Constant Temperature Anemometry (CTA) performed with hot wire probes, as described in Sec. 6.3.1, and Laser Doppler Velocimetry (LDV), as described in Sec. 6.3.2.

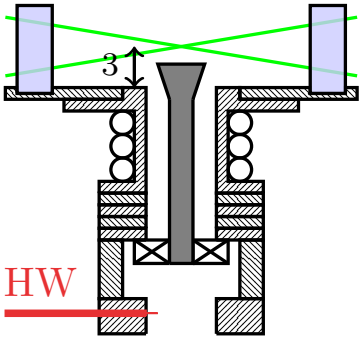

Figure 6.3: *Illustration of the velocity measurement techniques used in this study. The fresh gases velocity in the top-hat region of the velocity profile upstream the swirler and at the bottom of the combustion chamber are measured with a hot wire probe denoted by HW and with Laser Doppler Velocimetry respectively. All dimensions are in mm.*

6.3.1 Constant Temperature Anemometry with a hot wire probe

Basic principle

Constant Temperature Anemometry (CTA) probes are made of several elements: the sensor itself, where the velocity measurement is achieved, the sensor supports on which the sensor is welded, the probe body and the electrical connections. The hot wire probe sensor used in this study is a thin wire of diameter $D \sim 5$ μm and length $L \sim 1$ mm maintained at a constant temperature. When it is placed inside a flow, the hot wire tends to cool down through forced convection. A servo amplifier modulates the current going through the wire in order to keep the wire temperature constant. At any instant, the velocity of the fluid flowing around the wire can be precisely estimated by measuring the bridge voltage on which the hot wire probe is mounted.

The relation linking convective heat transfer Q_c to the flow velocity u passing around the hot wire is given by King's law (King 1914):

$$Q_c = A_l + B_l u^{n_l} \tag{6.1}$$

where A_l, B_l and n_l are parameters to be determined during the hot wire probe calibration procedure. Since the only sizable heat losses are convective, the power lost by the wire through Joule heating is equal to Q_c. Using Ohm's law and introducing the bridge voltage V_t, King's law becomes:

$$V_t^2 = A_1 + B_1 u^{n_1} \tag{6.2}$$

where A_1, B_1 and n_1 are new calibration parameters. Equation (6.2) is a simple expression linking the hot wire voltage output V_t to the incoming flow velocity

u. The physical complexity associated with convective heat transfer is hidden in parameters A_1, B_1 and n_1, which depend on the hot wire over-temperature and on the fluid's physical properties, such as the kinematic viscosity ν and thermal conductivity κ. It is often easier to consider Eq. (6.2) as an empiric expression with ad-hoc parameters which have to be determined with a calibration procedure.

Performing flow velocity measurements with a CTA hot wire probe has advantages and drawbacks. On one hand, hot wire probes are simple-to-use devices producing high-accuracy measurements if correctly calibrated and with a very high frequency response (up to 100 kHz). On the other hand, hot wire probes are fragile, do not withstand high temperatures, and can be used to determine the flow velocity at a given location only (0D measurements). Moreover, hot wire probes should always be orthogonal to the flow direction if a correct estimate of the flow velocity is to be achieved. Finally, the presence of a hot wire probe generates flow perturbations which may significantly alter the flow dynamics. The gas composition also alters the output signal of a hot wire probe (Guiberti 2015). All these aspects were considered in the present work in order to reduce the measurement uncertainties.

CTA measurements applied to the NoiseDyn burner

A hot wire probe, denoted by HW in Figs. 5.2 and 6.3, is used in the NoiseDyn burner. It is placed after the convergent, in the top-hat region of the velocity profile, in a tube of inner radius $R = 11$ mm. This hot wire probe (Dantec Dynamics Mini-CTA 54T30 with a 55P16 probe) is used to measure the average $\bar{u}$ and fluctuating u' velocity in the laminar region of the flow which leads to a value of the forcing level $|u'|/\bar{u}$ at a given frequency. The hot wire probe parameters A_1, B_1 and n_1 are determined during a calibration procedure performed before all experiments.

6.3.2 Laser Doppler Velocimetry

Basic principle

Laser Doppler Velocimetry (LDV), also called Laser Doppler Anemometry (LDA), is an absolute velocity measurement technique. It is based on the direct link between the luminosity variations of a pattern of two interfering laser beams crossed by moving targets and the velocity of these moving targets. Velocity measurements using this technique are local (e.g. 0D) but depending on the number of interfering laser beams, one to three components of the velocity may be measured concomitantly.

The first step is to seed the flow with a large amount of particles of very small radius, usually a few micrometers. These particles can be either liquid, in which

case they are produced by a nebulizer that generates a very fine mist of oil droplets, or solid, introduced inside the setup through a cyclonic chamber. The inertia of these particles is assumed to be negligible because of their dimension. As a consequence, the particles follow the flow instantly without any resistance.

Once the flow is seeded, two laser beams of coherent, monochromatic and collimated light are used to generate a pattern of straight fringes as they interfere in the region where the flow velocity is measured. The simplest way to obtain two laser beams with these properties is a use a single laser and a beam splitter. Though any kind of laser can be used in theory, it is preferable to use a laser emitting light in the visible spectrum for safety reasons.

A photodiode is then installed so that the light emitted by the interference pattern is entirely received. When a particle crosses the interference fringes, the luminosity measured by the photodiode varies. The frequency at which the luminosity oscillates is then related to the particle velocity and hence to the flow velocity (Boutier 2012).

Like all measurement techniques, Laser Doppler Velocimetry has advantages and drawbacks. On one hand, this technique provides accurate time resolved velocity measurements and it only requires one initial optical alignment procedure. If the seeding particles are small enough, the flow is not perturbed by the measurement. On the other hand, setting the laser, optics and electronics required for LDV measurements can quickly become tedious, even if modern ready-to-use LDV apparatus are much simpler to use. Furthermore, since the flow is seeded with particles, other measurement techniques such as CTA performed with hot wire probes are incompatible with LDV. Finally, a powerful laser is needed for LDV measurements, which raises safety issues.

LDV measurements applied to the NoiseDyn burner

In the present study, velocity scans are obtained by placing the NoiseDyn burner on two orthogonal step-by-step engines (Micro-contrôle MMTM-200PP commanded by a Micro-contrôle ITL09). The three components of the velocity are measured by Laser Doppler Velocimetry (LDV) at the burner outlet. The measurement volume is in this case located 3 mm above the injector outlet, as shown in Fig. 6.3.

A continuous 3-Watts Argon Laser is used to generate two sets of two interfering beams of wavelengths $\lambda = 488$ nm and $\lambda = 514$ nm in the radial and axial directions respectively. Each set of monochromatic beams are separated by a distance $l = 40$ mm before they reach a converging lens of focal distance $f = 250$ mm used to create the interference pattern. The flow is seeded with small oil droplets of diameter 3 μm produced by a nebulizer (Durox et al. 1999).

Table 6.3: *Correspondence between Sound Pressure Levels (SPL) in decibels, acoustic pressure fluctuations amplitudes p' in pascals and order of magnitude of the ratio between p' and the ambient pressure $\bar{p}$.*

SPL (dB)	0	20	40	60	80	100	120	140
p' (Pa)	2.10^{-5}	2.10^{-4}	2.10^{-3}	2.10^{-2}	2.10^{-1}	2	20	200
$p'/\bar{p}$	10^{-10}	10^{-9}	10^{-8}	10^{-7}	10^{-6}	10^{-5}	10^{-4}	10^{-3}

The data collection rate is always greater than 10000 s^{-1} and the LDV bench was checked before all measurements. Mean and RMS velocity profiles were obtained for the radial, orthoradial and axial velocity components for cold flow conditions, as depicted in Fig. 5.5. During these measurements, the combustion chamber was removed for accessibility reasons.

6.4 Acoustic pressure measurements

6.4.1 Sound Pressure Level

Sound waves propagating in a fluid are small-amplitude fluctuations of the fluid pressure, density and velocity around their respective average values (Rienstra and Hirschberg 2016). One way to quantify the acoustic level is the Sound Pressure Level (SPL), given in decibels, and defined as:

$$SPL = 20 \log_{10} \left(\frac{p'}{p_{ref}} \right) \tag{6.3}$$

where p' is the root-mean-square amplitude of the acoustic pressure fluctuations and $p_{ref} = 2.10^{-5}$ Pa is a reference pressure fluctuation amplitude corresponding to the human hearing threshold at a frequency $f = 1$ kHz. Using Eq. (6.3), the amplitude of the acoustic pressure fluctuations associated with several Sound Pressure Levels are summarized in Table 6.3.

According to Table 6.3, the amplitudes of the acoustic pressure fluctuations in a combustor are three to six orders of magnitude lower than the ambient pressure depending on the thermoacoustic stability of the combustor. Therefore, measuring the acoustic pressure fluctuations is not trivial and cannot be performed with a simple differential manometer. It requires specific devices, called microphones, that are able to detect small-amplitude variations of the fluid pressure at relatively high frequencies.

6.4.2 Externally polarized microphones

Basic principle

An ideal microphone is a device that converts the incoming acoustic waves into electrical signals with the same frequency spectrum and same relative amplitudes. When this signal is sent back to an ideal loudspeaker, the exact original acoustic wave is emitted. On the other hand, real microphones tend to distort the signals during conversion and transmission.

A variety of pressure transducers exists depending on the type of application (confined or unconfined environment), frequency range (minimum and maximum operating frequencies) and dynamic range (minimum and maximum Sound Pressure Levels) that are investigated. Externally polarized microphones with a 200 V polarization provide accurate and reproducible results. Their sensitivity is stable in time. Moreover, they can withstand higher temperatures compared to other types of microphones such as prepolarized microphones. As a consequence, all microphones used in this study are externally polarized microphones.

Externally Polarized Condenser Microphones (EPCM) are based on the following principle: a diaphragm, sometimes called a membrane, is placed at the tip of the microphone. When an acoustic wave of frequency f hits the diaphragm, it moves at the same frequency f and its displacement is related to the Sound Pressure Level. A few millimeters away from the membrane, a fixed backplate is supplied with a constant voltage (200 V). The association of the microphone membrane and backplate forms a capacitor which voltage is directly proportional to the amplitude of the incoming pressure wave. This voltage is then amplified by a preamplifier and conditioning amplifier before it can be further used.

Acoustic pressure measurements applied to the NoiseDyn burner

In addition to the acoustic velocity measurements obtained with the hot wire probe, the acoustic pressure inside the NoiseDyn burner is measured at various axial locations using several externally polarized microphones (Bruel & Kjaer 4938 1/4-inch pressure-field microphones) connected to preamplifiers (Bruel & Kjaer 4938-A-011) which are subsequently linked to conditioning amplifiers (Bruel & Kjaer 2690). All microphones are first calibrated with a known sound source (94 dB, 1000 Hz). The spectrum of this source, shown in Fig. 6.4, is measured with a calibrated microphone. The retained microphones frequency range is $4 - 70000$ Hz and their dynamic range is $30 - 172$ dB with a sensitivity $S = 1.6$ mV/Pa. The microphone can operate at temperatures up to 450 K and withstand temperatures up to 600 K before being damaged.

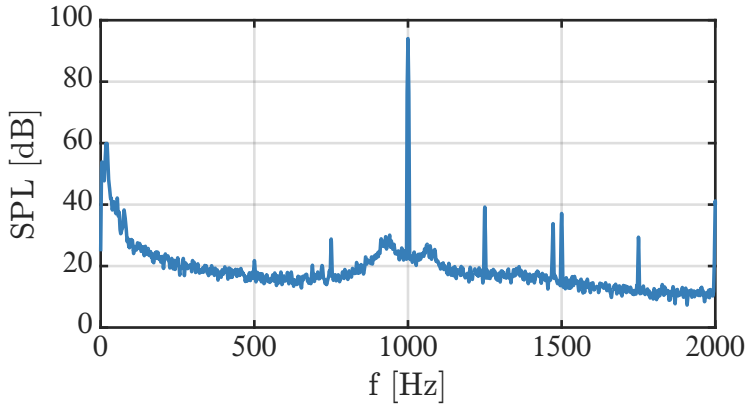

Figure 6.4: *Sound source (94 dB, 1000 Hz) spectrum measured with a calibrated microphone. The acoustic pressure was recorded during $t = 8$ s at a sampling frequency $f_s = 50$ kHz.*

Various microphones are mounted on the NoiseDyn burner at different axial locations, as represented in Fig. 6.5. Because of the geometry of the different upstream and downstream elements, some of these microphones have to be removed for certain configurations. The first microphone, denoted by **MB**, is flush-mounted on the rigid plate located at the bottom of the tranquilization box. It is not mounted when this rigid plate is replaced by a loudspeaker, e.g. when upstream forcing is applied. The second microphone, **MP**, is flush-mounted at the bottom of the plenum, downstream of the honeycomb. Another microphone, **MHW**, is flush-mounted in front of the hot wire probe, at the same axial location. The acoustic pressure is also measured at the bottom of the combustion chamber with microphone **MC** and in the first exhaust tube with microphones **ME** and **ME'**, located in front of each other at the same axial location, and **ME"** located 50 mm downstream. These last three microphones are used to reconstruct the acoustic velocity fluctuations in order to determine the acoustic reflection coefficient at the exhaust tube outlet, as explained in Sec. 6.7.

6.4.3 Water-cooled waveguides

Microphones **MC**, **ME**, **ME'** and **ME"** are not directly flush-mounted onto the NoiseDyn burner as they are located in the hot gases region. In this region, the temperature is well beyond the maximum operating temperature of these microphones (450 K) and the hot gases have to be cooled down before any acoustic measurement can be performed. Water-cooled waveguides, represented in Fig. 6.6, are subsequently used whenever an acoustic pressure measurement is performed in the hot gases region (Tran et al. 2009a).

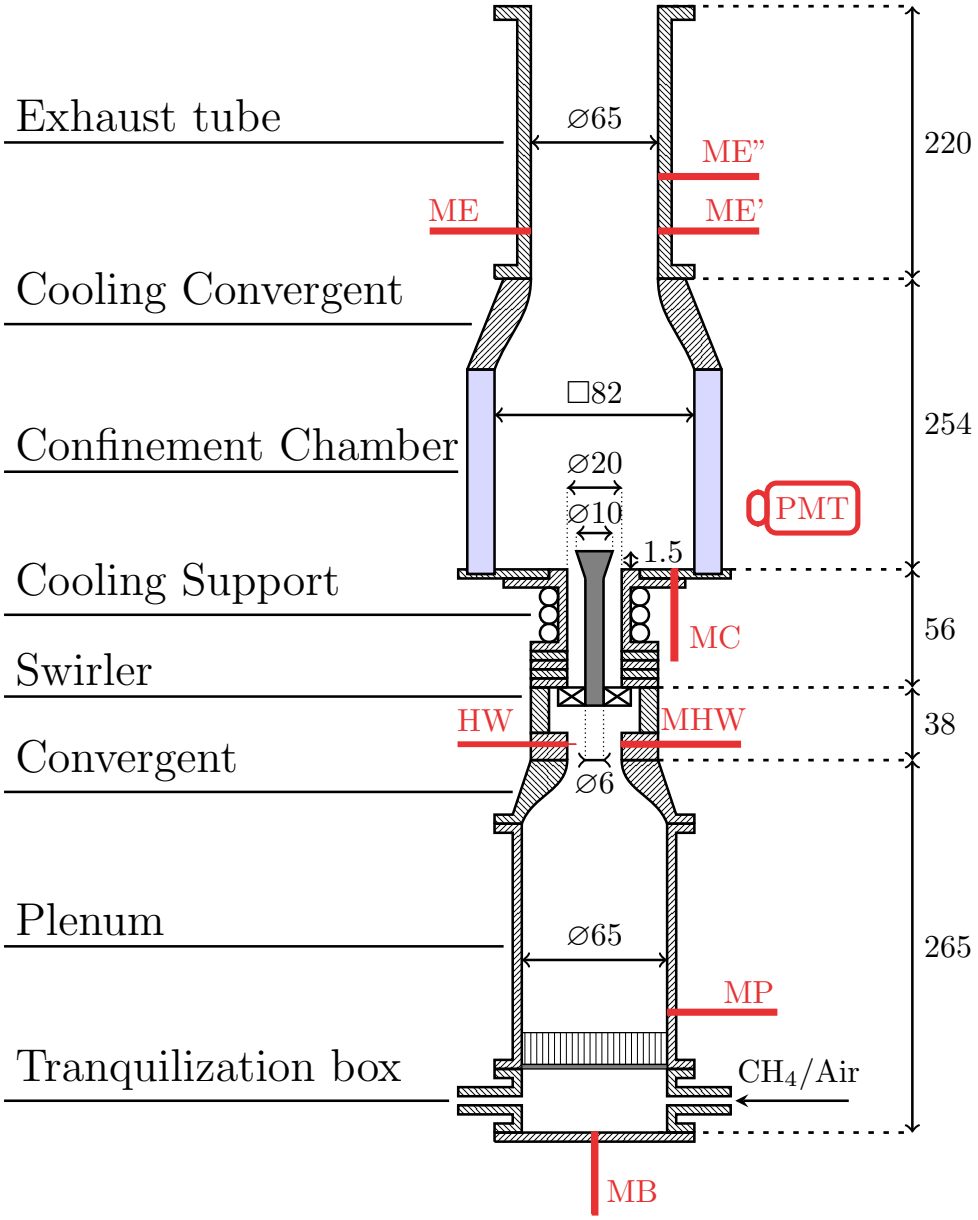

Figure 6.5: *Illustration of the base configuration of the NoiseDyn burner (Black & Gray) with various embedded diagnostics (Red). All dimensions are in mm.*

The water-cooled waveguides are used as follows. First, they are flush-mounted onto the setup at the desired location. A cavity filled with water is wrapped around the main pipe of inner radius $R = 4$ mm. Water enters at the bottom of the cavity and is exhausted at the top of the cavity, as depicted in Fig. 6.6. The water flowing through this cavity absorbs most of the heat present in the hot gases. The microphone is then flush-mounted on the main pipe after the

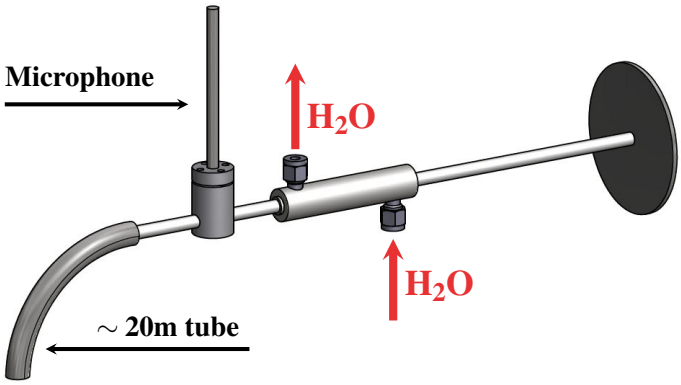

Figure 6.6: *Sketch of a water-cooled waveguide flush-mounted on the NoiseDyn burner (Right surface).*

water cavity, in the region where the gas are at the ambient temperature, as shown in Fig. 6.6. The distance between the microphone and the wall on which the waveguide is flush-mounted is $l = 230$ mm. After the microphone, a closed pipe of length $l = 20$ m is added in order to damp the reflected sound waves generated at the acoustic boundary. Since the pipe ending is closed, the gases do not flow through the waveguide. Each waveguide is associated with a given microphone and a given closed tube and the acoustic response of the whole system has to be measured in a separate experiment.

The waveguides represented in Fig. 6.6 distort the acoustic pressure signals because of acoustic propagation within the tube (phase shift) and sound absorption and reflections (gain distortions). In order to characterize these distortions, a first microphone is flush-mounted onto a straight pipe while a second microphone is mounted on the waveguide which is itself flush-mounted onto the pipe at the same axial position. An upstream loudspeaker is then driven by a constant voltage signal for forcing frequencies ranging from $f = 20$ Hz to $f = 1$ kHz for cold flow conditions ($\overline{T}_u = 293$ K). For each forcing frequency, the microphone signals are recorded at a sampling frequency $f_s = 20$ kHz during $t = 1$ s. The acoustic pressure signals corresponding to a forcing frequency $f = 1$ kHz are shown in Fig. 6.7. It is clear from this figure that both a phase shift and a gain distortion are generated by the waveguide.

The transfer functions of all waveguides are then determined as functions of the forcing frequency using these signals. One of these transfer functions is represented in Fig. 6.8 in blue. The transfer function corresponding to an ideal waveguide that only generates a phase shift is also represented in Fig. 6.8 in red. As expected, the waveguide generates a phase shift but also a gain distortion.

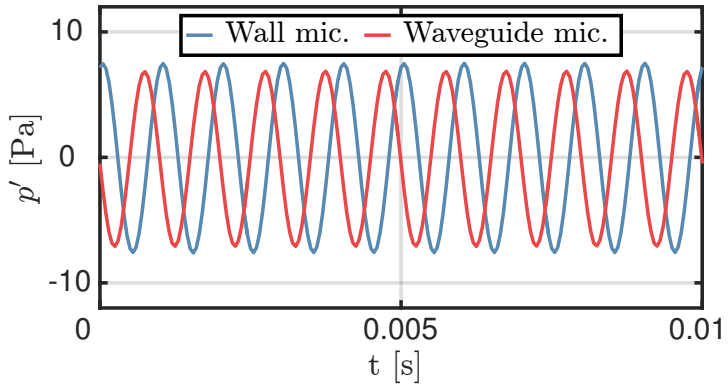

Figure 6.7: *Acoustic pressure inside a straight pipe as a function of time recorded at a sampling frequency $f_s = 20$ kHz. Flush-mounted microphone (Blue) and microphone mounted on a water-cooled waveguide (Red). Measurements were performed for cold flow conditions and with an upstream loudspeaker driven by a voltage signal of frequency $f = 1000$ Hz.*

These transfer functions are measured for cold flow conditions. However, they are still assumed to be valid for both cold and reactive conditions since the gas temperature inside the waveguide was checked to remain close to $\overline{T}_u = 293$ K even for reactive conditions. Once the waveguide transfer function is determined, the acoustic pressure inside the NoiseDyn burner at the waveguide location can be easily reconstructed. Phase shifts and gain distortions generated by waveguides are eliminated using this procedure.

6.5 Chemiluminescence measurements

Very high temperatures are reached at the flame front leading to the formation of free radicals such as OH* or CH* that are in an excited state and emit light during their transition to the fundamental state. This process is called chemiluminescence. The corresponding wavelengths are precisely known and can be used as flame front tracers (Gaydon 1957). Moreover, both the OH* and CH* chemiluminescence signals I emitted by lean premixed methane/air flames in which the equivalence ratio remains constant and uniform are linearly related to the flame heat release rate $\dot{Q}$ (Hurle et al. 1968):

$$I = a_1 \dot{Q} \tag{6.4}$$

where a_1 is a proportionality constant. When the flame heat release rate is perturbed, $\dot{Q} = \bar{\dot{Q}} + \dot{Q}'$, the chemiluminescence intensity is also perturbed

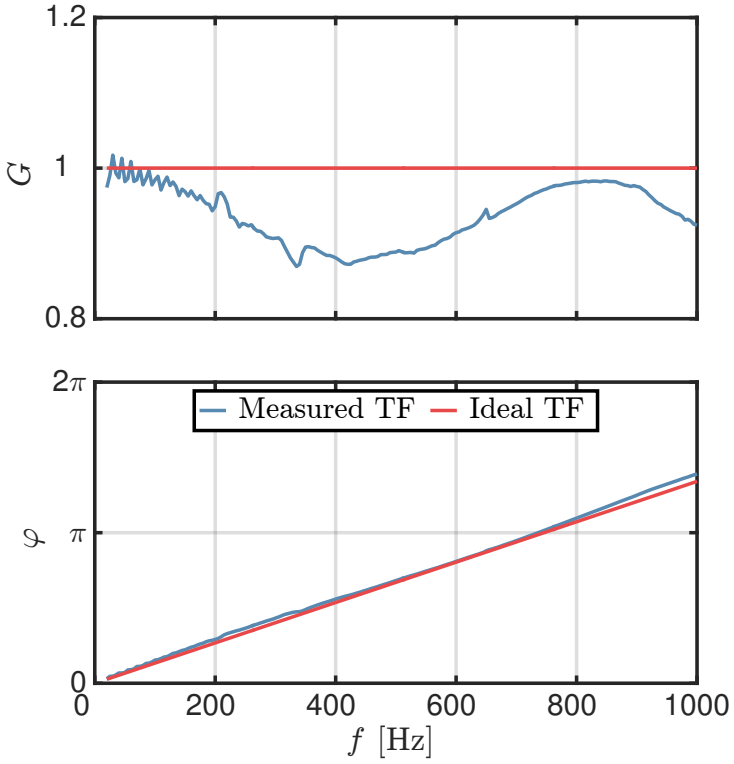

Figure 6.8: *Gain (Top) and phase lag (Bottom) of the transfer function of a water-cooled waveguide as a function of the forcing frequency obtained using an upstream loudspeaker. Measured transfer function (Blue) and ideal transfer function (Red).*

$I = \bar{I} + I'$. Using Eq. (6.4), it is easy to show that:

$$\left.\begin{aligned} \bar{I} &= a_1 \overline{\dot{Q}} \\ I' &= a_1 \dot{Q}' \end{aligned}\right\} \frac{\dot{Q}'}{\overline{\dot{Q}}} = \frac{I'}{\bar{I}} \tag{6.5}$$

In the end, it is possible to measure the relative oscillations of the flame heat release rate by measuring the relative oscillations of the OH* or CH* chemiluminescence signals.

In the present work, a photomultiplier (Hamamatsu H5784-04) mounted with a bandpass interferometric filter corresponding to the OH* emission wavelengths (Asahi Spectra ZBPA310, centered on $\lambda = 310$ nm and with a 10 nm bandwidth) is used to record the chemiluminescence signal. This leads to measurements of the average $\overline{\dot{Q}}$, fluctuating $\dot{Q}'$, and relative fluctuation $\dot{Q}'/\overline{\dot{Q}}$ of the flame heat release rate which are subsequently used to determine the Flame Describing Functions as described in Chapter 9.

6.6 Flame imaging

6.6.1 Average OH* chemiluminescence distribution

Photomultipliers are useful when the total luminosity emitted by a flame is needed. However, when the luminosity distribution is required, an Intensified Charge-Coupled Device (ICCD) is used. This camera is made of a standard CCD sensor coupled with an image intensifier tube. When a photon hits the intensifier tube, it is transformed into an electron and depending on the ICCD gain voltage, a cascade of electrons can be carried in its wake through a domino effect. In addition to this amplification process, the ICCD optical shuttering properties allow acquisition times as low as a few nanoseconds. Thanks to these two properties, ICCD cameras are a remarkable tool for studying quick modifications of flame structures. Moreover, the Signal-to-Noise ratio is usually very high for ICCD cameras, even when the ICCD gain is significant.

In this work, an ICCD camera (Princeton Instruments PI-MAX 4) equipped with an UV objective (Nikon U.V. Nikkor 105 mm f/4.5) and with a band-pass filter centered on $\lambda = 310$ nm with a 10 nm bandwidth (equivalent to that placed in front of the photomultiplier) is used to record the average flame OH* chemiluminescence distribution for all configurations. As explained in Sec. 6.5, the OH* chemiluminescence is directly linked to the flame heat release rate and is a good flame front tracer.

The same acquisition parameters are used for all configurations. The acquisition time, also called gate width, is set to 5 ms and the gain of the ICCD camera is set to 100. All mean OH* chemiluminescence distributions presented here are averaged over 100 frames.

The average flame shape was checked to be independent of the upstream and downstream elements of the NoiseDyn burner, even when a thermoacoustic instability is triggered. This implies that in the presence of a combustion instability, the flame oscillates around a state corresponding to the average state in the absence of such instabilities. On the other hand, the flame shape is strongly modified when the swirler is changed, as shown in Fig. 5.10, where the average flame shape obtained with swirler $\mathcal{S}$ generating a flow with a Swirl number $S = 0.8$ and swirler $\mathcal{S}_\varnothing$ generating a non-swirling flow are both displayed.

The OH* chemiluminescence distributions presented in Fig. 5.10 are integrated over the line of sight. Since all flames presented in this work are axisymmetric, an Abel deconvolution leads to the OH* chemiluminescence distributions in the symmetry plane, and thus to the average flame front positions, as represented in Fig. 6.9. The collection of dots located on the axis of symmetry are artifacts due to the Abel deconvolution procedure and do not indicate the presence of a

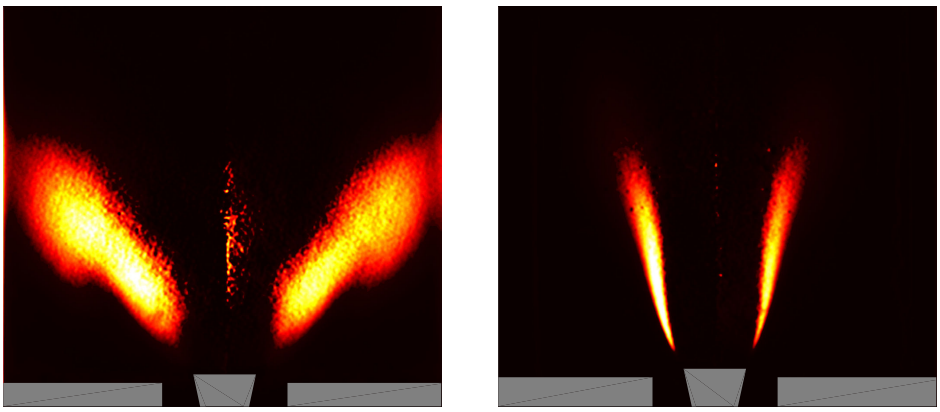

Figure 6.9: *Average OH* chemiluminescence distribution in the symmetry plane obtained with an ICCD camera for two different swirlers. (Left): Swirler $\mathcal{S}$ with $S = 0.8$ - (Right): Swirler $\mathcal{S}_{\varnothing}$ with $S \sim 0$.*

flame front.

Figure 6.9 clearly shows the impact of a swirling flow generated inside the injector on the average flame front position. When swirler $\mathcal{S}$ featuring a Swirl number $S = 0.8$ is used, the angle between the flame front, represented in Fig. 6.9-(Left), and the axis of symmetry is much larger compared to the non-swirling flame, represented in Fig. 6.9-(Right). Since the ICCD pictures represented here are obtained by averaging the data obtained from a hundred independent snapshots, the flame luminosity spreading is also a good indicator of the turbulent flame brush covered by the reaction zone in the absence of acoustic forcing. It is obvious from Fig. 6.9 that the flame stabilized within the non-swirling flow does not move as much as the flame stabilized within the swirling flow.

6.6.2 Phase average OH* chemiluminescence distribution

Mean OH* chemiluminescence distributions are used to determine the average flame front position. However, the instantaneous flame front position may depart considerably from this average position if the flame is submitted to acoustic forcing (generated by a loudspeaker for instance) or if a thermoacoustic instability is triggered. In order to study the flame response in such cases, two main options are available: first, a high-speed camera may be used, but the small flame luminosity due to the short exposure time is usually limiting, especially if an interferometric filter is used. The second option is to use an ICCD camera to obtain phase average pictures by the means of a synchronization signal.

For instance, the phase average pictures for configuration $\mathbf{A}^1$ (with upstream acoustic forcing and swirler $\mathcal{S}$ featuring a Swirl number $S = 0.8$) obtained with

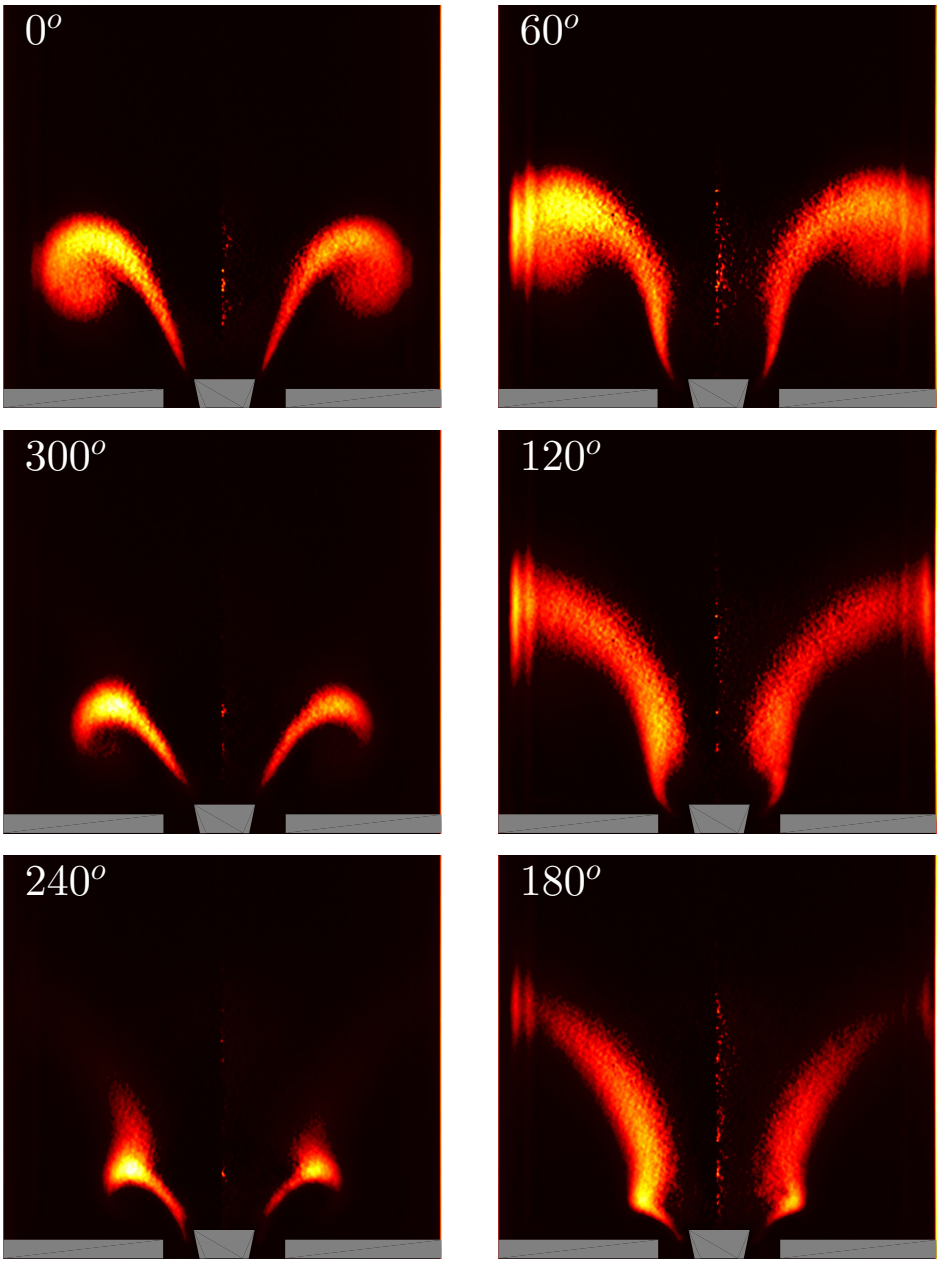

Figure 6.10: *Phase average pictures of an oscillating swirling flame (Swirl number $S = 0.8$) obtained with an ICCD camera with an OH* filter for a forcing frequency $f = 190$ Hz and at a forcing level $|u'|/\bar{u} = 0.72$ RMS, generated with an upstream loudspeaker. (Top left): $\varphi = 0°$ - (Top right): $\varphi = 60°$ - (Center right): $\varphi = 120°$ - (Bottom right): $\varphi = 180°$ - (Bottom left): $\varphi = 240°$ - (Center left): $\varphi = 300°$.*

an ICCD camera with an OH* filter for a forcing frequency $f = 190$ Hz and a forcing level $|u'|/\bar{u} = 0.72$ RMS are represented in Fig. 6.10. The ICCD gain is set to 100 and the gate width to 40 μs, approximately 1/100 of the oscillation period. Each frame is obtained by accumulating 40 images on the CCD sensor. All flame pictures are averaged over 100 frames. In this figure, φ designates the phase shift between the synchronization signal that triggers the ICCD camera and the voltage signal that drives the loudspeaker. Since the forcing level is very large, the flame interacts with the quartz windows for $\varphi = 60°$, $\varphi = 120°$ and $\varphi = 180°$ which causes artifacts in the left and right sides of these pictures.

The phase average imaging procedure is now detailed. A flame stabilized inside the combustion chamber is submitted to harmonic acoustic forcing originating from a loudspeaker sealed at the top or bottom of the burner. The flame is thus moving at the same frequency, but with a phase lag due to the acoustic wave propagation through the burner and to the flame response delay. The loudspeaker voltage is a harmonic signal which can be transformed into a TTL binary signal indicating whether the voltage is positive (TTL=+1 V if $U_{speaker} > 0$ V) or negative (TTL=0 V if $U_{speaker} < 0$ V). This signal is then used to trigger the ICCD camera by setting off the image acquisition when the TTL signal switches from 0 V to 1 V for example. The phase lag discussed before can be accounted for by adding a time offset. By doing so, the first image, corresponding to $\varphi = 0°$ in Fig. 6.10 for Configuration $\mathbf{A}^1$, is obtained. The following images in Fig. 6.10 are obtained by adding an additional time offset. For example, $\varphi = 180°$ is obtained by adding an additional time offset of $1/2f$ where f is the frequency of the signal.

The procedure is the same when a natural thermoacoustic instability is present inside the system, provided that the corresponding oscillations of the physical variables are roughly harmonic. In this study, the reference signal is provided by the hot wire probe located below the swirler because it features a high signal-to-noise ratio at the instability frequency.

6.7 Measurements of the acoustic impedance and reflection coefficient

The acoustic impedance $Z(\mathbf{x}, \omega)$ is a complex number that relates the acoustic pressure to the acoustic velocity at a given location $\mathbf{x}$ and at a given angular frequency ω (Rienstra and Hirschberg 2016):

$$Z(\mathbf{x}, \omega) = \frac{p'_\omega(\mathbf{x})}{\mathbf{u}'_\omega(\mathbf{x}) \cdot \hat{\mathbf{n}}(\mathbf{x})} \tag{6.6}$$

where p'_ω and $\mathbf{u}'_\omega$ are the Fourier components of the acoustic pressure and acoustic velocity assessed at the angular frequency ω and located at $\mathbf{x}$. The

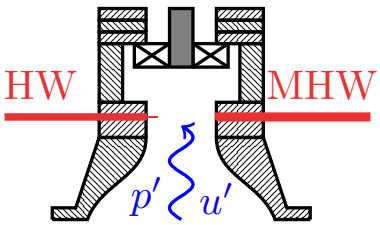

Figure 6.11: *Acoustic impedance measurement with a hot wire probe and a microphone. The hot wire probe (HW) and microphone (MHW) are located at the same axial position and their signals are recorded simultaneously.*

unit vector $\hat{\mathbf{n}}$ is normal to the surface of interest and pointing outward.

The acoustic reflection coefficient $\mathcal{R}(\omega)$ is defined as the ratio of the reflected wave amplitude to the incident wave amplitude at a given position and frequency. The acoustic reflection coefficient is equivalent to the acoustic impedance. Nevertheless, it is much easier to measure the impedance and reconstruct the reflection coefficient. This approach is adopted in this work. The properties of the acoustic impedance and acoustic reflection coefficient are described in Sec. 7.3.

6.7.1 First method: impedance measurements with a hot wire probe and a microphone

The simplest way to estimate the acoustic impedance from experiments is to measure the acoustic velocity and acoustic pressure simultaneously at a given axial location. Since the impedance is a function of the angular frequency ω, harmonic forcing has to be applied for each frequency of interest. In this work, the acoustic velocity is measured with a hot wire probe, denoted by HW in Fig. 6.11, and the acoustic pressure is measured with a microphone, denoted by MHW in the same figure. These quantities are measured just after a nozzle, in a region where the acoustic waves are one-dimensional. Moreover, there are no entropy fluctuations in that region so that the measured pressure and velocity fluctuations correspond to acoustic fluctuations. These diagnostics are presented in details in Sec. 6.3.1 and 6.4 respectively.

For each forcing frequency, the cross power spectral density between the microphone signal and the hot wire signal P_{pu} is computed using the Welch's averaged, modified periodogram method. The auto power spectral density of the hot wire signal P_{uu} is also computed with the same method. The components of the acoustic pressure p' and velocity u' at the forcing angular frequency ω are then given by:

$$p'(\omega) = P_{pu}(\omega)/\sqrt{|P_{uu}(\omega)|} \tag{6.7}$$

$$u'(\omega) = P_{uu}(\omega)/\sqrt{|P_{uu}(\omega)|} \tag{6.8}$$

Another method consists in computing the Fast Fourier Transform (FFT) of the hot wire and microphone signals and retaining the components of the signals corresponding to the forcing frequency ω. This method is much easier to implement but is not used in practice because of the large incoherent noise usually present in the recorded signals that lead to poor signal-to-noise ratios.

After $p'(\omega)$ and $u'(\omega)$ are obtained, the specific acoustic impedance Z_s and acoustic reflection coefficient $\mathcal{R}$ at the hot wire/microphone location can be computed using:

$$Z_s(\omega) = \pm\frac{1}{\bar{\rho}\bar{c}}\frac{p'}{u'} \tag{6.9}$$

$$\mathcal{R}(\omega) = \frac{Z_s(\omega) - 1}{Z_s(\omega) + 1} \tag{6.10}$$

where $\bar{\rho}$ and $\bar{c}$ are the mean gas density and sound speed respectively. The expression of the specific acoustic impedance given by Eq. (6.9) depends on the acoustic boundary orientation as well as the harmonic convention, as detailed in Appendix A. On the other hand, Eq. (6.10) does not depend on the acoustic boundary orientation or harmonic convention.

The reflection coefficient can be deduced further downstream or upstream as long as sound waves propagate in a 1D pipe with a constant cross section area in a uniform temperature field. The reflection coefficient $\mathcal{R}_l(\omega)$ at a distance l from the location where $\mathcal{R}_0(\omega)$ is measured is given by (Chung and Blaser 1980a):

$$\mathcal{R}_l(\omega) = \mathcal{R}_0(\omega)e^{\pm 2ikl} \qquad \text{with } e^{\pm i\omega t} \tag{6.11}$$

where $k = \omega/\bar{c}$ is the wave number. It should be noted that Eq. (6.11) depends on the harmonic convention retained ($e^{\pm i\omega t}$), as described in Appendix A.

6.7.2 Second method: impedance measurements with the Three Microphone Method (TMM)

It is not always possible to measure the acoustic velocity with a hot wire probe, especially in a reactive flow with high-temperature gases. In theory, Laser Doppler Velocimetry (LDV), presented in Sec. 6.3.2, could be used to measure the acoustic velocity but it requires an optical access to the region where the impedance is wanted. As a consequence, another method is used to reconstruct

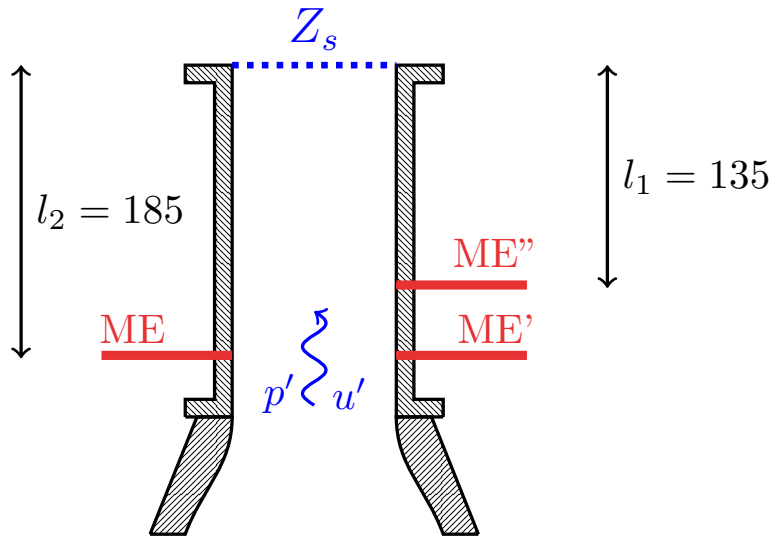

Figure 6.12: *Acoustic impedance measurement using the Three Microphone Method (TMM). The first microphone (ME) and second microphone (ME') are located at the same axial position, at a distance l_2 from the region where the impedance is assessed. The third microphone (ME") is located downstream, at a distance $l_1 < l_2$ from the region where the impedance is assessed. All dimensions are in mm.*

the impedance from acoustic measurements only: the Multiple Microphone Method (MMM) (Chung and Blaser 1980a; Chung and Blaser 1980b). Various versions of the MMM exist depending on the number of microphones utilized and their spatial arrangement. The version used in this work is the Three Microphone Method (TMM) consisting of two microphones at the same axial position and a third microphone further downstream (Tran et al. 2009b; Scarpato 2014).

The principle of the Three Microphone Method is now detailed. Two microphones, ME and ME', are placed in front of each other at a distance l_2 from the reference location where the acoustic impedance is wanted, as depicted in Fig. 6.12. A third microphone, ME", is placed further away from the first two microphones, at a distance $l_1 < l_2$ from the reference location. The specific acoustic impedance at the reference location is then given by (Chung and Blaser 1980a):

$$Z_s(\omega) = i\frac{H_{12}(\omega)\sin(kl_1) - \sin(kl_2)}{\cos(kl_2) - H_{12}(\omega)\cos(kl_1)} \tag{6.12}$$

where $H_{12}(\omega)$ is the transfer function between microphone ME' and microphone ME" at the angular frequency ω. The subscripts 1 and 2 refer to microphones ME' and ME" respectively. $H_{12}(\omega)$ is defined as:

$$H_{12}(\omega) = \frac{P_{12}(\omega)}{P_{11}(\omega)} \tag{6.13}$$

where $P_{12}(\omega)$ is the cross power spectral density between the signals measured by microphones ME' and ME" at the forcing angular frequency ω and $P_{11}(\omega)$ is the auto power spectral density of the signal measured by microphone ME' at ω.

Since Z_s is an impedance, Eq. (6.12) depends on the harmonic convention, here arbitrarily chosen as $e^{+i\omega t}$, and the acoustic boundary orientation, here chosen in the main direction (Case II in Appendix A).

In order to improve the signal-to-noise ratio when reconstructing the acoustic impedance using the TMM, two complementary techniques are employed: microphone switching and coherence functions (Chung and Blaser 1980a). The microphone switching method works as follow: in a first set of experiments, the original configuration $\circ$, depicted in Fig. 6.12, is used and the three microphone signals are recorded for all forcing frequencies of interest. In a second set of experiments, microphones ME' and ME" are exchanged, corresponding to the switched configuration s, and the same measurements are performed once again. The final transfer function $H_{12}^{f}(\omega)$ between microphones ME' and ME" is the geometrical mean between the two transfer functions $H_{12}^{\circ}(\omega)$ and $H_{12}^{s}(\omega)$ obtained for the original and switched configurations respectively:

$$H_{12}^{f}(\omega) = \sqrt{H_{12}^{\circ}(\omega) H_{12}^{s}(\omega)} \tag{6.14}$$

The second technique employed to improve the signal-to-noise ratio when determining the acoustic impedance using the TMM is a post-processing method involving coherence functions. The coherence function between the signals of microphones ME' and ME" is defined as:

$$C_{12}(\omega) = \frac{|P_{12}(\omega)|^2}{P_{11}(\omega) P_{22}(\omega)} \tag{6.15}$$

A coherence factor accounting for the coherence functions between microphones ME, ME' and ME" is then given by:

$$C(\omega) = \sqrt{\frac{C_{23}(\omega)}{C_{12}(\omega) C_{31}(\omega)}} \tag{6.16}$$

where the subscript 3 refers to microphone ME. The corrected transfer function $H_{12}^{c}(\omega)$ between microphones ME' and ME" is then obtained from the coherence factor and measured transfer function $H_{12}(\omega)$:

$$H_{12}^{c}(\omega) = C(\omega) H_{12}(\omega) \tag{6.17}$$

The corrections due to the switching method and coherence factor method can be combined (Chung and Blaser 1980a). In that case, Eq. (6.12) becomes:

$$Z_s(\omega) = i\frac{C^f(\omega)H_{12}^f(\omega)\sin(kl_1) - \sin(kl_2)}{\cos(kl_2) - C^f(\omega)H_{12}^f(\omega)\cos(kl_1)} \tag{6.18}$$

where the final coherence factor C^f is given by:

$$C^f(\omega) = \sqrt[4]{\frac{C_{23}^{\circ}(\omega)C_{23}^{s}(\omega)}{C_{12}^{\circ}(\omega)C_{12}^{s}(\omega)C_{31}^{\circ}(\omega)C_{31}^{s}(\omega)}} \tag{6.19}$$

and $H_{12}^f(\omega)$ is given by Eq. (6.14).

The Three Microphone Method may be used to reconstruct the acoustic impedance in a limited frequency range only. First, the phase difference between the signals corresponding to microphones ME' and ME" tends towards zero when the frequency is reduced. In this case, the impedance measurements may become inaccurate or even incorrect. Nevertheless, this erratic behavior is only observed for very low frequencies $f < 20$ Hz in the experiments performed in this work.

On the other hand, the high-frequency limit is prescribed by the spacing $l_2 - l_1$ between microphones ME' and ME" represented in Fig. 6.12. If $l_2 - l_1$ is a multiple of $\lambda/2$ where λ is the acoustic wavelength, then the expression for the reflection coefficient given by Eq. (6.18) blows up, thus placing an upper bound on the frequency at which the reconstruction of the acoustic impedance can be performed using the Three Microphone Method. This maximum frequency f_{max} is then given by:

$$l_2 - l_1 = \frac{\bar{c}}{2f_{max}} \tag{6.20}$$

In this work, the microphone spacing $l_2 - l_1 = 50$ mm corresponds to a maximum frequency $f_{max} = 3400$ Hz for cold flow conditions. Nevertheless, this maximum frequency is only an upper bound. In practice, when a frequency sweep is performed, the maximum frequency is reached as soon as a pressure node is located next to one of the microphones. In that case, the signal-to-noise ratio drops dramatically and the acoustic impedance cannot be determined properly.

Several measurements are performed with a Kundt's tube in order to validate the post-processing routines used to reconstruct the acoustic impedance and acoustic reflection coefficient using the Three Microphone Method. The microphone signals are recorded at a sampling frequency $f_s = 20$ kHz during

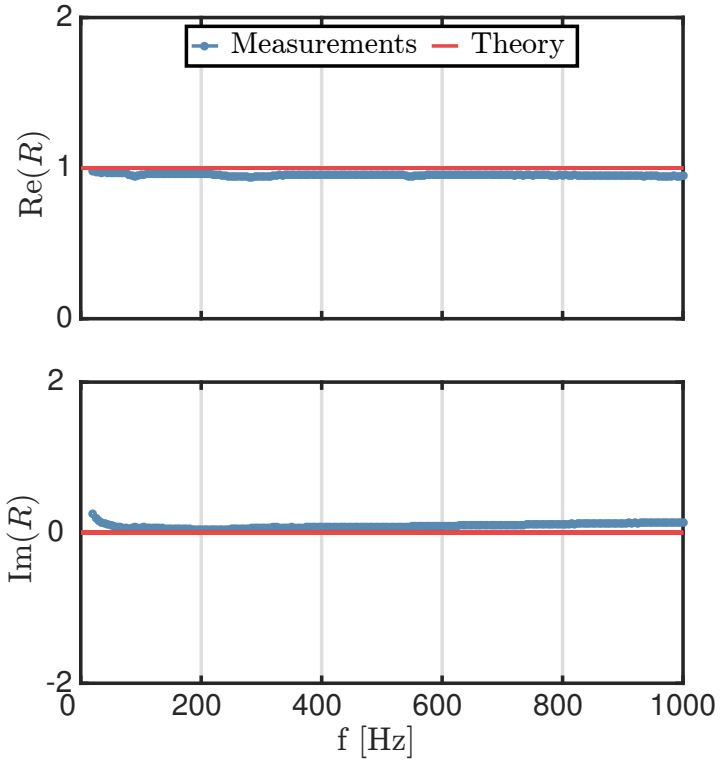

Figure 6.13: *Real part (Top) and imaginary part (Bottom) of the acoustic reflection coefficient corresponding to a rigid plate placed at the top of a Kundt's tube. Measurements are post-processed using the Three Microphone Method. The switching and coherence factor techniques are employed. (Blue): Measurements - (Red): Theoretical prediction.*

$t = 1$ s. For instance, the acoustic reflection coefficient corresponding to a rigid plate and obtained using the Three Microphone Method with both switching and coherence factor corrections is presented in Fig. 6.13. As demonstrated in Sec. 7.3.2, the acoustic reflection coefficient at the rigid plate location is $\mathcal{R} = 1$. The agreement between theory and measurements is satisfactory, as shown in Fig. 6.13.

The post-processing routines implementing the Three Microphone Method are also tested and validated for several additional test cases (not presented here). This technique is now employed to determine the acoustic impedance at the NoiseDyn burner exhaust tube outlet for various configurations and operating conditions.

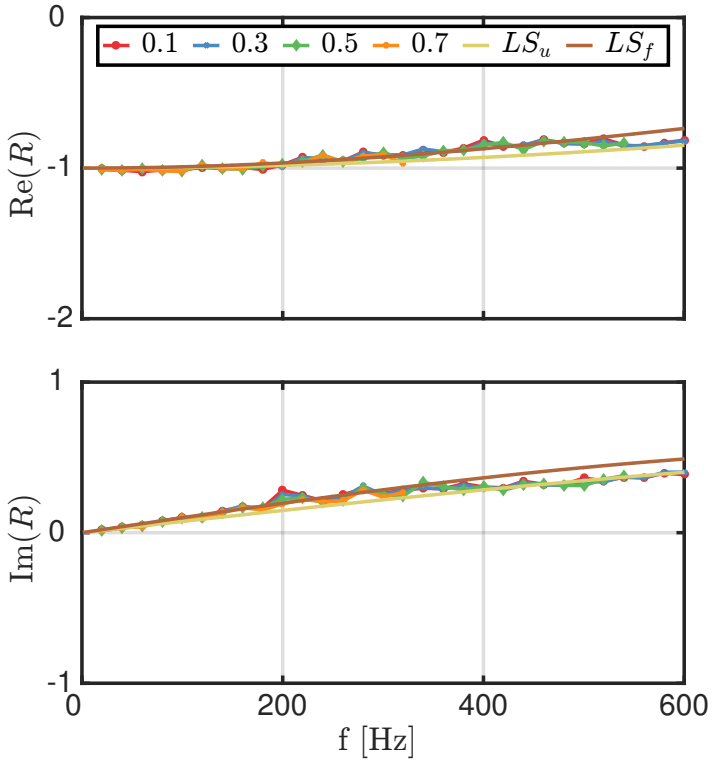

Figure 6.14: *Real part (Top) and imaginary part (Bottom) of the acoustic reflection coefficient at the NoiseDyn burner exhaust tube outlet for Configuration* ***C*** *for cold flow conditions. Measurements are post-processed using the Three Microphone Method for various forcing levels* $|u'|/\bar{u} = 0.1$ *RMS (Red),* $|u'|/\bar{u} = 0.3$ *RMS (Blue),* $|u'|/\bar{u} = 0.5$ *RMS (Green),* $|u'|/\bar{u} = 0.7$ *RMS (Orange). The switching and coherence factor techniques are employed. Theoretical prediction are also plotted according to the unflanged Levine-Schwinger (*LS_u*) model (Yellow) and infinitely flanged Levine-Schwinger (*LS_f*) model (Brown).*

6.7.3 Impedance measurements at the NoiseDyn burner exhaust tube outlet

Microphones ME, ME' and ME" are mounted on the first exhaust tube of the NoiseDyn burner, as depicted in Figs. 6.5 and 6.12. The acoustic reflection coefficient at the top of the NoiseDyn burner exhaust tube is then assessed for Configurations **A**, **B**, **C**, **D**, **E** and **F** for cold and reactive operating conditions. The various upstream elements and swirlers have no impact on this acoustic boundary condition. For reactive operating conditions, the waveguides described in Sec. 6.4.3 are used in combination with microphones ME, ME' and ME". Measurements are in this case corrected using the transfer functions of the associated waveguides.

The acoustic reflection coefficients at the NoiseDyn burner exhaust tube outlet for Configurations **A**, **B** and **C** (open end) and for cold flow conditions are reconstructed from measurements using the TMM at four different forcing levels: $|u'|/\bar{u} = 0.1$ RMS, $|u'|/\bar{u} = 0.3$ RMS, $|u'|/\bar{u} = 0.5$ RMS and $|u'|/\bar{u} = 0.7$ RMS measured with the hot wire probe located below the swirler. The microphone signals are recorded at a sampling frequency $f_s = 20$ kHz during $t = 1$ s. Results are represented in Fig. 6.14 for Configuration **C** along with the predictions associated with the unflanged (LS_u) and infinitely flanged (LS_f) Levine-Schwinger models, which are presented in details in Chapter 7. The acoustic reflection coefficients obtained for Configurations **A** and **B** are similar.

Figure 6.14 clearly shows that the acoustic reflection coefficient at the NoiseDyn burner exhaust tube exit is independent of the forcing level for all forcing frequencies investigated ($f < 600$ Hz) in the case of an open end boundary condition (e.g. for Configurations **A**, **B** and **C**). This also demonstrates the reliability and reproducibility of the acoustic impedance reconstructions using the Three Microphone Method. The reconstructed reflection coefficients are also in very good agreement with the theoretical models plotted in Fig. 6.14. The reflection coefficient assessed at the exhaust tube outlet, which has a flange of finite spatial extension, mostly lies between the curves corresponding to the infinitely flanged (LS_f) and unflanged (LS_u) Levine-Schwinger models.

The acoustic reflection coefficients at the NoiseDyn burner exhaust tube outlet corresponding to Configurations **A**, **B** and **C** are also reconstructed from measurements for reactive operating conditions. Since these reflection coefficients were shown to be independent of the forcing level for cold flow conditions, a simpler methodology is followed here. The forcing level is not kept constant at the hot wire location but a constant voltage is applied to the upstream loudspeaker used to generate harmonic forcing. The associated reconstruction of the reflection coefficient is presented for Configuration **C** in Fig. 6.15 along with the analytical predictions of the unflanged (LS_u) and infinitely flanged (LS_f) Levine-Schwinger models. Once again, the microphone signals are recorded at a sampling frequency $f_s = 20$ kHz during $t = 1$ s. These models are once again quite successful even though the values of the reconstructed reflection coefficient shown in Fig. 6.15 are more scattered compared to cold operating conditions. The imaginary part of the reflection coefficient is slighly underestimated by the models whereas the real part is accurately predicted. The acoustic reflection coefficients measured at the exhaust tube outlet for Configurations **A** and **B** are similar.

Given the results presented in Figs. 6.14 and 6.15, the acoustic reflection coefficient at the NoiseDyn burner exhaust tube outlet for cold and reactive conditions and for Configurations **A**, **B** and **C** are described with a flanged Levine-Schwinger (LS_f) impedance model for the remainder of this work. For reactive

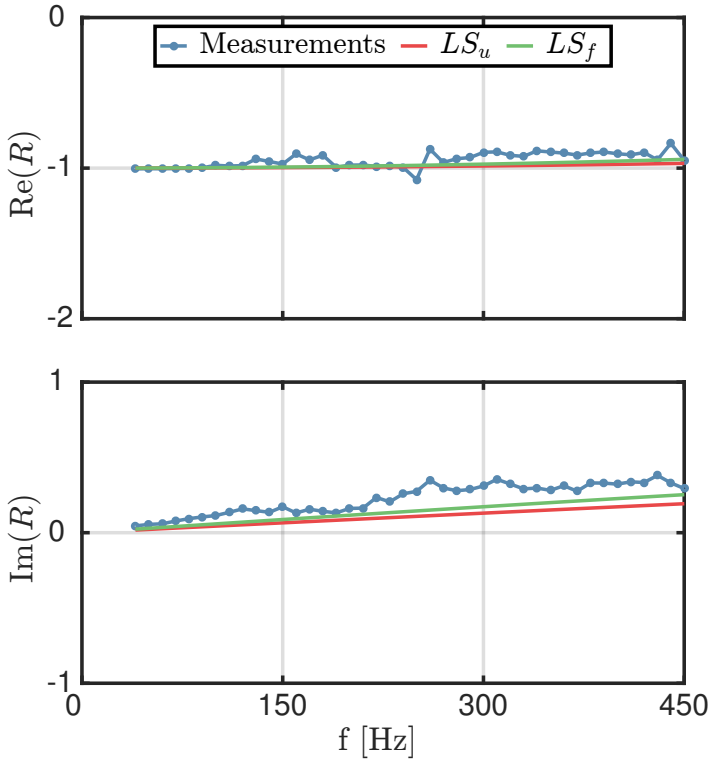

Figure 6.15: *Real part (Top) and imaginary part (Bottom) of the acoustic reflection coefficient at the NoiseDyn burner exhaust tube outlet for Configuration* ***C*** *for reactive conditions (Blue). Measurements are post-processed using the Three Microphone Method for a constant loudspeaker voltage. The switching and coherence factor techniques are employed. Theoretical prediction are also plotted according to the unflanged Levine-Schwinger (LS_u) model (Red) and infinitely flanged Levine-Schwinger (LS_f) model (Green).*

operating conditions, the speed of sound increases which in turn has an impact on the Levine-Schwinger model, as described in Sec. 7.3.3.

Finally, the acoustic reflection coefficient corresponding to the NoiseDyn burner exhaust tube outlet for Configurations **D**, **E** and **F** is investigated using the TMM. In this case, the NoiseDyn burner is topped by a perforated plate, as shown in Fig. 5.7. The microphone signals are still recorded at a sampling frequency $f_s = 20$ kHz during $t = 1$ s. The real part and imaginary part of the reflection coefficient reconstructed for Configuration **F** are represented in Fig. 6.16. Results for Configurations **D** and **E** are similar. Figures 6.14 and 6.16 demonstrate that the reflection coefficients for Configurations **A**, **B**, **C** and **D**, **E**, **F** are quite different for all forcing frequencies investigated: these two acoustic boundary conditions are said to be independent. When a perfo-

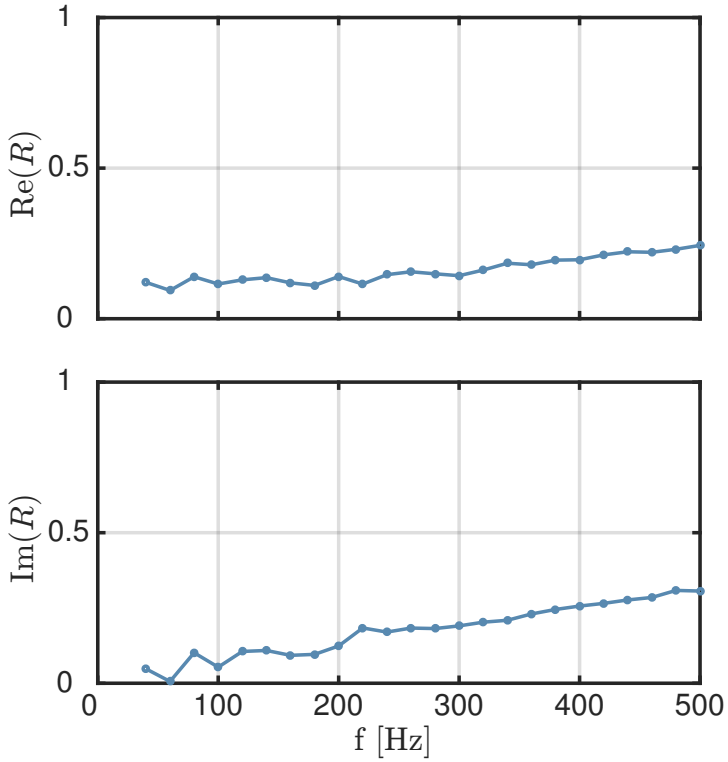

Figure 6.16: *Real part (Top) and imaginary part (Bottom) of the acoustic reflection coefficient at the NoiseDyn burner exhaust tube outlet for Configurations **D**, **E** and **F** for cold flow conditions. Measurements are post-processed using the Three Microphone Method for a constant loudspeaker voltage. The switching and coherence factor techniques are employed.*

rated plate is added at the top of the NoiseDyn burner exhaust tube, e.g. for Configurations **D**, **E** and **F**, the acoustic reflection coefficient coincides with anechoic conditions when the frequency tends towards zero and depart from these anechoic conditions when the frequency increases.

6.8 Conclusion

Various diagnostics employed in association with the NoiseDyn burner were introduced in this chapter. It is now worth exploring the linear acoustics theory in order to interpret the measurements obtained using the techniques presented in this chapter.

Chapter 7

Linear Acoustics: low-Mach Non-reactive flow

The linearized conservation equations describing sound wave propagation in a low-Mach non-reactive flow are derived in this chapter. The acoustic impedance and acoustic reflection coefficients are then introduced. Finally, the jump conditions for the acoustic pressure and acoustic velocity across various elements are derived in the case of a low-Mach non-reactive flow.

7.1 Linearized conservation equations

7.1.1 Assumptions

A few assumptions are made in order to derive the equations describing sound wave propagation in a low-Mach non-reactive flow. It is reminded that the mean physical variables are represented with an overline ($\bar{x}$) whereas the fluctuating physical variables are represented with a prime (x'). Vectors are denoted by bold characters for the sake of readability. The initial hypotheses related to the nature of the flow and acoustic perturbations are listed below with bullets ($\bullet$) and circles ($\circ$) respectively:

- The mean flow variables are time-independent.
- The flow is non-reactive: $\dot{q} = 0$.
- The fluid is an ideal gas.
- Body forces are neglected.
- Viscosity effects are neglected: $\mu = 0$.
- Thermal conduction and radiation are neglected.

- The flow has a low Mach number $\mathrm{M} = \bar{u}/\bar{c} \ll 1$.
  - Acoustic sources are not considered.
  - Acoustic perturbations are linear.

7.1.2 Conservation equations

The conservation equations for a non-reactive flow where body forces, viscous forces and thermal diffusion and radiation are neglected are (Morse and Ingard 1968; Candel and Poinsot 1988; Crighton et al. 1992):

Mass conservation

$$\frac{\partial \rho}{\partial t} + \nabla \cdot (\rho \mathbf{u}) = 0 \tag{7.1}$$

Momentum conservation

$$\rho \frac{\partial \mathbf{u}}{\partial t} + \rho \mathbf{u} \cdot \nabla \mathbf{u} = -\nabla p \tag{7.2}$$

Each of the physical variables in Eqs. (7.1)-(7.2) can be written as the sum of a mean flow variable and an acoustic perturbation (Morse and Ingard 1968; Candel and Poinsot 1988). This decomposition is presented explicitly below:

$$p = \bar{p} + p' \tag{7.3}$$
$$\mathbf{u} = \bar{\mathbf{u}} + \mathbf{u}' \tag{7.4}$$
$$\rho = \bar{\rho} + \rho' \tag{7.5}$$
$$T = \bar{T} + T' \tag{7.6}$$
$$c_p = \bar{c}_p + c_p' \tag{7.7}$$
$$c_v = \bar{c}_v + c_v' \tag{7.8}$$

Even though c_p and c_v are functions of the gas temperature, their variations are limited, especially since the acoustic perturbations are linear which implies that $|T'|/\bar{T} \ll 1$. Therefore, c_p' and c_v' are neglected in the remainder of this work.

Since the flow is non-reactive and non-viscous, it is isentropic and the conservation of energy is given by:

$$\frac{Ds}{Dt} = 0 \tag{7.9}$$

Equation (7.9) states that there is no entropy production within the flow. If it is further assumed that the mean flow variables are homogeneous, the entropy is initially the same everywhere. Since the material derivative of the entropy is zero, the entropy then remains equal to its initial value. As a consequence, the flow is homentropic if the mean flow variables are homogeneous and the entropy fluctuations cancel out in that case: $s' = 0$.

7.1.3 Constitutive equations

In this chapter, dimensional analysis is frequently used to assess the relative importance of each term in the equations. The constitutive equations for the mean flow are:

$$\bar{p} = \bar{\rho} r \overline{T} \tag{7.10}$$

$$\gamma \bar{p} = \bar{\rho} \bar{c}^2 \tag{7.11}$$

$$\gamma r \overline{T} = \bar{c}^2 \tag{7.12}$$

$$\bar{p} \bar{\rho}^{-\gamma} = S \tag{7.13}$$

where Eq. (7.10) is the ideal gas law, Eq. (7.11) is the expression of sound speed in an ideal gas, Eq. (7.12) is obtained by combining the first two equations and Eq. (7.13) is obtained by considering the expression of the entropy of an ideal gas, equal to a constant S here. Moreover, the mean flow variables are assumed to be homogeneous:

$$\nabla \bar{\rho} = 0 \tag{7.14}$$

$$\nabla \overline{T} = 0 \tag{7.15}$$

$$\nabla \bar{p} = 0 \tag{7.16}$$

On the other hand, the acoustic variables are linked through the following equation:

$$p' = \bar{c}^2 \rho' \tag{7.17}$$

Equation (7.17) comes from the linearized entropy of an ideal gas in the absence of entropy fluctuations (Morse and Ingard 1968; Candel and Poinsot 1988).

Using the linearized ideal gas law along with Eq. (7.17), a link between the temperature and density fluctuations can be established:

$$\frac{T'}{\overline{T}} = (\gamma - 1) \frac{\rho'}{\bar{\rho}} \tag{7.18}$$

The acoustic pressure and acoustic velocity of a travelling acoustic wave are also related by (Hirschberg and Rienstra 2004):

$$p' = \pm \bar{\rho} \bar{c} u' \tag{7.19}$$

7.1.4 Linearized mass conservation

The linearized mass conservation is obtained by injecting Eqs. (7.3)-(7.8) into Eq. (7.1). Terms of order 0 and 1 are kept while terms of higher order are neglected. The mass conservation for the mean flow is first obtained by considering terms of order 0 along with Eq. (7.14):

$$\nabla \cdot \bar{\mathbf{u}} = 0 \tag{7.20}$$

Then, the linearized mass conservation is obtained by considering terms of order 1 along with Eq. (7.14):

$$\underbrace{\frac{\partial \rho'}{\partial t}}_{(1)} + \underbrace{\nabla \cdot \left(\rho' \bar{\mathbf{u}}\right)}_{(2)} + \underbrace{\bar{\rho} \nabla \cdot \mathbf{u}'}_{(3)} = 0 \tag{7.21}$$

Using dimensional analysis, the relative weight of terms (1), (2) and (3) in Eq. (7.21) is assessed. It is found that (1)/(3) $\sim$ He where He $= \omega L / \bar{c}$ is the Helmholtz number (L is a characteristic length of the system) and (2)/(3) $\sim$ M where M is the Mach number. Since the flow is low-Mach, the second term in Eq. (7.21) can be neglected. Moreover, if the region of interest is compact, e.g. He $\ll 1$, the first term can also be neglected.

Linearized mass conservation in a low-Mach non-reactive flow

$$\frac{\partial \rho'}{\partial t} + \bar{\rho} \nabla \cdot \mathbf{u}' = 0 \tag{7.22}$$

Linearized compact mass conservation in a low-Mach non-reactive flow

$$\nabla \cdot \mathbf{u}' = 0 \tag{7.23}$$

7.1.5 Linearized momentum conservation

The same procedure is repeated with the momentum conservation: Eqs. (7.3)-(7.8) are injected into Eq. (7.2). If terms of order 0 are considered only, it is

found that:

$$\bar{\mathbf{u}} \cdot \nabla \bar{\mathbf{u}} = 0 \tag{7.24}$$

$$\tag{7.25}$$

Back to Eq. (7.2) combined with Eqs. (7.3)-(7.8), the linearized momentum conservation is obtained if terms of order 1 are considered only:

$$\underbrace{\bar{\rho}\frac{\partial \mathbf{u}'}{\partial t}}_{(1)} + \underbrace{\bar{\rho}\bar{\mathbf{u}} \cdot \nabla \mathbf{u}'}_{(2)} + \underbrace{\bar{\rho}\mathbf{u}' \cdot \nabla \bar{\mathbf{u}}}_{(3)} = \underbrace{-\nabla p'}_{(4)} \tag{7.26}$$

Once again, dimensional analysis can be used to simplify Eq. (7.26). It is found that (1)/(4) $\sim$ He, (2)/(4) $\sim$ M and (3)/(4) $\sim$ M. Since the flow is low-Mach, the second and third terms in Eq. (7.26) can be neglected. Moreover, if the region of interest is compact, the first term can also be neglected.

Linearized momentum conservation in a low-Mach non-reactive flow

$$\bar{\rho}\frac{\partial \mathbf{u}'}{\partial t} = -\nabla p' \tag{7.27}$$

Linearized compact momentum conservation in a low-Mach non-reactive flow

$$\nabla p' = 0 \tag{7.28}$$

7.2 Propagation of harmonic plane waves in a low-Mach non-reactive flow

7.2.1 Uniform mean temperature field

The divergence operator is applied to Eq. (7.27). Equations (7.17) and (7.22) are then injected into the resulting equation, thus leading to the wave equation describing sound wave propagation in a low-Mach non-reactive flow with a uniform mean temperature field.

Low-Mach non-reactive wave equation in a uniform mean temperature field

$$\nabla^2 p' - \frac{1}{\bar{c}^2}\frac{\partial^2 p'}{\partial t^2} = 0 \tag{7.29}$$

Plane waves propagating along the x-axis are now considered. Equation (7.29) becomes:

$$\frac{\partial^2 p'}{\partial x^2} - \frac{1}{\bar{c}^2}\frac{\partial^2 p'}{\partial t^2} = 0 \tag{7.30}$$

Moreover, the acoustic waves are assumed to be harmonic, thus prescribing the form of the solution in the complex plane:

$$p' = p'_\omega(x)e^{\pm i\omega t} \tag{7.31}$$

where p'_ω is the amplitude of the harmonic wave propagating at the angular frequency ω. The acoustic pressure in the time domain is a real variable, equal to the real part of p' in Eq. (7.31). Two harmonic conventions $e^{\pm i\omega t}$ are possible, as explained in Appendix A. From Eqs. (7.30) and (7.31) and introducing the wave number $k = \omega/\bar{c}$, a Helmholtz equation is obtained:

$$\frac{d^2 p'_\omega}{dx^2} + k^2 p'_\omega = 0 \tag{7.32}$$

The general solution of Eq. (7.32) is given by:

$$p'_\omega = A_\omega e^{ikx} + B_\omega e^{-ikx} \tag{7.33}$$

where A_ω and B_ω are two complex integration constants that are prescribed by the acoustic boundary conditions. The expression for the acoustic velocity can be retrieved from Eq. (7.27):

$$\mathbf{u}'_\omega = \mp\left(\frac{A_\omega}{\bar{\rho}\bar{c}}e^{ikx} - \frac{B_\omega}{\bar{\rho}\bar{c}}e^{-ikx}\right)\hat{\mathbf{e}}_\mathbf{x} \qquad \text{with } e^{\pm i\omega t} \tag{7.34}$$

where $\hat{\mathbf{e}}_\mathbf{x}$ is a unit vector along the x-axis. The expression for the acoustic velocity depends on the harmonic convention chosen ($e^{\pm i\omega t}$). The acoustic velocity in the time domain is a real variable, equal to the real part of $\mathbf{u}'_\omega$ in Eq. (7.34).

7.2.2 Linear mean temperature field

In this section, the mean flow variables are not homogeneous and as a consequence, the flow is not homentropic. The results presented in Sec. 7.1 do not apply.

The mean axial temperature gradient is assumed to be a non-zero constant in this section, which implies that $\bar{c}^2$ is linearly related to x. The x-axis origin is chosen such that $\bar{c}^2 = \beta x$ where β is a prescribed parameter, thus implying that $\nabla \bar{c}^2 = \beta$. This shift in origin greatly simplifies the mathematical derivation that follows. The wave equation in a fluid with a varying mean temperature field is given by (Hirschberg and Rienstra 2004):

$$\frac{\partial^2 p'}{\partial t^2} - \nabla \cdot \left(\bar{c}^2 \nabla p' \right) = 0 \tag{7.35}$$

By considering plane waves propagating along the x-axis in a linearly changing mean temperature field, Eq. (7.35) becomes:

$$\frac{\partial^2 p'}{\partial t^2} - \beta \frac{\partial p'}{\partial x} - \beta x \frac{\partial^2 p'}{\partial x^2} = 0 \tag{7.36}$$

If the acoustic waves are further assumed to be harmonic, Eqs. (7.31) and (7.36) lead to a canonical equation of solution (Abramowitz and Stegun 1972):

$$p'_\omega = A_\omega J_0(2\omega\sqrt{x/\beta}) + B_\omega Y_0(2\omega\sqrt{x/\beta}) \tag{7.37}$$

where A_ω and B_ω are complex integration constants and J_0 and Y_0 are Bessel functions of the first and second kind and of order 0. Equation (7.27) is still valid with non-homogeneous mean flow variables and can be used to express the acoustic velocity at the angular frequency ω:

$$\mathbf{u}'_\omega = \pm \frac{1}{i\bar{\rho}(x)\sqrt{\beta x}} \left[A_\omega J_1(2\omega\sqrt{x/\beta}) + B_\omega Y_1(2\omega\sqrt{x/\beta}) \right] \hat{\mathbf{e}}_\mathbf{x} \tag{7.38}$$

where J_1 and Y_1 are Bessel functions of the first and second kind and of order 1. Once again, the expression of the acoustic velocity depends on the harmonic convention ($e^{\pm i\omega t}$).

7.3 Acoustic impedance and reflection coefficient

7.3.1 Definitions

The acoustic impedance $Z(\mathbf{x}, \omega)$ is a complex number that relates the acoustic pressure to the acoustic velocity at a given location $\mathbf{x}$ and at a given angular

frequency ω (Rienstra and Hirschberg 2016):

$$Z\left(\mathbf{x},\omega\right)=\frac{p'_{\omega}(\mathbf{x})}{\mathbf{u}'_{\omega}(\mathbf{x})\cdot\hat{\mathbf{n}}(\mathbf{x})} \tag{7.39}$$

where p'_{ω} and $\mathbf{u}'_{\omega}$ are the Fourier components of the acoustic pressure and acoustic velocity assessed at the angular frequency ω and located at $\mathbf{x}$. The unit vector $\hat{\mathbf{n}}$ is normal to the surface of interest and pointing outward. With one-dimensional variables, Eq. (7.39) becomes:

$$Z\left(x,\omega\right)=\pm\frac{p'_{\omega}(x)}{u'_{\omega}(x)} \tag{7.40}$$

where the sign depends on surface direction, as explained in Appendix A. In the remainder of this work, this latter definition of the 1D acoustic impedance is retained. The acoustic impedance is expressed in $\mathrm{kg.m^{-2}.s^{-1}}$ and is usually split into its real part, the acoustic resistance $R_e\left(x,\omega\right)$, and its imaginary part, the acoustic reactance $X\left(x,\omega\right)$:

$$Z\left(x,\omega\right)=R_e\left(x,\omega\right)+iX\left(x,\omega\right) \tag{7.41}$$

An important acoustic property of a medium is its characteristic acoustic impedance z, defined as the acoustic impedance of a quiescent uniform medium traversed by a plane wave propagating in the positive direction. From the results presented in Sec. 7.2.1, it is found that z can be expressed as (Candel and Poinsot 1988; Rienstra and Hirschberg 2016):

$$z=\bar{\rho}\bar{c} \tag{7.42}$$

The ratio of the acoustic impedance $Z(x,\omega)$ to the characteristic acoustic impedance z is a dimensionless variable called the specific acoustic impedance $Z_s\left(x,\omega\right)$:

$$Z_s\left(x,\omega\right)=\frac{Z\left(x,\omega\right)}{\bar{\rho}\bar{c}} \tag{7.43}$$

Another important acoustic variable is the reflection coefficient $\mathcal{R}(x,\omega)$ defined as the ratio of the reflected wave amplitude to the incident wave amplitude at a given position and frequency. The reflection coefficient can be linked to the specific acoustic impedance through the following equations (Rienstra and Hirschberg 2016):

$$\mathcal{R}(x,\omega)=\frac{Z_s\left(x,\omega\right)-1}{Z_s\left(x,\omega\right)+1} \tag{7.44}$$

$$Z_s(x,\omega) = \frac{1+\mathcal{R}(x,\omega)}{1-\mathcal{R}(x,\omega)} \tag{7.45}$$

Equations (7.44) and (7.45) are valid for both harmonic conventions $e^{\pm i\omega t}$ and both surface orientations. However, it is important to note that the harmonic convention has an impact on the expression of the acoustic impedance and acoustic reflection coefficient. The following relations between the acoustic impedances and acoustic reflection coefficients for both harmonic conventions can be established:

$$Z_{\oplus} = (Z_{\ominus})^* \tag{7.46}$$
$$\mathcal{R}_{\oplus} = (\mathcal{R}_{\ominus})^* \tag{7.47}$$

where the subscripts $\oplus$ and $\ominus$ are used for the acoustic variables described with the $e^{+i\omega t}$ and $e^{-i\omega t}$ harmonic conventions respectively and the superscript * stands for the complex conjugate. These relations are derived in Appendix A.

7.3.2 Closed and open acoustic boundaries

At a closed boundary, the mean and instantaneous flow velocities cancel out. As a consequence, the acoustic velocity at a closed boundary is equal to zero. Using Eqs. (7.40) and (7.44), the acoustic impedance and reflection coefficient at a closed boundary are derived:

$$Z_{closed} = \pm\infty \tag{7.48}$$
$$\mathcal{R}_{closed} = +1 \tag{7.49}$$

These expressions are valid for both harmonic conventions. The $\pm$ sign comes from surface direction considerations. The reflection coefficient corresponding to a rigid plate mounted at the top of a Kundt's tube measured with the Three-Microphone Method (TMM) is presented in Fig. 6.13. It is clearly shown that $\mathcal{R} \simeq +1$ in this figure.

On the other hand, the acoustic boundary condition corresponding to an open end may be described as a pressure node as a first approximation. This crude model is valid for low frequencies only and for a quiescent fluid. Using Eqs. (7.40) and (7.44), the acoustic impedance and reflection coefficient at an open boundary for low frequencies are derived:

$$Z_{open} = 0 \tag{7.50}$$
$$\mathcal{R}_{open} = -1 \tag{7.51}$$

These expressions are valid for both harmonic conventions and for both surface orientations.

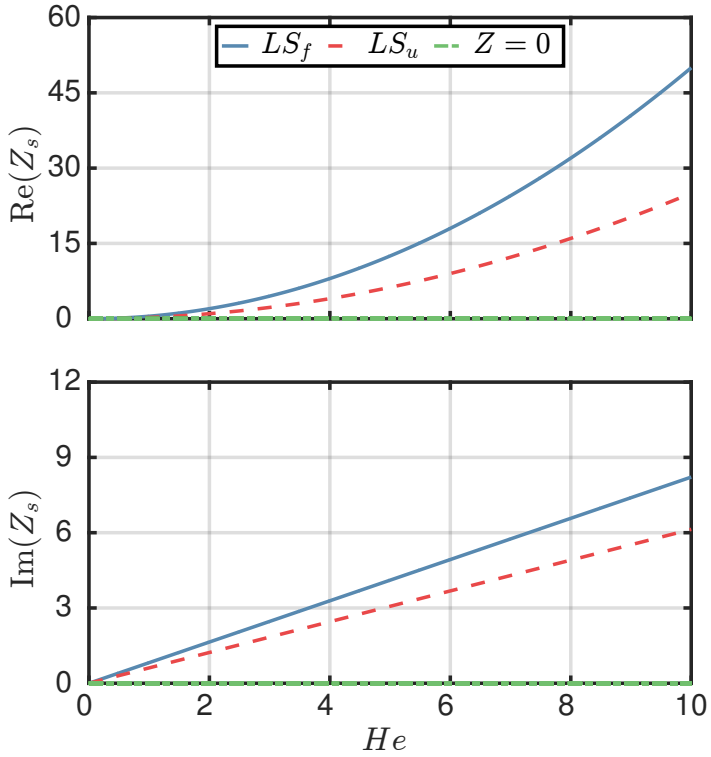

Figure 7.1: *Acoustic impedance of an open pipe. (Blue line): Levine-Schwinger model for an infinitely flanged pipe - (Red dashed line): Levine-Schwinger impedance for an unflanged pipe - (Green dotted line):* $Z_s = 0$.

7.3.3 Levine-Schwinger acoustic impedance

A tube with an open oulet is characterized by the presence of a pressure node located at the outlet for low Helmholtz numbers $\mathrm{He} = ka \ll 1$, where a is the tube radius and k is the wave number (e.g. for low frequencies), and for low-Mach number $\mathrm{M} \ll 1$ flows. As the angular frequency ω is increased, the inertia of the fluid located just after the outlet induces an end correction of order He and the acoustic radiation losses induce another correction of order He^2 (Levine and Schwinger 1948; Atig et al. 2004).

One possible model for the acoustic impedance of an unflanged open pipe traversed by a low-Mach flow $\mathrm{M} \ll 1$ which is not restricted to low frequencies is given by the Levine-Schwinger acoustic impedance model (Levine and Schwinger 1948):

$$Z_s = \frac{1}{4}(ka)^2 \pm ik\delta_0 \qquad \text{with } e^{\pm i\omega t} \tag{7.52}$$

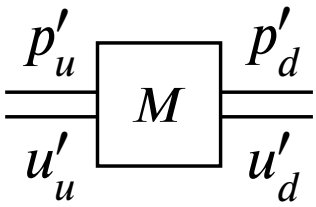

Figure 7.2: *Illustration of the Acoustic Transfer Matrix (ATM) formalism. A 2 × 2 matrix, denoted by M, relates the downstream acoustic pressure p'_d and acoustic velocity u'_d to the upstream acoustic pressure p'_u and acoustic velocity u'_u.*

where $\delta_0 = 0.6133a$ is the end correction in the unflanged case for a tube with sharp edges. This expression is valid for a unit vector normal to the surface of interest $\hat{\mathbf{n}} = \hat{\mathbf{e}}_x$ (Case II in Appendix A) and depends on the harmonic convention ($e^{\pm i\omega t}$). The alternative expression for an infinitely flanged pipe is given by (Nomura et al. 1960; Norris and Sheng 1989):

$$Z_s = \frac{1}{2}(ka)^2 \pm ik\delta_\infty \qquad \text{with } e^{\pm i\omega t} \tag{7.53}$$

where $\delta_\infty = 0.8216a$ is the end correction of a flanged aperture with sharp edges. More recent works proposed additional corrections accounting for high-forcing levels (Atig et al. 2004), Mach number (Munt 1977) and flow temperature (Cummings 1977). These corrections are neglected in the present work.

The Levine-Schwinger impedance models are plotted in Fig. 7.1 for the $e^{+i\omega t}$ convention. Three models are compared: the Levine-Schwinger impedance for infinitely flanged and unflanged tubes are represented in blue and red respectively. The additional green plot represents the usual open acoustic boundary condition $Z_s = 0$ as described in Sec. 7.3.2. For low Helmholtz numbers $\mathrm{He} \ll 1$, all three models collapse.

7.4 Acoustic Transfer Matrices in a low-Mach Non-reactive Flow

7.4.1 Concept of Acoustic Transfer Matrix

The Acoustic Transfer Matrix (ATM), represented by the symbol M in Fig. 7.2, is a black-box representation linking the acoustic variables (p'_d, u'_d) downstream an element to the acoustic variables (p'_u, u'_u) upstream the same element (Abom 1992; Paschereit and Polifke 1998). Mathematically, it corresponds to a 2 × 2 matrix as expressed by Eq. (7.54). The subscripts u and d refer to upstream and downstream variables respectively and the overline and prime refer to mean

and fluctuating variables respectively.

Since the acoustic pressure is expressed in pascals whereas the acoustic velocity is expressed in meters per second, the coefficients of the ATM in Eq. (7.54) are not dimensionless. One way to solve this issue is to divide the acoustic pressure by the characteristic impedance $z = \bar{\rho}\bar{c}$ at the same axial location. The resulting Dimensionless Acoustic Transfer Matrix (DATM) denoted by $\widetilde{M}$ is defined in Eq. (7.55).

Definition of the Acoustic Transfer Matrix (ATM)

$$\begin{pmatrix} p'_d \\ u'_d \end{pmatrix} = \underbrace{\begin{pmatrix} M(1,1) & M(1,2) \\ M(2,1) & M(2,2) \end{pmatrix}}_{M} \times \begin{pmatrix} p'_u \\ u'_u \end{pmatrix} \tag{7.54}$$

Definition of the Dimensionless Acoustic Transfer Matrix (DATM)

$$\begin{pmatrix} p'_d/z_d \\ u'_d \end{pmatrix} = \underbrace{\begin{pmatrix} \widetilde{M}(1,1) & \widetilde{M}(1,2) \\ \widetilde{M}(2,1) & \widetilde{M}(2,2) \end{pmatrix}}_{\widetilde{M}} \times \begin{pmatrix} p'_u/z_u \\ u'_u \end{pmatrix} \tag{7.55}$$

The harmonic convention has an impact on the ATM/DATM expressions presented thereafter. It is also worth mentioning that other acoustic representations such as Scattering Matrices or Mobility Matrices are equivalent to Transfer Matrices (Schuermans et al. 2000; Fischer et al. 2006). Nevertheless, these alternative formalisms are not used in the present work.

7.4.2 Transfer Matrix of a straight duct in a uniform low-Mach non-reactive flow

The case of a one-dimensional straight duct containing a uniform low-Mach non-reactive flow, as sketched in Fig. 7.3, is first examined. The acoustic pressure and acoustic velocity inside the duct at any axial location are given by Eqs. (7.33) and (7.34) respectively.

The acoustic pressure and acoustic velocity are expressed at the duct inlet (at $x = 0$) and outlet (at $x = l$). All variables related to these locations are denoted by the subscripts u and d respectively. The downstream acoustic variables are then expressed as functions of the upstream acoustic variables:

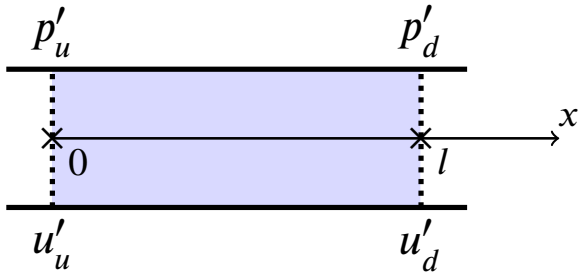

Figure 7.3: *Sketch of a straight duct containing a uniform low-Mach non-reactive flow. The acoustic pressure and acoustic velocity at the duct inlet at $x = 0$ are denoted by p'_u and u'_u respectively. The acoustic pressure and acoustic velocity at the duct outlet at $x = l$ are denoted by p'_d and u'_d respectively.*

$$p'_d = \cos(kl)p'_u \mp \bar{\rho}\bar{c}i\sin(kl)u'_u \qquad \text{with } e^{\pm i\omega t} \tag{7.56}$$

$$u'_d = \mp\frac{i\sin(kl)}{\bar{\rho}\bar{c}}p'_u + \cos(kl)u'_u \qquad \text{with } e^{\pm i\omega t} \tag{7.57}$$

From Eqs. (7.56) and (7.57), the ATM and DATM associated with sound waves propagating in a uniform low-Mach non-reactive flow within a straight duct are derived, as expressed in Eqs. (7.58) and (7.59) respectively (Paschereit and Polifke 1998; Polifke et al. 2001).

ATM/DATM of a straight duct in a uniform low-Mach non-reactive flow

$$M = \begin{pmatrix} \cos(kl) & \mp iz\sin(kl) \\ \mp i\sin(kl)/z & \cos(kl) \end{pmatrix} \qquad \text{with } e^{\pm i\omega t} \tag{7.58}$$

$$\widetilde{M} = \begin{pmatrix} \cos(kl) & \mp i\sin(kl) \\ \mp i\sin(kl) & \cos(kl) \end{pmatrix} \qquad \text{with } e^{\pm i\omega t} \tag{7.59}$$

ATM/DATM of a nearly compact straight duct in a uniform low-Mach non-reactive flow

$$M = \begin{pmatrix} 1 & \mp izkl \\ \mp ikl/z & 1 \end{pmatrix} \qquad \text{with } e^{\pm i\omega t} \tag{7.60}$$

$$\widetilde{M} = \begin{pmatrix} 1 & \mp ikl \\ \mp ikl & 1 \end{pmatrix} \qquad \text{with } e^{\pm i\omega t} \tag{7.61}$$

Equations (7.58) and (7.59) are valid for all Helmholtz numbers. It is interesting to derive the low-frequency limit of these equations, valid for low Helmholtz numbers only, which correspond to the solution for nearly compact systems. The Taylor series expansions of Eqs. (7.58) and (7.59) are thus performed up to the first order and presented in Eqs. (7.60) and (7.61), which correspond respectively to the ATM and DATM associated with sound waves propagating in a uniform low-Mach non-reactive flow within a nearly compact straight duct.

The general approach detailed in Sec. 7.4.4 may also be used to derive these ATM/DATM valid for low Helmholtz numbers.

7.4.3 Transfer Matrix of a straight duct in a low-Mach non-reactive flow with a linear mean axial temperature gradient

The expression for the acoustic pressure and acoustic velocity in a low-Mach non-reactive flow with a linear mean axial temperature gradient is given by Eqs. (7.37) and (7.38). These equations are expressed at $x = l_u$, corresponding to the element entrance, and $x = l_d$, corresponding to the element exit. These two locations are prescribed by the relation $\bar{c}^2 = \beta x$, as explained in Sec. 7.2.2. While not absolutely necessary, two additional parameters are introduced in order to simplify the expressions of the ATM/DATM:

$$\iota_u = 2\omega\sqrt{\left(\frac{l_u}{\beta}\right)} \tag{7.62}$$

$$\iota_d = 2\omega\sqrt{\left(\frac{l_d}{\beta}\right)} \tag{7.63}$$

where ι_u and ι_d are two dimensionless parameters that are reminiscent of reduced frequencies. The acoustic pressure p'_d and acoustic velocity u'_d at the

ATM/DATM of a straight duct in a low-Mach non-reactive flow with a linear mean axial temperature gradient

$$M = \begin{pmatrix} \dfrac{Y_1(\iota_u)J_0(\iota_d) - J_1(\iota_u)Y_0(\iota_d)}{Y_1(\iota_u)J_0(\iota_u) - Y_0(\iota_u)J_1(\iota_u)} & \mp i z_u \dfrac{Y_0(\iota_u)J_0(\iota_d) - J_0(\iota_u)Y_0(\iota_d)}{Y_1(\iota_u)J_0(\iota_u) - Y_0(\iota_u)J_1(\iota_u)} \\ \mp \dfrac{i}{z_d} \dfrac{Y_1(\iota_u)J_1(\iota_d) - J_1(\iota_u)Y_1(\iota_d)}{Y_1(\iota_u)J_0(\iota_u) - Y_0(\iota_u)J_1(\iota_u)} & \dfrac{z_u}{z_d} \dfrac{J_0(\iota_u)Y_1(\iota_d) - Y_0(\iota_u)J_1(\iota_d)}{Y_1(\iota_u)J_0(\iota_u) - Y_0(\iota_u)J_1(\iota_u)} \end{pmatrix} \tag{7.64}$$

$$\widetilde{M} = \frac{z_u}{z_d} \begin{pmatrix} \dfrac{Y_1(\iota_u)J_0(\iota_d) - J_1(\iota_u)Y_0(\iota_d)}{Y_1(\iota_u)J_0(\iota_u) - Y_0(\iota_u)J_1(\iota_u)} & \mp i \dfrac{Y_0(\iota_u)J_0(\iota_d) - J_0(\iota_u)Y_0(\iota_d)}{Y_1(\iota_u)J_0(\iota_u) - Y_0(\iota_u)J_1(\iota_u)} \\ \mp i \dfrac{Y_1(\iota_u)J_1(\iota_d) - J_1(\iota_u)Y_1(\iota_d)}{Y_1(\iota_u)J_0(\iota_u) - Y_0(\iota_u)J_1(\iota_u)} & \dfrac{J_0(\iota_u)Y_1(\iota_d) - Y_0(\iota_u)J_1(\iota_d)}{Y_1(\iota_u)J_0(\iota_u) - Y_0(\iota_u)J_1(\iota_u)} \end{pmatrix} \tag{7.65}$$

element exit are then expressed in terms of the acoustic pressure p'_u and acoustic velocity u'_u at the element entrance. The corresponding ATM/DATM are subsequently derived for both harmonic conventions $e^{\pm i\omega t}$ in Eqs. (7.64) and (7.65).

7.4.4 Transfer Matrix of a compact area change in a low-Mach non-reactive flow

The impact of a compact area change traversed by a low-Mach non-reactive flow is now investigated. Equations (7.14)-(7.16) lead to the jump conditions for the mean density, temperature and pressure:

$$\bar{\rho}_d = \bar{\rho}_u \tag{7.66}$$

$$\overline{T}_d = \overline{T}_u \tag{7.67}$$

$$\bar{p}_d = \bar{p}_u \tag{7.68}$$

The jump condition for the mean flow velocity is then obtained by integrating Eq. (7.20) over the control volume ($\mathcal{V}$) bounded by a surface (S), as depicted in Fig. 7.4.

$$A_d \bar{u}_d = A_u \bar{u}_u \tag{7.69}$$

The jump conditions for the acoustic variables are then obtained by integrating the linearized mass conservation given by Eq. (7.23) and the linearized momentum conservation given by Eq. (7.28) over the control volume ($\mathcal{V}$).

The integrated mass conservation yields:

$$\int_{(\mathcal{V})} \nabla \cdot \mathbf{u}' dV = 0 \tag{7.70}$$

Using the divergence theorem, Eq. (7.70) becomes:

$$\oint_{(S)} \mathbf{u}' \cdot \mathbf{dS} = 0 \tag{7.71}$$

The surface (S) can be decomposed into three smaller surfaces corresponding to the inlet A_u, lateral surface (Σ) and outlet A_d:

$$\int_{A_u} A_u \mathbf{u}'_u \cdot \mathbf{n}_u + \int_{(\Sigma)} \mathbf{u}' \cdot \mathbf{dS} + \int_{A_d} A_d \mathbf{u}'_d \cdot \mathbf{n}_d = 0 \tag{7.72}$$

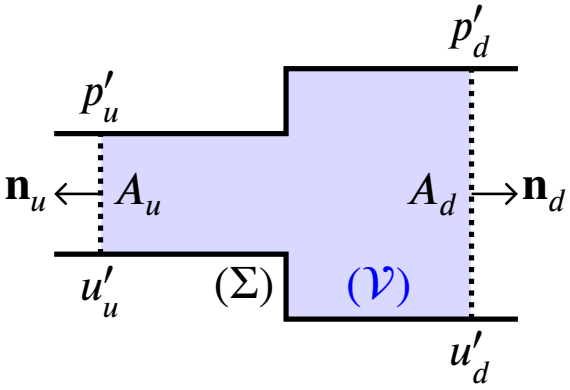

Figure 7.4: *Sketch of a compact area change in a low-Mach non-reactive flow. The subscripts u and d denote the upstream and downstream variables respectively. The control volume* $(\mathcal{V})$ *retained here is bounded by a surface* (S) *which can be split into three smaller surfaces:* A_u, (Σ) *and* A_d.

The second term in Eq. (7.72) is equal to zero because the lateral surface (Σ) is a rigid non-porous boundary which implies that $\mathbf{u}' = \mathbf{0}$ on this surface. The first and third terms in Eq. (7.72) are further simplified by assuming that the acoustic fields are one-dimensional in these regions. In the end, the jump condition for the acoustic velocity across a compact area change in a low-Mach non-reactive flow is given by (Poinsot and Veynante 2005):

$$u'_d A_d - u'_u A_u = 0 \tag{7.73}$$

The second step is to consider the integrated momentum conservation over the control volume $(\mathcal{V})$:

$$\int_{(\mathcal{V})} \nabla p' dV = 0 \tag{7.74}$$

Using the gradient theorem and splitting (S) into A_u, (Σ) and A_d, the following expression is obtained:

$$\int_{A_u} p'_u A_u \mathbf{n}_u + \int_{(\Sigma)} p' \mathbf{dS} + \int_{A_d} p'_d A_d \mathbf{n}_d = 0 \tag{7.75}$$

Using the system symmetries, the integral over the lateral surface (Σ) reduces to an integral over the area corresponding to the cross section jump $A_d - A_u$, where the acoustic pressure is p'_u (Dowling and Stow 2003). Hence, the second term in Eq. (7.75) can be approximated by:

$$\int_{(\Sigma)} p' \mathbf{dS} \simeq -p'_u \left(A_d - A_u\right) \mathbf{n}_d \tag{7.76}$$

Finally, the jump condition for the acoustic pressure across a compact area change in a low-Mach non-reactive flow (Poinsot and Veynante 2005) is obtained from Eqs. (7.75) and (7.76):

$$p'_d - p'_u = 0 \tag{7.77}$$

From Eqs. (7.54), (7.73) and (7.77), the associated ATM/DATM is given by (Paschereit and Polifke 1998; Poinsot and Veynante 2005; Fischer et al. 2006):

ATM/DATM of a compact area change in a low-Mach non-reactive flow

$$M = \widetilde{M} = \begin{pmatrix} 1 & 0 \\ 0 & A_u/A_d \end{pmatrix} \tag{7.78}$$

Equation (7.78) is valid for both harmonic conventions ($e^{\pm i\omega t}$). The ATM and DATM expressions for a compact area change in a low-Mach non-reactive flow are both given by Eq. (7.78) since the associated matrix is diagonal.

7.4.5 Transfer Matrix of a non-compact area change in a low-Mach non-reactive flow

In this section, acoustic waves propagating in a low-Mach non-reactive flow within a duct with a slowly-varying cross section area $A(x)$ are investigated. The propagation of acoustic waves within such a system is described using Webster's equation (Rienstra and Hirschberg 2016):

$$\frac{\partial^2 p'}{\partial x^2} - \frac{1}{\bar{c}^2}\frac{\partial^2 p'}{\partial t^2} + \frac{d\,(\log A)}{dx}\frac{\partial p'}{\partial x} = 0 \tag{7.79}$$

In this section, the function log refers to the natural logarithm. When harmonic waves are considered, Eq. (7.79) becomes:

$$k^2 p'_\omega + \frac{d^2 p'_\omega}{dx^2} + \frac{1}{A}\frac{dA}{dx}\frac{dp'_\omega}{dx} = 0 \tag{7.80}$$

where $k = \omega/\bar{c}$ is the wave number. Based on Eq. (7.80) and introducing λ the acoustic wavelength and L the characteristic length of variation of $A(x)$, three distinct cases are possible:

- $\lambda \ll L$: $A(x)$ varies very slowly along the x-axis. The third term in Eq. (7.80) vanishes and the results presented in Sec. 7.4.2 apply.

- $\lambda \gg L$: $A(x)$ varies very quickly along the x-axis. The system is compact and the results presented in Sec. 7.4.4 apply.

- $\lambda \sim L$: All terms in Eq. (7.80) have to be considered.

In that last case, another assumption is needed in order to derive an explicit expression for the acoustic pressure and acoustic velocity inside the system. It is assumed here that the expression of $A(x)$ is given by:

$$A(x) = A_0 e^{2bx} \tag{7.81}$$

where b is a positive or negative constant. Using this expression with Eq. (7.80) leads to:

$$\frac{d^2 p'_\omega}{dx^2} + 2b\frac{dp'_\omega}{dx} + k^2 p'_\omega = 0 \tag{7.82}$$

The general solution of this equation is:

$$p'_\omega = A_\omega e^{-bx} e^{ik_\bullet x} + B_\omega e^{-bx} e^{-ik_\bullet x} \tag{7.83}$$

where A_ω and B_ω are two complex integration constants and $k_\bullet = \sqrt{k^2 - b^2}$. The acoustic velocity is then obtained using Eqs. (7.27) and Eq. (7.83):

$$u'_\omega = \mp\frac{1}{\bar{\rho}\omega}\left[(k_\bullet + bi)\, A_\omega e^{-bx} e^{ik_\bullet x} - (k_\bullet - bi)\, B_\omega e^{-bx} e^{-ik_\bullet x}\right] \tag{7.84}$$

The acoustic pressure p'_d and acoustic velocity u'_d at the element outlet ($x = l$) are expressed in terms of the acoustic pressure p'_u and acoustic velocity u'_u at the element inlet ($x = 0$) using Eqs. (7.83) and (7.84), thus leading to the expressions of the ATM/DATM of a non-compact exponential area change in a low-Mach non-reactive flow for both harmonic conventions ($e^{\pm i\omega t}$) in Eqs. (7.85) and (7.86).

It is worth noting that imposing $b = 0$ in Eqs. (7.85) and (7.86) leads to Eqs. (7.58) and (7.59) that describe sound wave propagation in a straight duct with a constant cross section area.

ATM/DATM of a non-compact exponential area change in a low-Mach non-reactive flow

$$M = e^{-bl}\begin{pmatrix} \cos(k_\bullet l) + \frac{b}{k_\bullet}\sin(k_\bullet l) & \mp\frac{i\bar{\rho}\omega}{k_\bullet}\sin(k_\bullet l) \\ \mp\frac{i}{\bar{\rho}\omega}(k_\bullet + \frac{b^2}{k_\bullet})\sin(k_\bullet l) & \cos(k_\bullet l) - \frac{b}{k_\bullet}\sin(k_\bullet l) \end{pmatrix} \tag{7.85}$$

$$\widetilde{M} = e^{-bl}\begin{pmatrix} \cos(k_\bullet l) + \frac{b}{k_\bullet}\sin(k_\bullet l) & \mp\frac{ik}{k_\bullet}\sin(k_\bullet l) \\ \mp\frac{i}{k}(k_\bullet + \frac{b^2}{k_\bullet})\sin(k_\bullet l) & \cos(k_\bullet l) - \frac{b}{k_\bullet}\sin(k_\bullet l) \end{pmatrix} \tag{7.86}$$

7.4.6 Transfer Matrix of a compact perforated plate traversed by a high-Reynolds flow

A single perforation or an array of perforations traversed by a high-Reynolds flow generate an acoustic pressure drop due to the interaction between vortical structures and sound waves (Strutt and Rayleigh 1878; Howe 1979; Scarpato et al. 2013). In that case, the acoustic pressure p'_d downstream the perforation is different from the acoustic pressure p'_u upstream the perforation.

The Rayleigh conductivity K_r of a compact aperture (Strutt and Rayleigh 1878; Howe 1979; Scarpato et al. 2013) relates the rate of change of volumetric flow rate fluctuations $\partial\dot{V}'/\partial t$ inside the aperture to the acoustic pressure drop across the aperture:

$$\bar{\rho}\frac{\partial\dot{V}'}{\partial t} = -K_r\left(p'_d - p'_u\right) \tag{7.87}$$

The Reynolds number is assumed to be sufficiently large to neglect viscous effects except at the aperture rim, where unsteady vortical structures are shedded periodically (Howe 1979). Acoustic waves interact with these vortical structures convected away from the rim, thus accounting for the non-zero acoustic pressure drop across the aperture. As a consequence, when vorticity is neglected, the results obtained in Sec. 7.4.4 are applicable, leading to a zero acoustic pressure drop across the aperture.

The second jump condition is in this case the continuity of the acoustic volumetric flow rate:

$$A_u u'_u = A_d u'_d \tag{7.88}$$

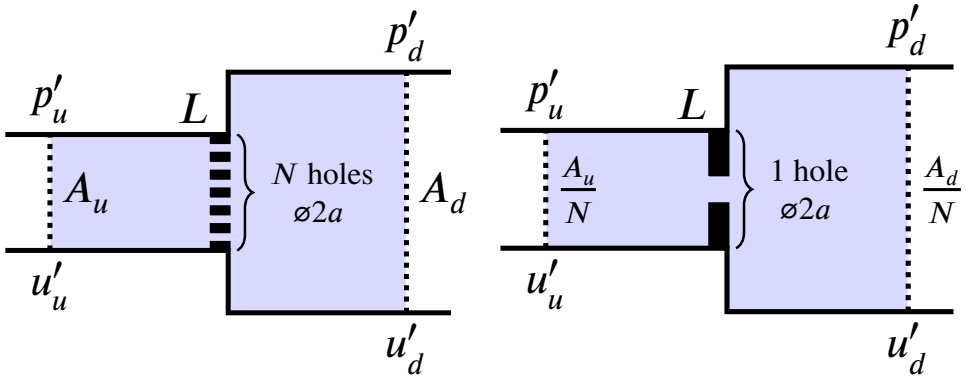

Figure 7.5: *Sketch of a perforated plate consisting of N identical evenly-distributed circular apertures of radius a traversed by a high-Reynolds flow and located at a compact area change. (Left): Original geometry - (Right): Equivalent geometry.*

The model retained for the Rayleigh conductivity K_r, called Howe's model, accounts for both the acoustic dissipation and the inertia of the fluid inside the perforation (Howe 1979). Howe's model was initially derived for a single circular aperture located inside a constant area duct (Strutt and Rayleigh 1878; Howe 1979). However, it can be extended to a collection of N identical non-interacting circular apertures of radius a evenly distributed over a plate located at a compact area change, as depicted in Fig. 7.5-(Left) (Howe 1979; Luong et al. 2005; Scarpato et al. 2013).

An equivalent geometry preserving the acoustic properties of the perforated plate is subsequently defined, as shown in Fig. 7.5-(Right). Assuming that the acoustic waves are harmonic and replacing $\dot{V}'$ in Eq. (7.87) by its explicit expression, the acoustic pressure jump across the perforated plate is obtained:

$$p'_d = p'_u \mp \frac{i\omega\bar{\rho}A_u}{NK_r}u'_u \tag{7.89}$$

The Rayleigh conductivity K_r depends on the harmonic convention (Gloerfelt 2009). The Rayleigh conductivity $K_{r\oplus}$ obtained with the $e^{+i\omega t}$ convention is the complex conjugate of $K_{r\ominus}$ obtained with the $e^{-i\omega t}$ convention. From Eqs. (7.88) and (7.89), the ATM/DATM of a compact perforated plate traversed by a high-Reynolds flow are derived in Eqs. (7.90) and (7.91).

For an infinitely thin perforated plate, the Rayleigh conductivity according to Howe's model is given by (Howe 1979):

$$K_{r\ominus} = 2a\zeta \tag{7.92}$$

ATM/DATM of a compact perforated plate traversed by a high-Reynolds flow

$$M = \begin{pmatrix} 1 & \mp i\omega\bar{\rho}A_u/(NK_r) \\ 0 & A_u/A_d \end{pmatrix} \qquad \text{with } e^{\pm i\omega t} \tag{7.90}$$

$$\widetilde{M} = \begin{pmatrix} 1 & \mp ikA_u/(NK_r) \\ 0 & A_u/A_d \end{pmatrix} \qquad \text{with } e^{\pm i\omega t} \tag{7.91}$$

where ζ is a function of a Strouhal number $\mathrm{St} = \omega a/u_c$ only, as expressed in:

$$\zeta = 1 + \frac{\frac{\pi}{2}I_1(St)e^{-St} - iK_1(St)\sinh(St)}{St\left[\frac{\pi}{2}I_1(St)e^{-St} + iK_1(St)\cosh(St)\right]} \tag{7.93}$$

where I_1 and K_1 are modified Bessel functions of the first and second kind respectively and of order 1. The velocity u_c is the speed at which vortical structures are convected away from the apertures' rim. Usually, u_c is assumed to be equal to the average velocity $\bar{u}$ inside the holes (Scarpato et al. 2013).

A modified version of this model for a perforated plate with a finite thickness L is given by (Jing and Sun 2000; Luong et al. 2005):

$$K_{r\ominus} = 2a\zeta_L \tag{7.94}$$

where ζ_L is expressed as:

$$\zeta_L^{-1} = \zeta^{-1} + \frac{2L}{\pi a} \tag{7.95}$$

7.4.7 Transfer Matrix of a compact perforated plate traversed by a high-Reynolds flow - Non-linear extension

The ATM/DATM of a compact perforated plate traversed by a high-Reynolds flow, as presented in Sec. 7.4.6, is linear because it was assumed that the convection velocity u_c at which vortical structures are swept away from the apertures is equal to $\bar{u}$. However, for large acoustic forcing levels $|u'|/\bar{u} \geq 1$, it was shown in a previous investigation that the convection speed of the vortical structures generated at the rim of the aperture is not equal to the mean flow velocity

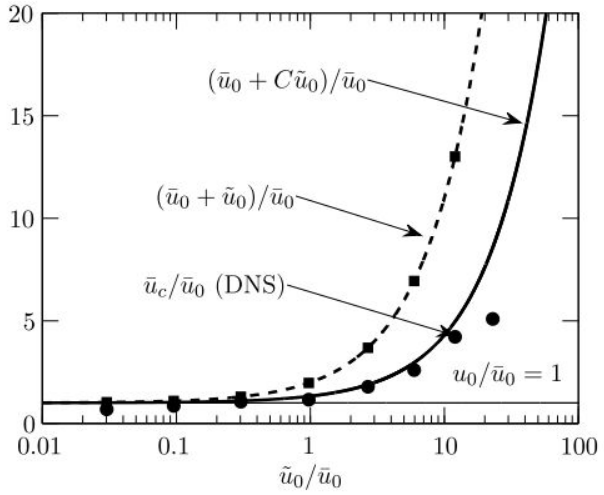

Figure 7.6: *Evolution of the convection velocity of the vortical structures as a function of the forcing level $|u'|/\bar{u}$ in the perforation for a forcing frequency $f = 400$ Hz. The average convection velocity u_c deduced from direct numerical simulations (dots) for each forcing amplitude is compared to the velocity ratio in the orifice $(\bar{u} + |u'|)/\bar{u}$ (dashed line and black squares), and to the model $u_c = \bar{u} + C|u'|$ with $C = 1/3$ (solid line). Reproduced from Scarpato (2014).*

inside the aperture (Scarpato 2014). Thus, the acoustic response of the perforated plate deviates from the linear model for large acoustic forcing levels.

A nonlinear extension of the previous linear model for high acoustic forcing levels is based on a modified expression for the convection velocity u_c (Scarpato 2014):

$$u_c = \bar{u} + K|u'| \tag{7.96}$$

where K is a constant fixed to 1/3 (Scarpato 2014) and u' is the acoustic velocity inside the holes. This heuristic model is based on experiments and simulations where the convection velocity of the vortical structures generated at the rim of the apertures was assessed for low forcing levels $|u'|/\bar{u} \ll 1$ and large forcing levels $|u'|/\bar{u} \geq 1$ (Scarpato 2014). Figure 7.6 demonstrates that the optimal value for K is 1/3 based on these simulations (Scarpato 2014).

A consequence of the previous analysis is that the Strouhal number St is now a function of both the angular frequency ω and forcing amplitude $|u'|$:

$$St(\omega, |u'|) = \frac{\omega a}{\bar{u} + K|u'|} \tag{7.97}$$

The Rayleigh conductivity, given by Eq. (7.92) for infinitely thin plates and Eq. (7.94) for plates with a finite thickness, and the associated ATM/DATM, given by Eqs. (7.90) and (7.91) respectively, are then written as functions of the angular frequency ω and forcing amplitude $|u'|$ following Eq. (7.97).

This approach is a simple extension of the linear model presented in Sec. 7.4.6, as opposed to more complex nonlinear approaches (Cummings 1984). As a consequence, the Acoustic Transfer Matrix formalism, which is intrinsically linear, may be still be used when large acoustic forcing levels are considered.

7.5 Conclusion

The propagation of linear acoustic waves in a low-Mach non-reactive flow was investigated in this chapter. The notion of Dimensionless Acoustic Transfer Matrix (DATM) was introduced and the DATM of various acoustic elements such as a straight duct in a uniform flow, a compact area change or a perforated plate traversed by a high-Reynolds flow were derived. It is now worth investigating the propagation of linear acoustic waves in a low-Mach reactive flow.

Chapter 8

Linear Acoustics: low-Mach Reactive flow

The linearized conservation equations describing sound wave propagation in a low-Mach reactive flow are derived in this chapter. The jump conditions for the acoustic pressure and acoustic velocity across a compact lean flame stabilized in a low-Mach flow within a straight duct are subsequently derived.

8.1 Linearized conservation equations

8.1.1 Assumptions

A few assumptions are made in order to derive the equations describing sound wave propagation in a low-Mach reactive flow. It is reminded that the mean physical variables are represented with an overline ($\overline{x}$) whereas the fluctuating physical variables are represented with a prime (x'). Vectors will be denoted by bold characters for the sake of readability. The initial hypotheses related to the nature of the flow and acoustic perturbations are listed below with bullets ($\bullet$) and circles ($\circ$) respectively:

- The mean flow variables are time-independent.
- The flame is a non-moving volumetric heat source $\overline{\dot{q}}$.
- The fluid is an ideal gas.
- Body forces are neglected.
- Viscosity effects are neglected: $\mu = 0$.
- Thermal conduction and radiation are neglected.

- The flow has a low Mach number $M = \bar{u}/\bar{c} \ll 1$.
  - Acoustic sources other than the unsteady flame are not considered.
  - Acoustic perturbations are linear.

8.1.2 Conservation equations

The conservation equations for a reactive flow where body forces, viscous forces and thermal diffusion and radiation are neglected are (Poinsot and Veynante 2005):

Mass conservation

$$\frac{\partial \rho}{\partial t} + \nabla \cdot (\rho \mathbf{u}) = 0 \tag{8.1}$$

Momentum conservation

$$\rho \frac{\partial \mathbf{u}}{\partial t} + \rho \mathbf{u} \cdot \nabla \mathbf{u} = -\nabla p \tag{8.2}$$

Energy conservation

$$\rho c_p \left(\frac{\partial T}{\partial t} + \mathbf{u} \cdot \nabla T \right) = \dot{q} + \frac{\partial p}{\partial t} + \mathbf{u} \cdot \nabla p \tag{8.3}$$

As opposed to Chapter 7, the flow is not isentropic because of the flame. Another expression of the energy conservation is thus employed in this chapter.

Each of the physical variables in Eqs. (8.1)-(8.3) can be written as the sum of a mean flow variable and an acoustic perturbation (Morse and Ingard 1968; Candel and Poinsot 1988). This decomposition is presented explicitly below:

$$p = \bar{p} + p' \tag{8.4}$$
$$\mathbf{u} = \bar{\mathbf{u}} + \mathbf{u}' \tag{8.5}$$
$$\rho = \bar{\rho} + \rho' \tag{8.6}$$
$$T = \bar{T} + T' \tag{8.7}$$
$$c_p = \bar{c}_p + c_p' \tag{8.8}$$
$$c_v = \bar{c}_v + c_v' \tag{8.9}$$

Even though c_p and c_v are functions of the gas temperature, their variations are limited, especially since the acoustic perturbations are linear which implies

that $|T'|/\overline{T} \ll 1$. Therefore, c'_p and c'_v are neglected in the remainder of this work.

It should be noted that even though the flow has a low Mach number, the mean flow velocity $\bar{\mathbf{u}}$ cannot be neglected because that would imply that the mean volumetric heat release rate $\bar{\dot{q}}$ is equal to zero.

8.1.3 Constitutive equations

By analogy with the non-reactive case presented in Chapter 7, dimensional analysis is employed to assess the relative importance of each term in the following derivations. The constitutive equations for the mean flow are:

$$\bar{p} = \bar{\rho} r \overline{T} \tag{8.10}$$

$$\gamma \bar{p} = \bar{\rho} \bar{c}^2 \tag{8.11}$$

$$\gamma r \overline{T} = \bar{c}^2 \tag{8.12}$$

$$\bar{p} \bar{\rho}^{-\gamma} = e^{\bar{s}/\bar{c}_v} \tag{8.13}$$

where Eq. (8.10) is the ideal gas law, Eq. (8.11) is the expression of sound speed in an ideal gas, Eq. (8.12) is obtained by combining the first two equations and Eq. (8.13) is the expression of the entropy of an ideal gas.

On the other hand, the acoustic variables are linked through the following equation:

$$p' = r \overline{T} \rho' + \bar{\rho} r T' \tag{8.14}$$

Equation (8.14) comes from the linearized ideal gas law (Candel and Poinsot 1988; Crighton et al. 1992).

The following estimate is also used in this chapter (Hirschberg and Rienstra 2004):

$$p' \sim \bar{\rho} \bar{c} u' \tag{8.15}$$

8.1.4 Linearized mass conservation

Following the procedure introduced in Sec. 7.1.4 and keeping terms of order 0 only, the mass conservation for the mean flow is obtained:

$$\nabla \cdot (\bar{\rho} \bar{\mathbf{u}}) = 0 \tag{8.16}$$

The linearized mass conservation in a low-Mach reactive flow is then obtained by considering terms of order 1. The resulting equations for compact and non-compact systems are expressed in Eqs. (8.17) and (8.18) respectively. These equations differ from those obtained in Chapter 7 because Eq. (7.17) cannot be used for a non-homentropic flow.

Linearized mass conservation in a low-Mach reactive flow

$$\frac{\partial \rho'}{\partial t} + \nabla \cdot \left(\rho' \bar{\mathbf{u}}\right) + \nabla \cdot \left(\bar{\rho} \mathbf{u}'\right) = 0 \tag{8.17}$$

Linearized compact mass conservation in a low-Mach reactive flow

$$\nabla \cdot \left(\rho' \bar{\mathbf{u}}\right) + \nabla \cdot \left(\bar{\rho} \mathbf{u}'\right) = 0 \tag{8.18}$$

8.1.5 Linearized momentum conservation

Equations (8.4)-(8.9) are injected into Eq. (8.2). If terms of order 0 are considered only, it is found that:

$$\underbrace{\bar{\rho} \bar{\mathbf{u}} \cdot \nabla \bar{\mathbf{u}}}_{(1)} = \underbrace{-\nabla \bar{p}}_{(2)} \tag{8.19}$$

In Eq. (8.19), the first term represents the inertial effects of the mean flow whereas the second term represents the mean pressure gradient effects. Their relative importance can be assessed by using dimensional analysis. It is found that $(1)/(2) \sim \gamma \mathrm{M}^2 \ll 1$ which implies that both terms are equal to zero:

$$\bar{\mathbf{u}} \cdot \nabla \bar{\mathbf{u}} = 0 \tag{8.20}$$

$$\nabla \bar{p} = 0 \tag{8.21}$$

Moreover, the linearized momentum conservation is still given by Eq. (7.26). The dimensional analysis performed in Sec. 7.1.5 still applies and the second and third terms in Eq. (7.26) are dropped because of the low-Mach flow assumption. Furthermore, if the region of interest is compact, the first term can also be dropped. In the end, the linearized momentum conservation in the reactive and non-reactive cases are similar. Equations (8.22) and (8.23) are the linearized momentum conservation in a low-Mach reactive flow for non-compact and compact systems respectively.

Linearized momentum conservation in a low-Mach reactive flow

$$\bar{\rho}\frac{\partial \mathbf{u}'}{\partial t} = -\nabla p' \tag{8.22}$$

Linearized compact momentum conservation in a low-Mach reactive flow

$$\nabla p' = 0 \tag{8.23}$$

8.1.6 Linearized energy conservation

Equations (8.4)-(8.9) are injected into Eq. (8.3). The energy conservation for the mean flow is obtained by considering terms of order 0 only:

$$\bar{\rho}\bar{c}_p\bar{\mathbf{u}}\cdot\nabla\overline{T} = \bar{\dot{q}} \tag{8.24}$$

Using Eq. (8.16), this equation can also be expressed as:

$$\nabla\cdot\left(\bar{\rho}\bar{c}_p\overline{T}\bar{\mathbf{u}}\right) = \bar{\dot{q}} \tag{8.25}$$

Next, the linearized energy conservation is obtained by repeating the procedure and considering terms of order 1 only:

$$\underbrace{\bar{\rho}\bar{c}_p\frac{\partial T'}{\partial t}}_{(1)} + \underbrace{\bar{\rho}\bar{c}_p\bar{\mathbf{u}}\cdot\nabla T'}_{(2)} + \underbrace{\bar{\rho}\bar{c}_p\mathbf{u}'\cdot\nabla\overline{T}}_{(3)} + \underbrace{\rho'\bar{c}_p\bar{\mathbf{u}}\cdot\nabla\overline{T}}_{(4)} = \underbrace{\dot{q}'}_{(5)} + \underbrace{\frac{\partial p'}{\partial t}}_{(6)} + \underbrace{\bar{\mathbf{u}}\cdot\nabla p'}_{(7)} \tag{8.26}$$

This equation can be further simplified by using dimensional analysis. It is found that (1)/(3) $\sim$ He $(T'\bar{c})/(\overline{T}u')$, (6)/(3) $\sim$ He $(\gamma-1)$ and (7)/(3) $\sim$ M $(\gamma-1)$. Since the flow is low-Mach, the seventh term in Eq. (8.26) is neglected. Moreover, if the region of interest is compact, the first and sixth terms may also be neglected. In the end, the linearized energy conservation in a low-Mach reactive flow is obtained for compact and non-compact regions of interest, as expressed in Eqs. (8.27) and (8.28).

Linearized energy conservation in a low-Mach reactive flow

$$\bar{\rho}\bar{c}_p\frac{\partial T'}{\partial t} + \bar{\rho}\bar{c}_p\bar{\mathbf{u}}\cdot\nabla T' + \bar{\rho}\bar{c}_p\mathbf{u}'\cdot\nabla\overline{T} + \rho'\bar{c}_p\bar{\mathbf{u}}\cdot\nabla\overline{T} = \dot{q}' + \frac{\partial p'}{\partial t} \tag{8.27}$$

Linearized compact energy conservation in a low-Mach reactive flow

$$\bar{\rho}\bar{c}_p\bar{\mathbf{u}}\cdot\nabla T' + \bar{\rho}\bar{c}_p\mathbf{u}'\cdot\nabla\overline{T} + \rho'\bar{c}_p\bar{\mathbf{u}}\cdot\nabla\overline{T} = \dot{q}' \tag{8.28}$$

8.1.7 Combination of the mass and energy conservation

An additional equation combining the linearized mass conservation given by Eq. (8.17) and the linearized energy conservation given by Eq. (8.27) is now derived (Poinsot and Veynante 2005).

From Eqs. (8.10), (8.14), (8.16), (8.17) and (8.27), the following equation is obtained:

$$\underbrace{\bar{c}_p\overline{T}\bar{\rho}\nabla\cdot\mathbf{u}'}_{(1)}+\underbrace{\frac{1}{\gamma-1}\frac{\partial p'}{\partial t}}_{(2)}+\underbrace{\frac{\gamma}{\gamma-1}\bar{\mathbf{u}}\cdot\nabla p'}_{(3)}-\underbrace{\frac{\gamma}{\gamma-1}\frac{p'}{\bar{\rho}}\bar{\mathbf{u}}\cdot\nabla\bar{\rho}}_{(4)}=\underbrace{\dot{q}'}_{(5)} \tag{8.29}$$

It is found that (2)/(1) $\sim$ He, (3)/(1) $\sim$ Mγ and (4)/(1) $\sim$ Mγ. Since the flow is low-Mach, the third and fourth terms in Eq. (8.29) are neglected. Furthermore, if the region of interest is compact, then the second term is dropped as well. Given these considerations, two extra equations valid for low-Mach reactive flows in non-compact and compact regions are respectively given by Eqs. (8.30) and (8.31).

Linearized equation in a low-Mach reactive flow

$$\nabla\cdot\mathbf{u}'+\frac{1}{\gamma\bar{p}}\frac{\partial p'}{\partial t}=\frac{\gamma-1}{\gamma\bar{p}}\dot{q}' \tag{8.30}$$

Linearized compact equation in a low-Mach reactive flow

$$\nabla\cdot\mathbf{u}'=\frac{\gamma-1}{\gamma\bar{p}}\dot{q}' \tag{8.31}$$

8.2 Wave equation in a low-Mach reactive flow

In Chapter 7, a wave equation describing sound wave propagation in a low-Mach non-reactive flow was obtained from the linearized conservation equations. The same procedure is now applied to the reactive case. By taking the time derivative of Eq. (8.30) and injecting the linearized momentum conservation given by Eq. (8.22), and finally using the constitutive equation given by Eq. (8.11), the wave equation in a low-Mach reactive flow is obtained (Dowling 1995; Nicoud et al. 2007), as expressed in Eq. (8.32).

Wave equation in a low-Mach reactive flow

$$\frac{1}{\bar{\rho}\bar{c}^2}\frac{\partial^2 p'}{\partial t^2} - \nabla\cdot\left(\frac{\nabla p'}{\bar{\rho}}\right) = \frac{\gamma-1}{\bar{\rho}\bar{c}^2}\frac{\partial \dot{q}'}{\partial t} \tag{8.32}$$

8.3 Transfer Matrix of a lean compact flame stabilized in a low-Mach flow within a straight duct

The jump conditions across a lean compact flame stabilized in a low-Mach flow within a straight duct are derived in this section. It is reminded that the subscripts u and d refer to upstream and downstream variables respectively.

The jump conditions for the mean flow variables are obtained by integrating Eqs. (8.16), (8.21) and (8.25) over the control volume $(\mathcal{V})$ bounded by a surface (S) as depicted in Fig. 8.1:

$$\bar{\rho}_d\bar{u}_d = \bar{\rho}_u\bar{u}_u \tag{8.33}$$

$$\bar{p}_d = \bar{p}_u \tag{8.34}$$

$$\bar{c}_p\bar{\rho}_u\bar{u}_u\left(\overline{T}_d - \overline{T}_u\right)A = \overline{\dot{Q}} \tag{8.35}$$

$$\bar{\rho}_d\overline{T}_d = \bar{\rho}_u\overline{T}_u \tag{8.36}$$

where $\overline{\dot{Q}}$ is the mean heat release rate integrated over the flame volume. Equation (8.36) is obtained from Eqs. (8.10) and (8.34).

The jump condition for the acoustic pressure is then obtained by integrating the linearized compact momentum conservation, given by Eq. (8.23), over the control volume $(\mathcal{V})$. The gradient theorem is then used, yielding the following

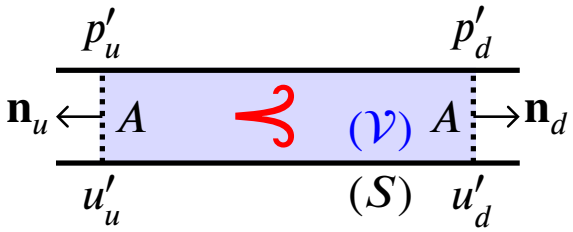

Figure 8.1: *Sketch of a compact flame stabilized in a low-Mach flow within a straight duct. The acoustic pressure and acoustic velocity at the duct inlet are denoted by p'_u and u'_u respectively. The acoustic pressure and acoustic velocity at the duct outlet are denoted by p'_d and u'_d respectively. The control volume $(\mathcal{V})$ retained here is bounded by a surface (S).*

equation:

$$\int_{(\mathcal{V})} \nabla p' dV = \oint_{(S)} p' \mathbf{n} dS = 0 \tag{8.37}$$

Using the axisymmetric properties of the control volume depicted in Fig. 8.1, this equation becomes:

$$\int_A p'_u \mathbf{n}_u dS + \int_A p'_d \mathbf{n}_d dS = 0 \tag{8.38}$$

Assuming that the acoustic pressure is uniform in the upstream and downstream cross sections, this latest equation leads to the jump condition for the acoustic pressure across a compact flame stabilized in a low-Mach flow within a straight duct (Dowling 1995):

$$p'_d = p'_u \tag{8.39}$$

In order to obtain the jump condition for the acoustic velocity, Eq. (8.31) is integrated over the control volume ($\mathcal{V}$):

$$\int_{(\mathcal{V})} \nabla \cdot \mathbf{u}' dV = \int_{(\mathcal{V})} \frac{\gamma - 1}{\gamma \bar{p}} \dot{q}' dV \tag{8.40}$$

The divergence theorem is then applied to the left-hand-side of Eq. (8.40). Since the mean pressure is a constant, the right-hand-side is simplified by introducing $\dot{Q}'$, the fluctuating heat release rate integrated over the flame volume:

$$\oint_{(S)} \mathbf{u}' \cdot \mathbf{n} dS = \frac{\gamma - 1}{\gamma \bar{p}} \dot{Q}' \tag{8.41}$$

As explained in Chapter 7, the acoustic velocity is equal to zero at the duct inner wall. By further assuming that the acoustic fields are one-dimensional at the upstream and downstream locations, Eq. (8.41) can be further simplified (Dowling 1995):

$$\left(u'_d - u'_u\right) A = \frac{\gamma - 1}{\gamma \bar{p}} \dot{Q}' \tag{8.42}$$

The heat release rate fluctuations $\dot{Q}'$ can be described using the Flame Transfer Function $F(\omega)$ (Crocco 1951; Crocco 1952; Candel 2002) or its nonlinear extension, the Flame Describing Function $F(\omega, |u'_u|/\bar{u}_u)$, defined as (Noiray et al.

2008):

$$F(\omega, |u'_u|/\bar{u}_u) = \frac{\dot{Q}'/\overline{\dot{Q}}}{u'_u/\bar{u}_u} \tag{8.43}$$

Using Eqs. (8.10), (8.35), (8.42) and (8.43), the jump condition for the acoustic velocity across a lean compact flame stabilized in a low-Mach flow within a straight duct is obtained:

$$u'_d = \left[1 + F\left(\frac{\overline{T}_d}{\overline{T}_u} - 1\right)\right] u'_u \tag{8.44}$$

Equations (8.39) and (8.44) are valid for both harmonic conventions ($e^{\pm i\omega t}$).

The ATM/DATM of a lean compact flame stabilized in a low-Mach flow within a straight duct (Keller 1995) are then derived from Eqs. (8.39) and (8.44), as expressed in Eqs. (8.45) and (8.46).

ATM/DATM of a lean compact flame stabilized in a low-Mach flow within a straight duct

$$M = \begin{pmatrix} 1 & 0 \\ 0 & 1 + F\left(\overline{T}_d/\overline{T}_u - 1\right) \end{pmatrix} \tag{8.45}$$

$$\widetilde{M} = \begin{pmatrix} z_u/z_d & 0 \\ 0 & 1 + F\left(\overline{T}_d/\overline{T}_u - 1\right) \end{pmatrix} \tag{8.46}$$

where $z = \bar{\rho}\bar{c}$ is the characteristic impedance. Once again, Eqs. (8.45) and (8.46) are valid for both harmonic conventions ($e^{\pm i\omega t}$). If the flame frequency response is described using a Flame Transfer Function (FTF), the associated ATM/DATM are linear. On the other hand, if a Flame Describing Function (FDF) is used, the nonlinearities of the flame acoustic response are accounted for and the ATM/DATM model is nonlinear.

8.4 Conclusion

The propagation of linear acoustic waves in a low-Mach reactive flow was investigated in this chapter. The DATM corresponding to a lean compact flame stabilized in a low-Mach flow within a straight duct was subsequently derived.

Chapter 9

Describing Functions with Upstream and Downstream Forcing

The describing functions of confined premixed swirling and non-swirling flames is explored in this chapter for a large set of forcing levels. In these experiments, the flame is either forced by an upstream loudspeaker or by a set of downstream loudspeakers. The experimental setup is equipped with a hot wire probe and a microphone located in front of each other, before the swirler. A second microphone is connected to the combustion chamber backplate. A photomultiplier equipped with an OH filter is used to measure the heat release rate fluctuations. The describing functions between the photomultiplier signal and the different pressure and velocity reference signals are then analyzed for upstream and downstream forcing. The describing function measured for a given reference signal is shown to vary depending on the type of forcing. It is shown that the Flame Describing Function measured with respect to the hot wire can be retrieved from the specific impedance at the hot wire location and the describing function determined with respect to the microphone located in front of the hot wire. It is then shown that a 1D acoustic model is able to reproduce the describing function computed with respect to the microphone inside the injector from the microphone located at the bottom of the combustion chamber for downstream forcing. This relation does not hold for upstream forcing because of the acoustic dissipation across the swirler which is much larger compared to downstream forcing for a given forcing level set at the hot wire location. When the nonlinear acoustic losses in the swirler holes are accounted for, this reconstruction is satisfactory. Finally, the upstream and downstream forcing techniques are found to be equivalent only if the reference signal is the acoustic velocity in the fresh gases just before the flame.*

9.1 Definition and purpose of describing functions

Coupling an acoustic solver with a Flame Transfer Function (FTF), or its nonlinear extension, the Flame Describing Function (FDF), is a powerful framework used to predict the thermoacoustic stability of practical combustors at a limited computational cost (Keller 1995; Dowling and Stow 2003; Sattelmayer and Polifke 2003; Nicoud et al. 2007; Camporeale et al. 2011; Laera et al. 2017). In these low-order models, the flame frequency response to acoustic waves is described by the complex function called FTF and defined as (Candel 2002):

$$F(\omega) = \frac{\dot{Q}'/\bar{\dot{Q}}}{u'/\bar{u}} \tag{9.1}$$

where $\dot{Q}$ denotes the heat release rate generated by the flame and u the velocity at some location inside the injector. The overline stands for mean conditions and the prime corresponds to the Fourier component of the signal at the forcing angular frequency ω.

The FTF can be generalized to take into account the effect of the forcing level $|u'|/\bar{u}$ (Dowling 1997; Noiray et al. 2008). In this case, the operator defined in Eq. (9.1) becomes nonlinear and is called a Flame Describing Function (FDF). The FDF can then be used to analyze the dynamics of each mode of the combustor and determine the level reached by the acoustic oscillations within the system. This procedure is applied to the NoiseDyn burner in Chapter 11.

The FDF framework is able to reproduce the nonlinear dynamics of labscale combustors equipped with swirling injectors (Palies et al. 2011b; Ćosić et al. 2014) and more recently the nonlinear dynamics of annular systems with multiple flames (Laera et al. 2017). One difficulty is to have a good knowledge of the FDF covering the frequency range of interest at low and high perturbation amplitudes (Laera et al. 2017). This requires high efficiency actuation systems and acoustic forcing can be generated from the upstream (Boudy et al. 2011; Mirat et al. 2015) or downstream (Hochgreb et al. 2013) sides of the combustor.

Another difficulty is to properly define the reference signal used to compute the describing function. This reference signal is sometimes defined as the velocity signal at some location inside the injector (Noiray et al. 2008; Gatti et al. 2017) and sometimes as the velocity signal at the flame location (Schuller et al. 2003b; Birbaud et al. 2007; Durox et al. 2009; Gaudron et al. 2017a). Other authors use the pressure signal inside the combustion chamber as a reference to characterize the nonlinear flame response (Schuermans et al. 2006; Noiray and Schuermans 2013; Ghirardo et al. 2015). However, no systematic comparison between the describing functions defined with these various reference signals has been performed so far.

The aim of this chapter is to measure and establish a link between the various describing functions based on three different reference signals: 1) The acoustic velocity before the swirler, measured with a hot wire probe. 2) The acoustic pressure before the swirler, measured with a microphone located at the same axial position as the hot wire probe. 3) The acoustic pressure at the bottom of the combustion chamber, in the hot gases region, also measured with a microphone. A reconstruction of the describing function with a reference signal corresponding to the acoustic velocity just before the flame is also attempted. These measurements are performed for a swirling and a non-swirling flame.

9.2 Measurement of describing functions

Configurations $\mathbf{G}^1$ and $\mathbf{G}^1_\varnothing$ are used to determine the various describing functions for both types of acoustic forcing in the swirling and non-swirling cases respectively. The corresponding experimental setup is depicted in Fig. 9.1. When upstream forcing is applied, a loudspeaker fixed below the tranquilization box is used to generate harmonic acoustic waves. When downstream forcing is applied, this bottom loudspeaker is idle. On the other hand, a downstream element is used to hold two loudspeakers at the top of the exhaust nozzle. This element is used to generate harmonic acoustic waves when downstream forcing is applied or is left idle when upstream forcing is applied. A detailed description of the experimental setup can be found in Chapter 5.

A hot wire probe called HW in Fig. 9.1 is used to determine the mean $\bar{u}_0$ and fluctuating u'_0 velocity signals at the top of the first convergent nozzle, in the top-hat region of the velocity profile. A microphone called MHW in Fig. 9.1 measures the fluctuating pressure signal p'_0 at the same axial position as the hot wire probe. A second microphone called MC in Fig. 9.1 and mounted on a water-cooled waveguide is used to measure the pressure fluctuations p'_8 at the combustion chamber backplate. The small acoustical distortions induced by the waveguide are corrected through the use of its transfer function. In addition to the acoustic measurements, a photomultiplier equipped with an interferometric filter records the OH* chemiluminescence signal, which is assumed to be linearly related to the heat release rate (Hurle et al. 1968). More information on these various diagnostics can be found in Chapter 6.

All time series contain at least 40 oscillation cycles recorded at a sampling rate $f_s = 20$ kHz. All pressure signals presented in this work are divided by the characteristic impedance $\bar{\rho}\bar{c}$ where $\bar{\rho}$ is the mean gas density and $\bar{c}$ the mean speed of sound at the microphone location. By doing so, the same dimension, a velocity in m/s, is prescribed for the hot wire and normalized microphone signals thus simplifying the comparison between the various describing functions

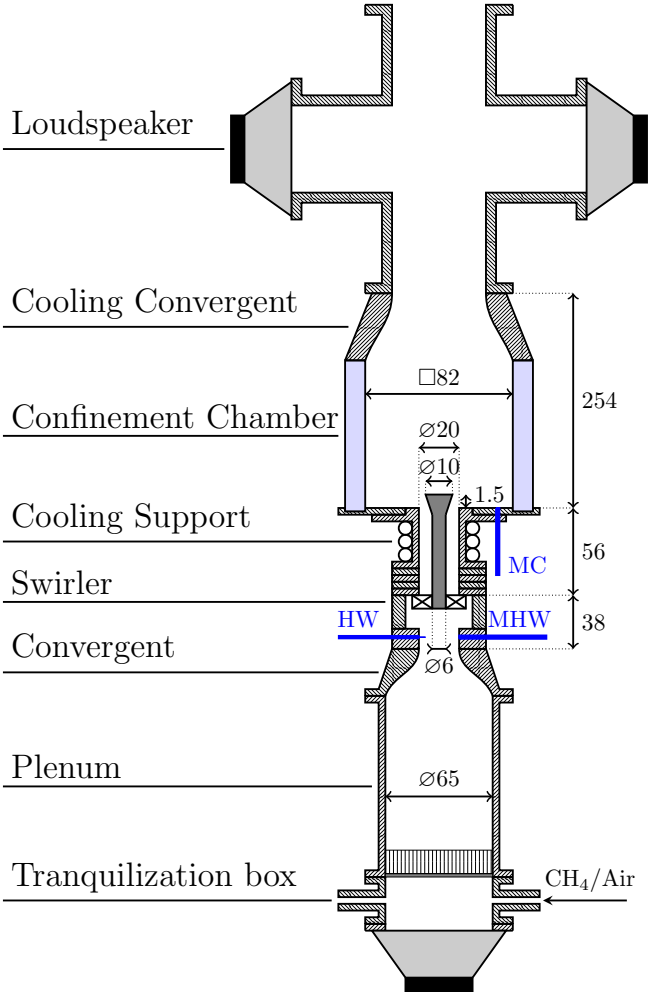

Figure 9.1: *Experimental setup used to determine the various describing functions with upstream and downstream acoustic forcing.*

introduced in the following sections. The original expressions can be easily retrieved by doing the reverse operation.

The operating conditions retained here correspond to a perfectly premixed methane/air flame with an equivalence ratio $\phi = 0.82$ and a thermal power of 5.5 kW. The associated bulk velocity at the hot wire location, in a tube of diameter $D = 22$ mm, is $\bar{u}_b = 5.4$ m/s. The highest mean velocity $\bar{u}_{max} = 12$ m/s is reached by the flow inside the six swirler injection holes, leading to a maximum Mach number $\mathrm{M}_{max} = 0.035$. The mean pressure drop in the test-rig is determined with a differential manometer between the plenum and the atmosphere and is lower than 400 Pa, corresponding to $\Delta p/\bar{p} = 0.4\%$. As a consequence, the mean pressure inside the burner is considered to be constant and equal to

the atmospheric pressure.

For each forcing frequency and each forcing level, the different describing functions are deduced from the cross power spectral density $P_{pa}(\omega, |u'|/\bar{u})$ between the photomultiplier signal and an arbitrary signal divided by the cross power spectral density $P_{ra}(\omega, |u'|/\bar{u})$ between the reference signal and the same arbitrary signal. The reference signals considered here are given by the hot wire probe (HW), the microphone located inside the injector (MHW) and the microphone located on the combustion chamber backplate (MC). The arbitrary signal, oscillating at the forcing frequency, is used as a phase reference. It may correspond to a physical signal (such as the voltage applied to the loudspeaker for instance) or to an artificial signal (sine wave at the forcing frequency). The average values of the photomultiplier signal $\bar{I}$ and reference signal $\bar{r}$ are measured as well. In the end, the describing function is defined as:

$$F(\omega, |u'|/\bar{u}) = \frac{P_{pa}(\omega, |u'|/\bar{u})/\bar{I}}{P_{ra}(\omega, |u'|/\bar{u})/\bar{r}} \tag{9.2}$$

Another method can be used to determine a describing function: first, the Fast Fourier Transform (FFT) of the photomultiplier and reference signals are computed. Then, the Fourier components of these signals at the forcing frequency ω are exctracted and finally the former coefficient is divided by the latter. This method is much easier to implement but it is not used in practice because the corresponding signal-to-noise ratio is usually poor.

9.3 Describing functions based on various reference signals

Four describing functions based on various reference signals corresponding to the acoustic pressure or acoustic velocity inside the NoiseDyn burner at several axial locations are first defined. A sketch of the injector of the NoiseDyn burner is depicted in Fig. 9.2 along with its associated acoustic equivalent. HW and MHW are located in section (0). The swirler is comprised between sections (3) and (6) and the combustion chamber starts in section (8), where MC is placed. In this chapter, the index j refers to variables assessed in section (j).

The first describing function F_{HW} is defined with respect to the hot wire probe (HW) signal:

$$F_{HW}(\omega, |u'_0|/\bar{u}_0) = \frac{\dot{Q}'/\bar{\dot{Q}}}{u'_0/\bar{u}_0} \tag{9.3}$$

where the fluctuating $\dot{Q}'$ and average $\bar{\dot{Q}}$ heat release rate are assessed at the same frequency as the fluctuating u'_0 and average $\bar{u}_0$ velocity at the hot wire

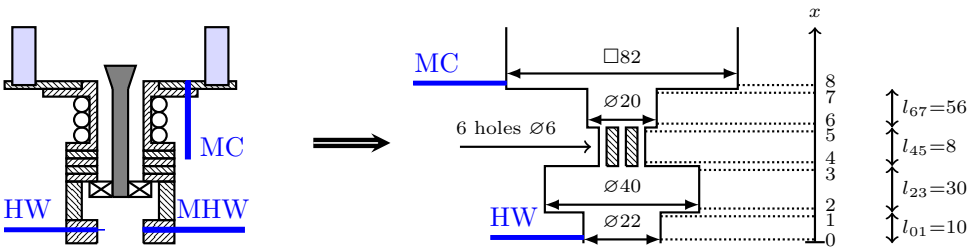

Figure 9.2: *Zoomed view of the injector of the NoiseDyn burner and acoustic model representing the injector dynamics. All dimensions are in mm.*

probe location (See Fig. 9.1). The flame nonlinearities are taken into account by including the forcing level $|u'_0|/\bar{u}_0$ as one of the variables of the describing function.

The second describing function F_{MHW} is defined with respect to the signal of the microphone (MHW) located inside the injector, in front of the hot wire probe:

$$F_{MHW}(\omega, |u'_0|/\bar{u}_0) = \frac{\dot{Q}'/\overline{\dot{Q}}}{p'_0/\bar{p}_0} \tag{9.4}$$

where p'_0 is the fluctuating pressure signal measured by MHW and $\bar{p}_0$ is a constant that has the same dimension as p'_0. Here, $\bar{p}_0$ is expressed in m/s, as explained in the previous section. Without loss of generality, it is taken equal to the atmospheric pressure divided by the characteristic impedance $\bar{\rho}_0\bar{c}_0$ at the hot wire location.

The third describing function F_{MC} is defined with respect to the signal of the microphone (MC) located at the bottom of the combustion chamber:

$$F_{MC}(\omega, |u'_0|/\bar{u}_0) = \frac{\dot{Q}'/\overline{\dot{Q}}}{p'_8/\bar{p}_8} \tag{9.5}$$

where p'_8 is the fluctuating pressure signal measured by MC and $\bar{p}_8$ is a constant that has the same dimension as p'_8. The quantity $\bar{p}_8$ is taken equal to the atmospheric pressure divided by the characteristic impedance $\bar{\rho}_8\bar{c}_8$ in the burnt gases, at the bottom of the combustion chamber.

A fourth describing function F_{HWC} is defined with respect to the acoustic velocity u'_7 at the injector outlet, just before the combustion chamber:

$$F_{HWC}(\omega, |u'_0|/\bar{u}_0) = \frac{\dot{Q}'/\overline{\dot{Q}}}{u'_7/\bar{u}_7} \tag{9.6}$$

where $\bar{u}_7$ and u'_7 are respectively the mean and fluctuating velocity at the injector outlet. This describing function is not measured in the present work but it is deduced from the previous describing functions using the models described thereafter.

It is worth recalling that the forcing level is always prescribed at the same axial location, the hot wire probe location, which explains why the variable $|u'_0|/\bar{u}_0$ is the same for all describing functions in Eqs. (9.3), (9.4), (9.5) and (9.6).

9.4 Relations between the describing functions

The link between F_{HW} and F_{MHW} is straight-forward since the hot wire HW and the microphone MHW are located in front of each other at the same axial location. By introducing the specific acoustic impedance $Z_s(\omega) = Z/(\bar{\rho}_0\bar{c}_0)$ at the hot wire location, it is easy to show that:

$$F_{HW}(\omega, |u'_0|/\bar{u}_0) = Z_s(\omega)\frac{\bar{u}_0}{\bar{p}_0}F_{MHW}(\omega, |u'_0|/\bar{u}_0) \tag{9.7}$$

The specific acoustic impedance Z_s remains independent of the forcing level if the acoustic response of the burner upstream the hot wire probe is linear. This condition was checked for the swirling and non-swirling flames and for upstream and downstream acoustic forcing, as shown in Fig. 9.3. Moreover, since Z_s represents the acoustic response of the elements located before the hot wire probe and thus before the swirler, its frequency response is independent of the Swirl number, as shown in Fig. 9.3, except for upstream forcing experiments at high forcing frequencies. In that case, the swirler seems to have a limited impact on the acoustics of the upstream elements.

Equation (9.7) will be used to check for the consistency of the experimental measurements in Secs. 9.5 and 9.6.

Two different approaches are used to relate F_{MC} to F_{MHW} and F_{HW}: first, a simple linear model accounting for the propagation of acoustic waves is derived. The second model is based on the Dimensionless Acoustic Transfer Matrix (DATM) formalism and the nonlinear acoustic losses across the swirler are accounted for. These two models are now described in details.

9.4.1 Linear acoustic model

In order to relate F_{MC} to F_{MHW} and F_{HW}, a link between the acoustic pressure p'_8 at the bottom of the combustion chamber and the acoustic variables p'_0 and u'_0 at the hot wire location has to be established. The acoustic equivalent of the injector of the NoiseDyn burner is depicted in Fig. 9.2-(Right). It

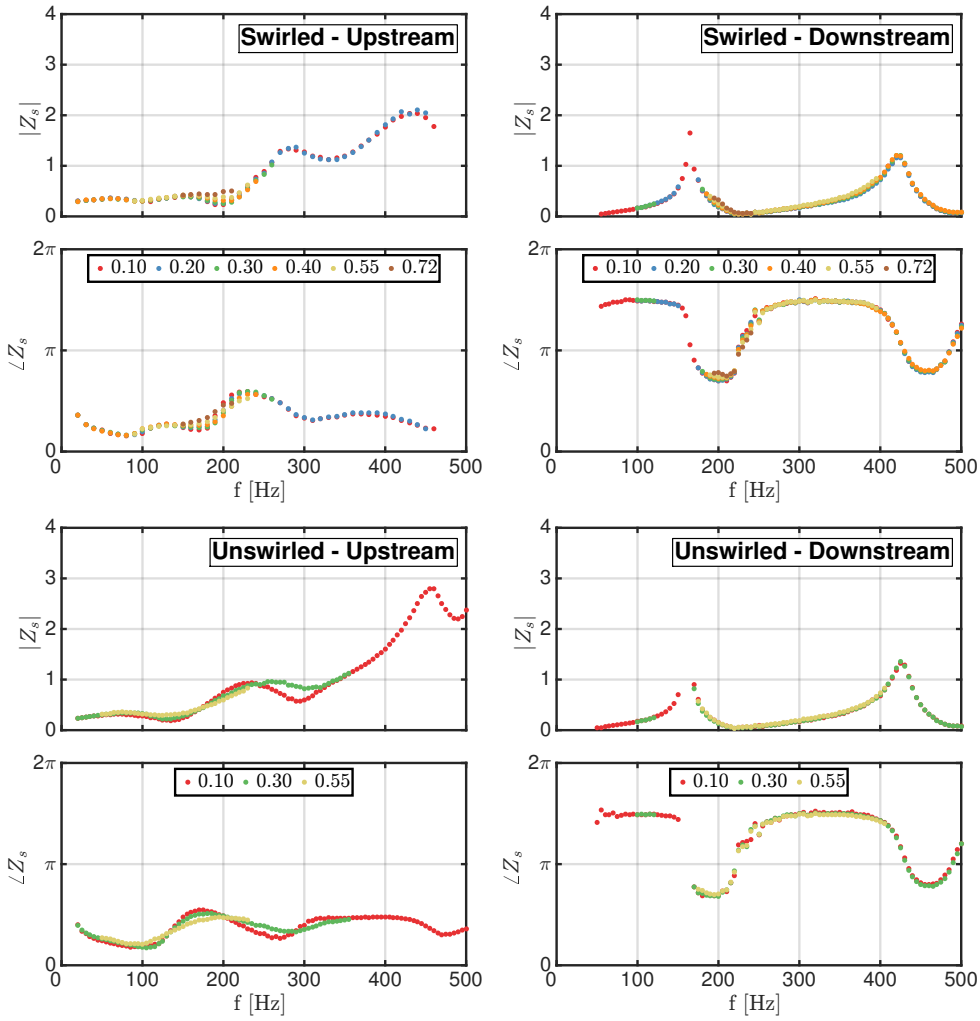

Figure 9.3: *Specific acoustic impedance Z_s as a function of the forcing frequency in the swirling (Top) and non-swirling (Bottom) cases and for upstream (Left) and downstream (Right) acoustic forcing. Results are shown for various forcing levels $|u'_0|/\bar{u}_0$.*

comprises eight elements, for which the downstream acoustic variables have to be related to the upstream acoustic variables. The change in temperature from $T_u = 293$ K in the fresh gases region to $T_b = 1200$ K in the burnt gases region is also accounted for. It is reminded that the index j refers to variables assessed in section (j) and that HW and MHW are located in section (0) while MC is placed in section (8).

In the remainder of this section, it is assumed that the acoustic waves inside the burner are linear harmonic plane waves propagating in a low-Helmholtz region. Moreover, the harmonic convention adopted here is $e^{+i\omega t}$ and all acoustic pres-

sures are divided by their respective characteristic impedances. The acoustic model represented in Fig. 9.2-(Right) features three different types of elements.

The first type of acoustic element is purely propagative and described by Eq. (7.61). The acoustic pressure p'_j and acoustic velocity u'_j in section (j) are expressed in terms of the acoustic pressure p'_i and acoustic velocity u'_i in section (i) located before (j):

$$\begin{cases} p'_j = p'_i - ikl_{ij}u'_i & (9.8) \\ u'_j = u'_i - ikl_{ij}p'_i & (9.9) \end{cases}$$

where l_{ij} is the length of the element between (i) and (j) in Fig. 9.2. Equations (9.8) and (9.9) are applied between sections (0) and (1), (2) and (3), (4) and (5) and finally (6) and (7) in the acoustic model.

The second type of acoustic element corresponds to a sudden cross section area change without a temperature jump and is described by Eqs. (7.73) and (7.77). The acoustic pressure p'_j and acoustic velocity u'_j in section (j) just after the area change are expressed in terms of the acoustic pressure p'_i and acoustic velocity u'_i in section (i), just before the area change:

$$\begin{cases} p'_j = p'_i & (9.10) \\ A_j u'_j = A_i u'_i & (9.11) \end{cases}$$

where A_j denotes the cross section area in (j). Equations (9.10) and (9.11) are applied between sections (1) and (2), (3) and (4) and finally (5) and (6) in the acoustic model represented in Fig. 9.2-(Right).

The last type of element is a sudden cross section area change combined with a jump in temperature between sections (i) and (j). It is a very simple model of a compact flame located at a sudden area change and it is applied between sections (7) and (8) in the acoustic model. The corresponding jump conditions are:

$$\begin{cases} z_j p'_j = z_i p'_i & (9.12) \\ A_j u'_j = A_i u'_i & (9.13) \end{cases}$$

where $z_i = \bar{\rho}_i \bar{c}_i$ and $z_j = \bar{\rho}_j \bar{c}_j$ are the characteristic acoustic impedances in sections (i) and (j) respectively. Using Eqs. (9.8)-(9.13) and keeping terms of order He only, it is possible to relate the acoustic pressure p'_8 in section (8) to the acoustic pressure p'_0 and acoustic velocity u'_0 in section (0), measured by

MHW and HW respectively:

$$p'_8 = \sqrt{T_b/T_u}\left[p'_0 - ikL_a u'_0\right] \tag{9.14}$$

The same procedure is applied to link the acoustic velocity u'_7 at the injector outlet, in section (7), to the acoustic velocity u'_0 and acoustic pressure p'_0 at the hot wire location, in section (0):

$$u'_7 = (A_1/A_6)\left(u'_0 - ikL_b p'_0\right) \tag{9.15}$$

The lengths L_a and L_b are equivalent lengths that take into account wave propagation inside the injector:

$$L_a = l_{01} + l_{23}\left(\frac{A_1}{A_2}\right) + l_{45}\left(\frac{A_1}{A_4}\right) + l_{67}\left(\frac{A_1}{A_6}\right) \tag{9.16}$$

$$L_b = l_{01} + l_{23}\left(\frac{A_2}{A_1}\right) + l_{45}\left(\frac{A_4}{A_1}\right) + l_{67}\left(\frac{A_6}{A_1}\right) \tag{9.17}$$

Using Eqs. (9.4), (9.5) and (9.14), the describing functions F_{MC} and F_{MHW} are connected by:

$$F_{MC}(\omega, |u'_0|/\bar{u}_0) = F_{MHW}(\omega, |u'_0|/\bar{u}_0)\frac{1}{(1 - ikL_a/Z_s)} \tag{9.18}$$

Using Eqs. (9.3), (9.6) and (9.15), the describing functions F_{HW} and F_{HWC} are connected by:

$$F_{HWC}(\omega, |u'_0|/\bar{u}_0) = F_{HW}(\omega, |u'_0|/\bar{u}_0)\frac{1}{(1 - ikL_b Z_s)} \tag{9.19}$$

The derivation presented in this section is valid at low frequencies only (Rienstra and Hirschberg 2016), when the Helmholtz number $\mathrm{He} = kL$ remains small. In this work, the maximum frequency investigated is $f_{max} = 500$ Hz corresponding to a maximum Helmholtz number $\mathrm{He} = 0.98$. Hence, the previous condition is respected and Eqs. (9.18) and (9.19) are applicable to the investigated configuration. Furthermore, this maximum Helmholtz number is small enough to justify the use of the hot wire HW and microphone MHW as reference signals.

Acoustic diffraction at the different jumps in cross section area (Lieuwen 2005), acoustic dissipation due to viscous dissipation and acoustic dissipation inside the swirler holes due to the interaction of acoustic waves with vortical structures (Howe 1998) are not taken into account with this reconstruction. Moreover, since the mean pressure drop across the setup remains small ($\Delta p/\bar{p} = 0.4\%$) and the Mach number is much smaller than unity ($\mathrm{M} = 0.035$), the mean pressure drop effects are neglected in this work (Paschereit and Polifke 1998).

9.4.2 Nonlinear acoustic network model

Two major assumptions were made in order to derive the linear acoustic model presented in the previous section: first, the injector was assumed to be nearly compact for the frequency range of interest, and second, all acoustic dissipation phenomena were neglected. The first assumption is reasonable since the maximum Helmholtz number is always lower than 1. On the other hand, acoustic dissipation may become important, especially inside the swirler channels where the acoustic velocity and Mach number are maximum. In fact, it is known that an important source of acoustic damping within the flow comes from the coupling between vortical structures generated in shear layers and acoustic waves (Lighthill 1952; Howe 1979; Ni et al. 2017). In order to drop these two assumptions, a network model based on the Transfer Matrix formalism and accounting for the acoustic pressure drop across the swirler is now derived.

The concept of Dimensionless Acoustic Transfer Matrix (DATM) used in this section is introduced in Chapter 7. The test-rig is modeled using acoustical two-port matrices (Abom 1992). Again, the harmonic convention retained is $e^{+i\omega t}$ and all pressure signals are divided by their respective characteristic acoustic impedances $z = \bar{\rho}\bar{c}$ in order to get Dimensionless Acoustic Transfer Matrix coefficients.

Various types of DATM are necessary in order to model the dynamics of the injector between section (0) and section (7) or (8) in Fig. 9.2-(Right):

- Transfer Matrices corresponding to a straight duct in a uniform non-reactive low-Mach flow, modeled with Eq. (7.59) and corresponding to the regions between sections (0) and (1), (2) and (3) and finally (6) and (7) in Fig. 9.2-(Right).
- A Transfer Matrix corresponding to a compact area change in a non-reactive low-Mach flow, modeled with Eq. (7.78) and corresponding to the region between sections (1) and (2) in Fig. 9.2-(Right).
- A Transfer Matrix corresponding to a compact area change in a low-Mach flow combined with a temperature jump, corresponding to the region between sections (7) and (8) in Fig. 9.2-(Right).
- A Transfer Matrix corresponding to a compact perforated plate traversed by a high-Reynolds flow, modeled with Eq. (7.91) and corresponding to the region between sections (3) and (6) in Fig. 9.2-(Right). The swirler finite thickness is taken into account as well as the nonlinear effects, as described in Sec. 7.4.7.

These various elements are then combined in order to build two total transfer

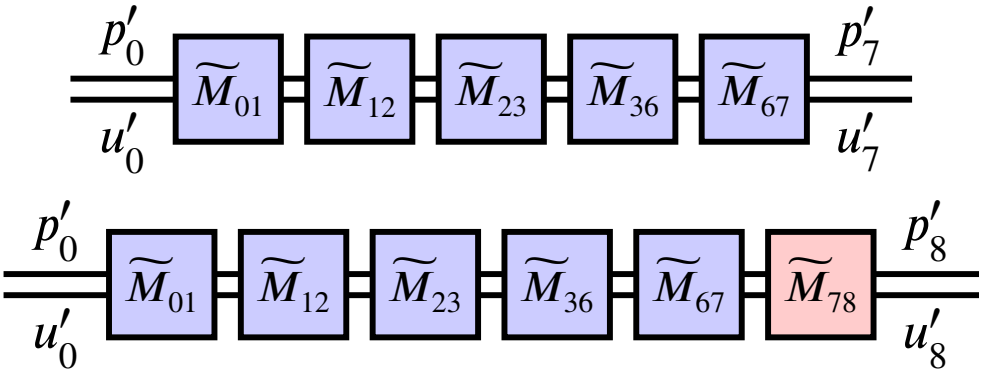

Figure 9.4: *Nonlinear acoustic network models representing the injector dynamics between sections (0) and (7) (Top) and between sections (0) and (8) (Bottom). The blue and red elements contain fresh and burnt gases respectively.*

matrices representing the injector dynamics between section (0) where HW and MHW record u'_0 and p'_0 respectively, and section (7) at the injector outlet or section (8) where MC records p'_8. These two acoustic networks are represented in Fig. 9.4 where each black box represents an element with an associated transfer matrix. The blue elements contain fresh gases whereas the red elements contain burnt gases.

From a mathematical viewpoint, the total transfer matrices $\widetilde{M}_{07}$ and $\widetilde{M}_{08}$ are obtained by multiplying the transfer matrices $\widetilde{M}_{ij}$ associated with each element located between sections (i) and (j). $\widetilde{M}_{07}$ and $\widetilde{M}_{08}$ are expressed in Eqs. (9.20) and (9.21) respectively.

$$\widetilde{M}_{07} = \widetilde{M}_{67}\ \widetilde{M}_{36}\ \widetilde{M}_{23}\ \widetilde{M}_{12}\ \widetilde{M}_{01} \tag{9.20}$$

$$\widetilde{M}_{08} = \widetilde{M}_{78}\ \widetilde{M}_{67}\ \widetilde{M}_{36}\ \widetilde{M}_{23}\ \widetilde{M}_{12}\ \widetilde{M}_{01} \tag{9.21}$$

From the definition of the Dimensionless Acoustic Transfer Matrix given by Eq. (7.55), the acoustic pressure p'_8 at the bottom of the combustion chamber and the acoustic velocity u'_7 at the injector outlet, just before the combustion chamber, are then related to the acoustic pressure p'_0 and the acoustic velocity u'_0 at the hot wire location through the following equations:

$$p'_8 = \widetilde{M}_{08}(1,1)p'_0 + \widetilde{M}_{08}(1,2)u'_0 \tag{9.22}$$

$$u'_7 = \widetilde{M}_{07}(2,1)p'_0 + \widetilde{M}_{07}(2,2)u'_0 \tag{9.23}$$

From Eqs. (9.4), (9.5) and (9.22), the describing functions F_{MC} and F_{MHW} are connected by:

$$F_{MC}(\omega, |u'_0|/\bar{u}_0) = F_{MHW}(\omega, |u'_0|/\bar{u}_0)\frac{\sqrt{T_b/T_u}}{\widetilde{M}_{08}(1,1) + \widetilde{M}_{08}(1,2)/Z_s} \tag{9.24}$$

where the specific acoustic impedance Z_s is assessed at the hot wire location, in section (0).

From Eqs. (9.3), (9.6) and (9.23), the describing functions F_{HW} and F_{HWC} are connected by:

$$F_{HWC}(\omega, |u'_0|/\bar{u}_0) = F_{HW}(\omega, |u'_0|/\bar{u}_0)\frac{A_0/A_7}{\widetilde{M}_{07}(2,2) + \widetilde{M}_{07}(2,1)Z_s} \tag{9.25}$$

where Z_s is also assessed in section (0).

9.5 Describing functions of a premixed confined swirling flame

9.5.1 Downstream forcing

A first set of experiments is conducted with downstream forcing with the setup shown in Fig. 9.1 and for a fully premixed confined swirling flame. The operating conditions are detailed in Chapter 5. The three describing functions defined previously are extracted from measurements. Results are presented in Fig. 9.5 with $F_{HW}(\omega, |u'_0|/\bar{u}_0)$ at the top left, $F_{MHW}(\omega, |u'_0|/\bar{u}_0)$ at the top right and $F_{MC}(\omega, |u'_0|/\bar{u}_0)$ at the bottom left. Finally, the plots at the bottom right represent $F_{MHW\to HW}(\omega, |u'_0|/\bar{u}_0)$, a reconstruction of $F_{HW}(\omega, |u'_0|/\bar{u}_0)$ using data gathered for $F_{MHW}(\omega, |u'_0|/\bar{u}_0)$ by means of the specific impedance Z_s as expressed in Eq. (9.7). For each describing function, the flame frequency response is measured for six different forcing levels set at the hot wire location $|u'_0|/\bar{u}_0$ = 0.10, 0.20, 0.30, 0.40, 0.55 and 0.72 RMS and the top and bottom plots represent the FDF gain and phase lag respectively.

For all three describing functions F_{HW}, F_{MHW} and F_{MC}, the gain plots in Fig. 9.5 depend on the forcing level $|u'_0|/\bar{u}_0$ for frequencies comprised between 180 Hz and 250 Hz. At lower and higher frequencies, the gain remains independent of the input level $|u'_0|/\bar{u}_0$. Furthermore, the phase lag plots of these describing functions remain independent of the forcing level over the full frequency range. This last feature is often observed for fully premixed swirling flames (Palies et al. 2011a).

Results for $F_{HW}(\omega, |u'_0|/\bar{u}_0)$ are now compared with $F_{MHW\to HW}(\omega, |u'_0|/\bar{u}_0)$, the reconstruction obtained from $F_{MHW}(\omega, |u'_0|/\bar{u}_0)$. Both the gain and phase

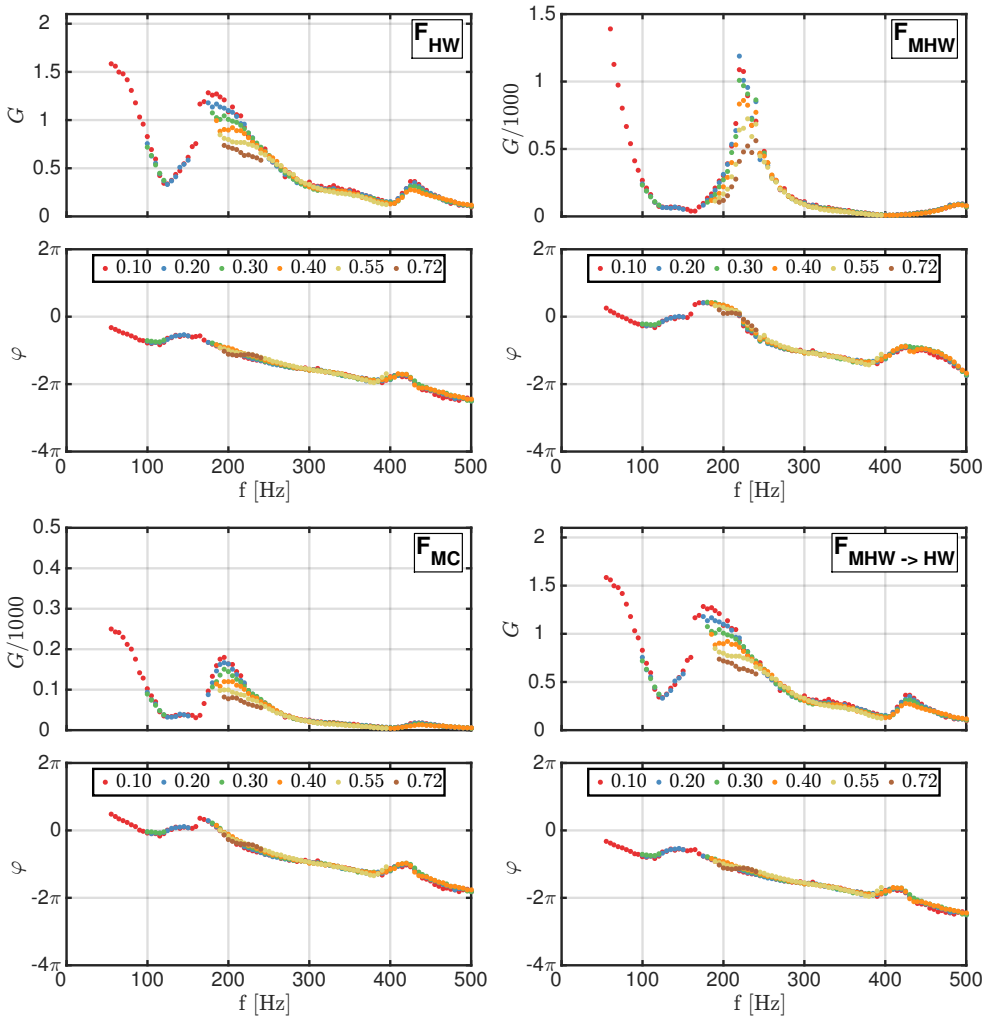

Figure 9.5: *Describing functions of a fully premixed confined swirling flame obtained with downstream forcing for six different forcing levels $|u'_0|/\bar{u}_0$ measured at the hot wire location.* F_{HW} *:* $(\dot{Q}'/\bar{\dot{Q}})/(u'_0/\bar{u}_0)$*.* F_{MHW} *:* $(\dot{Q}'/\bar{\dot{Q}})/(p'_0/\bar{p}_0)$*.* F_{MC} *:* $(\dot{Q}'/\bar{\dot{Q}})/(p'_8/\bar{p}_8)$*.* $F_{MHW\to HW} = Z_s\bar{u}_0 F_{MHW}/\bar{p}_0$*.*

lag plots of F_{HW} and $F_{MHW\to HW}$ are identical in Fig. 9.5 for all forcing levels and all frequencies. It proves that the describing functions $F_{HW}(\omega, |u'_0|/\bar{u}_0)$ and $F_{MHW}(\omega, |u'_0|/\bar{u}_0)$ measured with the hot wire probe and the microphone installed at the same axial location are fully equivalent as long as the specific impedance Z_s at the hot wire location is known.

The describing functions $F_{MHW}(\omega, |u'_0|/\bar{u}_0)$ and $F_{MC}(\omega, |u'_0|/\bar{u}_0)$, respectively determined with the microphone inside the injector (MHW) and at the bottom of the combustion chamber (MC), are now compared. The gain plots of F_{MHW}

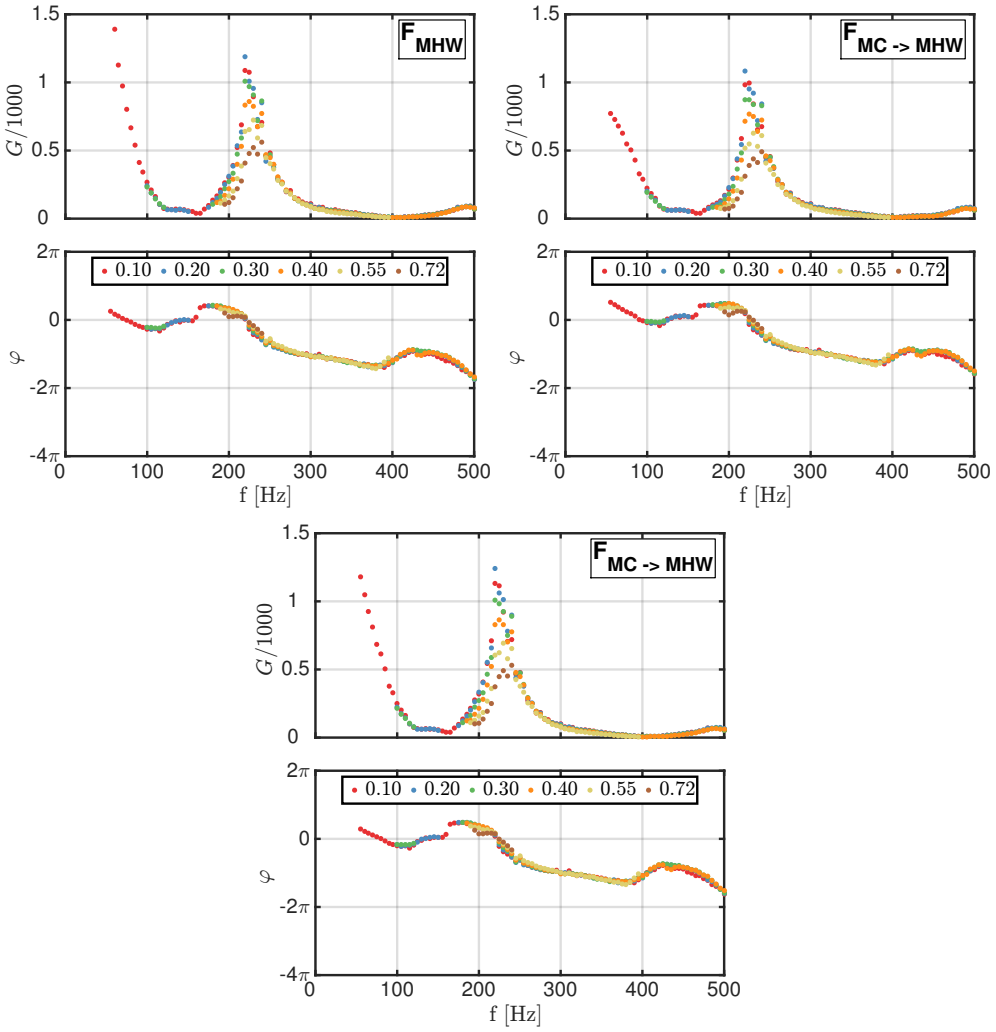

Figure 9.6: *Describing function of a fully premixed confined swirling flame determined with microphone MHW (Top-Left) and its associated reconstructions from the data gathered with microphone MC and the linear (Top-Right) and nonlinear (Bottom) acoustic models. Results are shown for six forcing levels $|u'_0|/\bar{u}_0$ measured at the hot wire location and for downstream acoustic forcing.*

and F_{MC} feature roughly the same type of evolution in Fig. 9.5 except that the gain values for $F_{MHW}(\omega, |u'_0|/\bar{u}_0)$ with the microphone set before the swirler are about 10 times larger than the ones found for the describing function $F_{MC}(\omega, |u'_0|/\bar{u}_0)$ determined with the microphone located in the combustion chamber. Moreover, there is a slight phase shift between the phase lags measured for $F_{MHW}(\omega, |u'_0|/\bar{u}_0)$ and $F_{MC}(\omega, |u'_0|/\bar{u}_0)$ due to acoustic wave propagation between the hot wire location and the bottom of the combustion chamber.

The next step is to compare the describing function $F_{MHW}(\omega, |u'_0|/\bar{u}_0)$ and the associated reconstructions $F_{MC\to MHW}(\omega, |u'_0|/\bar{u}_0)$ obtained from $F_{MC}(\omega, |u'_0|/\bar{u}_0)$ using the linear acoustic model given by Eq. (9.18) and the nonlinear acoustic model given by Eq. (9.24). Results are shown in Fig. 9.6. The linear acoustic model given by Eq. (9.18) yields an excellent reconstruction for the gain and phase lag over the entire frequency range and for all forcing levels. The nonlinear acoustic model predictions are closer to the original describing function $F_{MHW}(\omega, |u'_0|/\bar{u}_0)$ but overall, the gain and phase lag predictions are only slightly improved with respect to the predictions of the linear acoustic model. Therefore, it is not necessary to include the acoustic pressure losses across the swirler when the describing function of a fully premixed confined swirling flame stabilized inside the NoiseDyn burner is determined with downstream forcing. It is reminded that these results are obtained with the forcing level measured by the hot wire probe, upstream the swirler.

9.5.2 Upstream forcing

A second set of experiments is conducted for a fully premixed confined swirling flame but with acoustic forcing coming from the upstream side. As for the downstream forcing case, the signals corresponding to the hot wire probe, microphones and photomultiplier are measured for the same forcing levels, controlled with the hot wire probe. The describing functions F_{HW}, F_{MHW} and F_{MC} are determined from these data and plotted in Fig. 9.7. Again, the plots at the bottom right represent $F_{MHW\to HW}(\omega, |u'_0|/\bar{u}_0)$, the reconstruction of $F_{HW}(\omega, |u'_0|/\bar{u}_0)$ using the data from $F_{MHW}(\omega, |u'_0|/\bar{u}_0)$ and Eq. (9.7).

A common feature between upstream and downstream forcing experiments is that the phase lag plots of all measured describing functions in Figs. 9.5 and 9.7 are independent of the forcing level at all frequencies. This means that the describing function phase lag can be safely determined without considering the effects of the forcing level. Moreover, the phase lag plots of $F_{HW}(\omega, |u'_0|/\bar{u}_0)$ coincide for upstream and downstream forcing experiments implying that the way acoustic forcing is introduced in the system has no impact on the phase lag plot of the describing function computed with respect to the hot wire signal.

However, there are also differences between the describing functions obtained with downstream and upstream forcing. The gain plots of $F_{HW}(\omega, |u'_0|/\bar{u}_0)$ and $F_{MHW}(\omega, |u'_0|/\bar{u}_0)$ in Fig. 9.7 now depend on the forcing level $|u'_0|/\bar{u}_0$ for frequencies comprised between 20 Hz and 100 Hz, and between 180 Hz and 250 Hz while with downstream forcing, the gain plots of $F_{HW}(\omega, |u'_0|/\bar{u}_0)$ and $F_{MHW}(\omega, |u'_0|/\bar{u}_0)$ in Fig. 9.5 depend on the forcing level only between 180 Hz and 250 Hz. This difference comes from the limited low-frequency range explored with downstream forcing due to technical limitations. Acoustic

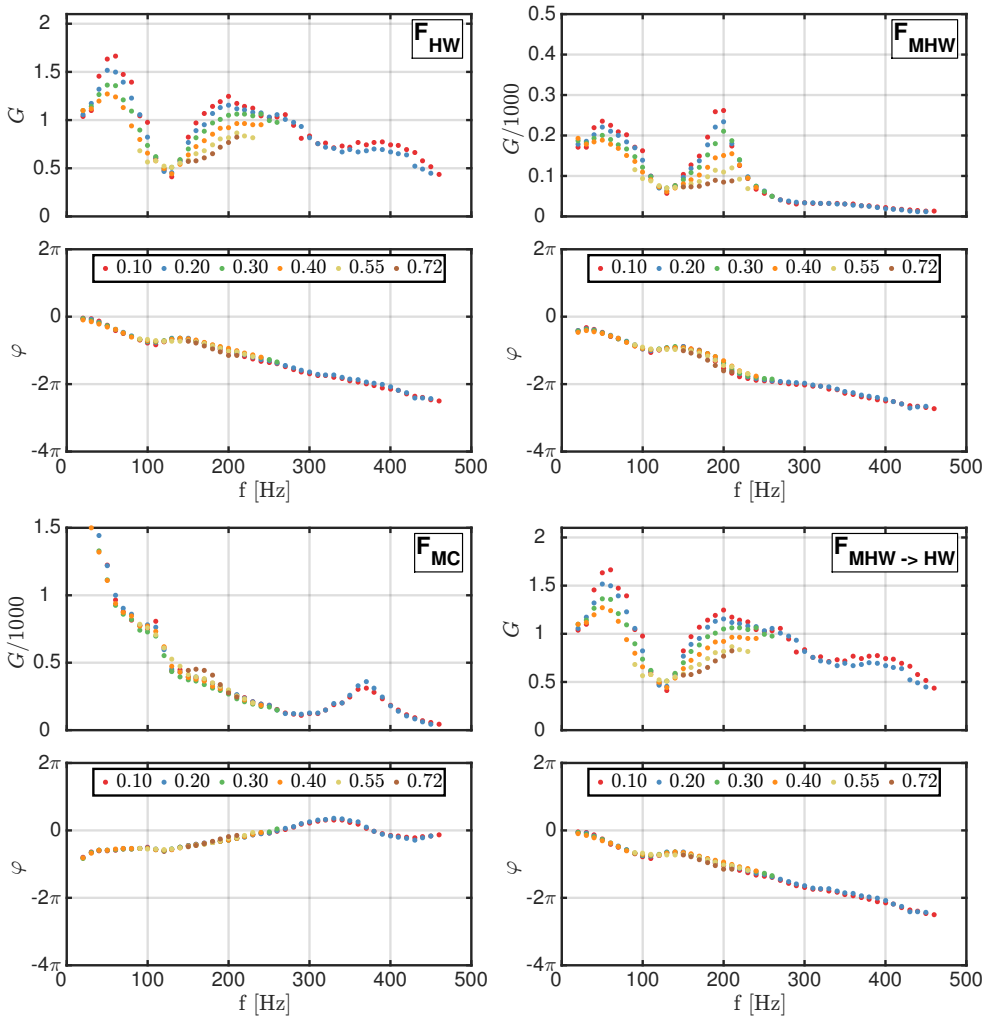

Figure 9.7: *Describing functions of a fully premixed confined swirling flame obtained with upstream forcing for six different forcing levels $|u'_0|/\bar{u}_0$ measured at the hot wire location.* $F_{HW} : (\dot{Q}'/\bar{\dot{Q}})/(u'_0/\bar{u}_0)$. $F_{MHW} : (\dot{Q}'/\bar{\dot{Q}})/(p'_0/\bar{p}_0)$. $F_{MC} : (\dot{Q}'/\bar{\dot{Q}})/(p'_8/\bar{p}_8)$. $F_{MHW\rightarrow HW} = Z_s\bar{u}_0 F_{MHW}/\bar{p}_0$.

forcing from the downstream side requires much more power than experiments conducted with upstream forcing, especially at low forcing frequencies, for a given oscillation level set at the hot wire probe location.

Moreover, the describing functions $F_{MHW}(\omega, |u'_0|/\bar{u}_0)$ determined with respect to the microphone in front of the hot wire probe largely differ in terms of gain and phase lag for downstream and upstream forcing experiments. For instance, the maximum gain achieved with downstream forcing is around 1200 in Fig. 9.5 compared to 300 with upstream forcing in Fig. 9.7. This is due

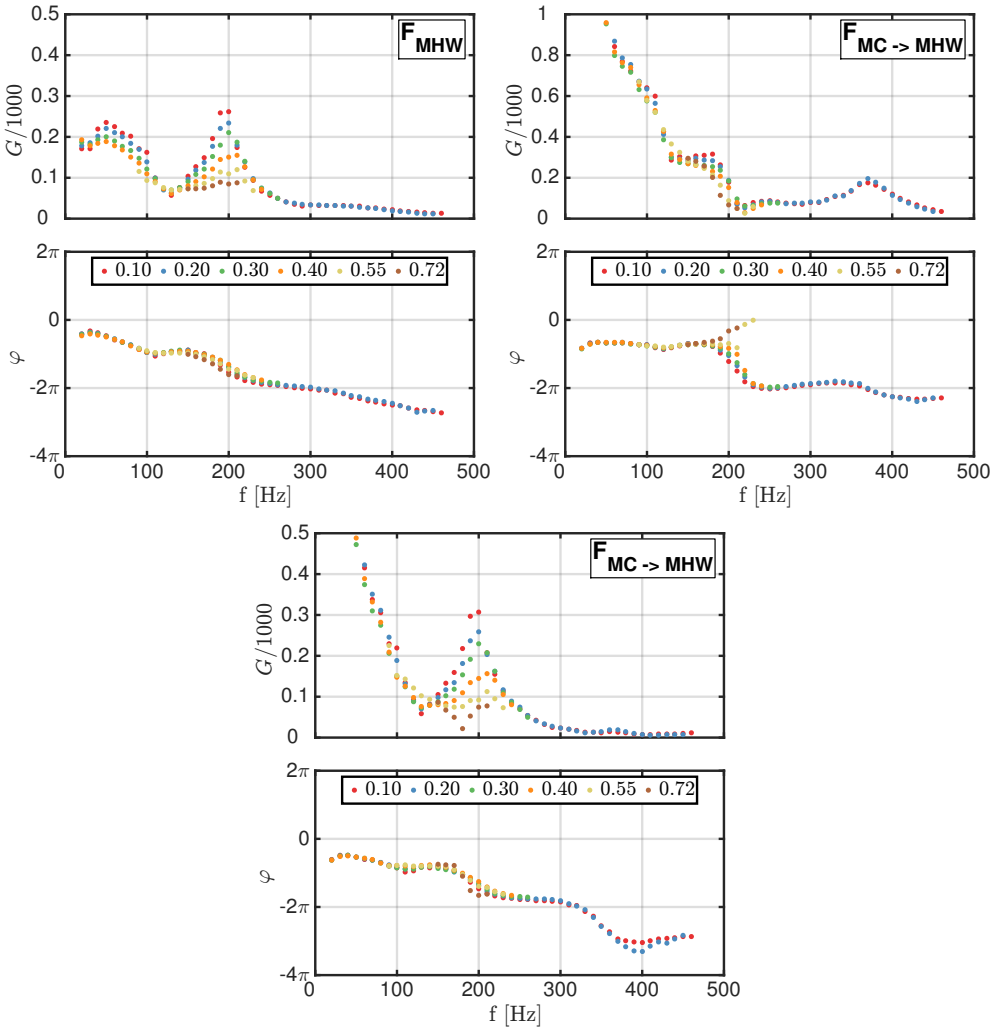

Figure 9.8: *Describing function of a fully premixed confined swirling flame determined with microphone MHW (Top-Left) and its associated reconstructions from the data gathered with microphone MC and the linear (Top-Right) and nonlinear (Bottom) acoustic models. Results are shown for six forcing levels $|u'_0|/\bar{u}_0$ measured at the hot wire location and for upstream forcing.*

to the fact that the specific acoustic impedance Z_s at the hot wire location depends on the type of forcing since the acoustic boundary condition at the hot wire location varies in these two cases. This impedance represents the acoustic response seen by MHW and HW from all the components located upstream these sensors when the system is perturbed from the downstream or upstream sides.

Furthermore, the gain plot of the describing function $F_{MC}(\omega, |u'_0|/\bar{u}_0)$

represented in Fig. 9.7 for upstream acoustic forcing now remains almost independent of the forcing level for all forcing frequencies. This is again in contrast with the results presented for $F_{MC}(\omega, |u'_0|/\bar{u}_0)$ in Fig. 9.5 obtained for downstream acoustic forcing. Moreover, the evolution of the gain of $F_{MC}(\omega, |u'_0|/\bar{u}_0)$ with the forcing frequency significantly differ depending on the type of forcing. This is due to the difference in acoustic pressure levels inside the combustion chamber between experiments conducted with upstream and downstream acoustic forcing. For a given oscillation level measured by the hot wire probe inside the injector, downstream excitation results in a much larger pressure oscillation amplitude at the bottom of the combustion chamber than upstream excitation. Moreover, for upstream forcing, the acoustic pressure at the bottom of the combustion chamber rapidly drops towards zero as the forcing frequency decreases thus explaining why the gain of $F_{MC}(\omega, |u'_0|/\bar{u}_0)$ rapidly increases at low frequencies.

It is now worth exploring whether the describing functions F_{HW}, F_{MHW} and F_{MC} can be reconstructed from one another in the case of upstream forcing. The describing function $F_{HW}(\omega, |u'_0|/\bar{u}_0)$ and the associated reconstruction $F_{MHW\rightarrow HW}(\omega, |u'_0|/\bar{u}_0)$ deduced from $F_{MHW}(\omega, |u'_0|/\bar{u}_0)$ and Eq. (9.7) are again found to be identical for all frequencies and forcing levels in Fig. 9.7. Determining $F_{HW}(\omega, |u'_0|/\bar{u}_0)$ or $F_{MHW}(\omega, |u'_0|/\bar{u}_0)$ is once again completely equivalent as long as the specific impedance Z_s at the hot wire location is known with precision.

The describing functions F_{MHW} determined with the microphone in front of the hot wire and F_{MC} determined with the microphone at the bottom of the combustion chamber are now further examined. The shapes of $F_{MHW}(\omega, |u'_0|/\bar{u}_0)$ and $F_{MC}(\omega, |u'_0|/\bar{u}_0)$ in Fig. 9.7 differ considerably. The main differences are that $F_{MC}(\omega, |u'_0|/\bar{u}_0)$ does not depend on the forcing level $|u'_0|/\bar{u}_0$ and that the peaks observed in all other describing functions are absent in the gain plot of $F_{MC}(\omega, |u'_0|/\bar{u}_0)$. In addition, the gain at zero frequency does not reach a fixed level but rapidly increases. Finally, the phase lag plot increases as the forcing frequency increases.

Since $F_{MHW}(\omega, |u'_0|/\bar{u}_0)$ depends on the forcing level in Fig. 9.7, it cannot be reconstructed from $F_{MC}(\omega, |u'_0|/\bar{u}_0)$, which does not depend on the forcing level, and a linear acoustic model. Figure 9.8 shows indeed that the reconstruction $F_{MC\rightarrow MHW}(\omega, |u'_0|/\bar{u}_0)$ of $F_{MHW}(\omega, |u'_0|/\bar{u}_0)$ from the data gathered for $F_{MC}(\omega, |u'_0|/\bar{u}_0)$ and the linear acoustic model given by Eq. (9.18) does not yield the correct results when the system is acoustically forced from the upstream side. On the other hand, when the nonlinear acoustic pressure losses across the swirler are accounted for, the reconstruction $F_{MC\rightarrow MHW}(\omega, |u'_0|/\bar{u}_0)$ of $F_{MHW}(\omega, |u'_0|/\bar{u}_0)$ from the data gathered for $F_{MC}(\omega, |u'_0|/\bar{u}_0)$ and the nonlinear acoustic model given by Eq. (9.24) is satisfactory. The overall shape

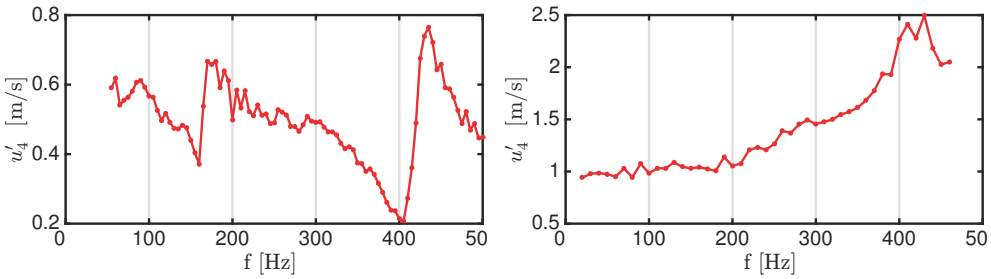

Figure 9.9: *Acoustic velocity u_4' inside the swirler channels in section (4) as a function of the forcing frequency f for a forcing level $|u_0'|/\bar{u}_0 = 0.10$ RMS measured at the hot wire location for downstream (Left) and upstream (Right) acoustic forcing.*

of both the gain and phase lag plots are retrieved accurately, except at low forcing frequencies, where the number of forcing cycles is limited and hence, the predictions worsen. The correct evolution of the gain with the forcing level $|u_0'|/\bar{u}_0$ is also retrieved from the nonlinear network model.

The dynamical state of the system is not symmetric for upstream and downstream acoustic forcing. This is attributed to the fact that the upstream and downstream acoustic boundary conditions differ depending on the type of forcing. As a consequence, the structure and level of the acoustic pressure and acoustic velocity fields inside the injector and combustion chamber differ for upstream and downstream forcing. This is exemplified in Fig. 9.9 where the acoustic velocity u_4' inside the swirler channels is represented for downstream and upstream forcing for a forcing level $|u_0'|/\bar{u}_0 = 0.10$ RMS prescribed at the hot wire location. These acoustic velocity signals were obtained from the hot wire probe signals and propagated to the swirler channel location. The Mach number of the flow inside the perforations is $\overline{M}_4 = 0.035 \ll 1$ which justifies the low-Mach flow assumption.

Figure 9.9 clearly shows that the acoustic velocity u_4' inside the swirler channels vastly differ depending on the type of forcing. For upstream forcing experiments, u_4' is 2 to 5 times larger compared to downstream forcing experiments depending on the forcing frequency. The swirler is essentially a perforated plate and it is shown in Sec. 7.4.6 that the acoustic pressure drop across a perforated plate is proportional to u_4'. As a consequence, the acoustic pressure drop across the swirler is much larger for upstream forcing compared to downstream forcing, where it remains negligible. The linear acoustic network model, used to link the acoustic variables at the bottom of the combustion chamber to the acoustic variables at the hot wire location, is adequate in the case of downstream forcing. On the other hand, a more complex network model accounting for the nonlinear acoustic losses at the swirler holes is needed in the case of upstream forcing to effectively link the acoustic variables across the injector. This result

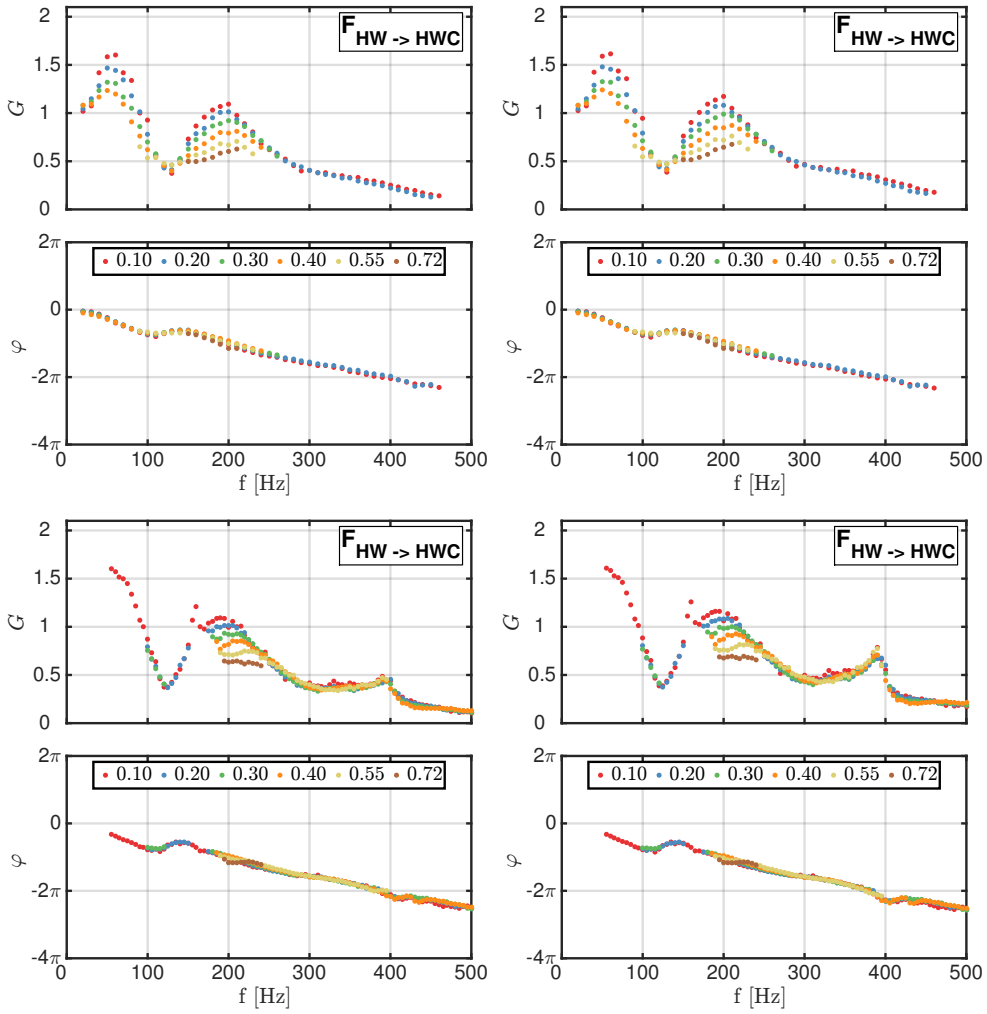

Figure 9.10: *Reconstructed describing function of a fully premixed confined swirling flame with respect to the acoustic velocity at the injector outlet, just before the combustion chamber, for six different forcing levels $|u'_0|/\bar{u}_0$ measured at the hot wire location for upstream forcing (Top) and downstream forcing (Bottom) using the linear (Left) and nonlinear (Right) acoustic models.*

depends on the detailed burner geometry and on the acoustic boundary conditions obtained for upstream and downstream acoustic forcing experiments. As a consequence, this conclusion may not be valid for other acoustic boundary conditions or for a different burner.

9.5.3 Discussion

The experiments conducted with a fully premixed confined swirling flame revealed that the FDF $F_{HW}(\omega, |u'_0|/\bar{u}_0)$ based on the acoustic velocity measured

with a hot wire probe inside the injector can be determined with upstream or downstream acoustic forcing. However, there are slight differences between results for F_{HW} in Fig. 9.5 and those shown in Fig. 9.7. Both methods yield the same results for the phase lag at all frequencies and velocity modulation amplitudes. The gain plots are also the same for forcing frequencies lower than 220 Hz. Differences appear in the high frequency region. The FDF gain plot rapidly drops below unity for $f > 220$ Hz and is strongly attenuated with gains lower than 0.5 when $f > 270$ Hz in the case of downstream forcing. When the flame is modulated from the upstream side, the FDF gain remains relatively large and above 0.5 in Fig. 9.7 up to $f > 440$ Hz at the low forcing levels $|u'_0|/\bar{u}_0 = 0.1$ and 0.2 RMS.

This effect can be counterbalanced by reconstructing the describing functions $F_{HWC}(\omega, |u'_0|/\bar{u}_0)$ defined with respect to the acoustic velocity at the injector outlet, in section (7), from $F_{HW}(\omega, |u'_0|/\bar{u}_0)$ using the linear and nonlinear acoustic models, corresponding respectively to Eqs. (9.19) and (9.25). In that case, the match between the plots corresponding to upstream and downstream forcing in Fig. 9.10 is almost perfect for all frequencies and all forcing levels. It should also be noted that the linear and nonlinear models predict almost the same describing function $F_{HWC}(\omega, |u'_0|/\bar{u}_0)$, even for upstream forcing, as the nonlinear acoustic losses across the swirler mainly affect the acoustic pressure. It is confirmed that the describing function defined with respect to the acoustic velocity at the injector outlet right under the flame is the only describing function that is fully independent of the type of forcing (e.g. of the acoustic boundary condition) (Truffin and Poinsot 2005).

As a consequence, the acoustic velocity at the injector outlet is the correct reference signal when computing the describing function of a fully premixed confined swirling flame. The reference signal may be chosen at a certain distance from the flame provided that two conditions are respected: 1) The distance between the reference signal and the flame should be compact with respect to the acoustic wavelengths investigated and 2) There should be no source of acoustic damping between the reference signal location and the flame location. When a reference signal located further away from the flame is used, or when a significant acoustic pressure drop is present between the reference signal location and the flame location, both the acoustic pressure and acoustic velocity need to be considered along with an acoustic model of the burner in order to reconstruct the acoustic velocity at the flame location. If this reconstruction is not performed, then the FDF associated with a reference signal other than the acoustic velocity at the flame location depends on both the amplitude of the acoustic velocity and that of the acoustic pressure.

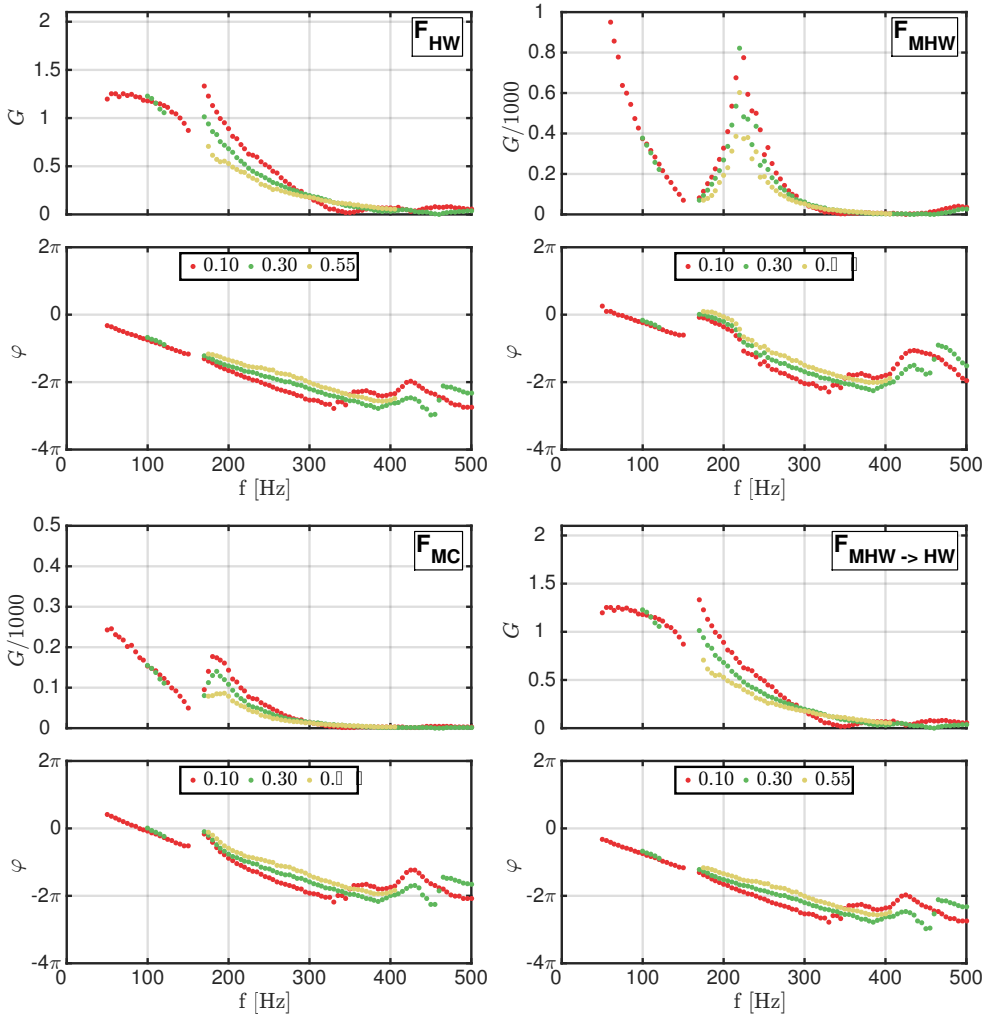

Figure 9.11: *Describing functions of a fully premixed confined non-swirling flame obtained with downstream forcing for three different forcing levels* $|u'_0|/\bar{u}_0$ *measured at the hot wire location.* F_{HW} *:* $(\dot{Q}'/\bar{\dot{Q}})/(u'_0/\bar{u}_0)$*.* F_{MHW} *:* $(\dot{Q}'/\bar{\dot{Q}})/(p'_0/\bar{p}_0)$*.* F_{MC} *:* $(\dot{Q}'/\bar{\dot{Q}})/(p'_8/\bar{p}_8)$*.* $F_{MHW\to HW} = Z_s\bar{u}_0 F_{MHW}/\bar{p}_0$*.*

9.6 Describing functions of a premixed confined non-swirling flame

9.6.1 Downstream forcing

The describing functions of a fully premixed confined non-swirling flame obtained with downstream forcing are presented in Fig. 9.11 with $F_{HW}(\omega, |u'_0|/\bar{u}_0)$ at the top left, $F_{MHW}(\omega, |u'_0|/\bar{u}_0)$ at the top right, $F_{MC}(\omega, |u'_0|/\bar{u}_0)$ at the bottom left and the reconstruction $F_{MHW\to HW}(\omega, |u'_0|/\bar{u}_0)$ of $F_{HW}(\omega, |u'_0|/\bar{u}_0)$

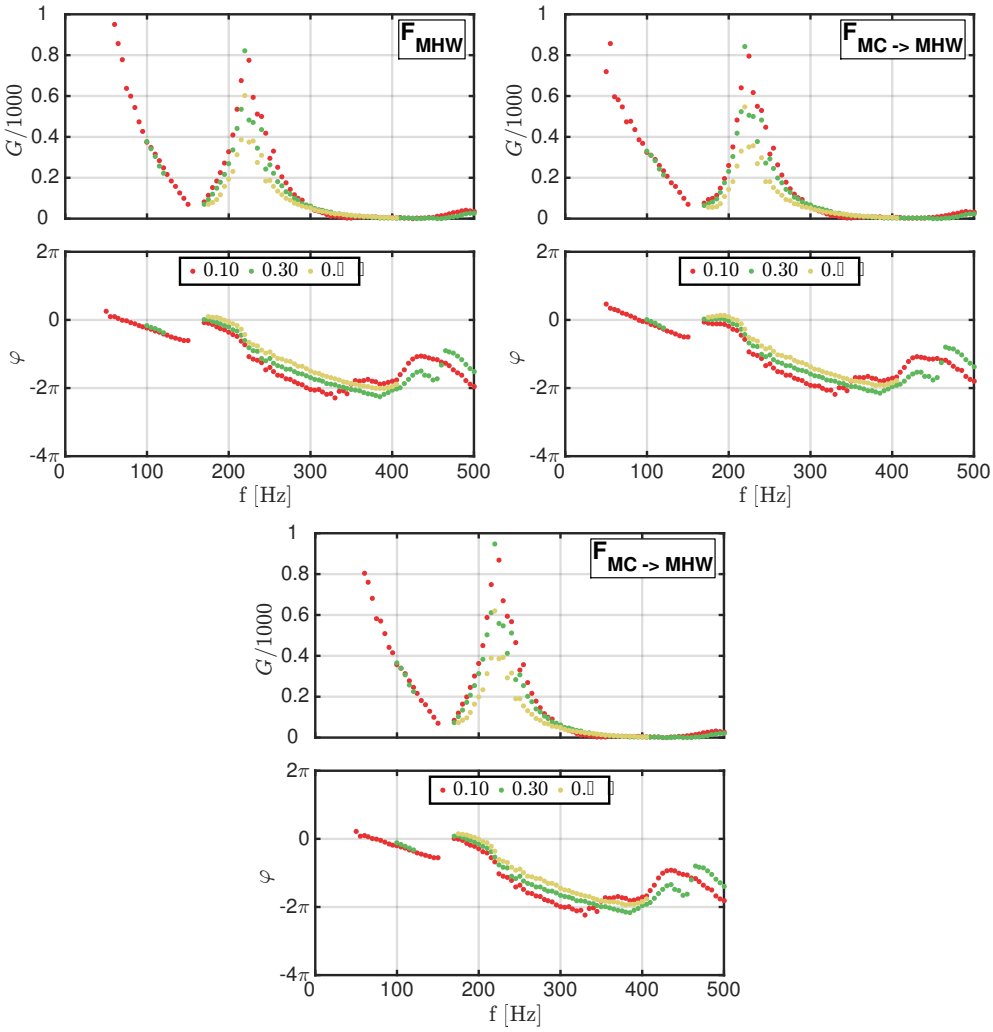

Figure 9.12: *Describing function of a fully premixed confined non-swirling flame determined with microphone MHW (Top-Left) and its associated reconstructions from the data gathered with microphone MC and the linear (Top-Right) and nonlinear (Bottom) acoustic models. Results are shown for three forcing levels $|u'_0|/\bar{u}_0$ measured at the hot wire location and for downstream forcing.*

using the data gathered for $F_{MHW}(\omega, |u'_0|/\bar{u}_0)$ and Eq. (9.7) at the bottom right. For each describing function, the flame frequency response is measured for three different forcing levels set at the hot wire location $|u'_0|/\bar{u}_0 = 0.10$, 0.30 and 0.55 RMS and the top and bottom plots represent the FDF gain and phase lag respectively.

The gain plots of F_{HW}, F_{MHW} and F_{MC} in Fig. 9.11 depend on the forcing level $|u'_0|/\bar{u}_0$ for frequencies comprised between 150 Hz and 300 Hz, a frequency

range much larger compared to the swirling flame case presented in Sec. 9.5. At lower and higher frequencies, the gain plots remain independent of the input level $|u'_0|/\bar{u}_0$. On the other hand, the phase lag plots are independent of the forcing level up to 150 Hz. For larger frequencies, the phase lag changes more rapidly as the forcing level is lowered.

Once again, the reconstruction $F_{MHW\rightarrow HW}(\omega, |u'_0|/\bar{u}_0)$ obtained from $F_{MHW}(\omega, |u'_0|/\bar{u}_0)$ and the specific acoustic impedance Z_s at the hot wire location is very accurate for all forcing levels and all forcing frequencies. Hence, these two describing functions are equivalent for a fully premixed confined non-swirling flame with downstream forcing as long as the specific impedance Z_s at the hot wire location is known.

The describing functions $F_{MHW}(\omega, |u'_0|/\bar{u}_0)$ and $F_{MC}(\omega, |u'_0|/\bar{u}_0)$ are now compared in Fig. 9.11. The gain plots feature roughly the same type of evolution except that the maximum gain reached by $F_{MHW}(\omega, |u'_0|/\bar{u}_0)$ determined with the microphone set at the hot wire location is about 10 times larger than the one reached by $F_{MC}(\omega, |u'_0|/\bar{u}_0)$ determined with the microphone located at the bottom of the chamber. This feature is also observed for a swirling flame, as described in Sec. 9.5.

The describing function $F_{MHW}(\omega, |u'_0|/\bar{u}_0)$ and the associated reconstructions $F_{MC\rightarrow MHW}(\omega, |u'_0|/\bar{u}_0)$ obtained from $F_{MC}(\omega, |u'_0|/\bar{u}_0)$ and the linear acoustic model given by Eq. (9.18) or the nonlinear acoustic model given by Eq. (9.24) are compared in Fig. 9.12. Both the linear and nonlinear acoustic models yield an excellent reconstruction for the gain and phase lag over the entire frequency range and for all forcing levels. As a conclusion, it is not necessary to include the acoustic pressure losses across the swirler when the describing functions of a fully premixed confined non-swirling flame stabilized inside the NoiseDyn burner are determined with downstream forcing.

9.6.2 Upstream forcing

The describing functions $F_{HW}(\omega, |u'_0|/\bar{u}_0)$, $F_{MHW}(\omega, |u'_0|/\bar{u}_0)$, $F_{MC}(\omega, |u'_0|/\bar{u}_0)$ and the reconstruction $F_{MHW\rightarrow HW}(\omega, |u'_0|/\bar{u}_0)$ of a fully premixed confined non-swirling flame obtained with upstream forcing are now presented in Fig. 9.13. Again, the flame frequency response is measured for three different forcing levels set at the hot wire location $|u'_0|/\bar{u}_0 = 0.10$, 0.30 and 0.55 RMS.

Both the gain and phase lag plots of the describing functions differ for swirling and non-swirling flames. For instance, the phase lag plots corresponding to a fully premixed confined non-swirling flame presented in Figs. 9.11 and 9.13 depend on the forcing level for forcing frequencies larger than 150 Hz. As a consequence, the phase lag plot of a describing function corresponding to

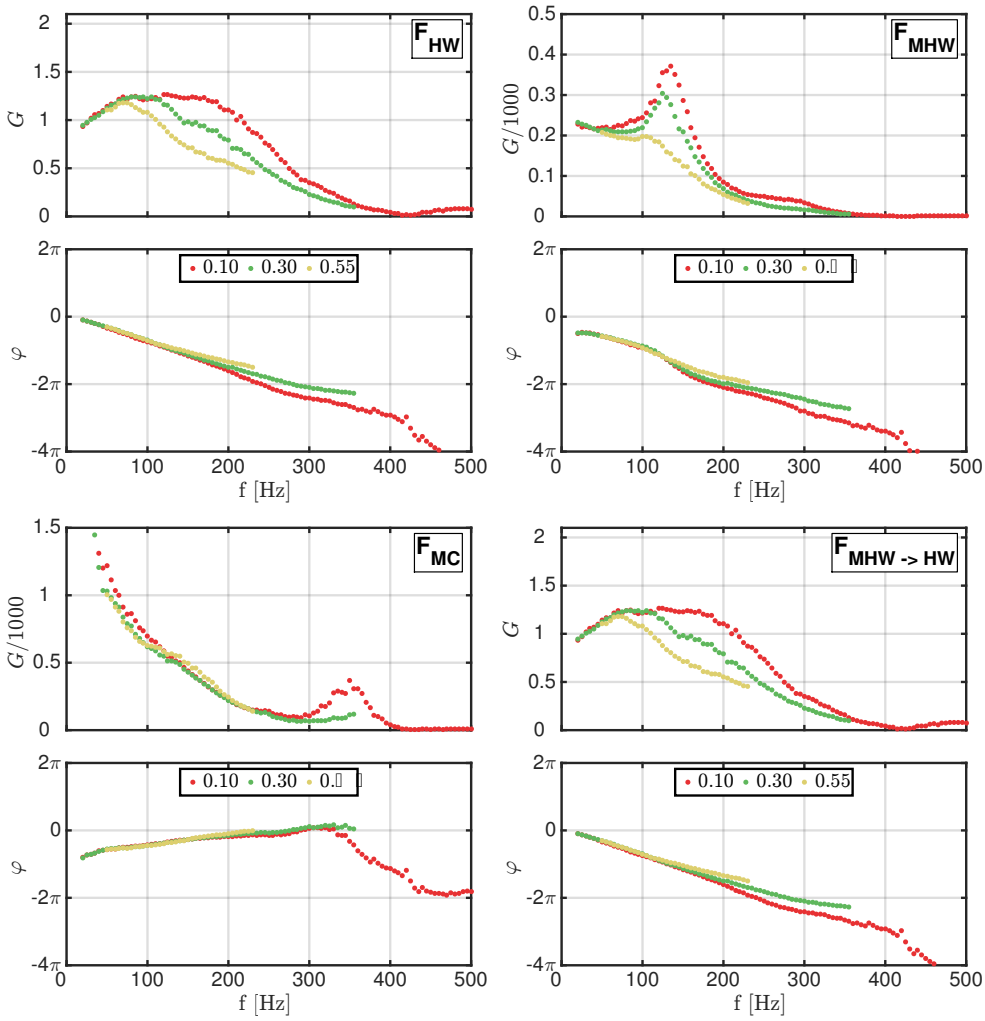

Figure 9.13: *Describing functions of a fully premixed confined non-swirling flame obtained with upstream forcing for three different forcing levels* $|u'_0|/\bar{u}_0$ *measured at the hot wire location.* F_{HW} *:* $(\dot{Q}'/\bar{\dot{Q}})/(u'_0/\bar{u}_0)$*.* F_{MHW} *:* $(\dot{Q}'/\bar{\dot{Q}})/(p'_0/\bar{p}_0)$*.* F_{MC} *:* $(\dot{Q}'/\bar{\dot{Q}})/(p'_8/\bar{p}_8)$*.* $F_{MHW\to HW} = Z_s\bar{u}_0 F_{MHW}/\bar{p}_0$*.*

a fully premixed confined non-swirling flame cannot be safely determined without considering the effects of the forcing level. This is in contrast with the results obtained for a swirling flame, presented in Sec. 9.5. Differences in the gain shapes are also observed between swirling and non-swirling flames. In Fig. 9.7, obtained for a swirling flame, the gain of F_{HW} features two narrow peaks whereas in Fig. 9.13, obtained for a non-swirling flame, the gain of F_{HW} features only one broad peak.

The phase lag plots of $F_{HW}(\omega, |u'_0|/\bar{u}_0)$ presented in Figs. 9.11 and 9.13

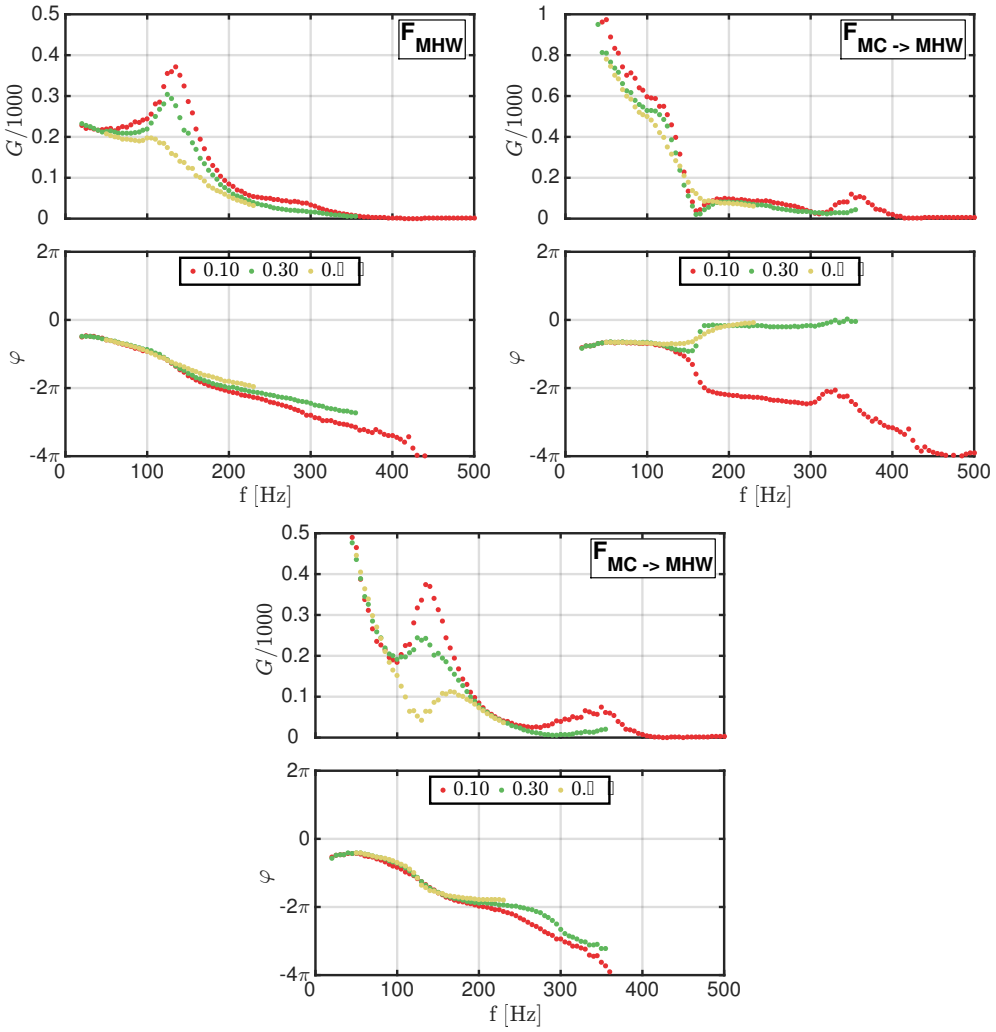

Figure 9.14: *Describing function of a fully premixed confined non-swirling flame determined with microphone MHW (Top-Left) and its associated reconstructions from the data gathered with microphone MC and the linear (Top-Right) and nonlinear (Bottom) acoustic models. Results are shown for three forcing levels $|u'_0|/\bar{u}_0$ measured at the hot wire location and for upstream forcing.*

coincide for upstream and downstream forcing, except in the high-frequency range where the signal-to-noise ratio is too low to determine the phase lag accurately. As a consequence, the way acoustic forcing is introduced in the system has no impact on the phase lag plot of the describing function computed with respect to the hot wire signal.

There are also remarkable differences between the describing functions $F_{HW}(\omega, |u'_0|/\bar{u}_0)$ and $F_{MHW}(\omega, |u'_0|/\bar{u}_0)$ in Figs. 9.11 and 9.13 obtained with

downstream and upstream forcing. First, the gain plot of $F_{HW}(\omega, |u'_0|/\bar{u}_0)$ is much smoother and features a different shape in the case of upstream forcing compared to downstream forcing. The same observation is valid for the gain plot of $F_{MHW}(\omega, |u'_0|/\bar{u}_0)$, but also for its phase lag plot.

Moreover, the gain plot of the describing function $F_{MC}(\omega, |u'_0|/\bar{u}_0)$ in Fig. 9.13 obtained with upstream forcing is almost independent of the forcing level for all forcing frequencies. This is again in contrast with the results presented for $F_{MC}(\omega, |u'_0|/\bar{u}_0)$ in Fig. 9.11 that was determined with downstream forcing experiments. Moreover, the evolution of the gain of $F_{MC}(\omega, |u'_0|/\bar{u}_0)$ with the forcing frequency significantly differ depending on the type of forcing. These observations are similar for a swirling flame, as shown in Sec. 9.5.

The describing function $F_{HW}(\omega, |u'_0|/\bar{u}_0)$ and the reconstruction $F_{MHW\rightarrow HW}(\omega, |u'_0|/\bar{u}_0)$ deduced from $F_{MHW}(\omega, |u'_0|/\bar{u}_0)$ and Eq. (9.7) are again found to be identical for all frequencies and forcing levels in Fig. 9.13. Once again, determining $F_{HW}(\omega, |u'_0|/\bar{u}_0)$ or $F_{MHW}(\omega, |u'_0|/\bar{u}_0)$ is completely equivalent if Z_s is known.

Again, Fig. 9.14 shows that the reconstruction $F_{MC\rightarrow MHW}(\omega, |u'_0|/\bar{u}_0)$ of $F_{MHW}(\omega, |u'_0|/\bar{u}_0)$ from the data gathered for $F_{MC}(\omega, |u'_0|/\bar{u}_0)$ and the linear acoustic model given by Eq. (9.18) does not yield the correct results when the system is acoustically forced from the upstream side. On the other hand, when the nonlinear acoustic pressure losses across the swirler are accounted for, the reconstruction $F_{MC\rightarrow MHW}(\omega, |u'_0|/\bar{u}_0)$ from the nonlinear acoustic model given by Eq. (9.24) retrieves the phase lag plot correctly for all forcing levels. The correct evolution of the gain with the forcing level $|u'_0|/\bar{u}_0$ is also retrieved from the nonlinear network model. However, the gain plot is correctly predicted for $|u'_0|/\bar{u}_0 = 0.1$ and 0.3 RMS only. For high forcing levels, even the nonlinear acoustic model is unable to accurately predict the gain of $F_{MHW}(\omega, |u'_0|/\bar{u}_0)$.

Once again, these results for upstream and downstream acoustic forcing experiments differ because the structure and level of the acoustic pressure and acoustic velocity in the combustion chamber and the injection unit depend on the type of forcing. The linear acoustic network model is sufficient in the case of downstream forcing. However, in the case of upstream forcing, a more complex network model accounting for the nonlinear acoustic losses across the swirler is needed in order to link the acoustic variables through the injector.

These results indicate that despite the very low pressure drop $\Delta p/\bar{p} \sim 0.1\%$ across the non-swirling injector unit, its acoustic response remains complex and depends on the way acoustic waves are introduced inside the burner.

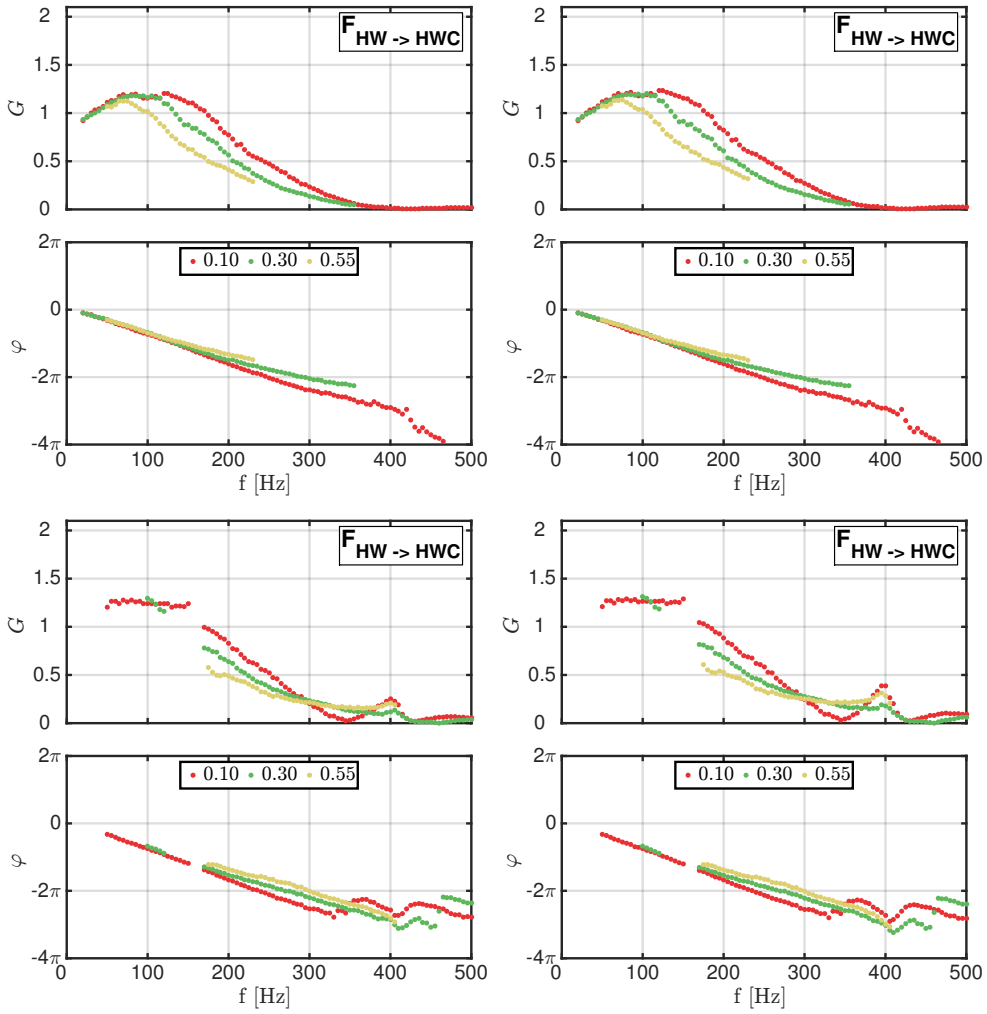

Figure 9.15: *Reconstructed describing function with respect to the acoustic velocity at the injector outlet for a fully premixed confined non-swirling flame and for three different forcing levels $|u'_0|/\bar{u}_0$ measured at the hot wire location for upstream forcing (Top) and downstream forcing (Bottom) using the linear (Left) and nonlinear (Right) acoustic models.*

9.6.3 Discussion

The Flame Describing Function $F_{HW}(\omega, |u'_0|/\bar{u}_0)$ based on the acoustic velocity measured with a hot wire probe inside the injector can be determined with upstream (Fig. 9.13) or downstream (Fig. 9.11) acoustic forcing. Nonetheless, there are disparities between results for F_{HW} in Fig. 9.11 and those shown in Fig. 9.13. Both methods yield the same phase lag plot at all forcing frequencies and velocity modulation amplitudes. However, the gain plots vary significantly depending on the type of forcing.

Based on the procedure used for a swirling flame in Sec. 9.5, the effect of the acoustic boundary conditions on the describing functions can be counterbalanced by reconstructing the describing functions with respect to the acoustic velocity at the injector outlet, just before the flame $F_{HW\rightarrow HWC}(\omega, |u'_0|/\bar{u}_0)$ from $F_{HW}(\omega, |u'_0|/\bar{u}_0)$ and the linear and nonlinear acoustic models, corresponding to Eqs. (9.19) and (9.25) respectively. The match between the gain and phase lag plots of $F_{HW\rightarrow HWC}(\omega, |u'_0|/\bar{u}_0)$ in Fig. 9.15 corresponding to upstream and downstream forcing is almost perfect for all frequencies and all forcing levels. It should also be noted that the linear and nonlinear models predict the same describing function $F_{HW\rightarrow HWC}(\omega, |u'_0|/\bar{u}_0)$, even for upstream forcing.

9.7 Conclusion

It is known that reliable predictions of thermoacoustic instability oscillation frequencies and limit cycle levels can be achieved by combining the Flame Describing Function F_{HW} determined with a velocity reference signal with different types of acoustic solvers (Noiray et al. 2008; Palies et al. 2011b). In many works, the relation F_{HW} between heat release rate and velocity disturbances remains unknown and is difficult to determine in practical combustors. As a consequence, F_{HW} is often replaced by another relationship between heat release rate and pressure fluctuations measured in the combustion chamber and designated by F_{MC} in this work.

The responses of confined premixed swirling and non-swirling flames submitted to acoustic forcing from the upstream and downstream sides of a combustor were determined in this chapter for a large set of forcing frequencies and forcing levels. The swirling injector unit featured a pressure drop $\Delta p/\bar{p} \sim 0.4\%$ whereas the non-swirling injector unit featured a much smaller pressure drop $\Delta p/\bar{p} \sim 0.1\%$. Three types of describing functions relating heat release rate fluctuations to different reference signals were defined. The first reference signal was the acoustic velocity inside the injector measured by the hot wire probe set before the swirler, the second reference signal was the acoustic pressure measured by a microphone set at the same axial location as the hot wire probe and the third reference signal was the acoustic pressure at the bottom of the combustion chamber determined with a microphone mounted on a water-cooled waveguide. The forcing level was in all cases controlled by the hot wire probe.

For downstream acoustic forcing experiments, the gain plots of these different describing functions were shown to depend on the forcing level over a certain frequency range. The phase lag plots were found to remain independent of the forcing level for swirling flames as opposed to the phase lag plots

of non-swirling flames which were shown to depend on the forcing level at high frequencies. Moreover, it was found that all three describing functions could be reconstructed from one another using a linear acoustic model linking the acoustic variables at the bottom of the combustion chamber to the acoustic variables inside the injector. This linear model accounted for acoustic wave propagation and the effects of sudden area changes but all dissipation mechanisms were neglected.

For upstream acoustic forcing experiments, the same describing functions were extracted from measurements. In this case, the describing function defined with respect to the acoustic pressure measured at the hot wire location could not be reconstructed from the describing function measured with the microphone located at the bottom of the combustion chamber through the use of a linear acoustic model of the injector. In fact, the upstream and downstream acoustic boundary conditions were shown to vary depending on the type of forcing, which in turn had an impact on the acoustic fields inside the system. The main source of acoustic losses in a closed system with rigid walls is known to come from the coupling between the vortical structures generated by the mean flow and the acoustic waves (Lighthill 1952; Howe 1979). In the NoiseDyn burner, a large acoustic pressure drop was shown to be generated across the swirler because of this coupling in the case of upstream forcing. When this acoustic pressure drop was taken into account in the model, the describing function based on the acoustic pressure measured at the hot wire location could be reconstructed from the describing function based on the acoustic pressure measured at the bottom of the combustion chamber. On the other hand, when downstream forcing was applied, the acoustic pressure drop across the swirler was found to be negligible and hence, a simple linear acoustic model was able to link these two describing functions accurately. It is emphasized that these results depend on the detailed burner geometry and acoustic boundary conditions and as a consequence cannot be generalized to all burner geometries.

It was also checked that for both downstream and upstream acoustic forcing experiments, the specific acoustic impedance Z_s at the hot wire location could be used to reconstruct the describing function based on the hot wire signal from the describing function based on the facing microphone signal and vice versa.

Furthermore, the gain and phase lag of the Flame Describing Function (FDF) linking heat release rate and velocity fluctuations measured by the hot wire inside the injector for a fully premixed confined swirling flame were found to be identical for upstream and downstream acoustic forcing as long as the forcing frequency was lower than $f < 220$ Hz. At higher frequencies, both FDF phase lags still matched, but the FDF gain dropped more rapidly with the forcing frequency for downstream acoustic forcing than for upstream acoustic forcing.

The discrepancies between upstream and downstream acoustic forcing were found to be even more prononced for a fully premixed confined non-swirling flame. These differences due to distinct acoustic boundary conditions could be suppressed by considering the reconstructed describing functions with respect to the acoustic velocity at the injector outlet, which were found to be almost identical for upstream and downstream forcing experiments at all frequencies and all forcing levels. This finding is valid for swirling and non-swirling flames.

In the end, the describing functions between heat release rate and acoustic fluctuations determined with upstream and downstream forcing were shown to be equivalent as long as the reference signal was the acoustic velocity in the fresh gases as close as possible to the flame and in the absence of acoustic damping between the reference signal location and the flame location. For all other reference signals, such as the acoustic velocity in the injector or the acoustic pressure anywhere in the system, the upstream and downstream acoustic forcing methods appeared as non equivalent techniques to determine the describing function. In that case, the FDF was found to depend on both the amplitude of the acoustic velocity and that of the acoustic pressure.

These experiments demonstrate that the frequency response of a perturbed reacting flow described in terms of heat release rate versus pressure oscillations inside the combustion chamber depends on the way acoustic forcing is introduced in the system. Differences for the resulting describing functions are due to the different acoustic pressure and acoustic velocity fields inside the combustion chamber for a given level of velocity oscillation measured inside the injector. The correct reference signal that should be used when defining describing functions is the acoustic velocity at the top of the injector, just before the flame.

Chapter 10

Measurement and Prediction of Acoustic Transfer Matrices

In this chapter, the Dimensionless Acoustic Transfer Matrix (DATM) coefficients are determined for a thermoacoustically stable configuration of the swirling and non-swirling NoiseDyn burner. The impact of the forcing level needs to be considered as the dynamics of the whole system is controlled by nonlinearities. The four transfer matrix coefficients are thus measured for cold flow and reactive conditions for increasing acoustic excitation levels. The velocity level is controlled by a hot wire probe located inside the injector, in a region with a laminar top-hat velocity profile. The upstream and downstream specific acoustic impedances are also measured for the different cases explored. Results for the response of the swirling and non-swirling configurations under cold flow conditions are first presented. In this case, the transfer matrix coefficients are found to be independent of the forcing level except for the modulus of the coefficients linking the downstream velocity fluctuations to the upstream pressure and velocity fluctuations. This behavior is linked to the nonlinear response of the injector but is not entirely retrieved by the acoustic network model developed in this work. For reactive conditions, measurements indicate that all transfer matrix coefficients depend on the forcing level to a certain extent. The Flame Describing Function, linking heat release rate fluctuations to velocity fluctuations measured by the hot wire, is used to reconstruct the transfer matrix through an acoustic network model. This network model accurately predicts the trend of the measured coefficients but the impact of the forcing level is not retrieved. Saturation for reactive conditions is shown to be not only related to the nonlinear flame response but also to the nonlinear injector dynamics. Finally, a reconstruction of the FDF using the acoustic network model along with the hot wire and microphone measurements is performed.

10.1 Introduction

As explained in Chapter 9, the Flame Transfer Function (FTF) or its nonlinear extension, the Flame Describing Function (FDF) can be combined with an acoustic solver to analyze the thermoacoustic stability of practical combustors at low computational cost (Keller 1995; Dowling and Stow 2003; Sattelmayer and Polifke 2003; Nicoud et al. 2007; Camporeale et al. 2011; Laera et al. 2017). This framework can be used to analyze the dynamics of each mode of the combustor and determine the oscillation frequency and oscillation level reached by the acoustic variables within the system.

The FDF is a function of the forcing angular frequency ω and acoustic forcing level $|u'|/\bar{u}$ (Dowling 1997; Noiray et al. 2008) linking the heat release rate fluctuations $\dot{Q}'/\overline{\dot{Q}}$ to the incoming velocity fluctuations $u'/\bar{u}$:

$$F(\omega, |u'|/\bar{u}) = \frac{\dot{Q}'/\overline{\dot{Q}}}{u'/\bar{u}} \tag{10.1}$$

Throughout this work, the overline stands for mean conditions while the prime corresponds to the Fourier component of the signal at the angular frequency ω.

The predictions obtained with this framework have been successfully compared to experiments for single swirling injector setups (Palies et al. 2011b; Ćosić et al. 2014). However, there are only a few analytical FTF expressions available for canonical flames (Schuller et al. 2003a; Preetham et al. 2008) and the effects of the forcing level are difficult to consider analytically. As a consequence, experiments or numerical simulations are used to determine the FDF of practical and lab scale flames (Noiray et al. 2008; Palies et al. 2011b; Han et al. 2015).

The effects of the perturbation level remain essentially studied by numerical means (Krediet et al. 2012; Han et al. 2015) or by combining experimental and numerical strategies (Silva et al. 2013; Laera et al. 2017). Simulations of the frequency response of practical swirling flames in industrial combustors are often limited to a single or a limited set of forcing frequencies due to the large computational ressources needed for these calculations and the forcing level is rarely varied (Poinsot 2017). There is a growing effort to reproduce the FDF over the entire frequency range of interest and for multiple perturbation amplitudes (Krediet et al. 2012; Han and Morgans 2015; Li et al. 2017). Simulations of the FDF of a premixed swirling flame in a lab scale burner over a wide range of forcing frequencies and forcing levels were recently carried out (Han and Morgans 2015). These data were then used to determine the combustor stability and the trajectories of the unstable modes when submitted

to perturbations of increasing amplitudes (Han et al. 2015).

However, simulations aiming at reproducing the FDF remain exceptions and large deviations are still observed between the simulated flame frequency responses and the corresponding measurements (Han and Morgans 2015). In many nonlinear stability analysis, the FDF is then modeled by a heuristic expression (Noiray and Schuermans 2013; Ghirardo et al. 2015) or determined by dedicated experimental means (Noiray et al. 2008; Palies et al. 2011b; Ćosić et al. 2014; Ćosić et al. 2015).

On the experimental side, large actuators are needed to perturb the flow and reach high forcing levels in the injection unit (Giuliani et al. 2012). Another difficulty is to determine the flame heat release rate. In fully premixed systems, it is common to rely on the proportionality between the chemiluminescence intensity and the combustion intensity (Hurle et al. 1968). The FTF/FDF can then be determined by an optical setup recording the light emission from selected intermediate combustion radicals, such as OH* or CH*, which concentrations are assumed to be proportional to the rate of heat released by the flame. This method requires an optical access that covers the full combustion region and as a consequence is often limited to the determination of FTF/FDF in lab scale setups.

In non premixed systems, where measuring the flame heat release rate is challenging, or in combustors operating at higher powers with limited access to the flame region, a purely acoustic method is preferred (Paschereit and Polifke 1998; Paschereit et al. 2002; Fischer et al. 2006; Alemela et al. 2008). In this framework, the flame frequency response to sound waves is represented by a 2×2 matrix linking the acoustic variables upstream and downstream the flame, as expressed mathematically in Eq. (7.55). The upstream and downstream locations should be as close to the flame as possible (Truffin and Poinsot 2005).

This approach was originally developed for non-reactive 1D duct systems (Munjal 1987; Abom 1992). This method was then used to model a thermoacoustic system by representing the flame with a simple time-lag model (Keller 1995). For a compact flame stabilized in a low-Mach number flow within a straight duct, the Dimensionless Acoustic Transfer Matrix (DATM) representing the flame is given by Eq. (8.46). This expression is reproduced here:

$$\widetilde{M} = \begin{pmatrix} z_u/z_d & 0 \\ 0 & 1 + F\left(\overline{T}_d/\overline{T}_u - 1\right) \end{pmatrix} \tag{10.2}$$

where $z = \bar{\rho}\bar{c}$ is the characteristic impedance of the medium, F is the Flame Describing Function, and $\overline{T}$ is the mean gas temperature. The subscripts u

and d refer to variables upstream and downstream the flame respectively.

The acoustic pressure signals p'_d and p'_u are divided by their respective characteristic impedances, z_d and z_u in order to obtain dimensionless coefficients. In many experimental setups, the acoustic pressure and acoustic velocity upstream (p'_u, u'_u) and downstream (p'_d, u'_d) the flame cannot be measured close enough to the combustion region as they need to be determined in regions of the flow where the waves are planar and in the absence of acoustic sources (Munjal 1987). Hence, measurements are generally achieved with a series of microphones located in straight ducts upstream the injector and downstream the combustion chamber (Paschereit et al. 2002; Fischer et al. 2006). The drawback is that the distance between the upstream and downstream measurement locations is no longer compact with respect to sound waves and a propagation model needs to be considered to reconstruct the acoustic states just upstream and downstream the flame (Truffin and Poinsot 2005). Additionally, other elements such as smooth or sudden area changes or elements modeling a pressure drop have to be considered in order to correctly describe the burner acoustics (Fischer et al. 2006).

Experimental determination of the acoustic transfer matrices of practical burners is now well mastered (Paschereit and Polifke 1998; Schuermans et al. 2000). The first measurements of the modulus and phase of the four coefficients of the transfer matrix for cold and reactive conditions (Paschereit and Polifke 1998; Schuermans et al. 2000; Paschereit et al. 2002) were achieved using a two-source method (Munjal 1987; Abom 1992) by forcing the flow from the upstream and downstream sides of the burner with harmonic sound waves. Due to the high level of noise produced by the turbulent flow inside the burner, a large number of forcing cycles needs to be recorded to extract the coherent response of the system. Further efforts were put into modeling and measuring the transfer matrix coefficients of a swirling burner for cold flow conditions (Fischer et al. 2006) and reactive conditions (Alemela et al. 2008), with a good agreement between theory and experiments.

The acoustic transfer matrix representing the flame can also be reconstructed using numerical simulations. Different strategies were developed and compared to analytical expressions or experiments with satisfactory agreement (Polifke et al. 2001; Gentemann and Polifke 2007; Tay Wo Chong et al. 2010; Tay-Wo-Chong et al. 2012).

Nevertheless, the forcing level is never considered in these experimental or numerical reconstructions of the flame response or is kept constant at an arbitrary small value. A consequence of this representation is that the flame response is assumed to be independent of the forcing amplitude $|u'|/\bar{u}$, an approximation which only holds for small acoustic levels (Dowling 1997;

Schuller et al. 2003a; Lieuwen 2005; Durox et al. 2009). The way the forcing level is handled in these previous works is rarely discussed or even accounted for. For sizable forcing levels, flame and flow nonlinearities have to be considered in the acoustic network models.

The objective of this chapter is to examine the four acoustic transfer matrix coefficients between $f = 20$ Hz and 400 Hz for swirling and non-swirling injectors operated under cold and reactive conditions and for increasing forcing levels $|u'_0|/\bar{u}_0$ measured with a hot wire probe located in the injection unit. For cold flow conditions, experiments are carried out for forcing levels ranging from $|u'_0|/\bar{u}_0 = 0.10$ to 0.72 RMS and $|u'_0|/\bar{u}_0 = 0.10$ to 0.55 RMS for the swirling and non-swiling injectors respectively. For reactive conditions, the same experiments are repeated for forcing levels $|u'_0|/\bar{u}_0 = 0.10$ to 0.55 RMS for the swirling and non-swirling injectors. Measurements of the acoustic transfer matrices are then analyzed and compared to a reconstruction based on the FDF, which is measured in a separate set of experiments with an optical technique. Finally, a reconstruction of the FDF based on the data obtained from purely acoustic measurements is attempted.

A description of the acoustic transfer matrix measurement technique is presented in Sec. 10.2. The acoustic network models used to represent the swirling and non-swirling injectors for cold and reactive conditions are described in Sec. 10.3. Measurements of the acoustic transfer matrix coefficients are then discussed in Sec. 10.4 and Sec. 10.5 for cold and reactive conditions respectively.

10.2 Measurement of acoustic transfer matrices

The experimental setup used in this chapter, represented in Fig. 10.1-(Left), is now described. A more thorough description of the various configurations of the NoiseDyn burner can be found in Chapter 5.

A loudspeaker sealed at the bottom of the tranquilization box (not shown in Fig. 10.1-(Left)) is used to generate harmonic sound waves. A hot wire probe denoted by HW in Fig. 10.1-(Left) measures the velocity signal $\bar{u}_0 + u'_0$ in the top-hat region of the flow, after the convergent. At the same axial location, a microphone denoted by MHW in Fig. 10.1-(Left) measures the acoustic pressure p'_0. A swirler featuring 6 holes of radius $R = 3$ mm generates a flow with a swirl number $S = 0.8$, measured by Laser Doppler Velocimetry at the burner outlet. Alternatively, a non-swirling flow is generated by replacing the swirling vane inside the injector. A bluff body of conical shape is used to help flame stabilization in both cases. A second convergent nozzle is added at the top of the combustion chamber, followed by an exhaust tube of variable length which may or may not be topped by a perforated plate.

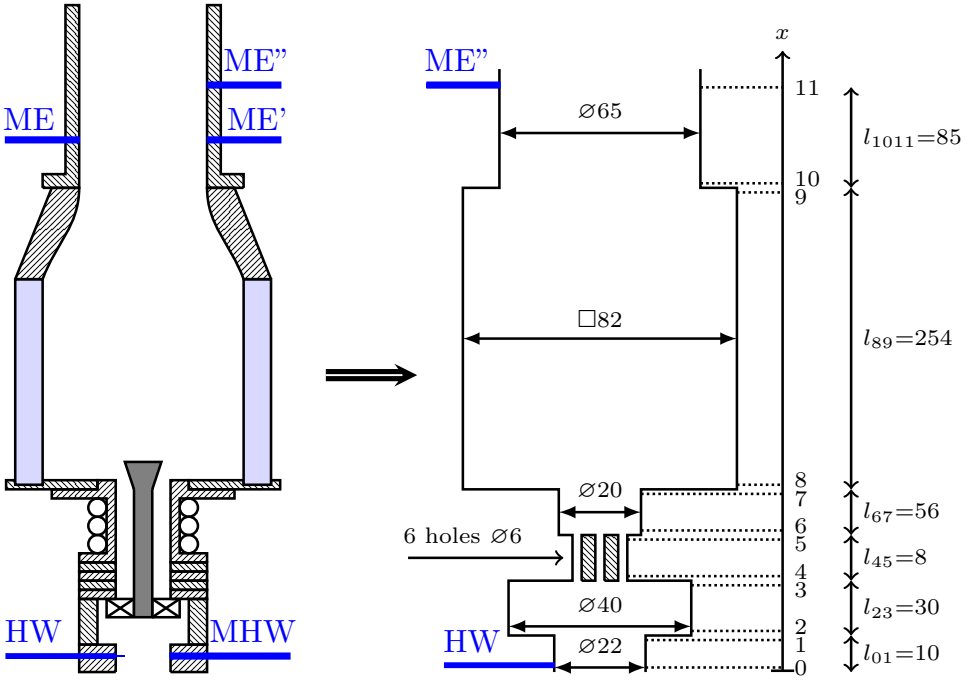

Figure 10.1: *(Left) Central elements of the experimental setup used to determine the acoustic transfer matrices for cold and reactive conditions. The hot wire probe HW and facing microphone MHW are used to determine the acoustic velocity u'_0 and acoustic pressure p'_0 in section (0). The downstream microphones ME, ME' and ME" are used to determine the acoustic velocity u'_{11} (using the Three-Microphone Method) and acoustic pressure p'_{11} in section (11). (Right) Acoustic network model representing the injector and burner dynamics for cold and reactive conditions. All dimensions are in millimeters.*

Three microphones denoted by ME, ME' and ME" in Fig. 10.1-(Left) are mounted on water-cooled waveguides. The small acoustic distortions induced by these waveguides are corrected through the use of their transfer functions, determined in a separate set of experiments, as explained in Chapter 6. The first two microphones, ME and ME', are located in front of each other in the exhaust tube. A third microphone, ME", is located 50 mm downstream. The Three-Microphone Method (Chung and Blaser 1980a) is used to reconstruct the acoustic velocity fluctuations u'_{11} at the same axial position as the acoustic pressure p'_{11} measured by ME". In order to increase the accuracy of the Three-Microphone Method, all experiments are made twice: one with the microphones set in their original configuration, as represented in Fig. 10.1-(Left), and another one with the microphones ME' and ME" switched (Chung and Blaser 1980a; Scarpato et al. 2012). Coherence functions are also used to further improve the signal-to-noise ratio (Chung and Blaser 1980a).

Table 10.1: *Various configurations of the NoiseDyn burner used to determine the acoustic transfer matrix for the swirling and non-swirling injectors operated for cold and reactive conditions.*

Operating conditions	Swirling	Non-swirling
Cold	$\mathbf{B}^1$, $\mathbf{C}^1$	$\mathbf{B}^1_\varnothing$, $\mathbf{C}^1_\varnothing$
Reactive	$\mathbf{B}^1$, $\mathbf{E}^1$	$\mathbf{B}^1_\varnothing$, $\mathbf{C}^1_\varnothing$

All pressure signals are divided by their respective characteristic impedance $\bar{\rho}\bar{c}$ where $\bar{\rho}$ is the mean gas density and $\bar{c}$ the speed of sound at the microphone location. More information about the hot wire probe, microphones and Three-Microphone Method can be found in Chapter 6.

Two distinct operating conditions are investigated in this chapter: cold flow and reactive conditions. The reactive configuration is a perfectly premixed methane/air flame with an equivalence ratio $\phi = 0.82$ and a thermal power of 5.5 kW for both the swirling and non-swirling injectors. The associated bulk velocity at the hot wire probe location is $\bar{u}_b = 5.4$ m/s in a tube of diameter $D = 22$ mm. For cold flow conditions, methane is not injected and the air mass flow rate is adjusted in order to reach the same bulk velocity $\bar{u}_b$ as for reactive conditions. For both cold and reactive conditions, the highest flow velocity (12 m/s) is reached inside the swirler injection holes. It corresponds to a maximum Mach number $M_{max} = 0.035$ meaning that the flow remains in the incompressible regime everywhere inside the setup.

The Dimensionless Acoustic Transfer Matrix (DATM), defined in Eq. (7.55), links the downstream acoustic fluctuations to the upstream acoustic fluctuations. This expression contains four unknowns ($\widetilde{M}_{11}$, $\widetilde{M}_{12}$, $\widetilde{M}_{21}$ and $\widetilde{M}_{22}$) for only two equations. As a consequence, two independent acoustic states are needed to determine these coefficients. In many experiments, the two source method is used (Paschereit and Polifke 1998; Paschereit et al. 2002; Fischer et al. 2006; Alemela et al. 2008). Here, the two load method is retained (Guedra et al. 2011). Both methods are based on a modification of the acoustic impedance at one or more boundaries of the experimental setup.

For each injector (swirling/non-swirling) and each operating conditions (cold/reactive), two configurations of the NoiseDyn burner are thus needed. These configurations may be different depending on the type of injector and operating conditions because the thermoacoustic stability of the system may vary depending on the acoustic boundary condition. A summary of all configurations of the NoiseDyn burner used in this chapter is presented in Table 10.1. For instance, Configurations $\mathbf{B}^1$ and $\mathbf{C}^1$ of the NoiseDyn burner

are used to determine the DATM coefficients for the swirling injector and for cold flow operating conditions. A detailed description of these configurations is presented in Chapter 5.

It was checked that the two configurations of the NoiseDyn burner retained in each case lead to independent acoustic states for all frequencies of interest. Moreover, each measurement has to be performed with the original and switched microphone arrangement.

Altogether, sixty-four experimental cases are explored in the present chapter, as summarized in Fig. 10.2. For each type of injector (level 0 branch in Fig. 10.2), an operating condition is set (level 1 branch in Fig. 10.2) and an acoustic forcing amplitude is chosen (level 2 branch in Fig. 10.2). The corresponding DATM is determined by measuring the acoustic variables for two distinct configurations (level 3 branch in Fig. 10.2) and with the original and switched microphone settings (level 4 branch in Fig. 10.2). For each of these sixty-four cases, a frequency sweep containing between 10 and 100 forcing frequencies is performed.

Once the data are post-processed, the acoustic states (p'_0,u'_0) and (p'_{11},u'_{11}) at the hot wire HW and microphone ME" locations are known as functions of the forcing frequency for each type of injector, operating conditions and forcing level for two independent configurations, obtained by modifying the downstream acoustic boundary condition. Using Eq. (7.55), the following system can be written:

$$\begin{pmatrix} p_{11}^{\alpha}/z_{11}^{\alpha} \\ u_{11}^{\alpha} \\ p_{11}^{\beta}/z_{11}^{\beta} \\ u_{11}^{\beta} \end{pmatrix} = \begin{pmatrix} \widetilde{M}(1,1) & \widetilde{M}(1,2) & 0 & 0 \\ \widetilde{M}(2,1) & \widetilde{M}(2,2) & 0 & 0 \\ 0 & 0 & \widetilde{M}(1,1) & \widetilde{M}(1,2) \\ 0 & 0 & \widetilde{M}(2,1) & \widetilde{M}(2,2) \end{pmatrix} \times \begin{pmatrix} p_0^{\alpha}/z_0^{\alpha} \\ u_0^{\alpha} \\ p_0^{\beta}/z_0^{\beta} \\ u_0^{\beta} \end{pmatrix} \quad (10.3)$$

where α and β denote the acoustic variables measured with the first and second acoustic boundary condition respectively and $\widetilde{M}$ is the DATM representing the acoustic response of the elements placed between the hot wire HW location and the microphone ME" location. All pressures and velocities appearing in Eq. (10.3) are acoustic variables even though the prime was omitted for the sake of readability.

The last step is to solve the system given by Eq. (10.3) which consists of four linear equations with four unknowns. The four transfer matrix coefficients are obtained by solving this system symbolically or numerically. It is also possible to acquire data from additional configurations with different acoustic boundary conditions in order to improve the measurements of the coefficients

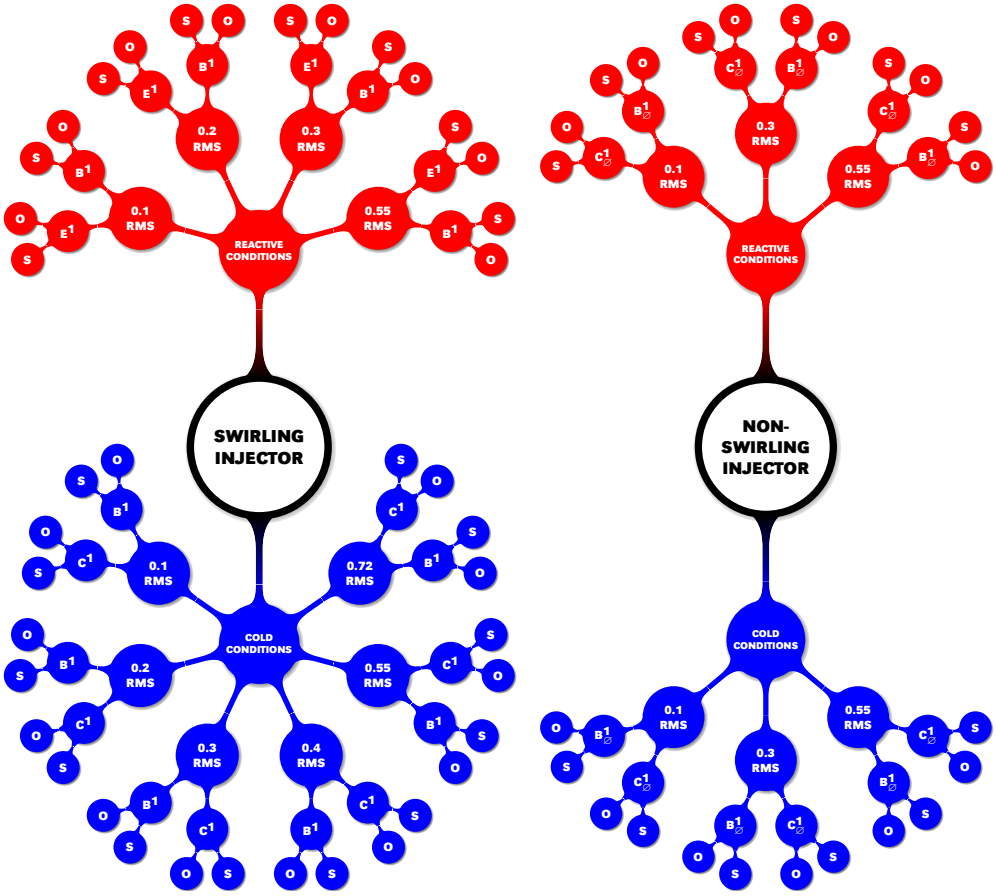

Figure 10.2: *Summary of all experimental configurations investigated in this chapter. (Left) Swirling injector. (Right) Non-swirling injector. For each type of injector, the first subdivision corresponds to the operating conditions (cold/reactive), the second subdivision corresponds to the forcing level, the third subdivision corresponds to the NoiseDyn configuration, e.g. to the acoustic boundary condition, and finally the fourth subdivision corresponds to the microphone arrangement (original or switched). For each of these 64 cases, between 10 and 100 forcing frequencies are explored.*

of the acoustic transfer matrix by using a least-square method.

Since the acoustic pressure and acoustic velocity are measured or reconstructed at the hot wire HW and microphone ME" locations, the specific acoustic impedances can be easily assessed at these locations by using Eq. (7.39).

Figure 10.3 represents the specific acoustic impedance Z_0^s at the hot wire HW location as a function of the forcing frequency for the swirling and non-swirling injector and for cold and reactive operating conditions. These results are obtained using configurations $\mathbf{B}^1$ and $\mathbf{B}^1_\varnothing$ for the swirling and non-swirling injectors respectively. Several forcing levels are investigated in each case.

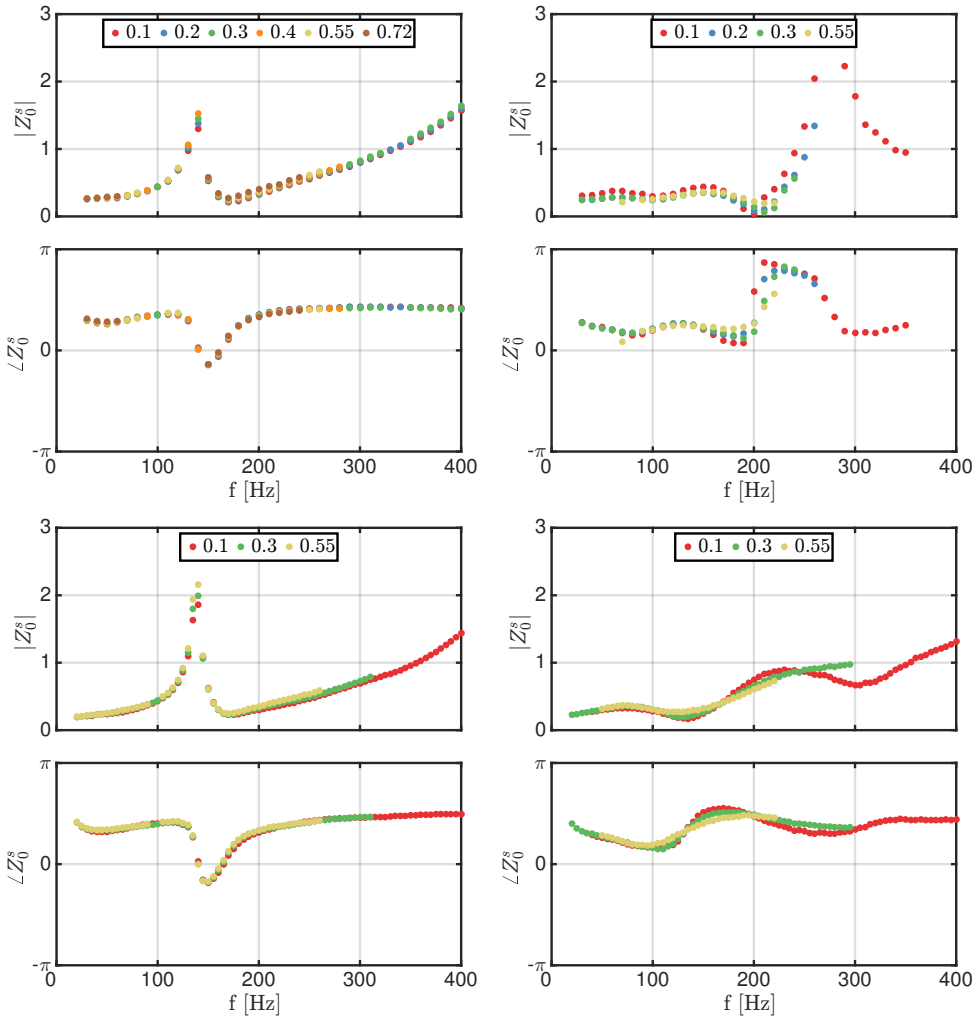

Figure 10.3: *Specific acoustic impedance Z_0^s at the hot wire HW location as a function of the forcing frequency with the swirling (Top) and non-swirling (Bottom) injectors and for cold (Left) and reactive (Right) operating conditions. Results are obtained using configuration $\boldsymbol{B}^1$ and $\boldsymbol{B}^1_\varnothing$ for the swirling and non-swirling injectors respectively. Results are shown for various forcing levels $|u'_0|/\bar{u}_0$ measured by the hot wire probe HW.*

For cold flow conditions, corresponding to the left plots in Fig. 10.3, the specific acoustic impedance does not depend on the forcing level for all forcing frequencies and for both the swirling and non-swirling injector. Moreover, the top-left and bottom-left plots in Fig. 10.3 are similar, implying that the type of injector has no impact on the specific acoustic impedance Z_0^s. It can be thus concluded that for cold operating conditions, the acoustic response of the burner elements placed before the hot wire probe is linear and does not depend on the injector type.

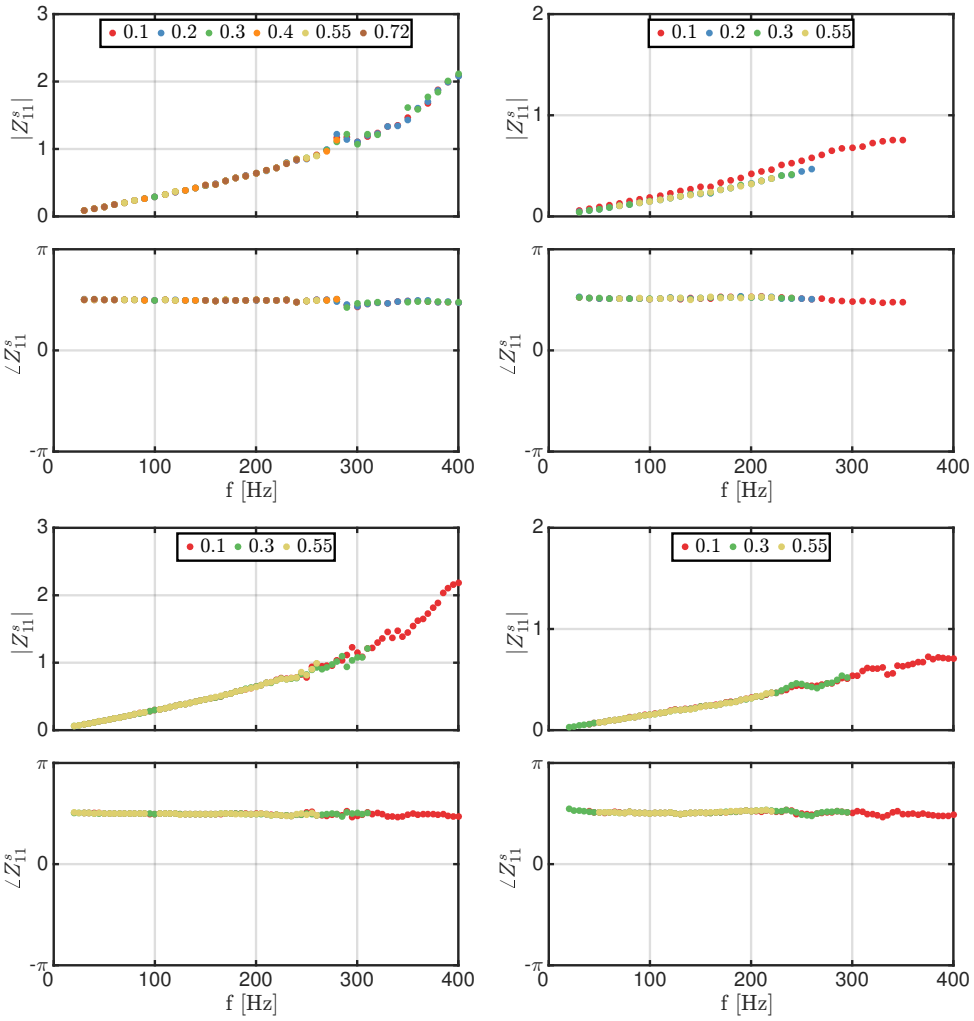

Figure 10.4: *Specific acoustic impedance Z^s_{11} at the microphone ME" location as a function of the forcing frequency with the swirling (Top) and non-swirling (Bottom) injectors and for cold (Left) and reactive (Right) operating conditions. The downstream boundary is a single exhaust tube with an open end, corresponding to configurations $\boldsymbol{B}^1$ and $\boldsymbol{B}^1_{\varnothing}$ for the swirling and non-swirling injectors respectively. Results are shown for various forcing levels $|u'_0|/\bar{u}_0$ measured by the hot wire probe HW.*

On the other hand, for reactive operating conditions, corresponding to the right plots in Fig. 10.3, the specific acoustic impedance Z^s_0 at the hot wire location slightly depends on the forcing level for forcing frequencies $f > 150$ Hz. This observation is valid for the swirling and non-swirling injectors. However, the amplitude of these variations is limited and will be neglected in the remainder of this work. Nevertheless, the specific acoustic impedance Z^s_0 significantly differs depending on the type of injector, as shown in the top-right and bottom-right plots in Fig. 10.3. This implies that the flame has a

considerable impact on the acoustic response of the burner elements placed before the hot wire probe and differs for the swirling and non-swirling injectors.

Figure 10.4 represents the specific acoustic impedance Z^s_{11} at the microphone ME" location as a function of the forcing frequency for the swirling and non-swirling injectors and for cold and reactive operating conditions. These data are obtained with configurations $\mathbf{B}^1$ and $\mathbf{B}^1_\varnothing$ of the NoiseDyn burner in the swirling and non-swirling cases respectively. Figure 10.4 clearly shows that the acoustic response of the elements placed after microphone ME" is linear for all forcing frequencies whatever the operating conditions and type of injector. Moreover, the specific acoustic impedance Z^s_{11} is the same for the swirling and non-swirling injectors for both cold and reactive operating conditions. However, the moduli of Z^s_{11} significantly differ between cold and reactive conditions. This is due to the increased sound speed $\bar{c}$ in the burnt gases. Similar measurements performed for configurations $\mathbf{C}^1$, $\mathbf{C}^1_\varnothing$ and $\mathbf{E}^1$ (not shown here) lead to the same conclusion.

10.3 Acoustic network models of the NoiseDyn burner

The experimental setup is now modeled for cold and reactive operating conditions using the acoustic two-port matrices network formalism (Abom 1992; Paschereit and Polifke 1998; Polifke et al. 2001; Dowling and Stow 2003; Poinsot and Veynante 2005; Fischer et al. 2006). This formalism is presented thoroughly in Chapter 9. It is reminded that the harmonic convention retained here is $e^{+i\omega t}$ and that all pressure signals are divided by the characteristic impedance $z = \bar{\rho}\bar{c}$ in order to obtain a Dimensionless Acoustic Transfer Matrix (DATM), defined in Eq. (7.55).

The burner sketched in Fig. 10.1-(Left) is represented by a network of two-port matrices representing the acoustic response of the setup between the hot wire HW location defined as section (0) in Fig. 10.1-(Right) and the microphone ME" location defined as section (11) in Fig. 10.1-(Right). The injector is comprised between section (0) and section (8) and includes the swirling vane and the injection tube. It is followed by the combustion chamber between section (8) and section (9) and the downstream elements between section (9) and section (11). The swirling vane is represented by the elements comprised between section (3) and section (6). For reactive operating conditions, the flame is assumed to be stabilized at the axial location corresponding to section (8) and is treated as a compact element in this model.

This acoustic network model is represented for cold and reactive operating conditions in Fig. 10.5 where each black box represents an element with an

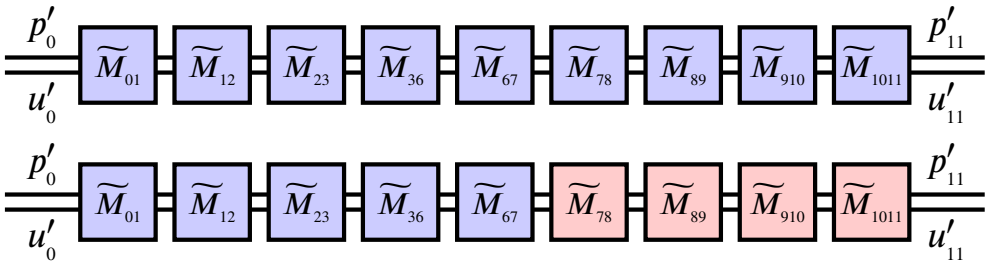

Figure 10.5: *Acoustic network models representing the Dimensionless Acoustic Transfer Matrix of the experimental setup between section (0) and section (11) for cold flow conditions (Top) and reactive conditions (Bottom).*

associated transfer matrix. The blue color indicates elements filled with fresh gases whereas the red color indicates those filled with burnt gases. The acoustic response of the burner elements comprised between section (0) and section (7) is the same as in the acoustic network model introduced in Sec. 9.4.2 and represented in Fig. 9.4.

Several DATM are used to model the acoustic response of the central elements of the NoiseDyn burner comprised between section (0) and section (11) for cold and reactive conditions. They correspond to the following models:

- **Section (0) → section (7):** The same DATM as those presented in Sec. 9.4.2 are used.
- **Section (7) → section (8):** For cold flow conditions, a DATM corresponding to a compact area change in a non-reactive low-Mach flow modeled with Eq. (7.78) is used. For reactive conditions, the previous DATM is combined with the DATM of a lean compact flame stabilized in a low-Mach flow within a straight duct given by Eq. (8.46).
- **Section (8) → section (9):** A DATM corresponding to a straight duct in a uniform non-reactive low-Mach flow is modeled with Eq. (7.59).
- **Section (9) → section (10):** A DATM corresponding to a compact area change in a non-reactive low-Mach flow is modeled with Eq. (7.78).
- **Section (10) → section (11):** A DATM corresponding to a straight duct in a uniform non-reactive low-Mach flow is modeled with Eq. (7.59).

The total Dimensionless Acoustic Transfer Matrix $\widetilde{M}$ representing the acoustic response of the injector and burner between section (0) and section (11) in Fig. 10.1-(Right) is then given by:

$$\widetilde{M} = \widetilde{M}_{1011}\ \widetilde{M}_{910}\ \widetilde{M}_{89}\ \widetilde{M}_{78}\ \widetilde{M}_{07} \tag{10.4}$$

Using the expression of $\widetilde{M}_{07}$ given by Eq. (9.20), $\widetilde{M}$ can be further expressed as:

$$\widetilde{M} = \widetilde{M}_{1011}\ \widetilde{M}_{910}\ \widetilde{M}_{89}\ \widetilde{M}_{78}\ \widetilde{M}_{67}\ \widetilde{M}_{36}\ \widetilde{M}_{23}\ \widetilde{M}_{12}\ \widetilde{M}_{01} \tag{10.5}$$

Based on this analysis, the acoustic network models for the swirling and non-swirling injectors are different for reactive operating conditions, when the Flame Describing Function is taken into account. For cold flow operating conditions, the swirling and non-swirling burners are modeled with the same acoustic network model.

10.4 Results for cold operating conditions

Figures 10.6 and 10.7 represent the modulus and phase of the four DATM coefficients $\widetilde{M}(1,1)$, $\widetilde{M}(1,2)$, $\widetilde{M}(2,1)$ and $\widetilde{M}(2,2)$ representing the acoustic response of the system between section (0) and section (11) in Fig. 10.5-(Top) and reconstructed from the experimental data for a swirling and non-swirling injector respectively and for cold operating conditions. Measurements are performed for increasing forcing levels ranging from $|u'_0|/\bar{u}_0 = 0.10$ to 0.72 RMS for the swirling injector and $|u'_0|/\bar{u}_0 = 0.10$ to 0.55 RMS for the non-swirling injector. These measurements are plotted as symbols in Figs. 10.6 and 10.7. The DATM coefficients predicted according to the acoustic network model shown in Fig. 10.5-(Top) are also plotted as solid lines in Figs. 10.6 and 10.7 for all forcing levels.

Both the modulus and angle of the DATM coefficients mostly coincide for the swirling and non-swirling injectors for all forcing levels and all forcing frequencies when the burner is operated for cold flow conditions, as shown in Figs. 10.6 and 10.7. As a consequence, the analysis presented in the remainder of this section will focus on the swirling case, corresponding to Fig. 10.6, without loss of generality.

The modulus and phase of the measured DATM coefficients shown in Fig. 10.6 are more scattered in the low-frequency region. This is due to low frequency noise, which is not fully eliminated by the averaging procedure of the raw data because they were recorded over a limited number of forcing cycles. Morever, the two independent acoustic boundary conditions needed to solve Eq. (10.3) are close at low frequencies, which also decreases the signal-to-noise ratio. Except in the low frequency region, the angle of the measured DATM coefficients $\widetilde{M}(1,1)$, $\widetilde{M}(1,2)$, $\widetilde{M}(2,1)$ and $\widetilde{M}(2,2)$ remain roughly independent of the forcing level. The moduli of $\widetilde{M}(1,1)$ and $\widetilde{M}(1,2)$ are also identical

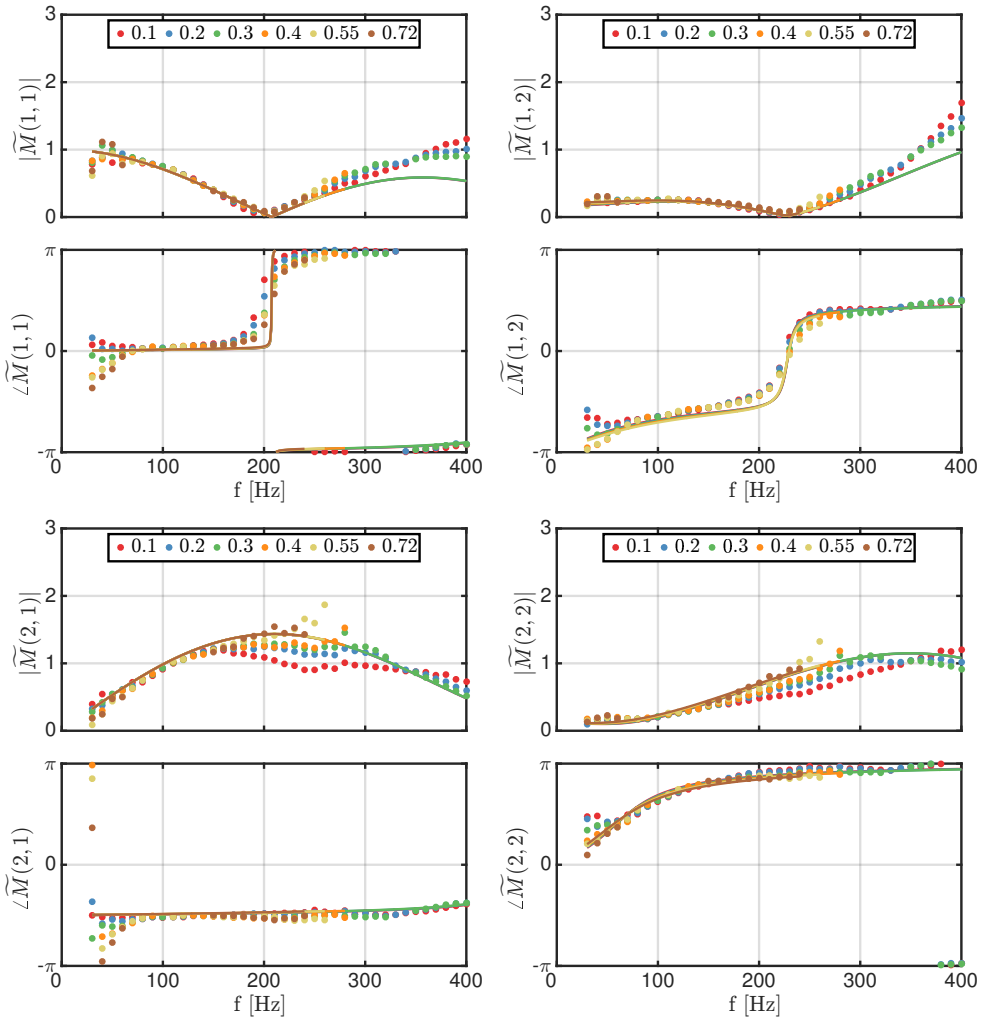

Figure 10.6: *Coefficients of the Dimensionless Acoustic Transfer Matrix (DATM) representing the acoustic response of the system between the hot wire HW location in section (0) and the microphone ME" location in section (11) for a swirling injector and for cold flow operating conditions. (Top left):* $\widetilde{M}(1,1)$ *- (Top right):* $\widetilde{M}(1,2)$ *- (Bottom left):* $\widetilde{M}(2,1)$ *- (Bottom right):* $\widetilde{M}(2,2)$*. Measurements are performed at various forcing levels:* $|u'_0|/\bar{u}_0 = 0.10$ *RMS (Red dots),* $|u'_0|/\bar{u}_0 = 0.20$ *RMS (Blue dots),* $|u'_0|/\bar{u}_0 = 0.30$ *RMS (Green dots),* $|u'_0|/\bar{u}_0 = 0.40$ *RMS (Orange dots),* $|u'_0|/\bar{u}_0 = 0.55$ *RMS (Yellow dots) and* $|u'_0|/\bar{u}_0 = 0.72$ *RMS (Brown dots). Acoustic network model predictions are represented as solid lines for all forcing levels. For each plot, the top and bottom figures represent the modulus and angle of the DATM coefficient respectively.*

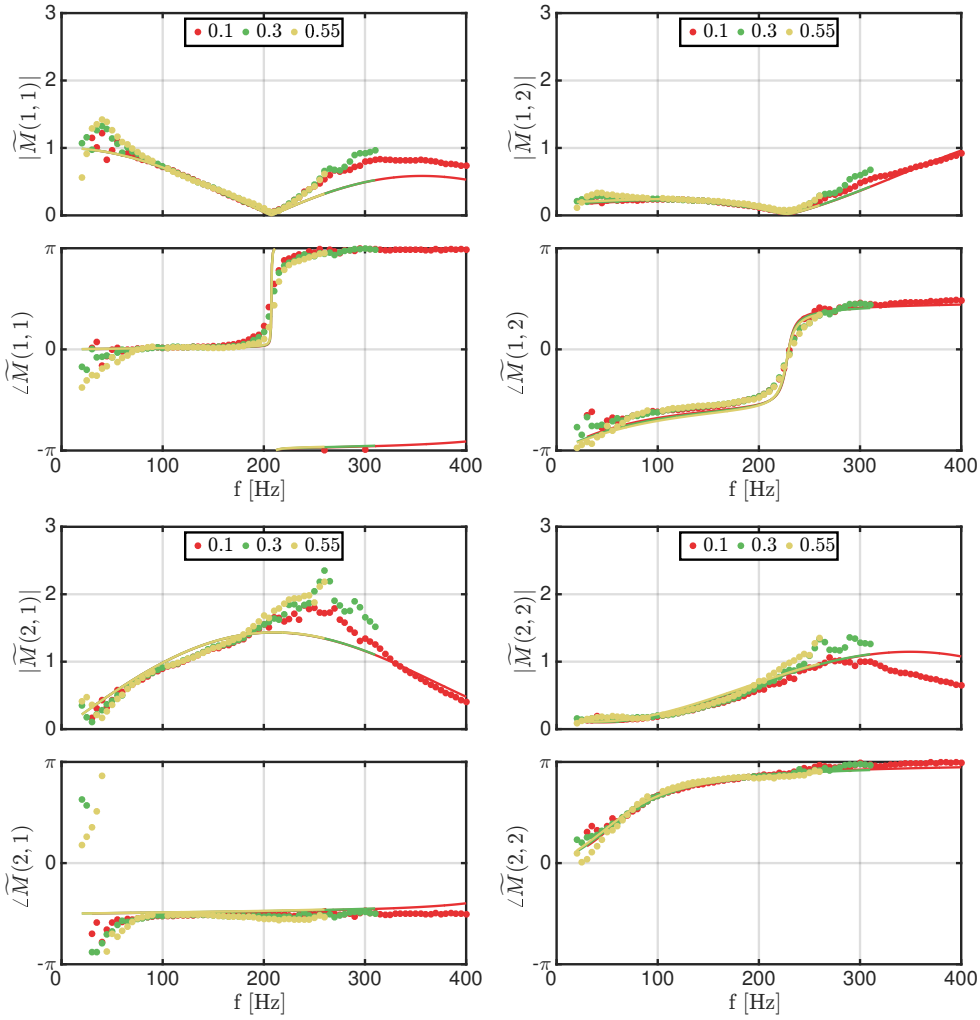

Figure 10.7: *Coefficients of the Dimensionless Acoustic Transfer Matrix (DATM) representing the acoustic response of the system between the hot wire HW location in section (0) and the microphone ME" location in section (11) for a non-swirling injector and for cold flow operating conditions. (Top left):* $\widetilde{M}(1,1)$ *- (Top right):* $\widetilde{M}(1,2)$ *- (Bottom left):* $\widetilde{M}(2,1)$ *- (Bottom right):* $\widetilde{M}(2,2)$*. Measurements are performed at various forcing levels:* $|u'_0|/\bar{u}_0 = 0.10$ *RMS (Red dots),* $|u'_0|/\bar{u}_0 = 0.30$ *RMS (Green dots) and* $|u'_0|/\bar{u}_0 = 0.55$ *RMS (Yellow dots). Acoustic network model predictions are represented as solid lines for all forcing levels. For each plot, the top and bottom figures represent the modulus and angle of the DATM coefficient respectively.*

for all forcing levels. For $f < 150$ Hz, the moduli of $\widetilde{M}(2,1)$ and $\widetilde{M}(2,2)$ are independent of the forcing level, but as the frequency becomes larger, an increasingly large gap appears between the data corresponding to the various forcing levels. The smaller the forcing level, the smaller the modulus of both coefficients $\widetilde{M}(2,1)$ and $\widetilde{M}(2,2)$.

This behavior cannot be reproduced by a linear acoustic network model. It is clear from Fig. 10.6 that the moduli of $\widetilde{M}(2,1)$ and $\widetilde{M}(2,2)$ linking the downstream acoustic velocity to the upstream acoustic pressure and acoustic velocity respectively appear to be nonlinear over a certain frequency range even in the absence of combustion. The origin of this nonlinear acoustic response for non-reactive conditions may be twofold.

First, nonlinear acoustic losses at the system boundaries may perturb the transfer matrix determination as the forcing level increases (Heckl 1990; Schuller et al. 2009). However, the specific acoustic impedances at the setup inlet and outlet are independent of the forcing level, as shown in Figs. 10.3 and 10.4. The acoustic nonlinearities are thus generated inside the region of interest, located between section (0), where the hot wire HW is located, and section (11), where the microphone ME" is located, as represented in Fig. 10.1-(Right).

The coupling between vorticity and sound waves may constitute another source of nonlinearities through the dissipation of acoustic energy as the sound waves interact with the large vortical structures (Howe 1979; Howe 1998) produced by the flow at the swirling vane and at the injector outlet. It has long been recognized that a fraction of the acoustic energy is dissipated inside a burner submitted to sound waves (Paschereit and Polifke 1998; Kruger et al. 2001; Su et al. 2015). This is generally modeled by a transfer matrix with additional lump parameters, such as an effective length taking into account the inertia of the fluid and a pressure loss coefficient. An example of such a model is the $\zeta - l_{eff}$ model (Paschereit and Polifke 1998; Hirschberg 2001; Gentemann et al. 2003; Polifke et al. 2003). These types of acoustic loss models yield good results for swirling injectors (Polifke et al. 2001; Ni et al. 2017), but they are linear and thus their predicted transfer matrix coefficients do not depend on the forcing level.

In this work, the response of the swirling vane to sound waves is modeled with a DATM corresponding to a compact perforated plate traversed by a high-Reynolds flow, modeled with Eq. (7.91) and corresponding to the region between section (3) and section (6) in Fig. 10.1-(Right). The swirler's finite thickness is taken into account as well as the nonlinear effects, following the description given in Sec. 7.4.7. For cold flow operating conditions, this analytical model constitutes the only source of nonlinearity in the acoustic network model represented in Fig. 10.5-(Top) as the amplitude of the acoustic

velocity does not appear in any other DATM.

The analytical predictions according to this acoustic network model are represented as solid lines in Figs. 10.6 and 10.7 for the swirling and non-swirling injectors respectively and for increasing forcing levels. These analytical predictions are similar for both injectors. Overall, the agreement between the analytical predictions and the modulus and angle of the measured DATM coefficients is excellent, except in the high-frequency range where the moduli of $\widetilde{M}(1,1)$ and $\widetilde{M}(1,2)$ are slightly underpredicted and the moduli of $\widetilde{M}(2,1)$ and $\widetilde{M}(2,2)$ are slightly overpredicted for the swirling injector. These observations are also valid for the non-swirling injector. On the other hand, the agreement between the model and the measurements for the angle of the DATM coefficients is very good for all frequencies investigated and for both the swirling and non-swirling injectors.

The acoustic network model represented in Fig. 10.5-(Top) accounts for the nonlinear acoustic losses at the swirling vane. Nevertheless, it is clear from Figs. 10.6 and 10.7 that the impact of the forcing level on the moduli of $\widetilde{M}(2,1)$ and $\widetilde{M}(2,2)$ is not correctly predicted by this network model. For instance, the modulus of $\widetilde{M}(2,1)$ measured at a forcing frequency $f = 240$ Hz and at a forcing level $|u'_0|/\bar{u}_0 = 0.10$ RMS for the swirling injector is 40% smaller than the same modulus measured at the same frequency but at a forcing level $|u'_0|/\bar{u}_0 = 0.72$ RMS. According to the acoustic network model represented in Fig. 10.5-(Top), this gap should be less than 1% at a forcing frequency $f = 240$ Hz.

It is thus concluded that for cold flow operating conditions, either the effects of the nonlinear acoustic losses at the swirling vane are highly underestimated by the acoustic network model or another source of nonlinearity was not taken into account. For instance, the acoustic waves may be damped at the injector outlet since vortical structures are known to be shed periodically at the injector rim, between section (7) and section (8) in Fig. 10.5-(Top). An additional modeling effort is thus needed to correctly predict the nonlinear acoustic losses inside a swirling and non-swirling premixed turbulent combustor. Moreover, the experiments conducted in this work for cold operating conditions show that nonlinear acoustic losses need to be considered when modeling the DATM coefficients of the system between section (0) and section (11) as the forcing level is increased.

It is now worth investigating the acoustic response of the NoiseDyn burner for reactive operating conditions. In this case, the flame constitutes another source of acoustic nonlinearity which also alters the acoustic response of the system.

10.5 Results for reactive operating conditions

Measurements and predictions according to the acoustic network model of the four DATM coefficients representing the acoustic response of the system between the hot wire HW location in section (0) and the microphone ME" location in section (11) are now reported for the swirling and non-swirling injectors operated under reactive conditions and for increasing acoustic forcing levels $|u'_0|/\bar{u}_0$.

Figures 10.8 and 10.9 represent the measured modulus and angle of the four DATM coefficients $\widetilde{M}(1,1)$, $\widetilde{M}(1,2)$, $\widetilde{M}(2,1)$ and $\widetilde{M}(2,2)$ for reactive operating conditions and for the swirling and non-swirling injectors respectively. Results are presented for forcing levels ranging from $|u'_0|/\bar{u}_0 = 0.10$ RMS to 0.55 RMS.

Once again, a higher variability of the DATM coefficients reconstructed from measurements is observed for low forcing frequencies because of the limited number of forcing cycles in the recorded signals and because the two independent acoustic boundary conditions become close at low frequencies. Moreover, the flame generates broadband combustion noise thus affecting the overall signal-to-noise ratio in Figs. 10.8 and 10.9 compared the results obtained for cold flow conditions presented in Figs. 10.6 and 10.7.

As opposed to the results obtained for cold flow operating conditions and presented in Sec. 10.4, both the modulus and angle of the DATM coefficients mostly differ for the swirling and non-swirling injectors operated under reactive conditions. This is particularly stricking when looking at the moduli of $\widetilde{M}(1,1)$, $\widetilde{M}(1,2)$ and $\widetilde{M}(2,2)$. This is due to the fact that the acoustic response of the flame depends on the type of injector, as demonstrated in Figs. 10.10-(Right) and 10.11-(Right) which represent the FDF for the swirling and non-swirling injectors respectively. As a consequence, the acoustic response of the flame/combustor system comprised between section (0) and section (11) in Fig. 10.1-(Right) is different for the swirling and non-swirling injectors.

Figures 10.8 and 10.9 highlight the fact that all four measured DATM coefficients depend on the forcing level $|u'_0|/\bar{u}_0$ to some extent over a certain frequency range. For both the swirling and non-swirling injectors and for all forcing frequencies investigated, the moduli of $\widetilde{M}(1,1)$ and $\widetilde{M}(2,1)$ are strongly affected when the forcing level is increased while the moduli of $\widetilde{M}(1,2)$ and $\widetilde{M}(2,2)$ are only slightly affected by changes of the forcing level. On the other hand, the angles of all measured DATM coefficients only marginally depend on the forcing level.

The impact of the forcing level on the measured DATM coefficients appears

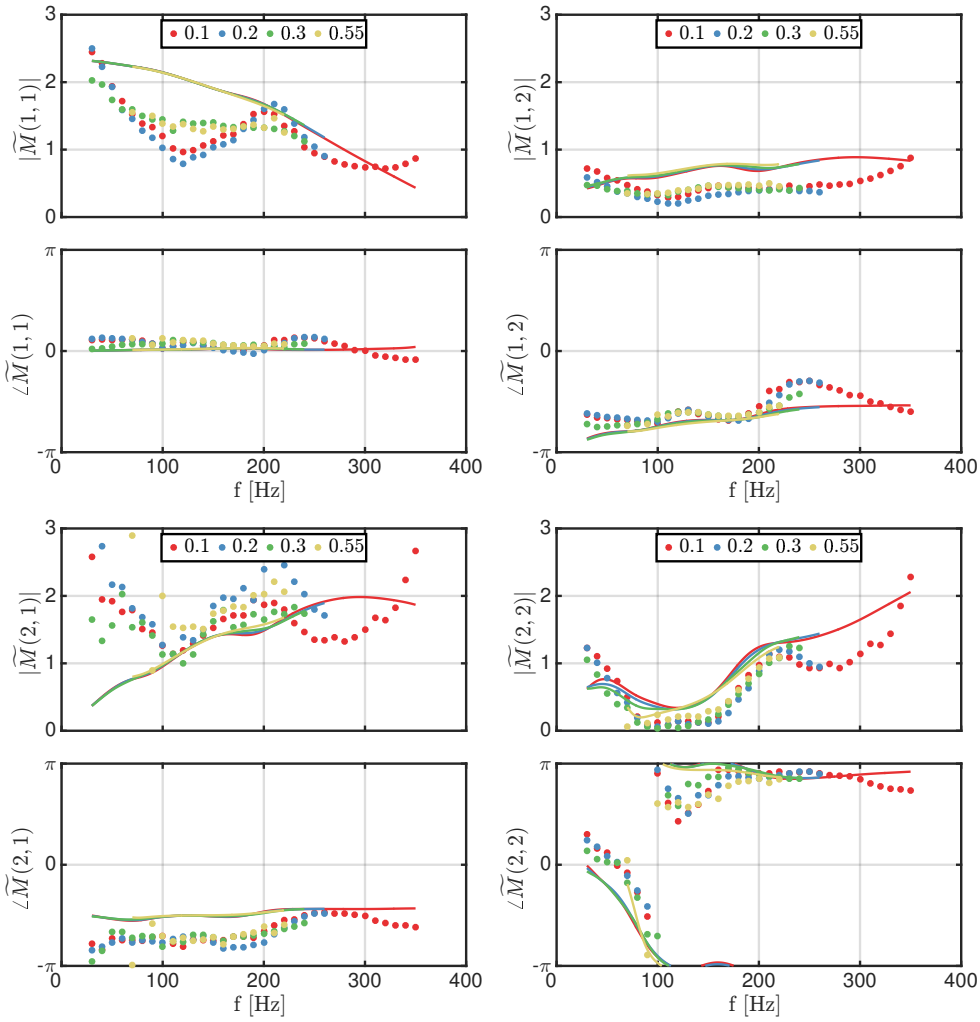

Figure 10.8: *Coefficients of the Dimensionless Acoustic Transfer Matrix (DATM) representing the acoustic response of the system between the hot wire HW location in section (0) and the microphone ME" location in section (11) for a swirling injector and for reactive operating conditions. (Top left):* $\widetilde{M}(1,1)$ *- (Top right):* $\widetilde{M}(1,2)$ *- (Bottom left):* $\widetilde{M}(2,1)$ *- (Bottom right):* $\widetilde{M}(2,2)$*. Measurements are performed at various forcing levels:* $|u'_0|/\bar{u}_0 = 0.10$ *RMS (Red dots),* $|u'_0|/\bar{u}_0 = 0.20$ *RMS (Blue dots),* $|u'_0|/\bar{u}_0 = 0.30$ *RMS (Green dots) and* $|u'_0|/\bar{u}_0 = 0.55$ *RMS (Yellow dots). Acoustic network model predictions are represented as solid lines for all forcing levels. For each plot, the top and bottom figures represent the modulus and angle of the DATM coefficient respectively.*

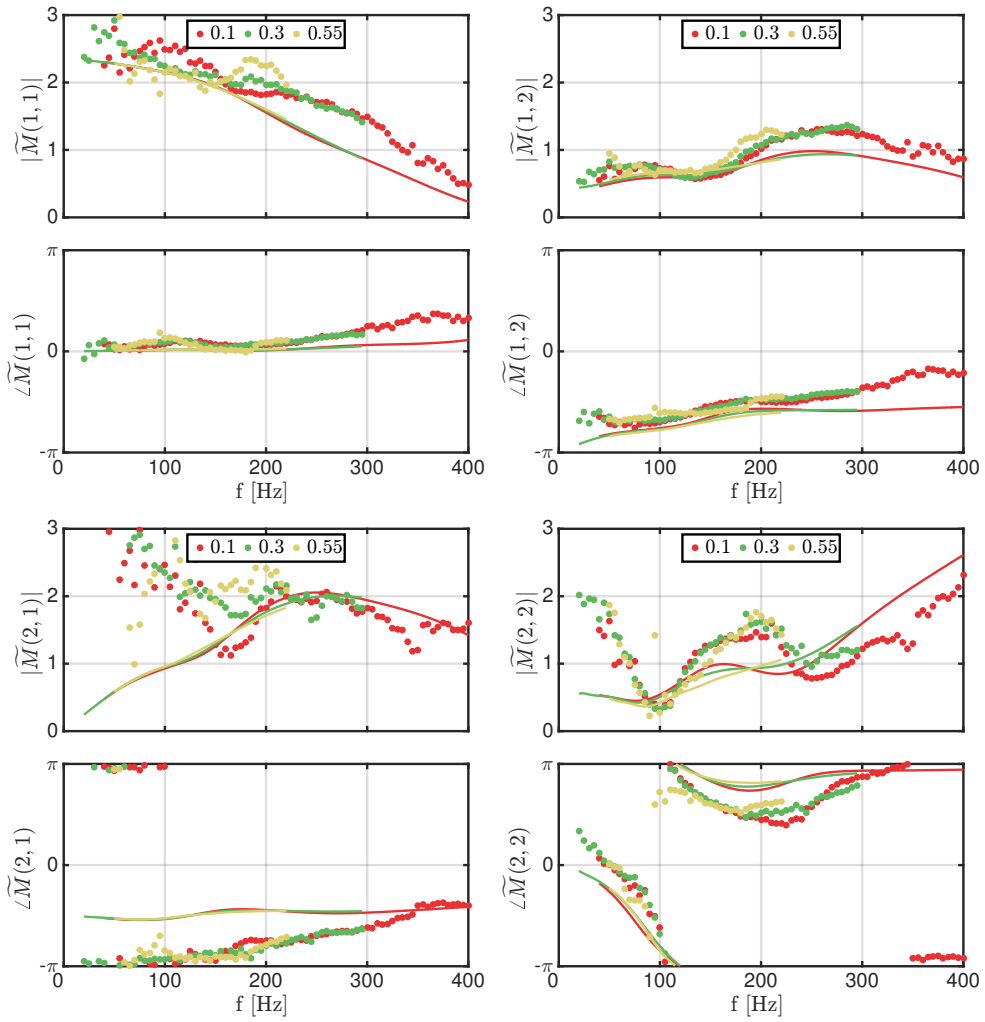

Figure 10.9: *Coefficients of the Dimensionless Acoustic Transfer Matrix (DATM) representing the acoustic response of the system between the hot wire HW location in section (0) and the microphone ME" location in section (11) for a non-swirling injector and for reactive operating conditions. (Top left):* $\widetilde{M}(1,1)$ *- (Top right):* $\widetilde{M}(1,2)$ *- (Bottom left):* $\widetilde{M}(2,1)$ *- (Bottom right):* $\widetilde{M}(2,2)$*. Measurements are performed at various forcing levels:* $|u'_0|/\bar{u}_0 = 0.10$ *RMS (Red dots),* $|u'_0|/\bar{u}_0 = 0.30$ *RMS (Green dots) and* $|u'_0|/\bar{u}_0 = 0.55$ *RMS (Yellow dots). Acoustic network model predictions are represented as solid lines for all forcing levels. For each plot, the top and bottom figures represent the modulus and angle of the DATM coefficient respectively.*

to be more important for reactive operating conditions, shown in Figs. 10.8 and 10.9, than for cold operating conditions, shown in Figs. 10.6 and 10.7. An initial conjecture would be to relate these observations to the nonlinear response of the flame when it is submitted to high-amplitude acoustic forcing.

The predictions of the DATM coefficients according to the acoustic network model represented in Fig. 10.5-(Bottom) for reactive operating conditions are also determined for all forcing levels and for both injectors. These predictions are plotted in Figs. 10.8 and 10.9 for the swirling and non-swirling injectors respectively. The nonlinear flame response is accounted for through the use of the Flame Describing Function, determined by optical means and represented in Figs. 10.10-(Right) and 10.11-(Right) for the swirling and non-swirling injectors respectively.

Both FDF are obtained by forcing the flame with the loudspeaker while recording the velocity signal $\bar{u}_0 + u'_0$ at the hot wire location, corresponding to section (0) in Fig. 10.1-(Right), and simultaneously recording the light emission from the combustion region with a photomultiplier equipped with an OH* filter. The acoustic velocity u'_7 at the top of the injector in section (7) is then deduced from the hot wire signal and the propagation model described in Chapter 9.

Despite the fact that the FDF for the swirling and non-swirling injectors are different, the analytical predictions obtained with this acoustic network model for these two injectors are comparable, as shown in Figs. 10.8 and 10.9. Overall, the agreement between the acoustic network model predictions and the corresponding measurements of $\widetilde{M}(1,2)$ and $\widetilde{M}(2,2)$ is satisfactory for the swirling injector. On the other hand, the modulus of $\widetilde{M}(1,1)$ and the modulus and angle of $\widetilde{M}(2,1)$ are only partly retrieved from the model for the swirling injector. For the non-swirling injector, the best match between the model and the experiments is obtained for coefficients $\widetilde{M}(1,1)$, $\widetilde{M}(1,2)$ and $\widetilde{M}(2,2)$ even though the match is still satisfactory for coefficient $\widetilde{M}(2,1)$.

The predictions of coefficients $\widetilde{M}(1,1)$, $\widetilde{M}(1,2)$ and $\widetilde{M}(2,1)$ according to the acoustic network model are found to be almost insensitive to the forcing level for both the swirling and non-swirling injectors, as shown in Figs. 10.8 and 10.9. For instance, even though the general trend for the modulus of $\widetilde{M}(1,1)$ is reproduced by the acoustic network model in the non-swirling case, the impact of the forcing level on the measured coefficient is much larger than expected from the acoustic network analysis fed with the FDF. On the other hand, the predictions for coefficient $\widetilde{M}(2,2)$ vary significantly when the forcing level is modified but these variations do not fully represent the experimental observations, as shown in Figs. 10.8 and 10.9.

It is worth emphasizing that the FDF appears in the velocity/velocity component $\widetilde{M}(2,2)$ of the DATM representing the acoustic response of the flame, given by Eq. (8.46). However, the DATM linking the acoustic pressure p'_{11} and acoustic velocity u'_{11} at the microphone ME" location to the acoustic pressure p'_0 and acoustic velocity u'_0 at the hot wire location is not compact due to the large distance separating these locations. As a consequence, the contribution of the DATM representing the compact flame spreads to the other DATM coefficients representing the entire burner/flame response to sound waves. Hence, nonlinearities due to the flame response may be present in all four DATM coefficients presented in Figs. 10.8 and 10.9.

In addition to the nonlinearities generated by the flame response, the coupling between vortical structures and sound waves described in Sec. 10.4 for cold flow operating conditions is still a source of nonlinearity for reactive operating conditions. In the end, the nonlinearities observed in Figs. 10.8 and 10.9 originate from both phenomena.

The last step is to reconstruct the FDF obtained with optical measurements from the acoustic network model and the hot wire HW and microphones MHW, ME, ME' and ME" signals. In most industrial burners, measuring the flame heat release rate is challenging. Optical access is often limited in such systems and the OH* or CH* chemiluminescence signals, which are tracers of the flame heat release rate, cannot be easily recorded. In non-premixed combustors, the OH* or CH* chemiluminescence signals are usually not linearly related to the flame heat release rate, which raises difficulties. Since the Flame Describing Function is an important tool that may be used to perform a thermoacoustic stability analysis, it is worth examining whether the FDF can be recontructed from acoustic measurements only.

The DATM describing the flame response to harmonic sound waves is extracted using the following procedure. The DATM denoted by $\widetilde{M}$, which describes the entire acoustic response of the combustor/flame system located between section (0) and section (11), is extracted from the hot wire and microphone measurements as explained in Sec. 10.2. Then, all the different DATM denoted by $\widetilde{M}_{ij}$ are modeled using the analysis presented in Sec. 10.3, except for $\widetilde{M}_{78}$ corresponding to the flame element. This latest DATM is deduced using Eq. (10.5) rearranged in the following way:

$$\widetilde{M}_{78} = \left(\widetilde{M}_{1011}\ \widetilde{M}_{910}\ \widetilde{M}_{89}\right)^{-1}\ \widetilde{M}\ \left(\widetilde{M}_{67}\ \widetilde{M}_{36}\ \widetilde{M}_{23}\ \widetilde{M}_{12}\ \widetilde{M}_{01}\right)^{-1} \tag{10.6}$$

The resulting DATM denoted by $\widetilde{M}_{78}$ describes the acoustic response of the system between section (7) and section (8), where the flame is located.

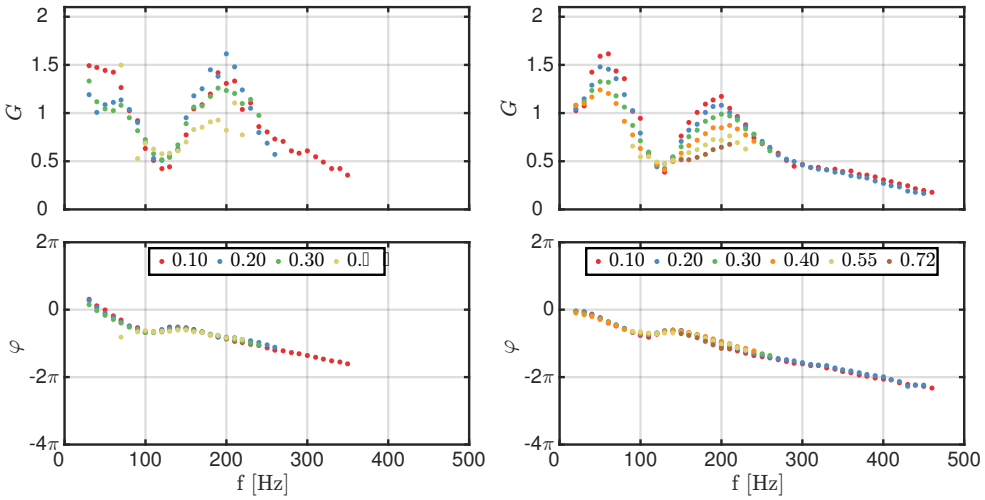

Figure 10.10: *Gain (Top) and phase (Bottom) of the Flame Describing Function (FDF) obtained with the swirling injector as a function of the forcing frequency for increasing forcing levels* $|u'_0|/\bar{u}_0 = 0.10$ *RMS (Red dots),* $|u'_0|/\bar{u}_0 = 0.20$ *RMS (Blue dots),* $|u'_0|/\bar{u}_0 = 0.30$ *RMS (Green dots),* $|u'_0|/\bar{u}_0 = 0.40$ *RMS (Orange dots),* $|u'_0|/\bar{u}_0 = 0.55$ *RMS (Yellow dots) and* $|u'_0|/\bar{u}_0 = 0.72$ *RMS (Brown dots). (Left): Reconstruction from the acoustic network model and the acoustic pressure and acoustic velocity measurements in section (0) and section (11). (Right): Reconstruction from the acoustic velocity measurement in section (0) and the chemiluminescence signal.*

The reconstruction of $\widetilde{M}_{78}$ is then compared with the analytical model given by Eq. (8.46) and the Flame Describing Function is subsequently deduced from the velocity/velocity component of the reconstructed coefficient $\widetilde{M}_{78}$. This procedure can be used to determine the FDF solely from acoustic pressure and acoustic velocity measurements at any distance from the flame when used in association with an acoustic network model of the reactive system.

Figures 10.10-(Left) and 10.11-(Left) represent this acoustic reconstruction for the swirling and non-swirling injectors while Figs. 10.10-(Right) and 10.11-(Right) represent the corresponding FDF determined optically using a photomultiplier with an OH* filter for the swirling and non-swirling injectors.

The FDF gains in Figs. 10.10-(Right) and 10.11-(Right) start at unity at low frequency, as expected from theory (Polifke and Lawn 2007). On the other hand, the FDF gains at low frequencies predicted by the DATM reconstructions are overestimated, as shown in Figs. 10.10-(Left) and 10.11-(Left) for the swirling and non-swirling injectors.

The FDF obtained from optical measurements with the swirling injector and shown in Fig. 10.10-(Right) is now described. First, the gain increases with

increasing frequencies before a sudden drop, followed by a second increase and then a smooth decrease at high frequencies. This type of frequency response is typical of premixed swirling flames (Palies et al. 2010; Gatti et al. 2017). The overall flame response drops as the forcing level $|u'_0|/\bar{u}_0$ increases except within the low-gain valley, for forcing frequencies between 100 Hz and 150 Hz. In this region, the FDF remains roughly independent of the forcing level whereas at lower and higher frequencies, the gain is impacted by the forcing level set at the hot wire location.

The overall shape of the reconstructed FDF obtained from acoustic measurements using the swirling injector, presented in Fig. 10.10-(Left), is in good agreement with the FDF obtained with the photomultiplier, presented in Fig. 10.10-(Right). The evolution of the reconstructed FDF gain with the forcing level is also fairly well retrieved. Nevertheless, for forcing frequencies $f < 50$ Hz and 150 Hz $< f <$ 250 Hz, the reconstructed FDF gain is overestimated. On the other hand, the FDF phase lag is perfectly predicted for forcing frequencies $f > 50$ Hz. At lower frequencies, the FDF reconstruction is less accurate because of the limited number of forcing cycles in the recorded signals. Finally, both the acoustically reconstructed and optically measured FDF phase lag are independent of the forcing level (Palies et al. 2010; Gatti et al. 2017) and are in excellent agreement with each other.

It is thus concluded that the phase lag of the Flame Describing Function of a premixed turbulent swirling flame can be accurately predicted from an acoustic network model used in association with acoustic measurements at the system inlet and outlet. On the other hand, the reconstruction of the gain of the FDF is more difficult and some deviations may be observed between the optical and purely acoustic techniques. However, the overall evolution of the gain of the FDF with the forcing frequency and forcing level is fairly well predicted.

For the non-swirling injector, the general trend of the FDF gain is once again fairly well predicted by the acoustic reconstruction, presented in Fig. 10.11-(Left), when it is compared to the FDF obtained with the photomultiplier, presented in Fig. 10.11-(Right). The gain of the Flame Describing Function corresponding to the non-swirling injector and measured with the optical technique first increases with the forcing frequency and then decreases until it reaches a value $G \sim 0$ at a forcing frequency $f = 400$ Hz. This FDF gain shape is typical of non-swirling injectors (Schuller et al. 2003b; Gatti et al. 2018). Moreover, the FDF gain decreases for increasing forcing levels at a given forcing frequency, as shown in Fig. 10.11-(Right). The impact of the forcing level is also predicted by the FDF reconstruction to a certain extent.

The gain of the acoustically reconstructed FDF are highly overestimated in the low frequency region, with gain values exceeding 2 for certain forcing

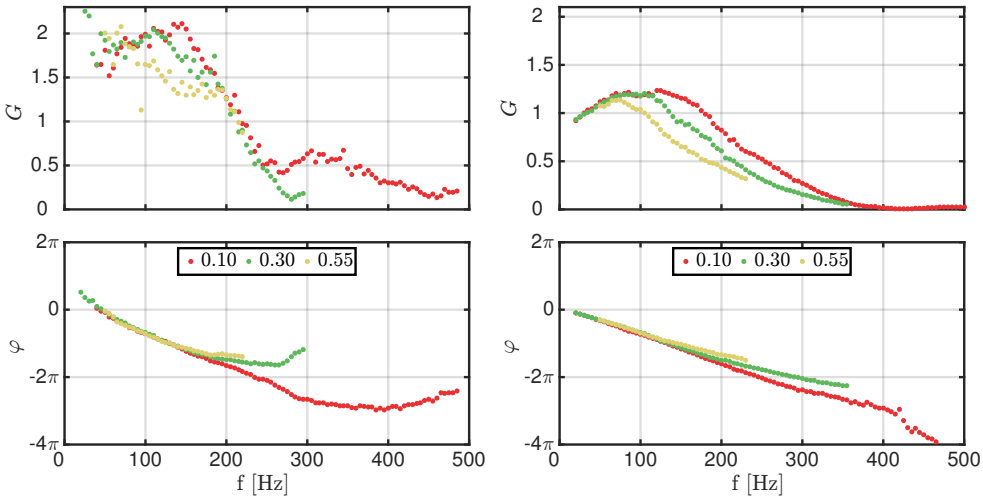

Figure 10.11: *Gain (Top) and phase (Bottom) of the Flame Describing Function (FDF) obtained with the non-swirling injector as a function of the forcing frequency for increasing forcing levels* $|u'_0|/\bar{u}_0 = 0.10$ *RMS (Red dots),* $|u'_0|/\bar{u}_0 = 0.30$ *RMS (Green dots) and* $|u'_0|/\bar{u}_0 = 0.55$ *RMS (Yellow dots). (Left): Reconstruction from the acoustic network model and the acoustic pressure and acoustic velocity measurements in section (0) and section (11). (Right): Reconstruction from the acoustic velocity measurement in section (0) and the chemiluminescence signal.*

frequencies and forcing levels compared to a maximum gain $G \sim 1.25$ for the FDF determined with an optical technique. In the high frequency range, a second FDF gain peak is predicted by the recontruction in Fig. 10.11-(Left) while it is absent in the FDF obtained from optical measurements presented in Fig. 10.11-(Right). Finally, the FDF phase lag for the non-swirling injector is accurately predicted for intermediate forcing frequencies 50 Hz $< f <$ 250 Hz. The general trend of the Flame Describing Function of a premixed turbulent non-swirling flame is fairly well retrieved by the acoustic network model used in association with acoustic measurements at the system inlet and outlet but large deviations for the values of the FDF gain are observed.

It is thus concluded that for both the swirling and non-swirling flames, some discrepancies between the optically-measured and acoustically-reconstructed Flame Describing Functions are observed. These deviations may be due to various phenomena:

- Even though the hot wire, photomultiplier and microphones signals were always recorded at the same time with the same sampling frequency and for the same duration, it appears that the acoustic reconstruction is more sensitive to low frequency noise than the optical technique. At low forcing frequencies, the specific acoustic impedances of the two

configurations of the NoiseDyn burner that are needed to extract the DATM coefficients tend to be relatively close. As a consequence, the quality of the acoustic reconstruction decreases at low frequencies.

- Moreover, the acoustic reconstruction of the Flame Describing Function relies on the quality and accuracy of the models used to describe the acoustic response of all the elements present inside the combustor between section (0) and section (11), except the element containing the flame. However, it was shown in Sec. 10.4 that the acoustic response of the burner for cold operating conditions is not fully reproduced by the acoustic network models. As a consequence, the acoustic reconstruction of the FDF is altered because the models are not accurate enough.

- Finally, the optical technique used to determine the FDF relies on the hypothesis that the OH* chemiluminescence signal is proportional to the flame heat release rate. Even though this relation is well-established for perfectly premixed lean hydrocarbon flames, the accuracy of this approximation is difficult to assess.

10.6 Conclusion

The impact of the forcing level $|u'_0|/\bar{u}_0$ on the Dimensionless Acoustic Transfer Matrix (DATM) coefficients describing the acoustic response of a swirling and non-swirling burner was determined for cold and reactive operating conditions. The specific acoustic impedances at the system inlet and outlet were also measured for all operating conditions and all forcing frequencies and were found to be independent of the forcing level. The Flame Describing Function (FDF) of the swirling and non-swirling flames were also measured with a photomultiplier mounted with an OH* filter for the same forcing levels and forcing frequencies.

For cold operating conditions, the acoustic response of the system comprised between the hot wire HW location and the uppermost microphone ME" location was found to be similar for both injectors. Moreover, the angles of the DATM coefficients representing the whole system were found to be mostly independent of the forcing level $|u'_0|/\bar{u}_0$. Likewise, the moduli of the DATM coefficients linking the downstream pressure fluctuations to the upsteam pressure and velocity fluctuations were found to be the same for all forcing levels. On the other hand, the moduli of the DATM coefficients linking the downstream velocity fluctuations to the upstream pressure and velocity fluctuations were found to be strongly impacted by the forcing level $|u'_0|/\bar{u}_0$ at high forcing frequencies.

For reactive operating conditions, the acoustic response of the entire system was found to be different for the swirling and non-swirling injectors. The angles of the DATM coefficients were still found to be mostly independent of the forcing level for all forcing frequencies and for both injectors. Moreover, the moduli of the DATM coefficients linking the downstream pressure and velocity fluctuations to the upsteam velocity fluctuations were found to be the same for all forcing levels while the moduli of the DATM coefficients linking the downstream pressure and velocity fluctuations to the upsteam pressure fluctuations were found to depend on the forcing level $|u'_0|/\bar{u}_0$ over a certain frequency range.

Two acoustic network models describing the response of the system between the hot wire HW location and the uppermost microphone ME" location were designed for cold flow and reactive operating conditions respectively. For cold flow conditions, the reconstructed DATM was shown to be the same for the swirling and non-swirling injectors. For reactive conditions, the reconstructed DATM was found to be injector-dependent as the Flame Describing Function (FDF), which was shown to be different for swirling and non-swirling injectors, was used to describe the acoustic response of the flame in the network model.

Two sources of acoustic nonlinearities were considered in the network models. First, the acoustic nonlinearities generated at the rim of the swirling vane channels because of the coupling between sound waves and vortical structures convected by the mean flow were included in the cold and reactive acoustic network models. Furthermore, the flame nonlinearities were also accounted for in the reactive case through the use of the FDF.

For cold operating conditions, the acoustic network model was found to be in good agreement with the measurements obtained with the swirling and non-swirling injectors. The angles of the reconstruced DATM coefficients were found to be independent of the forcing level, which corresponds to the experimental observations. Moreover, the agreement between the angles of the measured and predicted DATM coefficients was shown to be excellent. The moduli of the pressure/pressure and pressure/velocity DATM coefficients were also well predicted by the acoustic network model. On the other hand, the moduli of the velocity/pressure and velocity/velocity DATM coefficients were still found to be fairly well predicted but the impact of the forcing level was not correctly reproduced by the DATM reconstruction.

For reactive operating conditions, the general trends of the four DATM coefficients obtained with the swirling and non-swirling injectors were still shown to be roughly reproduced by the model but the agreement between the measured DATM coefficients and the corresponding reconstructions from the acoustic network model were found to worsen compared to cold flow conditions. The impact of the forcing level on the DATM coefficients was not

well retrieved by the acoustic network model.

Finally, the FDF associated with the swirling and non-swirling flames were reconstructed from the DATM measurements and the acoustic network models developed for reactive operating conditions. The corresponding predictions were compared to the FDF obtained with optical measurements. The agreement between the measured and reconstructed FDF was found to be good for the swirling injector even though the gain was shown to be largely overestimated for certain frequency ranges. The phase lag was shown to be well predicted and the variations of both the FDF gain and phase lag with the forcing level were found to be satisfactorily predicted. The agreement between the optically-measured and acoustically-reconstructed FDF was still found to be satisfactory for the non-swirling injector even though the FDF gain was found to be highly overestimated for most forcing frequencies. On the other hand, the FDF phase lag was shown to be accurately predicted for most forcing frequencies even with the non-swirling injector.

These experiments confirm that some of the Dimensionless Acoustic Transfer Matrix coefficients representing the acoustic response of the burner/flame system highly depend on the forcing level for cold and reactive operating conditions. The nonlinear acoustic losses at the swirler holes coupled with the flame nonlinearities (for reactive conditions) were modeled in the acoustic network model, but these elements do not allow to entirely reproduce the impact of the forcing level on the DATM coefficients. This chapter emphasizes the need for analytical models predicting the nonlinear acoustic losses inside premixed turbulent swirling and non-swirling burners.

This chapter also highlights the difficulties when extracting the Flame Describing Function from purely acoustic measurements. This method requires accurate DATM models for all the elements of the acoustic network model. It also requires precise measurements of the total DATM representing the whole response of the burner/flame system, which is achievable only if the two required acoustic states are independent for all forcing frequencies and all forcing levels.

Chapter 11

Measurement and Prediction of Thermoacoustic Modes

Thermoacoustic instabilities are due to a significant energy transfer from the flame to the acoustic field that is not counterbalanced by the linear acoustic losses generated within the combustor and at its boundaries. When these instabilities occur in a combustor, they may lead to flame extinction, structural damage, increased heat fluxes or even catastrophic failure. Predicting the onset of thermoacoustic instabilities in industrial combustors remains a challenging task. The aim of this chapter is to predict the thermoacoustic stability of various configurations of the NoiseDyn burner. For all unstable configurations, the frequency of the instability and its associated limit cycle amplitude is determined. First, the thermoacoustic stability of six distinct configurations is explored experimentally and the unstable modes are fully characterized. Then, two acoustic network models are constructed: in the first model, the flame response is directly modeled using a Flame Describing Function while in the second model, the flame response is embedded in an Acoustic Transfer Matrix that also accounts for the acoustic losses inside the setup. The predictions associated with both network models are then compared to measurements and it is concluded that both approaches lead to accurate predictions of the thermoacoustic state of the NoiseDyn burner. In the case of an unstable thermoacoustic mode, the instability frequency is also well predicted by both acoustic network models. On the other hand, the limit cycle oscillation amplitude is accurately predicted by the second model only while it is overestimated by the first model, in which the acoustic losses need to be modeled.

11.1 Introduction

Background on thermoacoustic instabilities

Modern gas turbines are operated with lean premixed flames in order to reduce the emissions of pollutants such as nitrogen oxides but they are prone to large-amplitude oscillations of the pressure, velocity, density and temperature inside the combustor (Keller 1995; Correa 1998; Candel 2002; Poinsot 2017). The oscillations of these physical variables are called thermoacoustic instabilities or combustion instabilities and may lead to various detrimental phenomena such as flame extinction (Candel 1992; Prieur et al. 2018), structural damage (Candel 1992; Lieuwen and Yang 2005), increased heat fluxes (McManus et al. 1993; Barbosa et al. 2008) and large noise emission at a few discrete frequencies (Noiray et al. 2006b; Barbosa et al. 2008; Tran et al. 2009a).

Gas turbines used for power generation (Seume et al. 1998) or propulsion (Zhu et al. 2001) have been known to suffer from combustion instabilities. It should be noted that thermoacoustic instabilities are not limited to gas turbines: they may develop in a variety of combustors, including rocket engines (Crocco 1951; Crocco 1952; Crocco et al. 1960), ramjets (Yang and Culick 1986; Yu et al. 1991), industrial furnaces (Putnam 1971; Rodriguez-Martinez et al. 2006) and many industrial or domestic heating appliances (de Goey et al. 2011).

Since thermoacoustic instabilities may appear in a large collection of combustors and may lead to disastrous consequences, there is large theoretical, experimental and numerical research effort to develop tools predicting the thermoacoustic stability of practical and labscale combustors at an early design stage (Candel 2002; Lieuwen 2005; Poinsot and Veynante 2005; Poinsot 2017). However, predicting the presence and growth of an unstable thermoacoustic mode in a practical combustor is challenging for three main reasons. First, complex unsteady interactions between acoustic waves, flow variables, heat transfer and chemistry take place inside the combustor (Candel 2002). Second, many of the mechanisms involved, such as the flame response to high-amplitude harmonic sound waves or the internal acoustic losses, are usually nonlinear (Cummings 1984; Dowling 1997; Noiray et al. 2008). Finally, the geometry of practical combustors is a complex arrangement of cavities and many modes may develop during operation (Poinsot 2017).

Thermoacoustic stability analysis

Various strategies based on analytical developments alone (Keller 1995; Dowling and Stow 2003) or used along with experiments (Paschereit and Polifke 1998; Schuermans et al. 2000; Polifke et al. 2003; Noiray et al. 2008) or simulations (Nicoud et al. 2007; Han et al. 2015) may be used to predict the

thermoacoustic stability of a combustor. In all cases, the acoustic response of the combustor is predicted using an acoustic equivalent consisting of a limited number of cavities - in which sound waves propagate - connected to one another with appropriate jump conditions. This framework is quickly introduced below.

From an acoustics viewpoint, gas turbines operated for reactive conditions can be represented by a network of cavities with a flame stabilized within one of these cavities (Keller 1995; Paschereit and Polifke 1998; Dowling and Morgans 2005). For cold flow operating conditions, an isothermal network model that does not account for the flame response may be constructed (Munjal 1987; Candel and Poinsot 1988; Fischer et al. 2006). Fresh gases feeding the flame are injected through inlets and burnt gases are exhausted through outlets, all of which are represented by measured, simulated or modeled acoustic boundary conditions.

A network of cavities coupled with non-anechoic acoustic boundary conditions possesses a set of discrete frequencies at which it acoustically resonates (Munjal 1987; Candel and Poinsot 1988). Each frequency associated with its acoustic flow fields is called a mode and depends on many parameters, including the combustor geometry (Paschereit and Polifke 1998; Schuermans et al. 2000), the inlet and outlet acoustic boundary conditions (Munjal 1987; Paschereit and Polifke 1998), the Mach number of the mean flow (Paschereit and Polifke 1998; Hirschberg and Rienstra 2004), the presence of a flame (Keller 1995; Paschereit and Polifke 1998) and the acoustic damping rate inside the setup (Paschereit and Polifke 1998; Fischer et al. 2006) among others.

The concept of acoustic resonance will now be introduced using a very simple model: a single one-dimensional cavity opened at both sides (the so-called open-open duct) containing a cold quiescent fluid. This representation may be used as a first approximation of the acoustic behavior of flutes and organ pipes for instance (Hartmann 2013). In that case, the frequencies at which the duct resonates are given by:

$$f = \frac{pc}{2L} \tag{11.1}$$

where L is the cavity length, c is the speed of sound and $p \in \mathbb{N}^*$ is a non-zero positive integer characterizing the acoustic mode. The first five modes corresponding to a one-dimensional cavity opened at both sides are represented in Fig. 11.1.

This one-dimensional cavity model is too simple to accurately describe the acoustic behavior of a real combustor. For more complex systems consisting of multiple cavities of various sizes and cross section areas that are bounded

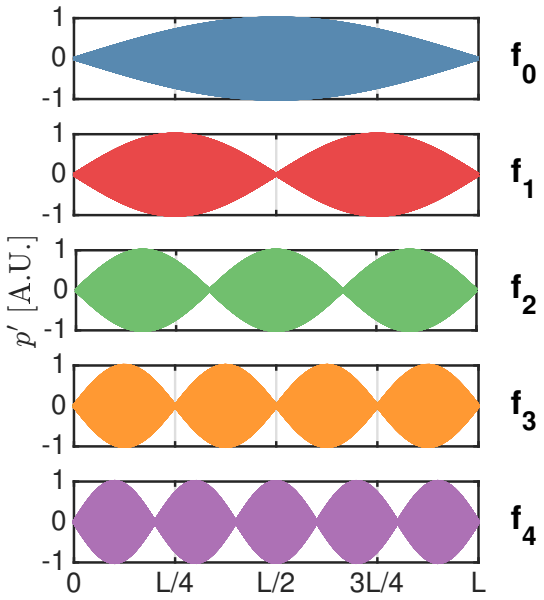

Figure 11.1: *Acoustic pressure envelope of the first five modes of a one-dimensional cavity opened at both sides. (Blue): Fundamental mode at $f_0 = c/2L$ - (Red): First harmonic at $f_1 = c/L$ - (Green): Second harmonic at $f_2 = 3c/2L$ - (Orange): Third harmonic at $f_3 = 2c/L$ - (Violet): Fourth harmonic at $f_4 = 5c/2L$*

by complex acoustic boundary conditions, acoustic modes and their associated acoustic flow fields can still be determined either analytically (Munjal 1987; Candel and Poinsot 1988), experimentally (Schuller et al. 2003b; Palies et al. 2011b) or using numerical strategies (Crighton et al. 1992; Selle et al. 2006).

For cold quiescent conditions and in the absence of an external source of energy, the acoustic modes will not develop and the system is said to be stable. On the other hand, acoustic modes may become unstable in the presence of a mean flow (Rienstra and Hirschberg 2016) or flame (Poinsot and Veynante 2005) for instance. In that case, the amplitude of the oscillations of the acoustic variables inside the combustor increases and may lead to limit cycle oscillations.

The prediction of acoustic modes is greatly complicated by the presence of a flame inside combustors operated for reactive conditions. This is due to the complexity of the flame response to incoming acoustic waves. Until recently, the acoustic response of the flame was assumed to be independent of the forcing level (Merk 1957; Becker and Günther 1971; Schuermans et al. 1999; Polifke et al. 2001; Candel 2002). In the past two decades, analytical developments

(Dowling 1997; Noiray et al. 2008), experiments (Durox et al. 2009; Gaudron et al. 2017c) and simulations (Krediet et al. 2012; Han and Morgans 2015) showed that this response is nonlinear as it depends on the amplitude of the sound waves impinging on the flame.

FTF/FDF formalism versus ATM/DATM formalism

The acoustic response of a premixed flame may be described using two formalisms that are equivalent from a theoretical viewpoint: the FTF/FDF formalism in which the flame response to sound waves is directly described and the ATM/DATM formalism in which the flame response is hidden in a black box relating the acoustic variables upstream and downstream the flame.

In the first framework, the flame frequency response is represented using a Flame Transfer Function (FTF) (Merk 1957; Candel 2002) or its nonlinear extension, a Flame Describing Function (Dowling 1997; Noiray et al. 2008). A detailed description of the FTF/FDF formalism can be found in Chapter 9. The FTF/FDF is then determined using experiments (Becker and Günther 1971; Durox et al. 2009; Gatti et al. 2018), simulations (Kornilov et al. 2009; Tay Wo Chong et al. 2010; Han and Morgans 2015) or analytical models (Crocco 1951; Merk 1957; Ducruix et al. 2000; Schuller et al. 2003a; Preetham et al. 2008; Palies et al. 2011). After the FTF/FDF is determined, it may be incorporated into an acoustic model of the combustor and the corresponding acoustic modes are predicted using an acoustic solver (Keller 1995; Dowling and Stow 2003; Noiray et al. 2008; Palies et al. 2011b; Silva et al. 2013; Laera et al. 2017).

The second formalism is based on the (Dimensionless) Acoustic Transfer Matrix (ATM/DATM) formalism where the flame acoustic response is modeled by a 2×2 matrix relating the acoustic pressure and acoustic velocity upstream and downstream the flame (Paschereit and Polifke 1998; Schuermans et al. 1999; Dowling and Stow 2003; Truffin and Poinsot 2005). A detailed description of this framework may be found in Chapter 10. Once again, the ATM/DATM representing the flame element may be determined using experiments (Paschereit and Polifke 1998; Guedra et al. 2011; Gaudron et al. 2017c), simulations (Polifke et al. 2001; Merk et al. 2018) or analytical models (Schuermans et al. 1999). The ATM/DATM representing the flame response may then be incorporated into an acoustic network model representing the entire combustor in order to perform a thermoacoustic stability analysis (Schuermans et al. 2000; Guedra et al. 2011).

A link between the FTF/FDF formalism and the ATM/DATM formalism can be established in the case of perfectly premixed lean flames (Schuermans et al.

1999; Truffin and Poinsot 2005), as described in Chapter 10. However, the flame nonlinearities are usually neglected in the ATM/DATM formalism as the impact of the forcing level on the acoustic transfer matrix describing the flame element is rarely accounted for. As a consequence, it is impossible to predict the limit cycle oscillation amplitude at which unstable thermoacoustic modes may develop using the ATM/DATM formalism unless the impact of the forcing level is considered.

Acoustic energy balance: the modified Rayleigh's criterion

Thermoacoustic instabilities occurring in industrial and labscale combustors are due to an energy transfer from the flame to the acoustic flow field variables (Strutt and Rayleigh 1878; Blackshear 1953; Candel 2002). The acoustic energy balance of a system containing a heat source is now detailed (Strutt and Rayleigh 1878; Dowling and Morgans 2005; Durox et al. 2009).

A positive energy transfer from the flame to the acoustic flow field variables is observed when the acoustic pressure at the flame location and the flame heat release rate are out of phase by less than 90° (Strutt and Rayleigh 1878; Poinsot and Veynante 2005). This law, called Rayleigh's criterion, is respected when the source term $\mathcal{S}$ defined below is positive.

$$\mathcal{S} = \frac{\gamma - 1}{\bar{\rho}\bar{c}^2} \frac{1}{\tau_\omega} \int_{V_f} \int_{\tau_\omega} p' \dot{q}' dt dV \tag{11.2}$$

where τ_ω is the oscillation period and V_f is the flame volume, i.e. the volume in which the combustion reactions take place. The volumetric heat release rate fluctuations $\dot{q}'$ and the acoustic pressure p' may vary significantly across the flame and should be integrated locally.

When the source term $\mathcal{S}$ is positive, the acoustic energy surplus may be dissipated by two distinct mechanisms: 1) it may be dissipated at the system boundaries (Dowling and Morgans 2005; Durox et al. 2009) and 2) it may be dissipated inside the setup by various sources of acoustic losses (Durox et al. 2009).

The amplitude of the acoustic oscillations increases if the source term $\mathcal{S}$ is larger than the sum of all acoustic damping mechanisms. This may be expressed mathematically through a modified version of Rayleigh's criterion corresponding to an acoustic energy balance and expressed as (Dowling and Morgans 2005; Nicoud and Poinsot 2005; Durox et al. 2009; Brear et al. 2012):

$$\mathcal{S} > \frac{1}{\tau_\omega} \int_{\partial\mathcal{V}} \int_{\tau_\omega} p' u' dt dS + \frac{1}{\tau_\omega} \int_{\mathcal{V}} \int_{\tau_\omega} \zeta_a dt dV \tag{11.3}$$

where $\mathcal{V}$ corresponds to the control volume containing the combustion chamber, $\partial\mathcal{V}$ denotes the control volume boundaries and ζ_a represent the local volumetric acoustic losses. The first term in Eq. (11.3) corresponds the acoustic energy generated by the unsteady flame, the second term stands for the acoustic dissipation at the system boundaries and the third term corresponds to the contribution of all acoustic dissipation mechanisms occurring within the control volume.

If the source term $\mathcal{S}$ is larger than the dissipation terms, as expressed in Eq. (11.3), the amplitude of the acoustic oscillations grows until the sum of the nonlinear acoustic losses at the boundaries (Dowling and Morgans 2005) and those inside the combustor (Durox et al. 2009) exactly compensate the source term $\mathcal{S}$, leading to finite amplitude oscillations, the so-called limit cycle oscillations. Complex phenomena such as mode switching (Noiray et al. 2008; Moeck 2010; Boudy et al. 2011) or hysteresis (Moeck 2010; Prieur et al. 2016) are not considered in this work.

On the other hand, if the source term $\mathcal{S}$ is smaller than the sum of all linear dissipation terms, the corresponding thermoacoustic mode will be damped. Reaching these conditions is the main objective of all thermoacoustic instability control strategies. These methods are either based on a reduction of the source term $\mathcal{S}$ or an increase of the acoustic losses terms (Dowling and Morgans 2005).

The aim of this chapter is to predict the thermoacoustic stability of various configurations of the NoiseDyn burner using the ATM/DATM formalism and the FTF/FDF formalism. First, experiments are performed in the absence of forcing, for reactive operating conditions and for six different configurations. All the unstable thermoacoustic modes are then fully characterized. Then, two acoustic network models based on either the ATM/DATM formalism or the FTF/FDF formalism are designed to reproduce the acoustic behavior of all six configurations. Finally, the thermoacoustic stability preditions according to these two network models are compared against measurements. The frequencies and limit cycle amplitudes of the unstable thermoacoustic modes according to the acoustic network models are also compared with measurements.

11.2 Thermoacoustic stability of the NoiseDyn burner

First, the thermoacoustic stability of six distinct geometrical configurations of the NoiseDyn burner, denoted by $\mathbf{A}^2$, $\mathbf{B}^2$, $\mathbf{C}^2$, $\mathbf{D}^2$, $\mathbf{E}^2$ and $\mathbf{F}^2$, is investigated with experiments performed in the absence of acoustic forcing and for reactive operating conditions. The frequencies and oscillation amplitudes of the unstable modes at limit cycle are then extracted for all unstable configurations.

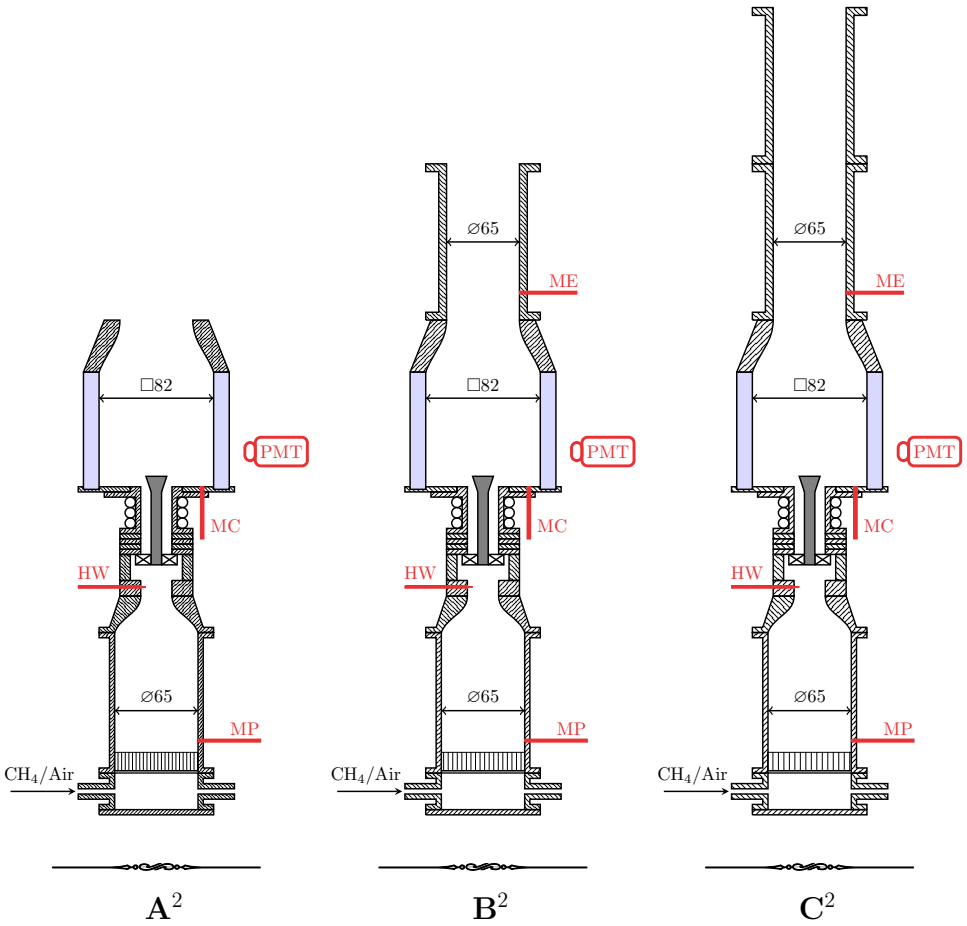

Figure 11.2: *Sketches depicting configurations* $\mathbf{A}^2$ *(Left),* $\mathbf{B}^2$ *(Center) and* $\mathbf{C}^2$ *(Right) of the NoiseDyn burner. Configurations* $\mathbf{D}^2$*,* $\mathbf{E}^2$ *and* $\mathbf{F}^2$ *are respectively obtained from configurations* $\mathbf{A}^2$*,* $\mathbf{B}^2$ *and* $\mathbf{C}^2$ *by adding a perforated plate at the top of the exhaust tubes. The thermoacoustic stability of these six configurations is investigated when a flame is stabilized inside the combustion chamber and in the absence of external forcing. Microphones MP, MC and ME are used to measure the acoustic pressure at various axial locations. A hot wire probe HW is used to measure the acoustic velocity. A photomultiplier PMT with an OH* filter is used to measure the flame heat release rate.*

All six configurations of the NoiseDyn burner investigated in this chapter are bounded by a rigid plate at the upstream boundary and include a swirling vane $\mathcal{S}$ that generates a flow of Swirl number $S = 0.8$. Three exhaust tubes of various lengths are investigated, all of which may or may not be topped by a perforated plate featuring a square pattern of 12 holes of radius 2.5 mm with an inter-hole space $d = 20$ mm, as represented in Fig. 5.8. More information about these configurations can be found in Chapter 5. Configurations $\mathbf{A}^2$,

$\mathbf{B}^2$ and $\mathbf{C}^2$ and their associated diagnostics are represented in Fig. 11.2. Configurations $\mathbf{D}^2$, $\mathbf{E}^2$ and $\mathbf{F}^2$ are obtained from configurations $\mathbf{A}^2$, $\mathbf{B}^2$ and $\mathbf{C}^2$ by adding the perforated plate at the top of the exhaust tubes.

Three polarized microphones denoted by MP, MC and ME are used to measure the acoustic pressure at the bottom of the plenum, at the bottom of the combustion chamber and at the entrance of the exhaust tube respectively. The acoustic velocity is measured inside the injector using a hot wire probe HW. The heat release rate is measured using a photomultiplier PMT mounted with an OH* filter recording the light originating from the entire flame region. An additional microphone MHW placed in front of the hot wire probe HW is used for configurations $\mathbf{D}^2$, $\mathbf{E}^2$ and $\mathbf{F}^2$. More information about these various diagnostics may be found in Chapter 6.

A perfectly premixed methane/air flame of equivalence ratio $\phi = 0.82$ and thermal power $P = 5.5$ kW is then stabilized inside the combustion chamber. When the experimental setup is thermalized, the microphones, hot wire probe and photomultiplier signals are recorded at a sampling frequency $f_s = 8192$ Hz for configurations $\mathbf{A}^2$, $\mathbf{B}^2$ and $\mathbf{C}^2$ and $f_s = 20000$ Hz for configurations $\mathbf{D}^2$, $\mathbf{E}^2$ and $\mathbf{F}^2$ during at least four seconds. The hot wire probe signals are then plotted as functions of time, as represented in Fig. 11.3-(Top left) for configurations $\mathbf{A}^2$, $\mathbf{B}^2$ and $\mathbf{C}^2$ and Fig. 11.3-(Top right) for configurations $\mathbf{D}^2$, $\mathbf{E}^2$ and $\mathbf{F}^2$.

From Fig. 11.3-(Top), it is obvious that configurations $\mathbf{B}^2$ and $\mathbf{C}^2$ are unstable whereas configuration $\mathbf{A}^2$ is stable. It is worth pointing out that configuration $\mathbf{B}^2$ is marginally unstable since oscillations appear and disappear intermittently and the system does not reach a well defined limit cycle with a constant oscillation amplitude. Nevertheless, this configuration is also considered to be unstable in the present section.

On the other hand, the time series corresponding to configurations $\mathbf{D}^2$, $\mathbf{E}^2$ and $\mathbf{F}^2$ are harder to interpret even though a mild instability with a small oscillation amplitude seems to be detected for all three configurations. These acoustic states may be due to the additional damping generated by the perforated plate added at the top of the exhaust tubes for configurations $\mathbf{D}^2$, $\mathbf{E}^2$ and $\mathbf{F}^2$.

The Power Spectral Density (PSD) of the hot wire signals are then computed using the Welch's averaged, modified periodogram method with 32 Blackman-Harris windows. The PSD is scaled by the equivalent noise bandwidth of the window, thus leading to an estimate of the power at each frequency. The Root-Mean Square (RMS) amplitudes of the relative acoustic velocity oscillations at the hot wire location are then obtained by dividing the square root of the moduli of the PSD of the hot wire signals by the corresponding average

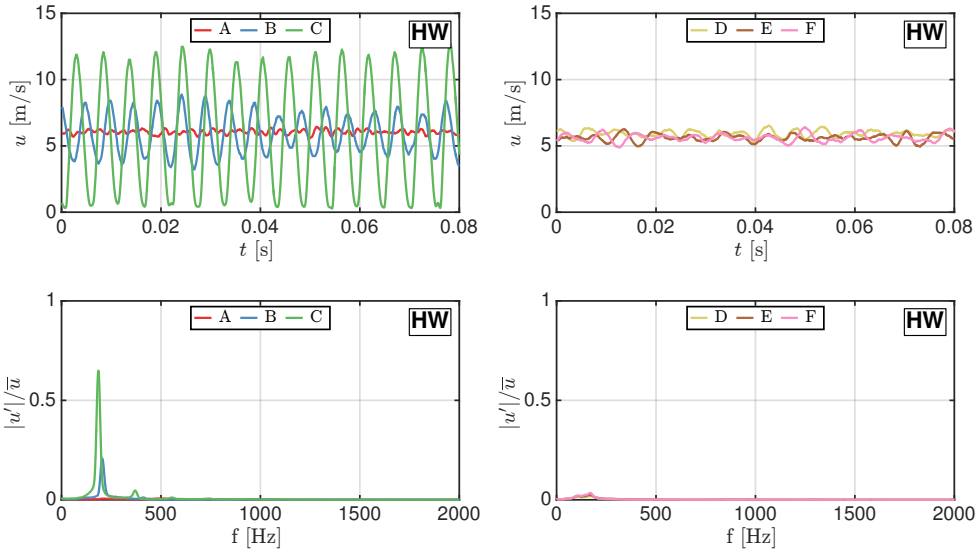

Figure 11.3: *Flow velocity inside the injector for reactive operating conditions and in the absence of acoustic forcing measured with the hot wire probe HW and plotted as a function of time (Top). Associated RMS amplitude of the relative acoustic velocity oscillations at the hot wire location (Bottom). Results for configurations* $\mathbf{A}^2$ *(Red),* $\mathbf{B}^2$ *(Blue) and* $\mathbf{C}^2$ *(Green) are presented on the left while results for configurations* $\mathbf{D}^2$ *(Yellow),* $\mathbf{E}^2$ *(Brown) and* $\mathbf{F}^2$ *(Pink) are presented on the right.*

velocities at the hot wire location. The corresponding plots are represented in Fig. 11.3-(Bottom). The frequencies of the unstable thermoacoustic modes and their associated limit cycle levels are then extracted from Fig. 11.3-(Bottom).

Figure 11.3-(Bottom) confirms that configurations $\mathbf{A}^2$, $\mathbf{D}^2$, $\mathbf{E}^2$ and $\mathbf{F}^2$ are stable or feature variations of the flow velocity at the hot wire location smaller than 3% of the average velocity. The source term in the acoustic energy balance given by Eq. (11.3) is either negative or slightly positive for these configurations.

On the other hand, configurations $\mathbf{B}^2$ and $\mathbf{C}^2$ feature thermoacoustic instabilities of frequency $f = 205.0$ Hz and $f = 185.2$ Hz respectively with limit cycle oscillations of amplitude $|u'|/\bar{u} = 0.21$ and $|u'|/\bar{u} = 0.65$ respectively. The frequency of the thermoacoustic instability is larger for configuration $\mathbf{B}^2$ compared to configuration $\mathbf{C}^2$ as the exhaust tube is shorter. Based on that observation, it is established that the thermoacoustic modes developing in the NoiseDyn burner are longitudinal. For these two configurations, the source term in Eq. (11.3) is positive and larger than the damping terms: the amplitude of the combustion instabilities increase until the nonlinear acoustic losses exactly compensate the source term for the limit cycle oscillations with the amplitudes and frequencies reported here. Since configuration

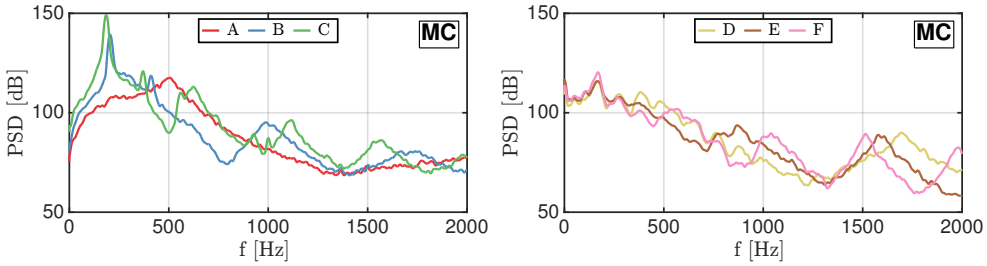

Figure 11.4: *Power Spectral Density (PSD) of the acoustic pressure at the bottom of the combustion chamber measured with microphone MC as a function of frequency for reactive operating conditions and in the absence of acoustic forcing. Results for configurations* $\mathbf{A}^2$ *(Red),* $\mathbf{B}^2$ *(Blue) and* $\mathbf{C}^2$ *(Green) are presented on the left while results for configurations* $\mathbf{D}^2$ *(Yellow),* $\mathbf{E}^2$ *(Brown) and* $\mathbf{F}^2$ *(Pink) are presented on the right.*

$\mathbf{B}^2$ is intermittently unstable, the validity of this analysis is limited in that case.

It is also worth looking at the Power Spectral Density of the acoustic pressure at the bottom of the combustion chamber measured with microphone MC for all six configurations. Once again, the PSD is computed using Welch's modified periodogram method with 32 Blackman-Harris windows. The results are presented in Fig. 11.4-(Left) for configurations $\mathbf{A}^2$, $\mathbf{B}^2$ and $\mathbf{C}^2$ and Fig. 11.4-(Right) for configurations $\mathbf{D}^2$, $\mathbf{E}^2$ and $\mathbf{F}^2$.

Figure 11.4 further demonstrates that configurations $\mathbf{B}^2$ and $\mathbf{C}^2$ are the only unstable or intermittently unstable configurations out of the six cases explored. The frequencies of the instabilities obtained from Fig. 11.4 are consistent with the results obtained using the PSD of the hot wire probe signals in Fig. 11.3. The Sound Pressure Level (SPL) reaches 149.1 dB inside the combustion chamber for the unstable mode of frequency $f = 185.2$ Hz appearing in configuration $\mathbf{C}^2$ whereas it only reaches 139.2 dB for the intermittently unstable mode of frequency $f = 205.0$ Hz appearing in configuration $\mathbf{B}^2$. The difference between the Sound Pressure Level of these two thermoacoustic modes and the surrounding noise level is between 20 dB and 40 dB which implies that the acoustic pressure signals are almost harmonic.

The next step is to reconstruct the structure of the unstable thermoacoustic modes. First, the time series corresponding to all acoustic pressure signals are plotted as functions of time for all six configurations, as represented in Fig. 11.5. The corresponding PSD of the acoustic pressure signals are represented in Fig. 11.6 using the procedure described earlier.

Once again, the results presented in Figs. 11.5 and 11.6 clearly demonstrate

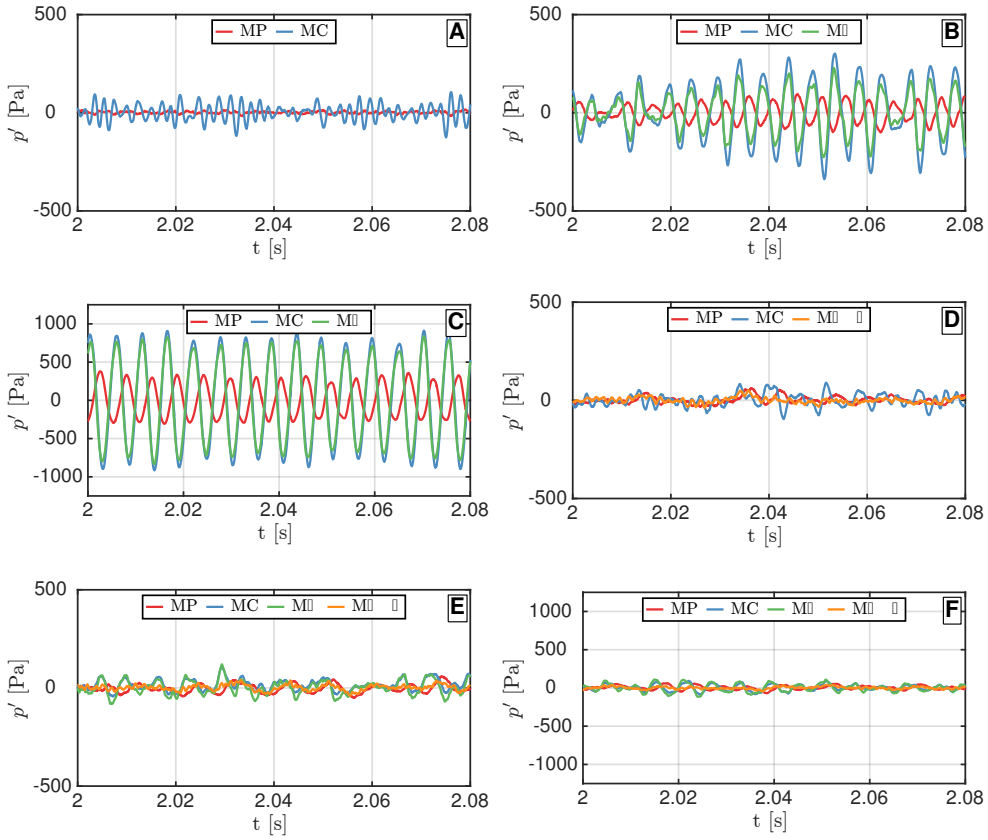

Figure 11.5: *Acoustic pressure measured with microphones MP (Red), MC (Blue), ME (Green) and MHW (Orange) as a function of time for reactive operating conditions and in the absence of acoustic forcing. Results for configurations* $\mathbf{A}^2$ *(Top left),* $\mathbf{B}^2$ *(Top right),* $\mathbf{C}^2$ *(Center left),* $\mathbf{D}^2$ *(Center right),* $\mathbf{E}^2$ *(Bottom left) and* $\mathbf{F}^2$ *(Bottom right).*

that configurations $\mathbf{A}^2$, $\mathbf{D}^2$, $\mathbf{E}^2$ and $\mathbf{F}^2$ are thermoacoustically stable. On the other hand, the acoustic pressure signals corresponding to configurations $\mathbf{B}^2$ and $\mathbf{C}^2$ experience large amplitude harmonic oscillations inside the setup.

The acoustic pressure at the bottom of the combustion chamber, measured with microphone MC, and at the entrance of the exhaust tube, measured with microphone ME, are in phase for configurations $\mathbf{B}^2$ and $\mathbf{C}^2$ in Fig. 11.5. On the other hand, the acoustic pressure at the bottom of the plenum, measured with microphone MP, is nearly in phase opposition with respect to the two abovementioned signals in Fig. 11.5. This observation advocates for the presence of a pressure node inside the injector.

Figures 11.6-(Top right) and 11.6-(Center left) establish the presence of higher

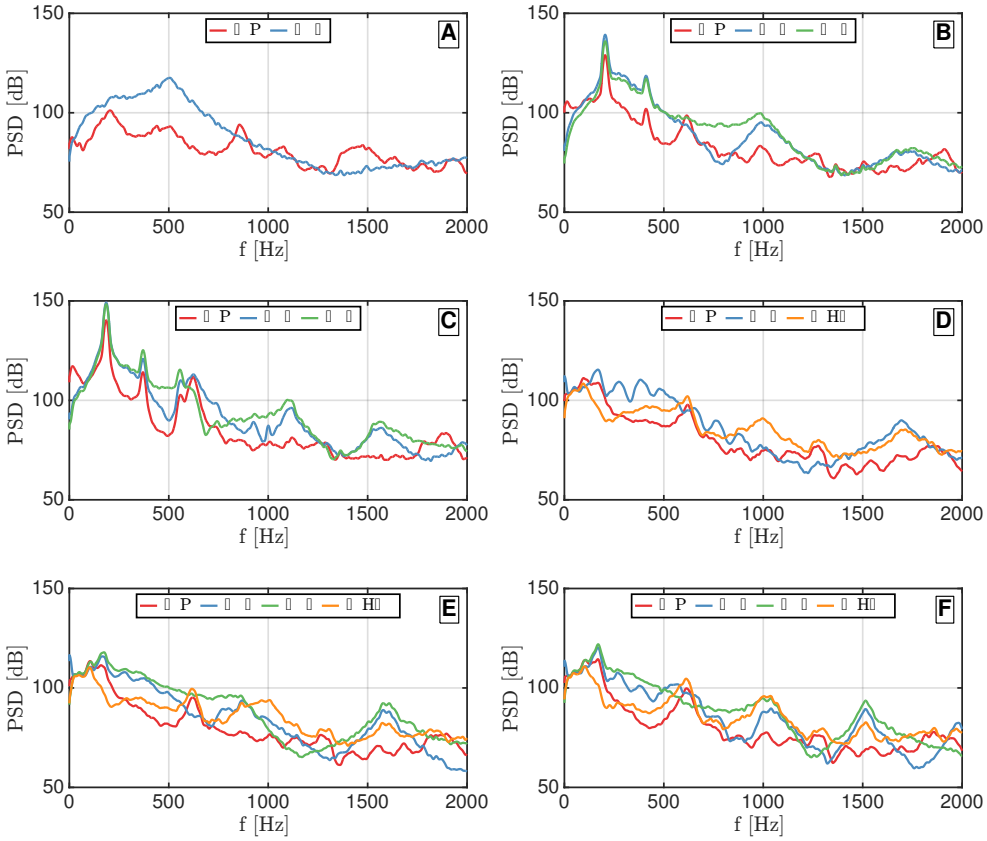

Figure 11.6: *Power Spectral Density (PSD) of the acoustic pressure measured by microphones MP (Red), MC (Blue), ME (Green) and MHW (Orange) as a function of the frequency for reactive operating conditions and in the absence of acoustic forcing. Results for configurations* $\mathbf{A}^2$ *(Top left),* $\mathbf{B}^2$ *(Top right),* $\mathbf{C}^2$ *(Center left),* $\mathbf{D}^2$ *(Center right),* $\mathbf{E}^2$ *(Bottom left) and* $\mathbf{F}^2$ *(Bottom right).*

order harmonics in the microphone signals corresponding to the unstable or intermittently unstable configurations. Part of the acoustic energy at the instability frequency is transferred to higher order harmonics through nonlinear processes.

The structure of the unstable thermoacoustic modes is now established based on the acoustic pressure measurements presented in Figs. 11.5 and 11.6. Figures 11.7-(Left) and 11.7-(Right) correspond to such reconstructions for configurations $\mathbf{B}^2$ and $\mathbf{C}^2$ respectively. The x-axis in these figures corresponds to the axial coordinate in the flow direction with $x = 0$ defined as the location of the combustion chamber backplate. Negative coordinates $x < 0$ correspond to the locations of the plenum and injector while positive coordinates $x > 0$ correspond to the locations of the combustion chamber and exhaust tube.

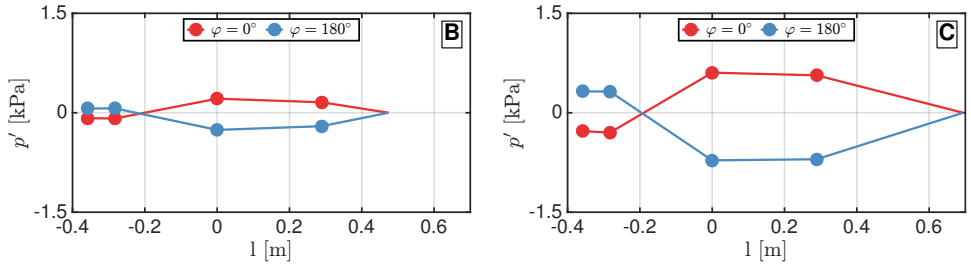

Figure 11.7: *Structure of the thermoacoustic modes associated with configurations* $\mathbf{B}^2$ *(Left) and* $\mathbf{C}^2$ *(Right). The acoustic pressure field is plotted as a function of the axial coordinate* x*, where* $x = 0$ *corresponds to the combustion chamber backplate location. Results are plotted when the acoustic pressure inside the combustion chamber is maximum (Red) and minimum (Blue). Measurements are represented as filled circles.*

The red curve represents the acoustic pressure measured by all microphones when the acoustic pressure inside the combustion chamber is maximum. The corresponding phase is arbitrarily defined as $\varphi = 0°$. The blue curve then represents the acoustic pressure at $\varphi = 180°$, when the acoustic pressure inside the combustion chamber is minimum.

Figure 11.7 demonstrates that the structure of the thermoacoustic modes developing inside configurations $\mathbf{B}^2$ and $\mathbf{C}^2$ are the same: the acoustic pressure inside the plenum is relatively low, followed by a pressure node inside the injector and then by a large acoustic pressure at the flame location. The acoustic pressure then drops and reaches zero near the exhaust tube exit. This structure corresponds to a longitudinal acoustic mode and it is reminiscent of a 3/4 wave mode for a single cavity. The amplitude of the acoustic pressure oscillations is much larger for configuration $\mathbf{C}^2$ compared to configuration $\mathbf{B}^2$, as shown in Fig. 11.7. This is once again consistent with the results presented in Figs. 11.5 and 11.6.

The source term $\mathcal{S}$ defined in Eq. (11.2) is now computed for all six configurations of the NoiseDyn burner (Tran et al. 2009a). $\mathcal{S}$ is expected to be largely positive for the unstable and intermittently unstable configurations - where it is balanced by large nonlinear acoustic losses - and slightly positive for the stable configurations. Assuming that the flame is compact, Eq. (11.2) is simplified and discretized in time:

$$\mathcal{S} = \frac{\gamma - 1}{\bar{\rho}\bar{c}^2} \frac{1}{\tau_\omega} \sum_{t=0}^{\tau_\omega} p' \dot{Q}' \Delta t \tag{11.4}$$

where p' is the acoustic pressure at the flame location, measured with microphone MC, and $\dot{Q}'$ is the flame heat release rate fluctuation, given by the

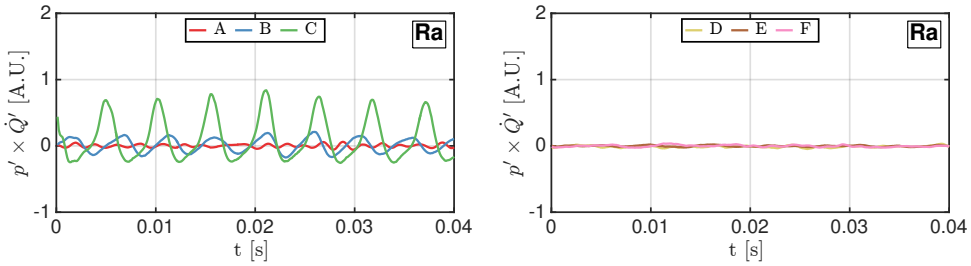

Figure 11.8: *Product of the microphone MC signal and the photomultiplier signal as a function of time for reactive operating conditions and in the absence of acoustic forcing. Results for configurations* $\mathbf{A}^2$ *(Red),* $\mathbf{B}^2$ *(Blue) and* $\mathbf{C}^2$ *(Green) are presented on the left while results for configurations* $\mathbf{D}^2$ *(Yellow),* $\mathbf{E}^2$ *(Brown) and* $\mathbf{F}^2$ *(Pink) are presented on the right.*

photomultiplier mounted with an OH* filter. In this expression, Δt is the inverse of the sampling frequency.

Figure 11.8 represents the product of the acoustic pressure p' at the flame location and the flame heat release rate fluctuation $\dot{Q}'$ as a function of time for configurations $\mathbf{A}^2$, $\mathbf{B}^2$ and $\mathbf{C}^2$ on the left and $\mathbf{D}^2$, $\mathbf{E}^2$ and $\mathbf{F}^2$ on the right. The integrals of the curves shown in Fig. 11.8 are directly related to $\mathcal{S}$. This source term is then computed for each configuration by extracting the oscillation period τ_ω from the maximum value of the PSD represented in Fig. 11.6 and using Eq. (11.4). The source term $\mathcal{S}_c$ obtained for configuration $\mathbf{C}^2$ is used as a reference and all other source terms are divided by $\mathcal{S}_c$. The corresponding results are summarized in Table 11.1.

Based on the results presented in Table 11.1, a few interesting facts can be established. First, the source terms for all six configurations are positive: the phase lag between the acoustic pressure at the flame location and the flame heat release rate fluctuation is always comprised between $\pm 90°$ and a positive energy transfer from the flame to the acoustic flow field is present for all six configurations. This implies that the linear acoustic losses are large enough to avoid the growth of an unstable mode for configurations $\mathbf{A}^2$, $\mathbf{D}^2$, $\mathbf{E}^2$ and $\mathbf{F}^2$ but not for configurations $\mathbf{B}^2$ and $\mathbf{C}^2$.

Moreover, the source term corresponding to configuration $\mathbf{C}^2$ is significantly larger than all other source terms. This accounts for the large limit cycle oscillation amplitude of the unstable mode observed for this configuration. On the other hand, the source terms for configurations $\mathbf{A}^2$ and $\mathbf{F}^2$ are small: these configurations are thus thermoacoustically stable. In between, the source terms corresponding to configurations $\mathbf{B}^2$, $\mathbf{D}^2$ and $\mathbf{F}^2$ are similar even though configuration $\mathbf{B}^2$ is intermittently unstable while configurations $\mathbf{D}^2$ and $\mathbf{E}^2$ are

Table 11.1: *Source terms appearing in the acoustic energy balance for six configurations of the NoiseDyn burner operated for reactive conditions and in the absence of acoustic forcing. Results are normalized by the source term $\mathcal{S}_c$ obtained for configuration* $\mathbf{C}^2$.

Config.	$\mathbf{A}^2$	$\mathbf{B}^2$	$\mathbf{C}^2$	$\mathbf{D}^2$	$\mathbf{E}^2$	$\mathbf{F}^2$
$\mathcal{S}/\mathcal{S}_c$	0.0058	0.062	1	0.084	0.057	0.012

thermoacoustically stable. As mentioned previously, this is likely due to the addition of the perforated plate at the top of the exhaust tubes that generates additional acoustic losses for configurations $\mathbf{D}^2$ and $\mathbf{E}^2$.

11.3 Thermoacoustic stability predictions using acoustic network models

In order to predict the thermoacoustic stability of the NoiseDyn burner, the experimental setup is modeled using the acoustic two-port matrices network formalism (Abom 1992; Paschereit and Polifke 1998; Polifke et al. 2001; Dowling and Stow 2003; Poinsot and Veynante 2005; Fischer et al. 2006) which was described extensively in Chapters 7 and 8. The harmonic convention retained is $e^{+i\omega t}$ and all pressure signals are divided by their respective characteristic impedance $z = \bar{\rho}\bar{c}$.

Two distinct acoustic network models are used to represent the NoiseDyn burner operated for reactive conditions. The first network model, called the Reactive Flame Describing Function ($\mathrm{R_{FDF}}$) model, is an extension of the network model presented in Sec. 10.3. In this model, the nonlinear response of the flame to incoming acoustic waves is taken into account using a Flame Describing Function (FDF). The FDF is measured using an optical technique based on measurements of both the OH* chemiluminescence emitted by the flame and the velocity signal inside the injector, as explained in Chapter 9. All other elements of the network model are represented using analytical expressions, as described in Chapter 7. A total of 13 acoustic elements are used to describe the propagation and damping of acoustic waves inside the NoiseDyn burner in the $\mathrm{R_{FDF}}$ model.

For instance, configuration $\mathbf{B}^2$ and its associated acoustic equivalent according to the $\mathrm{R_{FDF}}$ model are represented in Fig. 11.9. The acoustic equivalents corresponding to configurations $\mathbf{A}^2$ and $\mathbf{C}^2$ are obtained by changing the length of the exhaust tubes to $l_{1011} = 0$ mm and $l_{1011} = 440$ mm respectively. Configurations $\mathbf{D}^2$, $\mathbf{E}^2$ and $\mathbf{F}^2$ are obtained from configurations $\mathbf{A}^2$, $\mathbf{B}^2$ and $\mathbf{C}^2$ respectively by changing the downstream acoustic impedance.

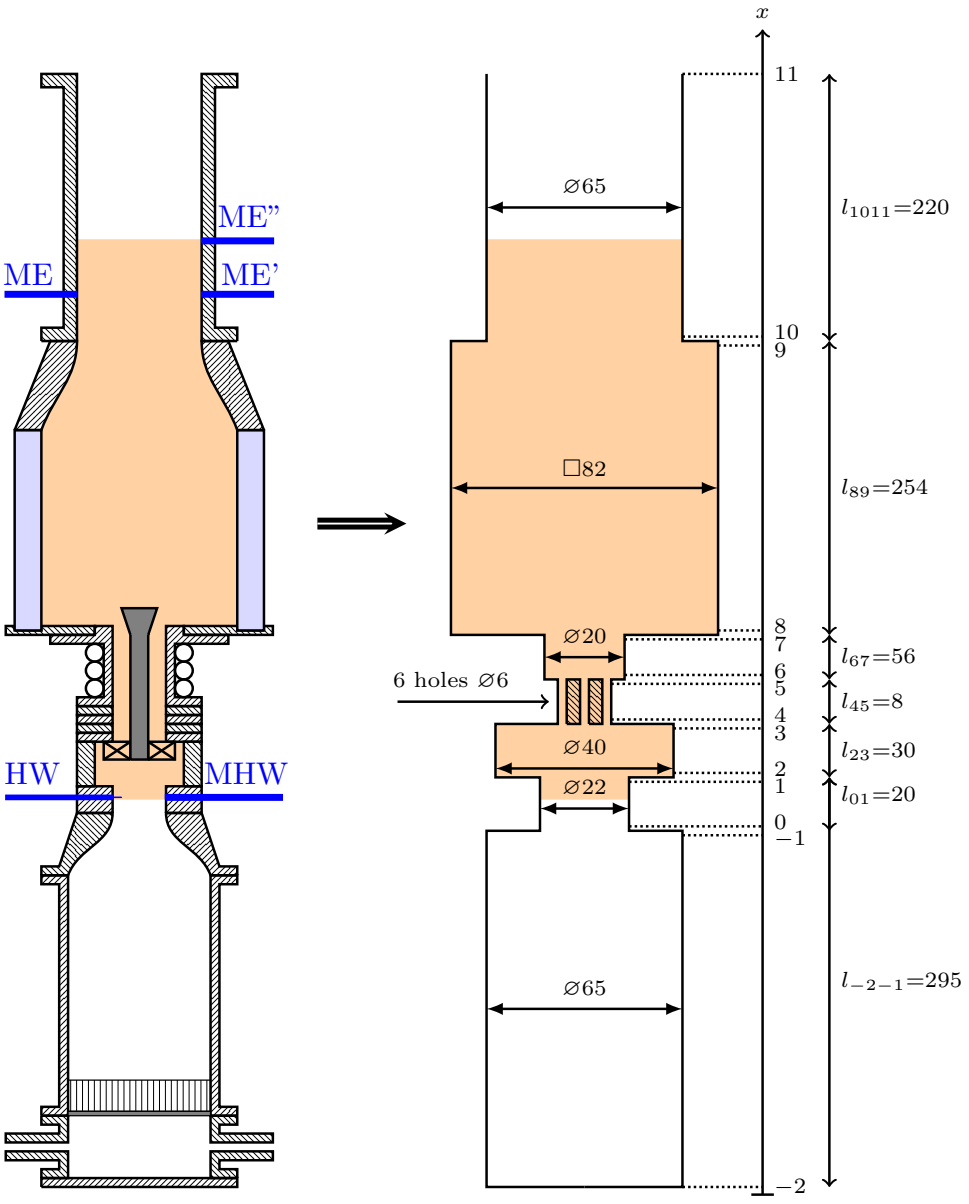

Figure 11.9: *Sketch depicting configuration* $\mathbf{B}^2$ *of the NoiseDyn burner (Left) and its associated acoustic equivalent according to the* $\mathrm{R}_{\mathrm{FDF}}$ *model (Right). The area shaded in orange corresponds to the acoustic elements that are replaced by the measured acoustic transfer matrix in the* R_{TM} *model. All dimensions are expressed in millimeters.*

The R_{FDF} model is then assembled using the appropriate analytical DATM expressions between each consecutive section of the acoustic equivalent:

- **Section (-2) → section (-1):** A DATM corresponding to a straight duct in a uniform non-reactive low-Mach flow, modeled with Eq. (7.59).
- **Section (-1) → section (0):** A DATM corresponding to a compact area change in a non-reactive low-Mach flow, modeled with Eq. (7.78).
- **Section (0) → section (10):** The same DATM as those presented in Sec. 10.3.
- **Section (10) → section (11):** A DATM corresponding to a straight duct in a uniform non-reactive low-Mach flow, modeled with Eq. (7.59). The length of this element depends on the explored configuration.

The only source of acoustic damping in the R_{FDF} model is located inside the swirling vane and is modeled using a nonlinear extension of Howe's model for all six configurations, as described in Sec. 9.4.2.

Three different gas temperatures are employed in the R_{FDF} model: for all elements between section **(-2)** and section **(7)**, the gas temperature is set to the ambient temperature $\overline{T}_u = 293$ K. Between section **(8)** and section **(9)**, corresponding to the combustion chamber, the temperature is set to 1600 K, around 80% of the adiabatic flame temperature, in order to account for the heat losses. Finally, between section **(10)** and section **(11)**, the temperature is set to the average gas temperature inside the exhaust tube, measured with a thermocouple for each configuration and summarized in Table 11.2.

The acoustic element located between section **(i)** and section **(j)** is mathematically represented by a DATM denoted by $\widetilde{M}_{ij}$. The total DATM representing the whole burner between section **(-2)** and section **(11)** according to the R_{FDF} network model is then expressed as:

$$\widetilde{M} = \widetilde{M}_{1011}\ \widetilde{M}_{910}\ \widetilde{M}_{89}\ \widetilde{M}_{78}\ \widetilde{M}_{67}\ \widetilde{M}_{36}\ \widetilde{M}_{23}\ \widetilde{M}_{12}\ \widetilde{M}_{01}\ \widetilde{M}_{-10}\ \widetilde{M}_{-2-1} \quad (11.5)$$

The second acoustic network model, called the Reactive Transfer Matrix (R_{TM}) model, is based on the Dimensionless Acoustic Transfer Matrices (DATM) measurements presented in Sec. 10.5 that were obtained from the microphones and hot wire probe signals. This DATM corresponds to the acoustic response of the elements located between the hot wire probe HW inside the injector and the microphone ME" inside the exhaust tube, such as represented in orange in Fig. 11.9. The analytical expressions corresponding to these acoustic

Table 11.2: *Average gas temperature in the exhaust tube for configurations* $\mathbf{A}^2$, $\mathbf{B}^2$, $\mathbf{C}^2$, $\mathbf{D}^2$, $\mathbf{E}^2$ *and* $\mathbf{F}^2$ *of the NoiseDyn burner.*

Config.	Temperature
$\mathbf{A}^2$ & $\mathbf{D}^2$	$\varnothing$
$\mathbf{B}^2$ & $\mathbf{E}^2$	1062 K
$\mathbf{C}^2$ & $\mathbf{F}^2$	986 K

elements in the R_{FDF} model are then replaced by the measured DATM and the acoustic elements located before the hot wire probe or after microphone ME" are modeled using the same DATM models as for the R_{FDF} model. It should be noted that this approach only works for configurations that feature at least one exhaust tube since the DATM is reconstructed using the signals of microphones ME, ME' and ME" located on the first exhaust tube. As a consequence, this method cannot be employed for configurations $\mathbf{A}^2$ and $\mathbf{D}^2$ in which the exhaust gases are directly released to the atmosphere after the combustion chamber.

The total DATM representing the whole burner between section **(-2)** and section **(11)** according to the R_{TM} network model is then expressed as:

$$\widetilde{M} = \widetilde{M}_{1011}\ \widetilde{M}_{xp}\ \widetilde{M}_{01}\ \widetilde{M}_{-10}\ \widetilde{M}_{-2-1} \tag{11.6}$$

where $\widetilde{M}_{xp}$ is the measured DATM and the length of the elements between section **(0)** and section **(1)** and between section **(10)** and section **(11)** are modified in order to account for wave propagation up to the hot wire probe and after microphone ME" respectively. The acoustic elements located before the hot wire probe are at the ambient temperature $\overline{T}_u = 293$ K while the gas temperature in the elements located after microphone ME" are set to the average gas temperature inside the exhaust tubes, as summarized in Table 11.2.

For both acoustic network models, two acoustic boundary conditions are needed in order to obtain a closed set of equations. The upstream acoustic boundary condition, located in section **(-2)** in Fig. 11.9, is described with the impedance of a rigid plate $Z^s_{-2} = -\infty$. The second acoustic boundary condition, located in section **(11)** in Fig. 11.9, is described with an open end acoustic boundary condition modeled using a flanged Levine-Schwinger impedance for configurations $\mathbf{A}^2$, $\mathbf{B}^2$ and $\mathbf{C}^2$, as detailed in Sec. 7.3.3. This acoustic impedance model accounts for acoustic radiation which is a source of acoustic damping. For configurations $\mathbf{D}^2$, $\mathbf{E}^2$ and $\mathbf{F}^2$, an anechoic acoustic boundary condition is used in section **(11)**. This is justified by the measurements of the acoustic impedance of the perforated plate placed at

the top of the exhaust tube for configurations $\mathbf{D}^2$, $\mathbf{E}^2$ and $\mathbf{F}^2$, as detailed in Sec. 6.7.3.

For both the R_{FDF} and R_{TM} network models, the thermoacoustic stability of each configuration of the NoiseDyn burner is obtained using the following procedure. First, the acoustic pressure p'_{-2} and acoustic velocity u'_{-2} in section **(-2)** are related to the acoustic pressure p'_{11} and acoustic velocity u'_{11} in section **(11)** using the DATM representing the whole burner and given by Eq. (11.5) for the R_{FDF} model and by Eq. (11.6) for the R_{TM} model:

$$\begin{pmatrix} p'_{11} \\ u'_{11} \end{pmatrix} = \begin{pmatrix} \widetilde{M}(1,1) & \widetilde{M}(1,2) \\ \widetilde{M}(2,1) & \widetilde{M}(2,2) \end{pmatrix} \times \begin{pmatrix} p'_{-2} \\ u'_{-2} \end{pmatrix} \tag{11.7}$$

Using Eq. (11.7) along with the definition of the specific acoustic impedances in section **(-2)** Z^s_{-2} and section **(11)** Z^s_{11}, the following characteristic equation is obtained:

$$\widetilde{M}(1,1)Z^s_{-2} + \widetilde{M}(1,2) - Z^s_{-2}Z^s_{11}\widetilde{M}(2,1) - \widetilde{M}(2,2)Z^s_{11} = 0 \tag{11.8}$$

Equation (11.8) fully characterizes the thermoacoustic stability of the NoiseDyn burner. If Eq. (11.8) has no real solution, then the investigated configuration is thermoacoustically stable. On the other hand, if Eq. (11.8) has at least one root for a given frequency f and a given forcing level $|u'|/\bar{u}$, then the system features a thermoacoustically unstable mode of frequency f and limit cycle oscillation amplitude $|u'|/\bar{u}$.

In practice, it is almost impossible to solve Eq. (11.8) symbolically if there are more than a few acoustic elements, especially if the acoustic response of the flame is described using a nonlinear model. Another strategy is to solve Eq. (11.8) numerically with a predetermined accuracy. In this study, the frequencies of the thermoacoustic modes are determined with a numerical accuracy of 0.1 Hz while the corresponding relative amplitudes of the acoustic velocity fluctuations at the hot wire location $|u'|/\bar{u}$ are determined with a numerical accuracy of 0.01. The left-hand side of Eq. (11.8) is then computed for frequencies comprised between 50 Hz and 500 Hz and for limit cycle amplitudes comprised between 0 and 1. The FDF and DATM used in the R_{FDF} and R_{TM} network models are linearly interpolated and extrapolated in order to cover the full range of frequencies and relative amplitudes of the acoustic velocity fluctuations explored. For instance, the measurements and interpolations/extrapolations retained for the FDF gain and phase lag are represented in Fig. 11.10.

Figure 11.11 is a semi-log plot representing the inverse of the left-hand side of Eq. (11.8) as a function of the frequency and relative amplitude of the acoustic

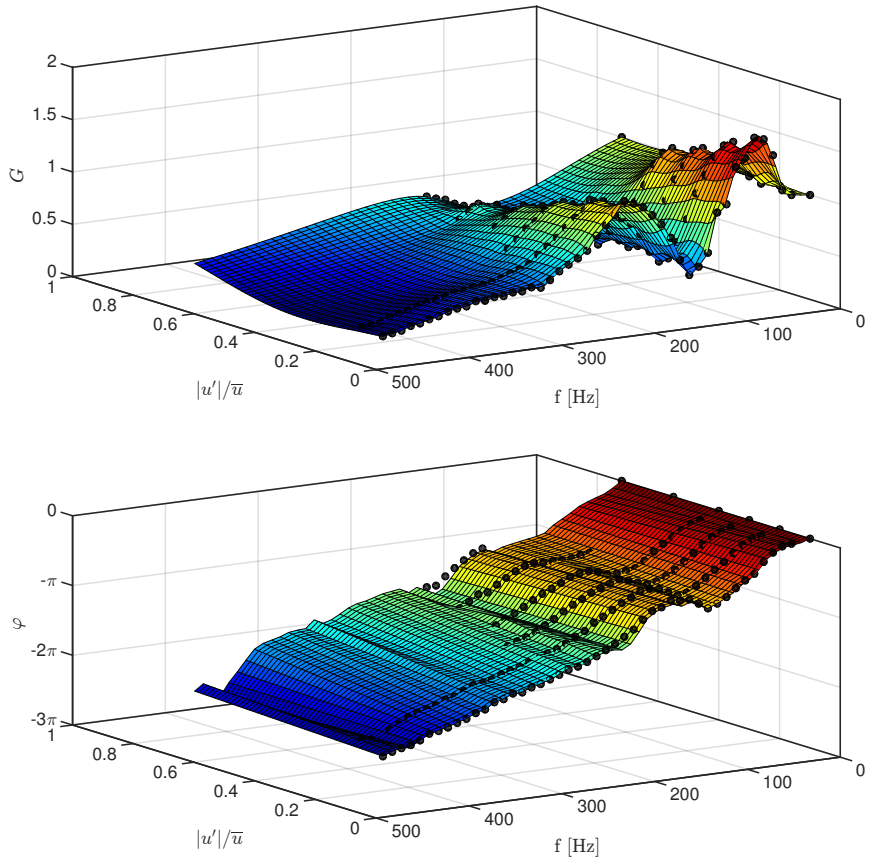

Figure 11.10: *FDF gain (Top) and phase lag (Bottom) as functions of the forcing frequency and relative amplitude of the acoustic velocity fluctuations at the hot wire location $|u'|/\overline{u}$. Measurements are represented as black spheres. The corresponding interpolated/extrapolated values are represented as smooth surfaces.*

velocity fluctuations at the hot wire location $|u'|/\overline{u}$. The results presented here are obtained using the R_{FDF} model representing configuration $\mathbf{C}^2$ of the NoiseDyn burner. The peaks correspond to the solutions of Eq. (11.8) and thus to the unstable thermoacoustic modes. Each thermoacoustic mode is then fully characterized by extracting the frequency and limit cycle amplitude from the associated peak. On the other hand, if no peak is observed, then the corresponding configuration is thermoacoustically stable.

Following this procedure, the thermoacoustic stability of the various configurations of the NoiseDyn burner investigated in Sec. 11.2 is predicted using both the R_{FDF} and R_{TM} acoustic network models. The results are summarized in Table 11.3. The predictions of the thermoacoustic stability of the NoiseDyn burner are the same for both acoustic network models. The results presented

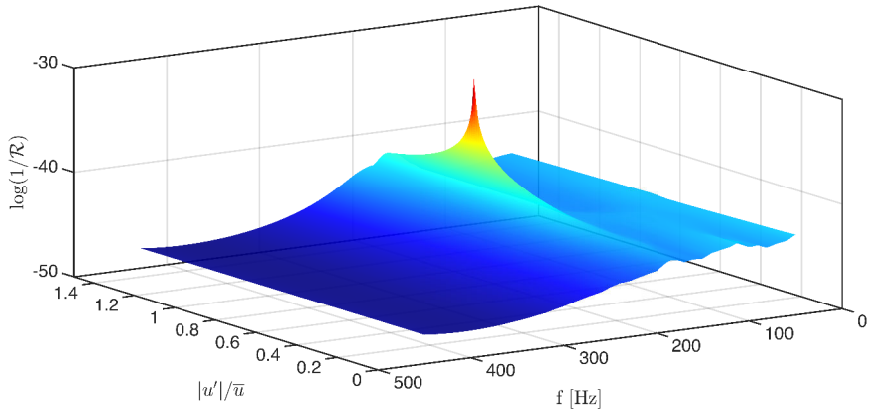

Figure 11.11: *Representation of the inverse of the left-hand side of Eq. (11.8) as a function of the frequency and relative amplitude of the acoustic velocity fluctuations at the hot wire location $|u'|/\bar{u}$ obtained using the* $\mathrm{R_{FDF}}$ *model for configuration* $\mathbf{C}^2$*. A peak indicates the presence of an unstable thermoacoustic mode.*

in Sec. 11.2 indicate that configurations $\mathbf{E}^2$ and $\mathbf{F}^2$ are stable, which is well retrieved by both network models. Configuration $\mathbf{A}^2$ and $\mathbf{D}^2$ are also stable, which is correctly predicted by the $\mathrm{R_{FDF}}$ model but not by the $\mathrm{R_{TM}}$ model that cannot be used in the absence of an exhaust tube, as explained before. Configuration $\mathbf{C}^2$ is also predicted to be thermoacoustically unstable by both acoustic network models, which is in conformity with experiments. On the other hand, configuration $\mathbf{B}^2$ is predicted to be stable by both network models even though it is intermittently unstable. In fact, predicting the onset of an intermittently unstable thermoacoustic mode using the conventional analysis employed here is challenging.

Table 11.3: *Thermoacoustic stability of six distinct configurations of the NoiseDyn burner obtained from experiments and predicted by the* $\mathrm{R_{FDF}}$ *and* $\mathrm{R_{TM}}$ *acoustic network models.*

Config.	Experiments	$\mathrm{R_{FDF}}$ model	$\mathrm{R_{TM}}$ model
$\mathbf{A}^2$	Stable	Stable	∅
$\mathbf{B}^2$	Intermittently unstable	Stable	Stable
$\mathbf{C}^2$	Unstable	Unstable	Unstable
$\mathbf{D}^2$	Stable	Stable	∅
$\mathbf{E}^2$	Stable	Stable	Stable
$\mathbf{F}^2$	Stable	Stable	Stable

Table 11.4: *Frequency and limit cycle oscillation amplitude associated with the unstable thermoacoustic mode appearing inside configuration* $\mathbf{C}^2$ *according to direct measurements and to the* R_{FDF} *and* R_{TM} *acoustic network models.*

Method	f [Hz]	$\lvert u'\rvert/\bar{u}$
Measurements	185.2	0.65
R_{FDF} model	182.6	0.98
R_{TM} model	180.0	0.54

Overall, the thermoacoustic stability of the NoiseDyn burner is well predicted by both acoustic network models. The predictions of the frequency and limit cycle amplitude of the unstable thermoacoustic mode developing inside configuration $\mathbf{C}^2$ is now investigated. Measurements are compared against predictions according to the R_{FDF} and R_{TM} acoustic network models in Table 11.4.

The frequency of the unstable thermoacoustic mode appearing in configuration $\mathbf{C}^2$ is well predicted by both acoustic network models, as shown in Table 11.4. However, the relative amplitude of the acoustic velocity fluctuations at the hot wire location $|u'|/\bar{u}$ is overpredicted by the R_{FDF} model. On the other hand, the limit cycle amplitude according to the R_{TM} model is in conformity with experiments.

This difference between the R_{FDF} and R_{TM} models is due to the fact that the acoustic losses inside the injector are naturally included in the R_{TM} model. In fact, these losses are contained in the measurements of the DATM representing the burner response between the hot wire probe HW and microphone ME". As a consequence, the limit cycle amplitude of the instability predicted by the R_{TM} model is in better agreement with the limit cycle amplitude obtained using direct measurements. On the other hand, the acoustic losses are entirely modeled in the R_{FDF} model. As mentioned in Chapter 10, these losses are underpredicted and thus, the limit cycle amplitude according to the R_{FDF} model is overpredicted.

11.4 Conclusion

The objective of this chapter was to compare the thermoacoustic stability predictions according to two acoustic network models with the experimental data gathered using the NoiseDyn burner.

Six configurations of the NoiseDyn burner, denoted by $\mathbf{A}^2$, $\mathbf{B}^2$, $\mathbf{C}^2$, $\mathbf{D}^2$, $\mathbf{E}^2$ and $\mathbf{F}^2$ and featuring various exhaust tube lengths and downstream acoustic bound-

ary conditions were first explored experimentally. Multiple microphones and a hot wire probe were placed at various axial locations and the corresponding signals were recorded during reactive operation. Based on these measurements, configurations $\mathbf{A}^2$, $\mathbf{D}^2$, $\mathbf{E}^2$ and $\mathbf{F}^2$ were shown to be thermoacoustically stable while configuration $\mathbf{C}^2$ was shown to be thermoacoustically unstable. Finally, configuration $\mathbf{B}^2$ was found to be intermittently unstable. The structures of the thermoacoustic modes appearing in configurations $\mathbf{B}^2$ and $\mathbf{C}^2$ as well as their frequencies and limit cycle amplitudes were also extracted from these experiments.

Two acoustic network models representing these configurations of the NoiseDyn burner were subsequently constructed. In the first model, denoted by R_{FDF}, the flame response to incoming acoustic waves was described using a Flame Describing Function (FDF) measured with an optical technique. All the other elements of the R_{FDF} acoustic network model were represented using various analytical expressions accounting for wave propagation and acoustic damping within the burner.

In the second acoustic network model, denoted by R_{TM}, the acoustic response of the NoiseDyn burner between the hot wire probe located inside the injector and microphone ME" located inside the exhaust tube was directly assessed using the acoustic transfer matrix measurements presented in Chapter 10. The acoustic elements located before the hot wire probe and after microphone ME" were still modeled using analytical expressions.

The thermoacoustic stability predictions according to both network models were then compared against measurements. Except for the intermittent instability occuring in configuration $\mathbf{B}^2$ which was not predicted by any of the network models, the thermoacoustic stability of the explored configurations of the NoiseDyn burner were well retrieved by both network models. The frequency of the instability occuring in configuration $\mathbf{C}^2$ was also well retrieved by both the R_{FDF} and R_{TM} models.

On the other hand, the limit cycle oscillation amplitude associated with the unstable thermoacoustic mode appearing in configuration $\mathbf{C}^2$ was well predicted by the R_{TM} model but not by the R_{FDF} model. This was attributed to the acoustic losses inside the injector that are not accurately predicted by the R_{FDF} model. In the R_{TM} model, these acoustic losses are included in the measured acoustic transfer matrix representing the burner response and as a consequence, the limit cycle oscillation amplitude is accurately predicted by this model.

Conclusion and perspectives

The acoustic response of a set of premixed flames submitted to harmonic sound waves was investigated in this work using experiments and various modeling strategies. The response of premixed laminar conical flames was first investigated in **Chapters 1 to 4**. These flames constitute an elementary case that can be used to validate theoretical models and numerical simulations and they are also found in many industrial and domestic heating appliances. The response of premixed confined turbulent swirling and non-swirling flames was then investigated in **Chapters 5 to 11**. These flames are used in a variety of high-power combustors such as gas turbines used for propulsion or power generation. These combustors are particularly prone to thermoacoustic instabilities.

The case of premixed laminar conical flames was examined first. A quick summary of the current state of knowledge related to the acoustic response of these flames was performed in **Chapter 1**. The notion of Flame Transfer Function (FTF) was introduced and it was shown that the FTF of premixed laminar conical flames can be split into two components: F_A, related to the velocity perturbation propagating in the fresh gases and F_B, related to the flame base motion. Three typical analytical models for F_A were introduced based on uniform, convective and incompressible convective velocity perturbation models. An additional model for F_B was also described based on previous works.

The acoustic response of premixed laminar conical flames was then measured with the setup presented in **Chapter 2**. Experiments were performed for methane/air and propane/air flames featuring the same aspect ratio $\overline{h}/R = 4$ and stabilized on burner outlets of decreasing radii, ranging from $R = 11$ mm to $R = 1.0$ mm. A total of twenty-two configurations featuring different fuels, bulk flow velocities, equivalence ratios and burner geometries were investigated.

The FTF predictions according to the analytical models presented in **Chapter 1** were then compared against measurements in **Chapter 3**. Overall, the best match was obtained using the incompressible convective velocity perturbation model. However, the predictions associated with this model worsened when the size of the injector was reduced. For small flames, the uniform ve-

locity perturbation model yielded better results for the FTF phase lag. It was also shown that the contribution of the flame base motion to the FTF of premixed laminar conical flames could be neglected for large flames stabilized over the injectors of radii $R = 11$ mm and $R = 7$ mm. On the other hand, this contribution had to be considered for smaller flames but the model retained was unable to reproduce the FTF measurements. It was thus concluded that an additional modeling effort was needed in order to predict the FTF of small premixed laminar conical flames.

It was then demonstrated in **Chapter 4** that premixed laminar conical flames submitted to harmonic sound waves experience heat release rate fluctuations due to flame volume oscillations and spatially-averaged volumetric heat release rate fluctuations. This last contribution was shown to be negligible for large flames, e.g. when the burner outlet radius is much larger than the flame thickness, but needs to be considered for small flames stabilized over the injectors of radii $R = 1.5$ mm and $R = 1.0$ mm.

It was also demonstrated that the reduced frequency $\omega_* = \omega R/(S_L \cos\overline{\alpha})$ is an adequate dimensionless parameter to scale the acoustic response of large premixed laminar conical flames of constant aspect ratio $\overline{h}/R$. For smaller flames, three additional dimensionless numbers were shown to control the shape of the FTF: the Lewis number Le, the dimensionless flame thickness δ_* and the dimensionless flame stand-off distance $\psi_* = \overline{\psi}/R$.

A new analytical model predicting the reduced frequency ω_*^0 at which the FTF gain of premixed laminar conical flames reaches its maximum value was also derived. This model was based on a bidimensional heat and mass transfer mechanism accounting for 1) the unsteady vertical heat losses between the flame base and the burner and 2) the lateral heat and mass transfers between adjacent flame elements. The reduced frequency ω_*^0 was shown to depend on the flame aspect ratio $\overline{h}/R$, the dimensionless flame thickness δ_* and the dimensionless flame stand-off distance ψ_*. The predictions of ω_*^0 associated with this new analytical model were shown to be in excellent agreement with experiments.

In the second part of this work, premixed confined turbulent flames were investigated using the NoiseDyn burner presented in **Chapter 5**. This modular burner was designed specifically to examine the acoustic response of such flames. Throughout this part, the cold and reactive operating conditions were prescribed and only the upstream elements, swirling vane and downstream elements of the NoiseDyn burner were modified. The associated diagnostics (including temperature, pressure drop, velocity, acoustic pressure and chemiluminescence measurements) were subsequently presented in **Chapter 6**. A thorough description of the acoustic impedance and acoustic reflection coefficient measurement techniques, including the Three Microphone Method, was

also included in this chapter.

The fundamental equations describing linear sound wave propagation in a low-Mach non-reactive flow were derived in **Chapter 7**. Various acoustic impedance models were also introduced in this chapter and the concept of Acoustic Transfer Matrix (ATM) was presented. Analytical models for the Acoustic Transfer Matrices corresponding to straight ducts in uniform and non-uniform temperature fields, compact and non-compact area changes and perforated plates traversed by high-Reynolds number flows were subsequently derived.

The same approach was applied to low-Mach reactive flows in **Chapter 8**. The analytical model for the Acoustic Transfer Matrix corresponding to a lean compact flame stabilized in a low-Mach flow within a straight duct was derived.

The acoustic response of premixed confined swirling and non-swirling flames submitted to harmonic sound waves generated from the upstream or downstream sides of the NoiseDyn burner was investigated in **Chapter 9** for a large set of forcing frequencies and forcing levels. Three describing functions were measured using the photomultiplier signal and various reference signals: the hot wire probe signal located inside the injector, the signal of the microphone located in front of the hot wire probe and the signal of another microphone located at the bottom of the combustion chamber. The forcing level was controlled at the hot wire location in all cases. The FTF phase lags of all describing functions were shown to be independent of the forcing level whereas the FTF gains were shown to depend on the forcing level for certain frequencies.

For downstream forcing experiments, it was shown that all describing functions could be retrieved from one another using a linear propagation model in which the acoustic losses inside the setup were neglected. On the other hand, for upstream forcing experiments, a more complex model accounting for the acoustic losses generated at the swirling vane due to the coupling between the acoustic flow field variables and the vortical structures was required in order to accurately relate the describing functions. This was attributed to the different acoustic pressure drops across the swirling vane for upstream and downstream forcing experiments due to different acoustic boundary conditions.

The Flame Describing Function (FDF) defined with respect to the hot wire probe signal was observed to be the same for upstream and downstream forcing experiments as long as the forcing frequency was lower than 220 Hz. For higher frequencies, the FDF phase lag plots still matched but not the FDF gain plots. Nevertheless, the FDF defined with respect to the acoustic velocity just before the flame was found to be identical for upstream and downstream forcing experiments over the entire frequency range. It was thus concluded that the

correct reference signal that should be used when defining a Flame Describing Function is the acoustic velocity at the top of the injector, just before the flame. It was also demonstrated that the describing functions based on acoustic pressure measurements depended on the upstream and downstream acoustic boundary conditions. It was thus concluded that these pressure signals should not be used as reference signals when defining a Flame Describing Function.

Next, the impact of the forcing level on the Dimensionless Acoustic Transfer Matrix (DATM) coefficients representing the acoustic response of a swirling and non-swirling injector was determined using cold flow and reactive flow experiments in **Chapter 10**. For cold flow conditions, the response of both injectors was found to be the same. The phases of the DATM coefficients were shown to be independent of the forcing level while the modulus of these coefficients was shown to be impacted by the forcing level in a certain frequency range. For reactive operating conditions, the response of the combustor was found to be different for the swirling and non-swirling injectors. The phases of the DATM coefficients were found to be independent of the forcing level but not the moduli of these coefficients.

Two acoustic network models representing the acoustic response of the Noise-Dyn burner for cold and reactive operating conditions were then assembled. For cold flow operating conditions, the network model was similar for both injectors whereas for reactive operating conditions, the swirling and non-swirling flames were found to have distinct acoustic responses and the network model predictions thus varied. Two sources of acoustic nonlinearities were accounted for in these acoustic network models: 1) the nonlinear acoustic damping generated at the swirling vane and 2) the nonlinear flame response which was considered through the use of a Flame Describing Function for reactive operating conditions only.

For cold flow operating conditions, the predicted DATM coefficients according to the acoustic network model was found to be in excellent agreement with the DATM measurements even though the effect of the forcing level was not correctly retrieved. For reactive operating conditions, the general trend of the DATM coefficients was still found to be correctly reproduced by the model but the overall accuracy of the predictions worsened. Once again, the effect of the forcing level was not entirely retrieved.

Both Flame Describing Functions associated with the swirling and non-swirling flames were measured using an optical technique and reconstructed using the DATM measurements along with the reactive acoustic network model. The overall evolution of the FDF gain and phase lag was shown to be fairly well predicted for both types of injectors and the effect of the forcing level on the FDF gain was retrieved to some extent.

Finally, the thermoacoustic stability of six different configurations of the NoiseDyn burner was investigated in **Chapter 11** using experiments. Furthermore, two acoustic network models were designed to represent the acoustic response of each configuration of the NoiseDyn burner. In the first network model, the acoustic response of the flame was considered using a Flame Describing Function. In the second network model, the flame response was included in a DATM measurement performed for reactive operating conditions. The acoustic losses generated inside the burner were described analytically in the first model whereas they were directly measured in the second model.

The thermoacoustic stability predictions according to these two acoustic network models were then compared against experimental data. Both network models were able to predict the thermoacoustic stability of the NoiseDyn burner. For thermoacoustically unstable configurations, the frequency of the instability was also accurately predicted by both models. However, the limit cycle oscillation amplitude was precisely predicted by the second network model only. This was attributed to the way acoustic losses are taken into account in the acoustic network models.

Perspectives

The analysis performed in this work for premixed laminar conical flames clearly indicates that new analytical models describing the Flame Transfer Function of collections of small flames are required. Moreover, the current models describing the impact of the flame base motion on the FTF of premixed laminar conical flames needs to be revisited.

Furthermore, the results presented in the second part of this work demonstrate that modeling the acoustic losses inside a combustor in order to accurately predict the onset of thermoacoustic instabilities is a difficult task. In order to improve these predictions, a fundamental understanding of the physical mechanisms at stake is necessary and new analytical models describing these acoustic losses are required. Used within suitable acoustic network models, these acoustic losses models could then lead to precise predictions of the frequencies of the unstable thermoacoustic modes and their associated limit cycle oscillation amplitudes without resorting to experiments or numerical simulations.

It should also be emphasized that the incoherent source terms due to the turbulent flame motion were neglected in the acoustic network models employed here. An interesting extension of this work would be to extract these source terms and the Acoustic Transfer Matrix coefficients concomittantly from the experimental data. Alternatively, the NoiseDyn burner could be operated for

reactive conditions with upstream and downstream anechoic boundary conditions in order to directly assess these acoustic source terms.

Finally, the results presented in this work were obtained with purely gaseous flames and for a limited set of operating conditions. Another possible extension of this work would be to explore the acoustic response of confined turbulent flames for different operating conditions and for various fuels. For instance, it would be worth exploring the acoustic response of spray flames, which are widely employed in the industry, using the experiments and analytical approaches described in the present study.

List of publications

Journal articles

- ▷ **R. Gaudron**, M. Gatti, C. Mirat, T. Schuller, Impact of the acoustic forcing level on the transfer matrix of a turbulent swirling combustor with and without flame, *Submitted.*

- ▷ M. Gatti, **R. Gaudron**, C. Mirat, L. Zimmer, T. Schuller, Impact of swirl and bluff-body on the transfer function of premixed flames, Proc. Combust. Inst., *In Press.*

- ▷ M. Merk, **R. Gaudron**, C. Silva, M. Gatti, C. Mirat, T. Schuller, W. Polifke, Prediction of combustion noise of an enclosed flame by simultaneous identification of noise source and flame dynamics, Proc. Combust. Inst., *In Press.*

- ▷ **R. Gaudron**, M. Gatti, C. Mirat, T. Schuller, Flame Describing Functions of a confined premixed swirled combustor with upstream and downstream forcing, J. Eng. Gas Turbines Power, *In Press.*

- ▷ M. Merk, **R. Gaudron**, M. Gatti, C. Mirat, W. Polifke, T. Schuller, Direct assessment of the acoustic scattering matrix of a turbulent swirl combustor by combining system identification, Large Eddy Simulation and analytical approaches, J. Eng. Gas Turbines Power, *In Press.*

- ▷ M. Merk, **R. Gaudron**, M. Gatti, C. Mirat, W. Polifke, T. Schuller, Measurement and simulation of combustion noise and dynamics of a confined swirl flame, AIAA J. 56 (5), pp. 1930-1942, 2018.

- ▷ **R. Gaudron**, M. Gatti, C. Mirat, T. Schuller, Impact of the injector size on the transfer functions of premixed laminar conical flames, Combust. Flame 179, pp. 138–153, 2017.

Conference proceedings

- ▷ **R. Gaudron**, M. Gatti, C. Mirat, T. Schuller, Flame describing functions of a confined premixed swirled combustor with upstream and downstream forcing - GT2018-76381, Proc. ASME Turbo Expo 2018, June 11-15, 2018, Lillestrøm (Oslo), Norway.

- ▷ M. Gatti, **R. Gaudron**, C. Mirat, T. Schuller, A comparison of the transfer functions and flow fields of flames with increasing swirl number - GT2018-76105, Proc. ASME Turbo Expo 2018, June 11-15, 2018, Lillestrøm (Oslo), Norway.

- ▷ M. Merk, **R. Gaudron**, M. Gatti, C. Mirat, T. Schuller, C. Silva, W. Polifke, Direct assessment of the acoustic scattering matrix of a turbulent swirl combustor by combining system identification, large eddy simulation and analytical approaches - GT2018-75529, Proc. ASME Turbo Expo 2018, June 11-15, 2018, Lillestrøm (Oslo), Norway.

- ▷ **R. Gaudron**, M. Gatti, C. Mirat, T. Schuller, Modeling and measurements of the transfer matrix of a swirling injector with and without flame for increasing forcing levels, $4^{ème}$ Colloque du réseau d'INitiative en Combustion Avancée (INCA 2017), October 18-19, 2017, Centre de R&T Safran Tech (Paris-Saclay).

- ▷ M. Merk, **R. Gaudron**, M. Gatti, C. Mirat, W. Polifke, T. Schuller, Quantitative comparisons between LES predictions and experimental measurements of sound pressure spectra in a confined swirl combustor, 53^{rd} AIAA/SAE/ASEE Joint Propulsion Conference, 2017 AIAA Propulsion and Energy Forum and Exposition, July 10-12, 2017, Atlanta, USA.

- ▷ M. Gatti, **R. Gaudron**, C. Mirat, T. Schuller, Effects of the injector design on the transfer function of premixed swirling flames - GT2017-63874, Proc. ASME Turbo Expo 2017, June 26-30, 2017, Charlotte, USA.

- ▷ **R. Gaudron**, M. Gatti, C. Mirat, T. Schuller, Analysis of the transfer function of large and small premixed laminar conical flames - GT2017-64231, Proc. ASME Turbo Expo 2017, June 26-30, 2017, Charlotte, USA.

- ▷ M. Gatti, **R. Gaudron**, C. Mirat, T. Schuller, Injection system design impact on the stabilization and acoustic response of premixed swirling flames, 8^{th} European Combustion Meeting (ECM 2017), April 18-21, 2017, Dubrovnik, Croatia.

Other conference talks

- ▷ **R. Gaudron**, M. Gatti, C. Mirat, T. Schuller, Analyse du bruit généré par une flamme de prémélange swirlée confinée, Journée François Lacas (Journée des doctorants en combustion), December 9, 2016, Marseille, France.

- ▷ **R. Gaudron**, M. Gatti, C. Mirat, T. Schuller, Transfer functions of premixed laminar conical flames: effects of the burner size, 2^{nd} Colloquium on Combustion Dynamics and Combustion Noise (CDCN2), September 19-22, 2016, Villa Vigoni, Menaggio, Italy.

- ▷ M. Merk, **R. Gaudron**, M. Gatti, C. Mirat, T. Schuller, W. Polifke, Numerical and experimental investigation of the noise level in a confined premixed swirl-stabilized combustor, 2^{nd} Colloquium on Combustion Dynamics and Combustion Noise (CDCN2), September 19-22, 2016, Villa Vigoni, Menaggio, Italy.

Poster

- ▷ M. Gatti, **R. Gaudron**, C. Mirat, T. Schuller, Injection system design impact on the stabilization and acoustic response of premixed swirling flames, 8^{th} European Combustion Meeting (ECM 2017), April 18-21, 2017, Dubrovnik, Croatia.

Appendix A

Harmonic Convention and Acoustic Boundary Orientation

This appendix constitutes an extension of the theoretical developments presented in Chapters 7 and 8. The origin of the acoustic harmonic convention and its consequences on the expression of the acoustic impedance and acoustic reflection coefficient are first discussed. Then, the impact of the acoustic boundary orientation on the expression of the acoustic impedance and acoustic reflection coefficient is investigated.

A.1 Origin of the harmonic convention

The propagation of acoustic waves in a low-Mach non-reactive flow with a uniform temperature field is described with the following wave equation (Rienstra and Hirschberg 2016):

$$\nabla^2 p' - \frac{1}{\bar{c}^2}\frac{\partial^2 p'}{\partial t^2} = 0 \tag{A.1}$$

where p' denotes the acoustic pressure and $\bar{c}$ the mean speed of sound.

If the acoustic waves are further assumed to be harmonic, e.g. if their spectra contain a single angular frequency ω, one specific set of complex solutions following this equation, denoted by a subscript $\oplus$, is given by:

$$p'_{\oplus} = p'_{\oplus\omega}(\mathbf{x})e^{+i\omega t} \tag{A.2}$$

where $\mathbf{x}$ is the position vector and p'_{ω} is the complex amplitude of the acoustic pressure at the angular frequency ω.

However, Eq. (A.1) also admits another set of complex solutions, denoted by a subscript $\ominus$:

$$p'_{\ominus} = p'_{\ominus\omega}(\mathbf{x})e^{-i\omega t} \tag{A.3}$$

These two distinct sets of solutions expressed in Eqs. (A.2) and (A.3) are equally valid and physically equivalent. The harmonic convention is said to be $e^{+i\omega t}$ or $e^{-i\omega t}$ depending on the set of solutions retained, and the associated variables are denoted by a subscript $\oplus$ or $\ominus$ respectively. The physical signal corresponding to the acoustic pressure is then obtained by considering the real part of Eqs. (A.2) or (A.3).

A.2 Impact of the harmonic convention on the acoustic impedance and acoustic reflection coefficient

In this section, the acoustic waves are assumed to be harmonic plane waves propagating in a duct along the x-axis. The acoustic pressure inside the duct is given by:

$$p' = p'_{\omega}(x)e^{\pm i\omega t} \tag{A.4}$$

where the $\pm$ sign depends on the harmonic convention retained. Using Eq. (A.4), the wave equation given by Eq. (A.1) becomes a Helmholtz equation:

$$\frac{d^2 p'_{\omega}}{dx^2} + k^2 p'_{\omega} = 0 \tag{A.5}$$

where $k = \omega/\bar{c}$ is the wave number.

Equation (A.5) is valid for both harmonic conventions. The acoustic pressure at any axial location inside the duct is obtained by solving this equation. The associated acoustic velocity is then derived from Eq. (7.27), which is reproduced here:

$$\bar{\rho}\frac{\partial \mathbf{u}'}{\partial t} = -\nabla p' \tag{A.6}$$

Using the harmonic plane wave assumption, the resulting equation differs depending on the harmonic convention retained:

$$\pm i\omega\bar{\rho}\mathbf{u}'_{\omega} = -\frac{dp'_{\omega}}{dx} \tag{A.7}$$

From Eqs. (A.4), (A.5) and (A.7), the acoustic pressure and acoustic velocity with the $e^{+i\omega t}$ harmonic convention are given by:

$$\begin{cases} p'_{\oplus} = A_{\oplus\omega} e^{ikx} e^{+i\omega t} + B_{\oplus\omega} e^{-ikx} e^{+i\omega t} & \text{(A.8)} \\ \mathbf{u}'_{\oplus} = \left(-\dfrac{A_{\oplus\omega}}{\bar{\rho}\bar{c}} e^{ikx} e^{+i\omega t} + \dfrac{B_{\oplus\omega}}{\bar{\rho}\bar{c}} e^{-ikx} e^{+i\omega t} \right) \mathbf{e}_x & \text{(A.9)} \end{cases}$$

where $A_{\oplus\omega}$ and $B_{\oplus\omega}$ are complex integration constants.

On the other hand, the acoustic pressure and acoustic velocity with the $e^{-i\omega t}$ harmonic convention are given by:

$$\begin{cases} p'_{\ominus} = A_{\ominus\omega} e^{ikx} e^{-i\omega t} + B_{\ominus\omega} e^{-ikx} e^{-i\omega t} & \text{(A.10)} \\ \mathbf{u}'_{\ominus} = \left(\dfrac{A_{\ominus\omega}}{\bar{\rho}\bar{c}} e^{ikx} e^{-i\omega t} - \dfrac{B_{\ominus\omega}}{\bar{\rho}\bar{c}} e^{-ikx} e^{-i\omega t} \right) \mathbf{e}_x & \text{(A.11)} \end{cases}$$

where $A_{\ominus\omega}$ and $B_{\ominus\omega}$ are complex integration constants that differ from $A_{\oplus\omega}$ and $B_{\oplus\omega}$. All these integration constants $A_{\oplus\omega}$, $B_{\oplus\omega}$, $A_{\ominus\omega}$ and $B_{\ominus\omega}$ depend on the frequency.

A link between these two conventions can be established with the following reasoning. Even though two different harmonic conventions are possible, the physical signals corresponding to the acoustic pressure and acoustic velocity are the same for both harmonic conventions:

$$\begin{cases} \mathrm{Re}(p'_{\oplus}) = \mathrm{Re}(p'_{\ominus}) & \text{(A.12)} \\ \mathrm{Re}(u'_{\oplus}) = \mathrm{Re}(u'_{\ominus}) & \text{(A.13)} \end{cases}$$

where $\mathrm{Re}(e)$ denotes the real part of any complex number e. From Eqs. (A.8)-(A.13), it is found that:

$$\begin{cases} A_{\oplus\omega} = (B_{\ominus\omega})^* & \text{(A.14)} \\ B_{\oplus\omega} = (A_{\ominus\omega})^* & \text{(A.15)} \end{cases}$$

where the superscript * denotes the complex conjugate. The expression of the acoustic impedance with the $e^{+i\omega t}$ convention is then given by:

$$Z_{\oplus} = \pm \frac{p'_{\oplus}}{u'_{\oplus}} = \pm \bar{\rho}\bar{c} \frac{A_{\oplus\omega} e^{ikx} + B_{\oplus\omega} e^{-ikx}}{-A_{\oplus\omega} e^{ikx} + B_{\oplus\omega} e^{-ikx}} \quad \text{(A.16)}$$

where the symbol $\pm$ is due to the surface orientation, as explained in Sec. A.3. Likewise, the expression of the acoustic impedance with the $e^{-i\omega t}$ harmonic convention is given by:

$$Z_{\ominus} = \pm\frac{p'_{\ominus}}{u'_{\ominus}} = \pm\bar{\rho}\bar{c}\frac{A_{\ominus\omega}e^{ikx} + B_{\ominus\omega}e^{-ikx}}{A_{\ominus\omega}e^{ikx} - B_{\ominus\omega}e^{-ikx}} \tag{A.17}$$

By taking the complex conjugate of Eq. (A.17) and using Eqs. (A.14)-(A.16), the relation between the acoustic impedances with both harmonic conventions is found:

$$Z_{\oplus} = (Z_{\ominus})^* \tag{A.18}$$

Furthermore, the analytical link between the specific acoustic impedance Z_s and the acoustic reflection coefficient $\mathcal{R}$ is given by Eq. (7.44), reproduced here:

$$\mathcal{R}(x,\omega) = \frac{Z_s\,(x,\omega) - 1}{Z_s\,(x,\omega) + 1} \tag{A.19}$$

where Z_s is the ratio between the acoustic impedance Z and the characteristic acoustic impedance of the medium $z = \bar{\rho}\bar{c}$.

Using this equation, the relation between the acoustic reflection coefficients with both harmonic conventions is found as well:

$$\mathcal{R}_{\oplus} = (\mathcal{R}_{\ominus})^* \tag{A.20}$$

In the end, switching between harmonic conventions for the acoustic impedance and acoustic reflection coefficient is simply done by taking the complex conjugate of these physical quantities.

A.3 Impact of the acoustic boundary orientation

As explained in Chapter 7, the acoustic impedance Z is defined as:

$$Z\,(\mathbf{x},\omega) = \frac{p'_{\omega}(\mathbf{x})}{\mathbf{u}'_{\omega}(\mathbf{x}) \cdot \hat{\mathbf{n}}(\mathbf{x})} \tag{A.21}$$

In this expression, $\hat{\mathbf{n}}$ stands for the unit vector normal to the surface of interest and pointing outward and p'_{ω} and $\mathbf{u}'_{\omega}$ are the complex amplitudes of the acoustic pressure and acoustic velocity assessed at the angular frequency ω. As

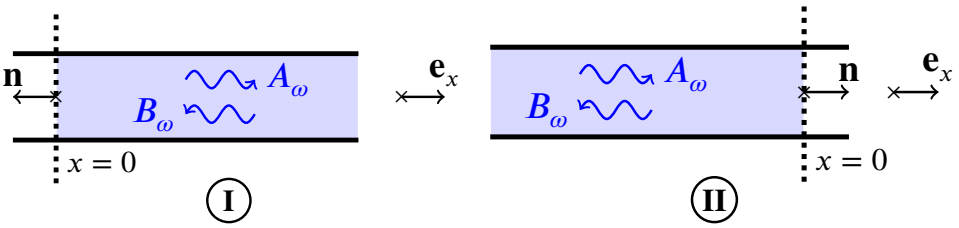

Figure A.1: *Acoustic boundary orientation in the case of harmonic plane waves propagating along the x-axis. The axial location at which the acoustic impedance and acoustic reflection coefficient are defined is $x = 0$. Case (I) corresponds to acoustic waves propagating on the right of the boundary (Left). Case (II) corresponds to acoustic waves propagating on the left of the boundary (Right).*

a consequence, the acoustic impedance Z and subsequently the acoustic reflection coefficient $\mathcal{R}$ depend on the orientation of $\hat{\mathbf{n}}$. In other words, Z and $\mathcal{R}$ depend on surface orientation.

When harmonic plane waves propagating along the x-axis are considered, two possible cases arise. The first case, called (I) in Fig. A.1, corresponds to an acoustic boundary with sound waves propagating on its right whereas in the second case, called (II) in Fig. A.1, the sound waves are propagating on the left of the boundary. Without loss of generality, the surface on which the acoustic impedance and acoustic reflection coefficient are assessed is defined as the x-axis origin.

From Eq. (A.21) and Fig. A.1-(Left), the expressions of the acoustic impedance and acoustic reflection coefficient for Case (I) are given by Eqs. (A.22) and (A.23) respectively.

$$Z_{\text{(I)}}(0,\omega) = -\frac{p'_\omega(0)}{u'_\omega(0)} \tag{A.22}$$

$$\mathcal{R}_{\text{(I)}}(0,\omega) = \frac{A_\omega}{B_\omega} \tag{A.23}$$

where A_ω and B_ω represent the complex amplitudes of the acoustic waves propagating in the positive and negative directions respectively.

On the other hand, the expressions of the acoustic impedance and acoustic reflection coefficient for Case (II) are given by Eqs. (A.24) and (A.25) respectively.

$$Z_{\textcircled{II}}(0,\omega) = \frac{p'_\omega(0)}{u'_\omega(0)} \tag{A.24}$$

$$\mathcal{R}_{\textcircled{II}}(0,\omega) = \frac{B_\omega}{A_\omega} \tag{A.25}$$

In the end, it was shown that the acoustic impedance and acoustic reflection coefficient both depend on the orientation of the acoustic boundary.

Appendix B

Cold Flow Acoustic Characterization

The procedure used to determine the frequencies and damping rates of the cold flow acoustic modes developing inside a combustor using experiments and analytical approaches is exemplified in this appendix using the NoiseDyn burner. The issues associated with this procedure are then described in details.

B.1 Acoustic characterization of the NoiseDyn burner using cold flow experiments

In this section, configurations $\mathbf{A}^2$, $\mathbf{B}^2$ and $\mathbf{C}^2$ of the NoiseDyn burner are operated for cold flow conditions while submitted to external acoustic forcing generated by a loudspeaker (Schuller et al. 2003b; Mirat 2015), as represented in Fig. B.1. This experimental setup is used to characterize the cold flow acoustic modes developing in these three configurations of the NoiseDyn burner. Microphones MP, MHW, MC, ME and ME" are flush-mounted on the burner, except for configuration $\mathbf{A}^2$ where microphones ME and ME" are removed. The distance between microphones ME and ME" is set to 50 mm.

The frequency of the sound waves emitted by the loudspeaker is then varied between 50 Hz and 1000 Hz and the various microphone signals are recorded at a sampling frequency $f_s = 20000$ Hz during one second for each forcing frequency. These measurements are performed with a mean cold flow across the NoiseDyn burner in order to accurately assess the damping rates of the acoustic modes. The auto power spectral densities of each microphone signal are then computed using a single flat-top window. The corresponding plots, represented in Fig. B.2, are used to determine the frequencies and damping rates of the acoustic modes for all three configurations of the NoiseDyn burner.

Based on the assumption that the acoustic response of the combustor is a sec-

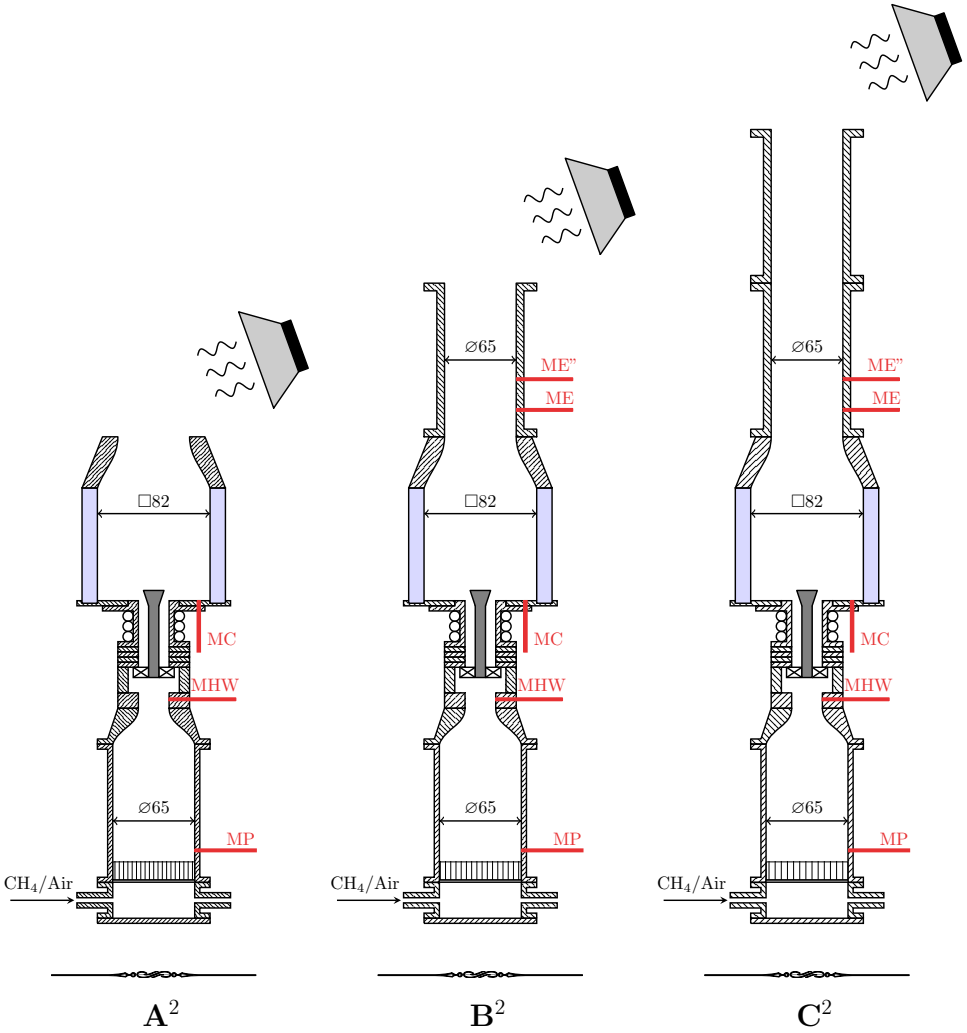

Figure B.1: *Sketches depicting configurations* $\mathbf{A}^2$ *(Left),* $\mathbf{B}^2$ *(Center) and* $\mathbf{C}^2$ *(Right) of the NoiseDyn burner submitted to harmonic sound waves generated by an external loudspeaker for forcing frequencies up to* 1000 *Hz. Microphones MP, MHW, MC, ME and ME" are used to measure the acoustic pressure at various axial locations for all forcing frequencies.*

ond order damped harmonic oscillator (Mirat 2015), the damping rate ω_i of each acoustic mode is simply given by:

$$\omega_i = \pi \Delta f \tag{B.1}$$

where Δf is the full width at half maximum for each acoustic mode, obtained from Fig. B.2. The frequencies and damping rates of all the acoustic modes appearing in configurations $\mathbf{A}^2$, $\mathbf{B}^2$ and $\mathbf{C}^2$ between 50 Hz and 1000 Hz are

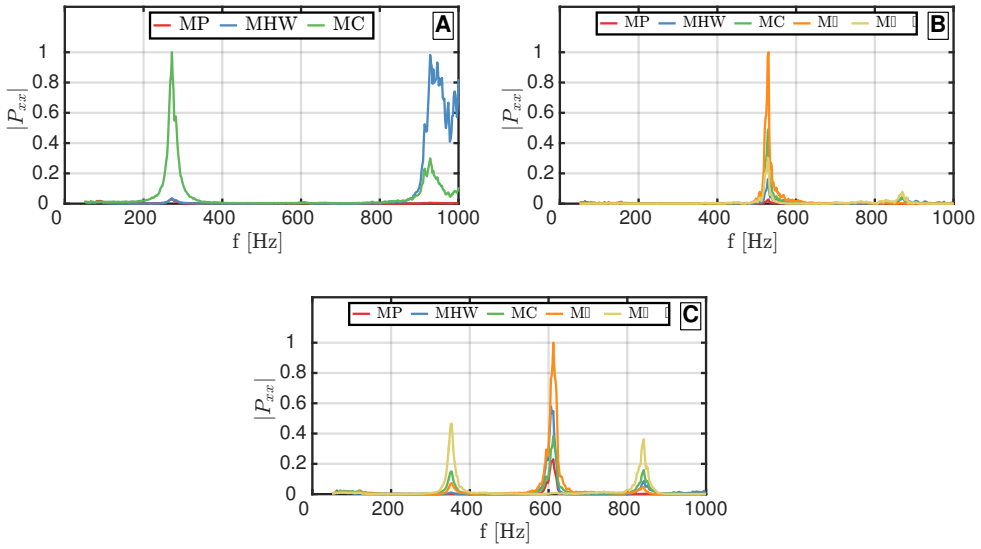

Figure B.2: *Auto power spectral density of the microphone signals at the forcing frequency in the presence of a mean cold flow and plotted as a function of the forcing frequency. Results for configurations* $\mathbf{A}^2$ *(Top left),* $\mathbf{B}^2$ *(Top right) and* $\mathbf{C}^2$ *(Bottom).*

obtained following this procedure. The corresponding results are summarized in Table B.1.

B.2 Prediction of the acoustic modes of the NoiseDyn burner for cold flow operating conditions

The experimental setup is now modeled for cold flow operating conditions using the acoustic two-port matrices network formalism (Abom 1992; Paschereit and Polifke 1998; Polifke et al. 2001; Dowling and Stow 2003; Poinsot and Veynante 2005; Fischer et al. 2006). Following the procedure presented in Sec. 11.3 for reactive operating conditions, an acoustic network model representing the NoiseDyn burner may be constructed by analogy with the $\mathrm{R_{FDF}}$ model but with a constant gas temperature $\overline{T}_u = 293$ K throughout the burner. Moreover, the element corresponding to the flame response is removed here.

Combining this acoustic network model with relevant acoustic boundary conditions at the combustor inlet (closed boundary) and outlet (open boundary), the characteristic equation given by Eq. (11.8) is explicitly derived.

The next step is to look for the complex roots $f = f_r + i f_i$ of this characteristic equation, where f_r is the frequency of the acoustic mode and $\omega_i = 2\pi f_i$ is the associated damping rate. Using the method introduced in Sec. 11.3, these roots

Table B.1: *Frequencies and damping rates of the acoustic modes appearing in configurations* $\mathbf{A}^2$, $\mathbf{B}^2$ *and* $\mathbf{C}^2$ *of the NoiseDyn burner for cold flow operating conditions with* $\bar{u}_b = 5.4$ *m/s at the hot wire probe location. Results were obtained using an external louspeaker generating harmonic sound waves between* 50 *Hz and* 1000 *Hz (Experiments) and using the acoustic network model representing the NoiseDyn burner (Predictions).*

Config.	Mode	Experiments			Predictions	
		f [Hz]	Δf [Hz]	ω_i [1/s]	f [Hz]	ω_i [1/s]
$\mathbf{A}^2$	**1**	82	28	88	80.5	200
	2	272	20	63	297.1	61
	3	608	24	75	573.4	16
	4	928	38	119	869.0	209
$\mathbf{B}^2$	**1**	70	36	113	75.0	143
	2	156	12	38	156.3	71
	3	530	10	31	551.1	28
	4				579.5	28
	5	870	14	44	827.6	80
$\mathbf{C}^2$	**1**	62	14	44	67.9	85
	2	118	18	57	123.1	121
	3	354	16	50	364.6	18
	4				570.7	13
	5	612	18	57	622.3	31
	6	842	17	53	813.2	52

are found and summarized in Table B.1.

The frequencies of the acoustic modes corresponding to configurations $\mathbf{A}^2$, $\mathbf{B}^2$ and $\mathbf{C}^2$ for cold flow operating conditions are adequately predicted, as shown in Table B.1. Two acoustic modes predicted by the acoustic network model for configurations $\mathbf{B}^2$ and $\mathbf{C}^2$ are not detected in the experiments but this is likely due to the presence of other modes at neighboring frequencies which may cover up these undetected modes.

On the other hand, the acoustic damping rates according to the experiments and to the acoustic network model predictions are in contradiction. This is not surprising since many assumptions are necessary in order to relate the results obtained from the experiments, presented in Sec. B.1, to the analytical

predictions, presented in Sec. B.2. The main limitations associated with these assumptions are discussed in the next section.

B.3 Issues associated with the cold flow acoustic characterization procedure

The first issue associated with the cold flow acoustic characterization procedure presented in Secs. B.1 and B.2 is due to the downstream acoustic boundary condition set in the acoustic network model. Usually, this acoustic boundary is modeled using an open end condition, or any other acoustic boundary condition corresponding to the experimental setup in the absence of external forcing. However, the downstream acoustic boundary condition may be strongly impacted by the external source of forcing.

In the absence of acoustic forcing, no acoustic mode will develop inside the burner. The addition of an external loudspeaker introducing acoustic energy through the downstream boundary is necessary for the acoustic modes to develop inside the setup. As a consequence, the downstream acoustic boundary condition is modified to some extent in the presence of external forcing compared to the unforced regime. Unless the downstream acoustic impedance is measured for all frequencies and used as a boundary condition in the acoustic network model, the frequencies and damping rates of the acoustic modes obtained from the experiments and predicted by the acoustic network models may not be the same.

The second issue associated with the cold flow acoustic characterization procedure presented earlier is related to the assumption that the combustor is a second order damped harmonic oscillator. This assumption is necessary in order to obtain the acoustic damping rates by extracting the full width at half maximum from Fig. B.2 for each acoustic mode. However, this assumption is inconsistent with the nonlinear acoustic response of the combustor observed in Chapter 10 for both cold and reactive operating conditions. In that case, part of the acoustic energy is transfered to higher order harmonics and the damping rate of each acoustic mode cannot be obtained using the previous method.

Even if the acoustic response of the combustor can be assumed to be linear and the correct acoustic impedance is set at the downstream boundary, a fundamental difficulty arises when one tries to predict the damping rates of the acoustic modes using the procedure described in Sec. B.2. In fact, some elements in the acoustic network model, such as the Levine-Schwinger impedance, are not functions of a complex variable $f = f_r + if_i$. As a consequence, these elements are often considered to be a function of the frequency f_r only. When reactive operating conditions are explored, the Flame Describing Function is typically

assumed to be a function of f_r as well. This implies that these elements do not participate in the damping of the acoustic waves occurring inside the combustor since f_i is artificially set to zero for these elements. On the other hand, acoustic damping is known to occur at an open end boundary for instance which is in contradiction with the previous assumption.

This problem becomes obvious when the combustor is modeled using an experimental DATM, measured as a function of f_r only, along with acoustic boundary conditions that depend on f_r only (such as closed or open end acoustic boundary conditions). In that case, the characteristic equation is a function of f_r only and it is concluded that there is no acoustic damping inside the combustor, which is evidently false.

It is thus concluded that the cold flow acoustic characterization procedure presented in this appendix is rudimentary and should be utilized with great care. Moreover, determining the damping rates of the acoustic modes by looking for the complex roots of the characteristic equation is problematic, especially when considering acoustic elements that were measured as a function of the frequency only.

References

Abel, N. H. (1826). Auflösung einer mechanischen aufgabe. *J. für die reine und Angew. Math. 1*, 153–157. *(p. 47)*

Abom, M. (1992). A note on the experimental determination of acoustical two-port matrices. *J. Sound Vib. 155*(1), 185–188. *(p. 149, 182, 206, 207, 215, 248, 275)*

Abramowitz, M. and I. A. Stegun (1972). *Handbook of mathematical functions with formulas, graphs, and mathematical tables*. Dover printing. *(p. 145)*

Alemela, P., D. Fanca, F. Ettner, C. Hirsch, and S. Sattelmayer (2008). Flame transfer matrices of a premixed flame and a global check with modelling and experiments - GT2008-501. In *Proc. ASME Turbo Expo 2008*, pp. 1–9. *(p. 206, 207, 210)*

Altay, H. M., K. S. Kedia, R. L. Speth, and A. F. Ghoniem (2010). Two-dimensional simulations of steady perforated-plate stabilized premixed flames. *Combust. Theor. Model. 14*(1), 125–154. *(p. 87)*

Altay, H. M., S. Park, D. Wu, D. Wee, A. M. Annaswamy, and A. F. Ghoniem (2009). Modeling the dynamic response of a laminar perforated-plate stabilized flame. *Proc. Combust. Inst. 32*, 1359–1366. *(p. 25, 83, 85, 87)*

Atig, M., J. P. Dalmont, and J. Gilbert (2004). Termination impedance of open-ended cylindrical tubes at high sound pressure level. *C. R. Mec. 332*(4), 299–304. *(p. 148, 149)*

Baillot, F., A. Bourehla, and D. Durox (1996). The characteristics method and cusped flame fronts. *Combust. Sci. Technol. 112*, 327–350. *(p. 18, 19)*

Baillot, F., D. Durox, and R. Prud'Homme (1992). Experimental and theoretical study of a premixed vibrating flame. *Combust. Flame 88*, 149–168. *(p. 18, 19)*

Barbosa, S., P. Scouflaire, and S. Ducruix (2008). Characterization of the reactive flow field dynamics in a gas turbine injector using high frequency PIV. *HAL*. *(p. 234)*

Becker, R. and R. Günther (1971). The transfer function of premixed turbulent jet flames. *Symp. (Int.) Combust. 13*, 517–526. *(p. 6, 236, 237)*

Birbaud, A. L., D. Durox, and S. Candel (2006). Upstream flow dynamics of a laminar premixed conical flame submitted to acoustic modulations.

Combust. Flame 146(3), 541–552. *(p. 19, 22, 41, 57)*

Birbaud, A. L., D. Durox, S. Ducruix, and S. Candel (2007). Dynamics of developing round jets submitted to upstream acoustic modulations. *Phys. Fluids 19*, 1–48. *(p. 173)*

Blackshear, P. L. (1953). Driving standing waves by heat addition. *Symp. (Int.) Combust. 1*(4), 553–566. *(p. 5, 18, 238)*

Blanchard, M., T. Schuller, D. Sipp, and P. J. Schmid (2015). Response analysis of a laminar premixed M-flame to flow perturbations using a linearized compressible Navier-Stokes solver. *Phys. Fluids 27*(4), 043602. *(p. 22, 79)*

Boudy, F., D. Durox, T. Schuller, G. Jomaas, and S. Candel (2011). Describing function analysis of limit cycles in a multiple flame combustor. *J. Eng. Gas Turbines Power 133*(6), 061502. *(p. 6, 8, 173, 239)*

Boutier, A. (2012). *Vélocimétrie laser pour la mécanique des fluides*. Lavoisier. *(p. 116)*

Bouvet, N., F. Halter, C. Chauveau, and Y. Yoon (2013). On the effective Lewis number formulations for lean hydrogen/hydrocarbon/air mixtures. *Int. J. Hydrog. Energy 38*(14), 5949–5960. *(p. 76)*

Bowman, D. M. J. S., J. K. Balch, P. Artaxo, W. J. Bond, J. M. Carlson, M. A. Cochrane, C. M. D Antonio, R. S. DeFries, J. C. Doyle, S. P. Harrison, F. H. Johnston, J. E. Keeley, M. A. Krawchuk, C. A. Kull, J. B. Marston, I. C. Prentice, C. I. Roos, A. C. Scott, T. W. Swetnam, G. R. Werf, and S. J. Pyne (2009). Fire in the earth system. *Science (80-.). 324*, 481–484. *(p. 1)*

Boyer, L. and J. Quinard (1990). On the dynamics of anchored flames. *Combust. Flame 82*(1), 51–65. *(p. 18, 29, 35)*

Brear, M. J., F. Nicoud, M. Talei, A. Giauque, and E. R. Hawkes (2012). Disturbance energy transport and sound production in gaseous combustion. *J. Fluid Mech. 707*, 53–73. *(p. 238)*

Camporeale, S. M., B. Fortunato, and G. Campa (2011). A finite element method for three-dimensional analysis of thermo-acoustic combustion instability. *J. Eng. Gas Turbines Power 133*(1), 011506. *(p. 173, 205)*

Candel, S. (1992). Combustion instabilities coupled by pressure waves and their active control. *Symp. (Int.) Combust. 20*, 1277–1296. *(p. 4, 234)*

Candel, S. (2002). Combustion dynamics and control: progress and challenges. *Proc. Combust. Inst. 29*, 1–28. *(p. 5, 6, 13, 170, 173, 234, 236, 237, 238)*

Candel, S., D. Durox, and T. Schuller (2004). Flame interactions as a source of noise and combustion instabilities. In *Proc. AIAA/CEAS Aeroacoustics Conf.*, Number AIAA-2004-2928. *(p. 44)*

Candel, S. and T. Poinsot (1988). *A tutorial on acoustics*. Châtenay Malabry: Ecole Centrale Paris. *(p. 6, 140, 141, 146, 164, 165, 235, 236)*

Chigier, N. A. and A. Chervinsky (1967). Experimental investigation of swirling vortex motion in jets. *J. Appl. Phys. 34*(2), 443–451. *(p. 101)*

Cho, J. H. and T. Lieuwen (2005). Laminar premixed flame response to equivalence ratio oscillations. *Combust. Flame 140*, 116–129. *(p. 70)*

Chung, J. Y. and D. A. Blaser (1980a). Transfer function method of measuring in-duct acoustic properties. I. Theory. *J. Acoust. Soc. Am. 68*, 907–913. *(p. 129, 130, 131, 132, 209)*

Chung, J. Y. and D. A. Blaser (1980b). Transfer function method of measuring in-duct acoustic properties. II. Experiment. *J. Acoust. Soc. Am. 68*, 914–921. *(p. 130)*

Clanet, C. and G. Searby (1998). First experimental study of the Darrieus-Landau instability. *Phys. Rev. Lett. 80*(17), 3867–3870. *(p. 22)*

Correa, S. M. (1993). A review of NOx formation under gas turbine combustion conditions. *Combust. Sci. Technol. 87*(1-6), 329–362. *(p. 3, 5)*

Correa, S. M. (1998). Power generation and aeropropulsion gas turbines: from combustion science to combustion technology. *Symp. (Int.) Combust. 27*(2), 1793–1807. *(p. 234)*

Ćosić, B., J. P. Moeck, and C. O. Paschereit (2014). Nonlinear instability analysis for partially premixed swirl flames. *Combust. Sci. Technol. 186*, 713–736. *(p. 173, 205, 206)*

Ćosić, B., S. Terhaar, J. P. Moeck, and C. O. Paschereit (2015). Response of a swirl-stabilized flame to simultaneous perturbations in equivalence ratio and velocity at high oscillation amplitudes. *Combust. Flame 162*(4), 1046–1062. *(p. 206)*

Crighton, D. G., A. P. Dowling, J. E. Ffwocs Williams, M. Heckl, and F. G. Leppington (1992). *Modern methods in analytical acoustics. Lectures notes.* London: Springer Verlag. *(p. 140, 165, 236)*

Crocco, L. (1951). Aspects of combustion stability in liquid propellant rocket motors (Part 1). *J. Am. Rocket Soc.*, 163–178. *(p. 5, 6, 18, 170, 234, 237)*

Crocco, L. (1952). Aspects of combustion stability in liquid propellant rocket motors (Part 2). *J. Am. Rocket Soc.*, 7–16. *(p. 170, 234)*

Crocco, L., J. Grey, and H. D. (1960). Theory of liquid propellent rocket combustion instability and its experimental verification. *J. Am. Rocket Soc. 30*(2), 159–168. *(p. 234)*

Cummings, A. (1977). High temperature effects on the radiation impedance of an unflanged duct exit. *J. Sound Vib. 52*(2), 299–304. *(p. 149)*

Cummings, A. (1984). Acoustic nonlinearities and power losses at orifices. *AIAA J. 22*(6), 786–792. *(p. 161, 234)*

Cuquel, A. (2013). *Dynamics and nonlinear thermo-acoustic stability analysis of premixed conical flames.* Ph. D. thesis, Ecole Centrale Paris. *(p. 19, 33, 35, 37, 41, 57)*

Cuquel, A., D. Durox, and T. Schuller (2013a). Impact of flame base dynamics on the non-linear frequency response of conical flames. *C. R. Mec. 341*, 171–180. *(p. 21, 26, 27, 28, 29, 35, 36, 37, 41, 60, 63, 65, 67, 89)*

Cuquel, A., D. Durox, and T. Schuller (2013b). Scaling the flame transfer

function of confined premixed conical flames. *Proc. Combust. Inst. 34*(1), 1007–1014. *(p. 21, 63, 79)*

de Goey, L. P. H., J. A. van Oijen, and J. H. M. ten Thije Bookkamp (2011). Propagation, dynamics and control of laminar premixed flames. *Proc. Combust. Inst. 33*, 863–886. *(p. 14, 23, 24, 35, 36, 66, 83, 87, 234)*

Dowling, A. P. (1995). The calculation of thermoacoustic oscillations. *J. Sound Vib. 180*(4), 557–581. *(p. 13, 168, 170)*

Dowling, A. P. (1997). Nonlinear self-excited oscillations of a ducted flame. *J. Fluid Mech. 346*, 271–290. *(p. 6, 173, 205, 208, 234, 237)*

Dowling, A. P. (1999). A kinematic model of a ducted flame. *J. Fluid Mech. 394*, 51–72. *(p. 27)*

Dowling, A. P. and A. S. Morgans (2005). Feedback control of combustion oscillations. *Annu. Rev. Fluid Mech. 37*(1), 151–182. *(p. 4, 235, 238, 239)*

Dowling, A. P. and S. R. Stow (2003). Acoustic analysis of gas turbine combustors. *J. Propul. Power 19*(5), 751–764. *(p. 6, 154, 173, 205, 215, 234, 237, 248, 275)*

Duchaine, F., L. Selle, and T. Poinsot (2011). Sensitivity analysis of transfer functions of laminar flames. *Combust. Flame 158*(12), 2384–2394. *(p. 14)*

Ducruix, S., D. Durox, and S. Candel (2000). Theoretical and experimental determination of the transfer function of a laminar premixed flame. *Proc. Combust. Inst. 28*, 765–773. *(p. 6, 14, 15, 16, 18, 23, 30, 31, 41, 43, 54, 57, 70, 237)*

Ducruix, S., T. Schuller, D. Durox, and S. Candel (2003). Combustion dynamics and instabilities: elementary coupling and driving mechanisms. *J. Propul. Power 19*(5), 722–734. *(p. 4)*

Durox, D., A. L. Birbaud, T. Schuller, and S. Candel (2004). Dynamique de l'écoulement dans les flammes oscillantes prémélangées. In *Neuvième Congrès Francoph. Vélocimétrie Laser, Bruxelles, Belgium, Sept. 14-17. (p. 16, 43)*

Durox, D., S. Ducruix, and F. Lacas (1999). Flow seeding with an air nebulizer. *Exp. Fluids 27*(5), 408–413. *(p. 44, 116)*

Durox, D., T. Schuller, and S. Candel (2005). Combustion dynamics of inverted conical flames. *Proc. Combust. Inst. 30*(1717-1724). *(p. 87)*

Durox, D., T. Schuller, N. Noiray, A. L. Birbaud, and S. Candel (2009). Rayleigh criterion and acoustic energy balance in unconfined self-sustained oscillating flames. *Combust. Flame 156*(1), 106–119. *(p. 14, 238, 239)*

Durox, D., T. Schuller, N. Noiray, and S. Candel (2009). Experimental analysis of nonlinear flame transfer functions for different flame geometries. *Proc. Combust. Inst. 32*, 1391–1398. *(p. 8, 15, 16, 22, 23, 31, 41, 54, 173, 208, 237)*

Echekki, T., J. H. Chen, and I. Gran (1996). The mechanism of mutual annihilation of stoechiometric premixed methane-air flames. *Symp. (Int.)*

Combust. 26(1), 855–863. *(p. 87)*

Fischer, A., C. Hirsch, and T. Sattelmayer (2006). Comparison of multi-microphone transfer matrix measurements with acoustic network models of swirl burners. *J. Sound Vib. 298*(1-2), 73–83. *(p. 6, 150, 155, 206, 207, 210, 215, 235, 248, 275)*

Fleifil, M., A. M. Annaswamy, Z. A. Ghoneim, and A. F. Ghoniem (1996). Response of a laminar premixed flame to flow oscillations: a kinematic model and thermoacoustic instability results. *Combust. Flame 106*, 487–510. *(p. 14, 16, 18, 23, 27, 30, 43, 54, 57)*

Gatti, M., R. Gaudron, C. Mirat, and T. Schuller (2017). Effects of the injector design on the transfer function of premixed swirling flames - GT2017-63874. In *Proc. ASME Turbo Expo 2017*, pp. 1–11. *(p. 97, 103, 173, 228)*

Gatti, M., R. Gaudron, C. Mirat, and T. Schuller (2018). A comparison of the transfer functions and flow fields of flames with increasing swirl numbers - GT2018-76105. In *Proc. ASME Turbo Expo 2018*, pp. 1–12. *(p. 6, 103, 228, 237)*

Gaudron, R., M. Gatti, C. Mirat, and T. Schuller (2017a). Analysis of the transfer function of large and small premixed laminar conical flames - GT2017-64231. In *Proc. ASME Turbo Expo 2017*, pp. 1–11. *(p. 173)*

Gaudron, R., M. Gatti, C. Mirat, and T. Schuller (2017b). Impact of the injector size on the transfer functions of premixed laminar conical flames. *Combust. Flame 179*, 138–153. *(p. 15, 45)*

Gaudron, R., M. Gatti, C. Mirat, and T. Schuller (2017c). Modeling and measurements of the transfer matrix of a swirling injector with and without flame for increasing forcing levels. In *Proc. INCA 2017*, pp. 1–9. *(p. 6, 237)*

Gaydon, A. G. (1957). *The spectroscopy of flames*. Chapman & Hall LTD., London. *(p. 122)*

Gentemann, A., A. Fischer, S. Evesque, and W. Polifke (2003). Acoustic transfer matrix reconstruction and analysis for ducts with sudden change of area. In *9th AIAA/CEAS Aeroacoustics Conf. Exhib. May 12-14, 2003, Hilt. Head, South Carolina*, pp. 1–11. *(p. 220)*

Gentemann, A. and W. Polifke (2007). Scattering and generation of acoustic energy by a premix swirl burner - GT2007-27238. In *Proc. ASME Turbo Expo 2007*. *(p. 207)*

Ghirardo, G., B. Ćosić, M. P. Juniper, and J. P. Moeck (2015). State-space realization of a describing function. *Nonlinear Dyn. 82*(1-2), 9–28. *(p. 206)*

Ghirardo, G., M. P. Juniper, and J. P. Moeck (2015). Stability criteria for standing and spinning waves in annular combustors - GT2015-43127. In *Proc. ASME Turbo Expo 2015*. *(p. 173)*

Giuliani, F., A. Lang, K. Johannes Gradl, P. Siebenhofer, and J. Fritzer (2012). Air flow modulation for refined control of the combustion dynamics using a novel actuator. *J. Eng. Gas Turbines Power 134*, 021602–18.

(p. 206)

Gloerfelt, X. (2009). Cavity noise. Technical report. *(p. 158)*

Gubareff, G. G., J. E. Janssen, and R. H. Torborg (1960). Thermal radiation properties survey: a review of the literature. Technical report. *(p. 110)*

Guedra, M., G. Penelet, P. Lotton, and J. Dalmont (2011). Theoretical prediction of the onset of thermoacoustic instability from the experimental transfer matrix of a thermoacoustic core. *J. Acoust. Soc. Am. 130*(7), 145–152. *(p. 210, 237)*

Guiberti, T. (2015). *Analysis of the topology of confined premixed swirling flames*. Ph. D. thesis. *(p. 43, 97, 100, 115)*

Guiberti, T. F., D. Durox, P. Scouflaire, and T. Schuller (2015). Impact of heat loss and hydrogen enrichment on the shape of confined swirling flames. *Proc. Combust. Inst. 35*(2), 1385–1392. *(p. 111)*

Gunder, D. F. and D. R. Friant (1950). Stability of flow in a rocket motor. *J. Appl. Mech. T. ASME 17*(3), 327–333. *(p. 5)*

Han, X., J. Li, and A. S. Morgans (2015). Prediction of combustion instability limit cycle oscillations by combining flame describing function simulations with a thermoacoustic network model. *Combust. Flame 162*(10), 3632–3647. *(p. 6, 205, 206, 234)*

Han, X. and A. S. Morgans (2015). Simulation of the flame describing function of a turbulent premixed flame using an open-source LES solver. *Combust. Flame 162*(5), 1778–1792. *(p. 6, 205, 206, 237)*

Hartmann, W. M. (2013). *Principles of musical acoustics*. Springer. *(p. 235)*

Heckl, M. (1990). Non-linear acoustic effect in the Rijke tube. *Acoustica 72*, 63–71. *(p. 220)*

Higgins, B., M. Q. McQuay, F. Lacas, J. C. Rolon, N. Darabiha, and S. Candel (2001). Systematic measurements of OH chemiluminescence for fuel-lean, high-pressure, premixed, laminar flames. *Fuel 80*(1), 67–74. *(p. 44)*

Higgins, W. (1802). On the sound produced by a current hydrogen gas passing through a tube. *A J. Nat. Philos. Chem. Arts 1-2*(56), 129–131. *(p. 4)*

Higuera, F. J. (2009). Aerodynamics of a slender axisymmetric Bunsen flame with large gas expansion. *Combust. Flame 156*, 1063–1064. *(p. 21)*

Hindasageri, V., R. P. Vedula, S. V. Prabhu, V. Hindasageri, R. P. Vedula, and S. V. Prabhu (2013). Thermocouple error correction for measuring the flame temperature with determination of emissivity and heat transfer coefficient. *Rev. Sci. Instrum. 024902*(84), 1–12. *(p. 109)*

Hirschberg, A. (2001). Introduction to aero-acoustics of internal flow. Technical report. *(p. 220)*

Hirschberg, A. and S. W. Rienstra (2004). *An introduction to aeroacoustics*. *(p. 6, 142, 145, 165, 235)*

Hochgreb, S., D. Dennis, I. Ayranci, W. Bainbridge, and S. Cant (2013). Forced and self-excited instabilities from lean premixed, liquid-fuelled aeroengine injectors at high pressures and temperatures - GT2013-95311. In *Proc. ASME Turbo Expo 2013*. *(p. 8, 173)*

Howe, M. S. (1979). On the theory of unsteady high Reynolds number flow through a circular aperture. *Proc. R. Soc. Lond. A 366*, 205–223. *(p. 157, 158, 182, 202, 220)*

Howe, M. S. (1998). *Acoustics of fluid-structure interactions*. Cambridge: Cambridge University Press. *(p. 181, 220)*

Hurle, I. R., R. B. Price, T. M. Sugden, and A. Thomas (1968). Sound emission from open turbulent premixed flames. *Proc. R. Soc. A 303*, 409–427. *(p. 29, 44, 72, 122, 174, 206)*

International Energy Agency (2017). Key world energy statistics. Technical report. *(p. 1)*

Jing, X. and X. Sun (2000). Effect of plate thickness on impedance of perforated plates with bias flow. *AIAA J. 38*(9). *(p. 159)*

Karimi, N. (2014). Response of a conical, laminar premixed flame to low amplitude acoustic forcing. A comparison between experiment and kinematic theories. *Energy 78*, 490–500. *(p. 15, 19, 31)*

Karimi, N., M. J. Brear, S. Jin, and J. P. Monty (2009). Linear and non-linear forced response of a conical, ducted, laminar premixed flame. *Combust. Flame 156*(11), 2201–2212. *(p. 15, 16, 18, 19, 20, 54)*

Kastner, G. F. E. (1876). *Les flammes chantantes: théorie des vibrations et considérations sur l'électricité*. Paris: Dentu et Lacroix. *(p. 5)*

Kedia, K. S., H. M. Altay, and A. F. Ghoniem (2011). Impact of flame-wall interaction on premixed flame dynamics and transfer function characteristics. *Proc. Combust. Inst. 33*, 1113–1120. *(p. 14, 25, 37, 60, 66, 83)*

Kedia, K. S. and A. F. Ghoniem (2013). An analytical model for the prediction of the dynamic response of premixed flames stabilized on a heat-conducting perforated plate. *Proc. Combust. Inst. 34*(1), 921–928. *(p. 25)*

Keller, J. J. (1995). Thermoacoustic oscillations in combustion chambers of gas turbines. *AIAA J. 33*(12), 2280–2287. *(p. 3, 5, 6, 171, 173, 205, 206, 234, 235, 237)*

Kerstein, A. R., W. T. Ashurst, and F. A. Williams (1988). Field equation for interface propagation in an unsteady homogeneous flow field. *Phys. Rev. A 37*(7), 2728–2731. *(p. 27)*

King, L. V. (1914). On the convection of heat from small cylinders in a stream of fluid: determination of the convection constants of small platinum wires, with applications to hot-wire anemometry. *Proc. R. Soc. A 90*(622), 563–570. *(p. 114)*

Kirchhoff, G. (1868). Ueber den einfluss der warmteleitung in einem gas auf die schallbewegung. *Ann. Phys. 134*(1), 177. *(p. 4)*

Kornilov, V. N., R. Rook, J. H. M. ten Thije Bookkamp, and L. P. H. de Goey (2009). Experimental and numerical investigation of the acoustic response of multi-slit Bunsen burners. *Combust. Flame 156*(10), 1957–1970. *(p. 6, 26, 237)*

Kornilov, V. N., K. R. A. M. Schreel, and L. P. H. de Goey (2007). Experimental assessment of the acoustic response of laminar premixed Bunsen

flames. *Proc. Combust. Inst. 31*, 1239–1246. *(p. 20, 27, 31)*

Krebs, W. and P. Flohr (2002). Thermoacoustic stability chart for high-intensity gas turbine combustion systems. *Combust. Sci. Technol. 174*, 99–128. *(p. 8)*

Krediet, H. J., C. H. Beck, W. Krebs, S. Schimek, and C. O. Paschereit (2012). Identification of the flame describing function of a premixed swirl flame from LES. *Combust. Sci. Technol. 184*(7-8), 888–900. *(p. 6, 205, 237)*

Kruger, U., J. Hüren, S. Hoffmann, W. Krebs, P. Flohr, and D. Bohn (2001). Prediction and measurement of thermoacoustic improvements in gas turbines with annular combustion systems. *J. Eng. Gas Turbines Power 123*(3), 557. *(p. 220)*

Laera, D., T. Schuller, K. Prieur, D. Durox, and S. M. Camporeale (2017). Flame describing function analysis of spinning and standing modes in an annular combustor and comparison with experiments. *Combust. Flame 184*, 136–152. *(p. 173, 205, 237)*

Lee, D. H. and T. C. Lieuwen (2003). Premixed flame kinematics in a longitudinal acoustic field. *J. Propul. Power 19*, 837–846. *(p. 27, 35)*

Levine, H. and J. Schwinger (1948). On the radiation of sound from an unflanged circular pipe. *Phys. Rev. 73*(4), 383–406. *(p. 148)*

Lewis, B. and G. von Elbe (1987). *Combustion, flames and explosions of gases*. New York: Academic Press. *(p. 45, 87)*

Li, J., D. Durox, F. Richecoeur, and T. Schuller (2015). Analysis of chemiluminescence, density and heat release rate fluctuations in acoustically perturbed laminar premixed flames. *Combust. Flame 162*(10), 3934–3945. *(p. 44, 72, 73, 74)*

Li, J., Y. Xia, A. S. Morgans, and X. Han (2017). Numerical prediction of combustion instability limit cycle oscillations for a combustor with a long flame. *Combust. Flame 185*, 28–43. *(p. 205)*

Lieuwen, T. and V. Yang (2005). *Combustion instabilities in gas turbine engines: operational experience, fundamental mechanisms, and modeling*, Volume 210. AIAA. *(p. 234)*

Lieuwen, T. C. (2005). *Unsteady combustor physics*. Cambridge University Press. *(p. 13, 14, 15, 20, 27, 181, 208, 234)*

Lighthill, M. J. (1952). On sound generated aerodynamically. *Proc. R. Soc. Lond. A 211*, 564–587. *(p. 182, 202)*

Luong, T., M. S. Howe, and R. S. McGowan (2005). On the Rayleigh conductivity of a bias-flow aperture. *J. Fluids Struct. 21*(8), 769–778. *(p. 158, 159)*

Manohar, M. (2011). *Thermo-acoustics of bunsen type premixed flames*. Ph. D. thesis. *(p. 25)*

Markstein, G. H. (1964). *Nonsteady flame propagation*. Markstein, G.H., Ed., Pergamon Press, Elmsford, NY. *(p. 28)*

Marx, C. (1841). Ueber das tönen erhitzter gläserner röhren. *J. für Prakt.*

Chemie 22. (p. 4)

Matsui, Y. (1981). An experimental study on pyro-acoustic amplification of premixed laminar flames. *Combust. Flame 43*, 199–209. *(p. 22, 23)*

McManus, K. R., T. Poinsot, and S. Candel (1993). A review of active control of combustion instabilities. *Prog. Energy Combust. Sci. 19*, 1–29. *(p. 4, 234)*

Mehta, P. G., M. C. Soteriou, and A. Banaszuk (2005). Impact of exothermicity on steady and linearized response of a premixed ducted flame. *Combust. Flame 141*(4), 392–405. *(p. 21)*

Mejia, D., L. Selle, R. Bazile, and T. Poinsot (2015). Wall-temperature effects on flame response to acoustic oscillations. *Proc. Combust. Inst. 35*(3), 3201–3208. *(p. 15, 21, 27)*

Merk, H. J. (1957). An analysis of unstable combustion of premixed gases. *Symp. (Int.) Combust. 6*(1), 500–512. *(p. 5, 6, 18, 236, 237)*

Merk, M., R. Gaudron, M. Gatti, C. Mirat, W. Polifke, and T. Schuller (2017). Quantitative comparisons between LES predictions and experimental measurements of sound pressure spectra in a confined swirl combustor. In *53rd AIAA/SAE/ASEE Jt. Propuls. Conf.*, pp. 1–16. *(p. 102, 110)*

Merk, M., C. Silva, W. Polifke, R. Gaudron, M. Gatti, M. Mirat, and T. Schuller (2018). Direct assessment of the acoustic scattering matrix of a turbulent swirl combustor by combining system identification, large eddy simulation and analytical approaches - GT2018-75529. In *Proc. ASME Turbo Expo 2018. (p. 237)*

Mirat, C. (2015). *Analyse des instabilités de combustion dans des foyers de centrale thermique fonctionnant au fioul lourd*. Ph. D. thesis. *(p. 273, 274)*

Mirat, C., D. Durox, and T. Schuller (2015). Stability analysis of a swirl spray combustor based on flame describing function. *Proc. Combust. Inst. 35*(3), 3291–3298. *(p. 173)*

Moeck, J. P. (2010). *Analysis, modeling, and control of thermoacoustic instabilities*. Ph. D. thesis. *(p. 239)*

Morse, P. M. and K. U. Ingard (1968). *Theoretical acoustics*. New York: McGraw-Hill. *(p. 140, 141, 164)*

Munjal, M. L. (1987). *Acoustics of ducts and mufflers*. John Wiley and Sons, Inc., New York. *(p. 6, 206, 207, 235, 236)*

Munt, R. M. (1977). The interaction of sound with a subsonic jet issuing from a semi-infinite cylindrical pipe. *J. Fluid Mech. 83*, 609–640. *(p. 149)*

Ni, F., M. Miguel-Brebion, F. Nicoud, and T. Poinsot (2017). Accounting for acoustic damping in a Helmholtz solver. *AIAA J. 55*(4), 1205–1220. *(p. 182, 220)*

Nicoud, F., L. Benoit, C. Sensiau, and T. Poinsot (2007). Acoustic modes in combustors with complex impedances and multidimensional active flames. *AIAA J. 45*(2), 426–441. *(p. 6, 168, 173, 205, 234)*

Nicoud, F. and T. Poinsot (2005). Thermoacoustic instabilities: Should the Rayleigh criterion be extended to include entropy changes. *Combust. Flame 142*, 153–159. *(p. 238)*

Noiray, N. (2007). *Analyse linéaire et non-linéaire des instabilités de combustion : application aux systèmes à injection multipoints et stratégies de contrôle*. Ph. D. thesis. *(p. 43)*

Noiray, N., D. Durox, T. Schuller, and S. Candel (2006a). Dynamique de flammes laminaires et couplage acoustique-combustion. In *Congrès Francoph. Tech. Laser, CFTL 2006*, Toulouse, France. *(p. 23)*

Noiray, N., D. Durox, T. Schuller, and S. Candel (2006b). Self-induced instabilities of premixed flames in a multiple injection configuration. *Combust. Flame 145*(3), 435–446. *(p. 22, 23, 83, 234)*

Noiray, N., D. Durox, T. Schuller, and S. Candel (2007). Passive control of combustion instabilities involving premixed flames anchored on perforated plates. *Proc. Combust. Inst. 31*(1), 1283–1290. *(p. 83)*

Noiray, N., D. Durox, T. Schuller, and S. Candel (2008). A unified framework for nonlinear combustion instability analysis based on the flame describing function. *J. Fluid Mech. 615*, 139. *(p. 6, 8, 171, 173, 201, 205, 206, 234, 237, 239)*

Noiray, N. and B. Schuermans (2013). On the dynamic nature of azimuthal thermoacoustic modes in annular gas turbine combustion chambers. *Proc. Roy. Soc. A 469*(2151). *(p. 173, 206)*

Nomura, Y., I. Yamamura, and S. Inawashiro (1960). On the acoustic radiation from a flanged circular pipe. *(p. 149)*

Norris, A. N. and I. C. Sheng (1989). Acoustic radiation from a circular pipe with an infinite flange. *J. Sound Vib. 135*(1), 85–93. *(p. 149)*

Orchini, A. and M. P. Juniper (2016). Linear stability and adjoint sensitivity analysis of thermoacoustic networks with premixed flames. *Combust. Flame 165*, 97–108. *(p. 19, 33, 57)*

Palies, P., D. Durox, T. Schuller, and S. Candel (2010). The combined dynamics of swirler and turbulent premixed swirling flames. *Combust. Flame 157*, 1698–1717. *(p. 228)*

Palies, P., D. Durox, T. Schuller, and S. Candel (2011a). Experimental study on the effect of swirler geometry and swirl number on flame describing functions. *Combust. Sci. Technol. 183*, 704–717. *(p. 97, 184)*

Palies, P., D. Durox, T. Schuller, and S. Candel (2011b). Nonlinear combustion instability analysis based on the flame describing function applied to turbulent premixed swirling flames. *Combust. Flame 158*(10), 1980–1991. *(p. 173, 201, 205, 206, 236, 237)*

Palies, P., T. Schuller, D. Durox, and S. Candel (2011). Modeling of premixed swirling flames transfer functions. *Proc. Combust. Inst. 33*(2), 2967–2974. *(p. 6, 237)*

Paschereit, C. O. and W. Polifke (1998). Investigation of the thermoacoustic characteristics of a lean premixed gas turbine burner - 98-GT-582. In

Proc. ASME Turbo Expo 1998, pp. 1–10. *(p. 6, 8, 113, 149, 151, 155, 181, 206, 207, 210, 215, 220, 234, 235, 237, 248, 275)*

Paschereit, C. O., B. Schuermans, W. Polifke, and O. Mattson (2002). Measurement of transfer matrices and source terms of premixed flames. *J. Eng. Gas Turbines Power 124*, 239–247. *(p. 8, 206, 207, 210)*

Pertersen, R. E. and H. W. Emmons (1961). Stability of laminar flames. *Phys. Fluids 4*, 456–464. *(p. 27)*

Pinaud, A. (1837). Ueber eine neue Art der Ton-Erzeugung. *Ann. Phys. 118*, 610–618. *(p. 4)*

Poinsot, T. (2017). Prediction and control of combustion instabilities in real engines. *Proc. Combust. Inst. 36*(1), 1–28. *(p. 4, 6, 13, 205, 234)*

Poinsot, T. and D. Veynante (2005). *Theoretical and numerical combustion*. *(p. 154, 155, 164, 168, 215, 234, 236, 238, 248, 275)*

Polifke, W., A. Fischer, and T. Sattelmayer (2003). Instability of a premix burner with nonmonotonic pressure drop characteristic. *J. Eng. Gas Turbines Power 125*, 20–27. *(p. 6, 220, 234)*

Polifke, W. and C. J. Lawn (2007). On the low-frequency limit of flame transfer functions. *Combust. Flame 151*(3), 437–451. *(p. 31, 57, 59, 227)*

Polifke, W., A. Poncet, C. Paschereit, and K. Döbbeling (2001). Reconstruction of acoustic transfer matrices by instationary computational fluid dynamics. *J. Sound Vib. 245*, 483–510. *(p. 6, 113, 151, 207, 215, 220, 236, 237, 248, 275)*

Preetham, S. H., S. Hemchandra, and T. Lieuwen (2008). Dynamics of laminar premixed flames forced by harmonic velocity disturbances. *J. Propul. Power 24*(6), 1390–1402. *(p. 14, 19, 20, 23, 27, 28, 30, 33, 54, 57, 205, 237)*

Prieur, K., D. Durox, T. Schuller, and S. Candel (2016). A hysteresis phenomenon leading to spinning or standing azimuthal instabilities in an annular combustor. *Combust. Flame 175*, 283–291. *(p. 239)*

Prieur, K., D. Durox, T. Schuller, and S. Candel (2018). Strong azimuthal combustion instabilities in a spray annular chamber with intermittent partial blow-off. *J. Eng. Gas Turbines Power 140*, 1–10. *(p. 234)*

Putnam, A. (1971). *Combustion driven oscillations in industry*. New-York: Elsevier. *(p. 234)*

Quinard, J. (1996). Acoustic induced instabilities of a V-shaped flame anchored on a rod. *Combust. Sci. Technol.*, 261–280. *(p. 27)*

Rayleigh, J. W. S. (1878). The explanation of certain acoustical phenomena. *Not. Proc. members R. Inst. (of Gt. Britain) 3*, 536–542. *(p. 4)*

Rienstra, S. W. and A. Hirschberg (2016). *An Introduction to acoustics*. Rienstra & Hirschberg. *(p. 117, 127, 146, 155, 181, 236, 267)*

Rijke, P. L. (1859). On the vibration of the air in a tube open at both ends. *Philos. Mag. 17*(1), 419–422. *(p. 4)*

Rodriguez-Martinez, V. M., J. R. Dawson, T. O'Doherty, and N. Syred

(2006). Low-frequency combustion oscillations in a Swirl burner/furnace. *J. Propul. Power 22*(1). *(p. 234)*

Rook, R. and L. P. H. De Goey (2003). The acoustic response of burner stabilized flat flames: a two dimensional numerical analysis. *Combust. Flame 133*, 119–132. *(p. 23)*

Rook, R., L. P. H. de Goey, L. M. T. Somers, K. R. A. M. Schreel, and R. Parchen (2002). Response of burner-stabilized flat flames to acoustic perturbations. *Combust. Theor. Model. 6*, 223–242. *(p. 23, 24, 26, 35, 37, 66, 83, 85, 87)*

Sattelmayer, T., M. P. Felchlin, J. Haumann, J. Hellat, and D. Styner (1992). Second generation low-emission combustors for ABB gas turbines: burner development and tests at atmospheric pressure. *J. Eng. Gas Turbines Power 114*, 118–125. *(p. 3, 5)*

Sattelmayer, T. and W. Polifke (2003). Assessment of methods for the computation of linear stability of combustors. *Combust. Sci. Technol. 175*(3), 453–476. *(p. 13, 173, 205)*

Scarpato, A. (2014). *Linear and nonlinear analysis of the acoustic response of perforated plates traversed by a bias flow*. Ph. D. thesis, Ecole Centrale Paris. *(p. 130, 160)*

Scarpato, A., S. Ducruix, and T. Schuller (2013). Optimal and off-design operations of acoustic dampers using perforated plates backed by a cavity. *J. Sound Vib. 332*(20), 4856–4875. *(p. 157, 158, 159)*

Scarpato, A., N. Tran, S. Ducruix, and T. Schuller (2012). Modeling the damping properties of perforated screens traversed by a bias flow and backed by a cavity at low Strouhal number. *J. Sound Vib. 331*, 276–290. *(p. 209)*

Schlimpert, S., S. Hemchandra, M. Meinke, and W. Schröder (2015). Hydrodynamic instability and shear layer effect on the response of an acoustically excited laminar premixed flame. *Combust. Flame 162*(2), 345–367. *(p. 14, 22)*

Schreel, K. R. A. M., R. Rook, and L. P. H. de Goey (2002). The acoustic response of burner stabilized premixed flat flames. *Proc. Combust. Inst. 29*, 115–122. *(p. 23, 24, 66)*

Schreel, K. R. A. M., E. L. van den Tillaart, and L. P. H. de Goey (2005). The influence of burner material properties on the acoustical transfer function of radiant surface burners. *Proc. Combust. Inst. 30*, 1741–1748. *(p. 23)*

Schuermans, B., C. O. Paschereit, and P. Monkewitz (2006). Non-linear combustion instabilities in annular gas-turbine combustors. In *44th AIAA Aerosp. Sci. Meet. Exhib. (p. 173)*

Schuermans, B., W. Polifke, C. O. Paschereit, and J. H. van der Linden (2000). Prediction of acoustic pressure spectra in combustion systems using swirl stabilized gas turbine burners - 2000-GT-0105. In *Proc. ASME Turbo Expo 2000. (p. 6, 8, 150, 207, 234, 235, 237)*

Schuermans, B. B. H., W. Polifke, and C. O. Paschereit (1999). Modeling

transfer matrices of premixed flames and comparison with experimental results. In *Proc. ASME Turbo Expo 1999. (p. 6, 236, 237, 238)*

Schuller, T. (2003). *Mécanismes de couplage dans les interactions acoustique-combustion.* Ph. D. thesis, Ecole Centrale Paris, Châtenay-Malabry, France. *(p. 4, 41)*

Schuller, T., S. Ducruix, D. Durox, and S. Candel (2002). Modeling tools for the prediction of premixed flame transfer function. *Proc. Combust. Inst. 29*, 107–113. *(p. 15, 19, 30, 31, 41, 58)*

Schuller, T., D. Durox, and S. Candel (2002). Dynamics of and noise radiated by a perturbed impinging premixed jet flame. *Combust. Flame 128*(1-2), 88–110. *(p. 44, 72, 74)*

Schuller, T., D. Durox, and S. Candel (2003a). A unified model for the prediction of laminar flame transfer functions: comparisons between conical and V-flame dynamics. *Combust. Flame 134*, 21–34. *(p. 6, 15, 16, 19, 22, 23, 28, 29, 30, 31, 54, 57, 87, 205, 208, 237)*

Schuller, T., D. Durox, and S. Candel (2003b). Self-induced combustion oscillations of laminar premixed flames stabilized on annular burners. *Combust. Flame 135*(4), 525–537. *(p. 16, 173, 228, 236, 273)*

Schuller, T., N. Tran, N. Noiray, D. Durox, S. Ducruix, and S. Candel (2009). The role of nonlinear acoustic boundary conditions in combustion/acoustic coupled instabilities. In *Proc. ASME Turbo Expo 2009*, Number GT2009-59390. *(p. 220)*

Selle, L., L. Benoit, T. Poinsot, F. Nicoud, and W. Krebs (2006). Joint use of compressible large-eddy simulation and Helmholtz solvers for the analysis of rotating modes in an industrial swirled burner. *Combust. Flame 145*(1-2), 194–205. *(p. 236)*

Seume, J. R., N. Vortmeyer, W. Krause, J. Hermann, C.-C. Hantschk, P. Zangl, S. Gleis, D. Vortmeyer, and A. Orthmann (1998). Application of active combustion instability control to a heavy duty gas turbine. *J. Eng. Gas Turbines Power 120*(4), 721–726. *(p. 234)*

Shepherd, W. (2003). *Energy studies* (2nd ed.). Imperial College Press. *(p. 2)*

Silva, C. F., F. Nicoud, T. Schuller, D. Durox, and S. Candel (2013). Combining a Helmholtz solver with the flame describing function to assess combustion instability in a premixed swirled combustor. *Combust. Flame 160*(9), 1743–1754. *(p. 205, 237)*

Sondhauss, K. (1850). Über die schallschwingungen der luft in erhitzten glasrohren und in gedeckten pfeifen von ungleicher weite. *Ann. der Phys. und Chemie (Johann Christ. Poggendorff) 79*(1), 1–34. *(p. 4)*

Strutt, J. W. and B. Rayleigh (1878). *The theory of sound - volume II. (p. 157, 158, 238)*

Su, J., A. Garmory, and J. Carrotte (2015). The aerodynamic response of fuel injector passages to incident acoustic waves - GT2015-43248. In *Proc. ASME Turbo Expo 2015. (p. 220)*

Sugimoto, T. and Y. Matsui (1982). An experimental study on the dynamic

behavior of premixed laminar flames. *Symp. (Int.) Combust. 19*(1), 245–250. *(p. 22, 23)*

Talei, M., M. J. Brear, and E. R. Hawkes (2011). Sound generation by laminar premixed flame annihilation. *J. Fluid Mech. 679*, 194–218. *(p. 87)*

Tay-Wo-Chong, L., S. Bomberg, A. Ulhaq, and W. Polifke (2012). Comparative validation study on identification of premixed flame transfer function. *J. Eng. Gas Turbines Power 134*(2), 021502 (1–8). *(p. 207)*

Tay Wo Chong, L., T. Komarek, R. Kaess, S. Föller, and W. Polifke (2010). Identification of flame transfer functions from LES of a premixed swirl burner. *Proc. ASME Turbo Expo 2010*. *(p. 6, 207, 237)*

Tran, N., S. Ducruix, and T. Schuller (2009a). Damping combustion instabilities with perforates at the premixer inlet of a swirled burner. *Proc. Combust. Inst. 32*(2), 2917–2924. *(p. 119, 234, 246)*

Tran, N., S. Ducruix, and T. Schuller (2009b). Passive control of the inlet acoustic boundary of a swirled burner at high amplitude combustion instabilities. *J. Eng. Gas Turbines Power 131*(5), 051502. *(p. 130)*

Truffin, K. and T. Poinsot (2005). Comparison and extension of methods for acoustic identification of burners. *Combust. Flame 142*(4), 388–400. *(p. 15, 31, 193, 206, 207, 237, 238)*

Vagelopoulos, C. M. and F. N. Egolfopoulos (1998). Direct experimental determination of laminar flame speeds. *Symp. (Int.) Combust. 27*, 513–519. *(p. 47)*

Wakeham, W. A. and D. H. Slater (1973). Diffusion coefficients for n-alkanes in binary gaseous mixtures with nitrogen. *J. Phys. B Atom. Molec. Phys. 6*, 886–896. *(p. 77)*

Wichman, I. S. and R. Vance (1997). A study of one-dimensional laminar premixed flame annihilation. *Combust. Flame 110*(4), 508–523. *(p. 87)*

Yamaoka, I. and H. Tsuji (1985). Determination of burning velocity using counterflow flames. *Proc. Combust. Inst. 20*(1), 1883–1892. *(p. 47, 74, 89)*

Yang, V. and F. E. C. Culick (1986). Analysis of low frequency combustion instabilities in a laboratory ramjet combustor. *Combust. Sci. Technol. 45*, 1–25. *(p. 234)*

Yu, K. H., A. Trouvé, and J. W. Daily (1991). Low-frequency pressure oscillations in a model ramjet combustor. *J. Fluid Mech. 232*, 47–72. *(p. 234)*

Zähringer, K., D. Durox, and F. Lacas (2003). Helmholtz behavior and transfer function of an industrial fuel swirl burner used in heating systems. *Int. J. Heat Mass Transf. 46*(18), 3539–3548. *(p. 14)*

Zhu, M., A. P. Dowling, and K. N. C. Bray (2001). Self-excited oscillations in combustors with spray atomizers. *J. Eng. Gas Turbines Power 123*(1), 8. *(p. 234)*

université PARIS-SACLAY
ÉCOLE DOCTORALE
Sciences mécaniques et énergétiques, matériaux et géosciences (SMEMAG)

Titre : Réponse acoustique de flammes prémélangées soumises à des ondes sonores harmoniques

Mots clés : Thermoacoustique, FTF, FDF, Réseaux d'éléments acoustiques, Analyse de stabilité

Résumé : Les instabilités thermoacoustiques sont un problème majeur pour la production d'électricité ainsi que dans l'industrie aérospatiale. Ces instabilités sont dues à un transfert d'énergie entre une source chaude, le plus souvent une flamme stabilisée dans un brûleur, et le champ acoustique environnant. Les instabilités de combustion peuvent avoir de nombreuses conséquences délétères telles que l'extinction de la flamme, l'augmentation des flux de chaleur pariétaux, l'émission d'ondes sonores de grande amplitude à certaines fréquences, des vibrations importantes, des dégâts structurels et même l'explosion du moteur dans certains cas. Cependant, la prédiction de la stabilité thermoacoustique d'un brûleur demeure une tâche ardue. Une technique pour prédire l'apparition d'instabilités de combustion est de coupler un solveur acoustique avec une fonction décrivant la réponse de la flamme lorsque celle-ci est soumise à des ondes acoustiques harmoniques. Cette fonction, appelée Fonction de Transfert de Flamme (FTF) ou Fonction Descriptive de Flamme (FDF) lorsqu'elle est non-linéaire, est ensuite déterminée en utilisant des expériences, des simulations numériques ou des modèles analytiques. Néanmoins, l'impact de divers paramètres tels que le niveau de forçage acoustique, la façon dont le forçage est introduit dans le système ou encore la modification de la taille de la zone de réaction sur la réponse acoustique de la flamme est encore mal compris. L'objectif de cette thèse est donc d'étudier la réponse acoustique de flammes prémélangées laminaires et turbulentes soumises à des ondes acoustiques harmoniques dans le but d'améliorer la prédiction de la stabilité thermoacoustique des brûleurs, qu'ils soient industriels ou de taille plus réduite. Le cas des flammes prémélangées laminaires coniques, qui sont rencontrées dans de nombreux brûleurs industriels et domestiques de faible puissance, est d'abord examiné. Dans un second temps, la réponse acoustique de flammes prémélangées confinées turbulentes soumises à des ondes acoustiques harmoniques est étudiée d'une part expérimentalement et d'autre part en employant plusieurs approches analytiques. Une première série d'expériences est consacrée à l'étude des FDF définies par rapport à différents signaux de référence. Il est démontré que toutes ces FDF peuvent être reliées entre elles analytiquement en utilisant un réseau non-linéaire d'éléments acoustiques. De plus, il est observé que la FDF est différente en fonction de la façon dont le forçage acoustique est introduit dans le brûleur, excepté lorsque le signal de référence est la vitesse acoustique juste avant la flamme. Dans une seconde série d'expériences, la matrice de transfert acoustique représentant le brûleur est mesurée à froid et à chaud (en présence d'une flamme) et pour un injecteur tourbillonnant et non-tourbillonnant. Le niveau de forçage acoustique est contrôlé au niveau du fil chaud et des mesures sont effectuées pour plusieurs niveaux de forçage prédéfinis. Il est ainsi démontré que la réponse acoustique du brûleur est non-linéaire aussi bien à froid qu'à chaud. De plus, deux réseaux d'éléments acoustiques représentant le brûleur à froid et à chaud sont conçus. Les mesures et prédictions de la matrice de transfert acoustique sont en accord aussi bien à froid qu'à chaud. La FDF mesurée en utilisant une technique optique est également reconstruite avec succès à partir des mesures de la matrice de transfert acoustique. Enfin, la stabilité thermoacoustique de six configurations différentes du brûleur est prédite en utilisant deux réseaux d'éléments acoustiques. Dans le premier réseau, la réponse acoustique de la flamme est prise en compte en utilisant une FDF préalablement mesurée tandis que dans le second réseau, la réponse de la flamme est incluse dans la mesure de la matrice de transfert acoustique correspondant à la majeure partie du brûleur. Ces deux modèles sont capables de prédire l'apparition d'instabilités thermoacoustiques ainsi que la fréquence de ces instabilités le cas échéant. Néanmoins, le modèle basé sur la FDF ne prédit pas l'amplitude du cycle limite de façon satisfaisante contrairement au modèle basé sur la mesure de la matrice de transfert acoustique. Cette observation s'explique par la façon dont les pertes acoustiques à l'intérieur du brûleur sont prises en compte.

Title: Acoustic response of premixed flames submitted to harmonic sound waves

Keywords: Thermoacoustics, FTF, FDF, Acoustic network models, Acoustic Transfer Matrices, Stability analysis

Abstract: Thermoacoustic instabilities are a major concern in the aerospace and energy production industries. They are due to an energy transfer between a heat source, usually a flame stabilized inside a combustor, and the surrounding acoustic field and may lead to undesirable phenomena such as flame extinction, increased heat fluxes, very large sound emissions at certain frequencies, vibration, structural damage and even catastrophic failure in some cases. However, predicting the thermoacoustic stability of a combustor at an early design stage is a challenging task. One way to predict the onset of thermoacoustic instabilities is to couple an acoustic solver with a function that describes the frequency response of the flame when submitted to harmonic sound waves. This function, called a Flame Transfer Function (FTF) or a Flame Describing Function (FDF) when it is nonlinear, is then determined using experiments, numerical simulations or analytical models. However, the impact of many parameters such as the forcing level, the way sound waves are introduced inside the combustor, or a modification of the flame size on the flame frequency response remain poorly understood. The objective of this thesis is to study the acoustic response of various laminar and turbulent premixed flames submitted to harmonic sound waves using experiments and analytical approaches in order to improve the thermoacoustic stability predictions of lab scale and industrial combustors. The case of premixed laminar conical flames, used in a variety of domestic and industrial low-power combustors, is first investigated. The acoustic response of premixed confined turbulent flames submitted to harmonic forcing is then investigated using experiments and various modeling strategies. In a first set of experiments, the FDF defined with respect to various reference signals is measured using an optical technique. All these describing functions are then related using a nonlinear acoustic network model. Moreover, the FDF is shown to be different depending on the way acoustic forcing is introduced inside the combustor, except when the reference signal is the acoustic velocity assessed just before the flame. In a second set of experiments, the Dimensionless Acoustic Transfer Matrix (DATM) of the burner is measured for cold and reactive conditions and with a swirling and non-swirling injector. The acoustic forcing level is controlled at the hot wire location and measurements are performed for various predefined forcing levels. The acoustic response of the burner is found to be nonlinear for both cold and reactive conditions. Moreover, two acoustic network models representing the burner operated for cold and reactive conditions are assembled. The measured and predicted DATM are then found to be in good agreement for cold and reactive conditions and for both injectors. The FDF measured using optical techniques is also reconstructed from the DATM measurements with excellent agreement. Finally, the thermoacoustic stability of six distinct configurations of the burner is predicted for reactive conditions using two acoustic network models. In the first model, the acoustic response of the flame is accounted for using a measured FDF while in the second model, the flame response is embedded inside a measured DATM. Both models are able to predict the onset of thermoacoustic instabilities and the associated frequency of the instability. However, the model based on the FDF does not predict the correct limit cycle amplitude as opposed to the model based on the DATM measurement. This is attributed to the way acoustic losses occurring inside the combustor are taken into account.

Université Paris-Saclay
Espace Technologique / Immeuble Discovery
Route de l'Orme aux Merisiers RD 128 / 91190 Saint-Aubin, France